SUBMILLIMETER AND INFRARED STUDIES OF MASS LOST BY ASYMPTOTIC GIANT BRANCH STARS

Thesis by

Kenneth Harbour Young

In Partial Fulfillment of the Requirements

for the Degree of

Doctor of Philosophy

California Institute of Technology

Pasadena, California

1994

(Submitted August, 1993)

Acknowledgements

Gosh this has taken a lot longer than it should have! On the other hand, being a graduate student off and on for the last 13 years has allowed me to meet many wonderful folks, some of whom I'd like to thank here.

First thanks must go to my advisor, Tom Phillips, who convinced me to return to graduate school after an extensive hiatus. I can't imagine why he puts himself through the agony of running the CSO, but I and many others are lucky that he does. He has always made time for me when I needed help of any kind.

Jill Knapp introduced me to the study of evolved stars, and has been encouraging and helpful at every turn. Gene Serabyn has a unique way of cutting to the heart of an issue; I'd have never written any of this had he not talked some sense into me. Jocelyn Keene has been a great pleasure to work with because she puts uncommon effort into collaborative projects.

Fellow grad. students *Luftdoktor* Thomas Büttgenbach and Todd Groesbeck have helped me maintain some sense of perspective. James Fillmore convinced me to "Stop torturing Caltech."

Caltech is a great place to be a grad. student, and some of the staff really go beyond the call of duty to be helpful. I've yet to run into anyone who's spent time in the astronomy department who does not sing the praises of Helen Knudsen, the department's marvelous librarian. Antony Schinckel, technical manager of the CSO, works at least two full time jobs keeping the observatory from disintegrating. Thanks must also go to administrative assistants Pat Neill and Susan McCurdy, who have struggled mightily to keep the submillimeter astronomy group in approximate compliance with the laws of man and nature.

I'd like to thank the Loose Cannons of Southern California. Specifically Nader Enghetta, the Phantom of the Community College; Barry Mauer, the incarnation of the Midwestern ethos; Mark "Dolson"*, who introduced me to the twin joys of hiking and over-eating; Afshin Nasiri (hereafter in this thesis referred to as "The 'Har" except in the appendix to chapter 2 and the figures in chapter 4 wherein he is referred to as "The Big 'Har") who must be given a great

* Member, Poker and Pan Casino Association of Gardina

deal of credit (because he demands it); and finally Marios Vassiliou, who along with The 'Har has greatly expanded upon the traditional definition of science, and with whom I cofounded *The Center for Gracious Living* at Apt. 7, 435 North Euclid, Pasadena.

Final and deepest thanks must go to my family. My siblings, Lorna, Bob and Joanne, have provided frequent expressions of love and support, and three sympathetic sets of ears. Most of all I thank my parents, Robert and Helen Young; even *I* am enough of a theoretician to know that none of this would have been done without them.

Abstract

This thesis consists of four separate studies of the material ejected from highly evolved red giant stars, preceded by a brief introductory chapter.

Chapter 2 presents the results of an attempt to identify all the post main sequence stars in the sky with circumstellar shells large enough to have been resolved by the *IRAS* satellite. Both the 60μm and 100μ survey mode data were used. A total of 512 stars were examined, including all evolved stars with envelopes which had been detected in surveys of mm or submm CO emission. A total of 76 stars were found to have shells with radii exceeding 2' in the 60μ data. Most of these resolved shells surround semiregular variable stars. Although only 40% of the resolved objects are carbon stars, the fraction of carbon stars with resolved envelopes is higher than that of oxygen–rich stars. The linear sizes of these shells were calculated; the average shell size is 0.76 pc. If a measurement of the expansion velocity was available from CO observations, the age of the shell was estimated using a simple model of the shell's interaction with the ISM. Some of the shells appear to be detached, and in most cases shells with inner radii greater than $\sim$ 0.3 pc have no detectable CO. The duration of mass loss for Mira variables and carbon stars is estimated to be 10^5 and 2×10^5 years, respectively. The procedure by which the data were analysed is explained in the appendix to chapter 2, which also contains the results of several tests performed to verify the results statistically.

A survey of CO(3–2) emission from Mira variables comprises chapter 3. The survey examined nearby oxygen–rich Miras, without regard to their infrared properties. Several new detections were made, including some circumstellar shells with expansion velocities lower than any previously reported. Mass loss rates for the detected stars were calculated. While the mass loss rate shows significant correlation with all 4 *IRAS* fluxes (when normalized by distance), it appears completely uncorrelated with any color derived from these fluxes. A star's spectral type at maximum light was found to be a good predictor of which stars would be detectable; no star earlier than M5.5 was detected even though some such stars had large *IRAS* fluxes. A power–law

relationship was found between the envelope expansion velocity and the star's mass loss rate. Extrapolation of this result implies that envelopes with expansion velocities above ~ 18 km s^{-1} must be optically thick.

The peculiar submm emission line profiles of CRL 2688, a protoplanetary nebula, are examined in chapter 4. The molecular envelope was found to have three kinematic components, including a previously undetected ~ 100 km s^{-1} wind. The mechanical momentum in this high velocity wind appears to be much too large to have been supplied by radiation pressure. A strong self–absorption feature seen in the CO emission lines was examined at very high spectral resolution, and was found to have an extremely sharp blue edge. The sharpness of this feature shows that the velocity field in the extended envelope is very well ordered.

The final chapter examines atomic carbon emission in the envelope of the young planetary nebula NGC 7027. Neutral carbon, traced by the 609μm hyperfine line, is extended over a region 30–40" in diameter, and appears to be coextensive with CO throughout most of the neutral envelope. A 158μm spectrum of C II was used to calculate a lower limit to the C II mass. There appears to be roughly equal amounts of CO, C I and C II in the inner neutral envelope. Most of the atomic carbon must have been liberated by photodissociation of CO. Estimates of the mass loss rate for this object derived from CO observations may be too low by a factor of ~ 3.

Table of Contents

List of Figures

List of Tables

Introduction

The subject of this thesis is the material lost from Asymptotic Giant Branch (AGB) stars, a class of red giant star. This chapter will provide a sketch of the history, the current status, and the unresolved questions in the study of these objects.

1. Discovery of Mass Loss from Red Giants

In 1956 Shklovsky published a seminal paper which outlined in broad strokes the interrelationship of red giants, planetary nebulae and white dwarfs. He first estimated the distance to nearby planetary nebulae, from which he calculated their local space density. Extrapolating this result, he concluded that our galaxy contains some 6×10^4 of these objects. The expansion velocities of planetary nebulae are easily obtained from their emission lines, and from this velocity he concluded that a planetary nebula would remain visible for about $\sim 10^4$ years. Thus several must be formed each year. This rate is far higher than the rate of supernovae in our galaxy ($\sim 10^{-2}$ yr^{-1}), therefore supernovae could not have given birth to most of these nebulae. He speculated on what the progenitor of a planetary nebula must have looked like, before the slowly expanding envelope had been ejected. His conclusion was that it must have consisted of a large neutral envelope resting upon a hidden white dwarf. This was just the structure that had recently been deduced theoretically (Schwarzschild, Rabinowitz and Härm, 1953) for red giant stars. He noted that while some of the planetary nebula central stars resembled extremely hot white dwarfs, most did not, and concluded that the central stars were in a period of rapid evolution. In this one paper he presented the sequence of events which to this day is believed to terminate the evolution of most stars: Red giant stars somehow eject all the mass above their dense cores. The super–hot core ionizes a portion of the envelope, and the material is visible briefly as a planetary nebula. Once the envelope material has dissipated, what is left is an isolated white dwarf which cools and rapidly drops in luminosity.

That same year Deutsch (1956) provided proof that evolutionarily significant amounts of material were indeed expelled from some red giants. He presented optical spectra of both stars

in the visual binary system α Her, which consists of a supergiant M star and a fainter G giant, which is itself a spectroscopic binary. Toward the red giant, he detected many narrow absorption lines from neutral and singly ionized atomic species, which were blue–shifted with respect to the rest of the stellar spectrum. Such absorption lines are visible in the spectra of many red supergiants, however the unique geometry of α Her allowed Deutsch to deduce the location of the absorbing material. Several of these same absorption lines were visible against the G star's spectrum, but they did not share the velocity shifts of the spectroscopic binary pair. From this he was able to determine that the entire 3 star system was embedded in a circumstellar envelope, with a minimum radius of 1000 AU. The expansion velocity implied by the blue–shifted absorption line, 10 km s^{-1}, was well above the escape velocity at such a distance, and showed that material must be lost from the entire system. He calculated the mass loss rate to be $3 \times 10^{-8}\ M_{\odot}\mathrm{yr}^{-1}$.

The cool red giant stars and their dusty envelopes radiate most of their energy in the infrared, while the molecular gas in the envelope is cooled by millimeter and submillimeter emission lines. Thus the detailed study of the ejected material became possible with the near simultaneous advent of infrared and high–frequency radio astronomy. The first survey of most of the sky in the near infrared was the Two Micron Sky Survey (Neugebauer and Leighton, 1969). In addition to detecting strong emission from well–known red giant stars, the survey discovered a new class of heavily dust enshrouded supergiants. One of these stars, IRC+10°216, is the brightest object in the near–infrared sky (outside of the solar system), yet it is difficult to detect the visible light. Later the AFGL four color survey (Price and Walker, 1976), explored the sky at longer wavelengths, and detected even cooler objects. Two of these, CRL 618 and CRL 2688, are the best examples of protoplanetary nebulae, an evolutionary "missing link" between red giants and planetary nebulae.

While these early infrared surveys were being conducted, radio astronomy progressed to the point where the gaseous component of the circumstellar shell (CSS) could be detected. Maser lines of SiO, H_2O and OH were detected around many stars (an extensive review of maser emission from these stars is given by Herman and Habing, 1985). The most important of these maser lines is the 1612 MHz OH transition, which was first detected in an evolved star's envelope in 1968 by Wilson and Barret. This OH maser emission is so intense, it can be detected from stars many kiloparsecs away. Several surveys of OH emission were undertaken in the mid 1970's, and

stars discovered in this way were christened OH/IR stars. The 1612 MHz transition is usually saturated, and produces a simple two–spike spectrum from which the envelope expansion velocity can easily be calculated. The intense maser emission also makes these stars excellent candidates for interferometer mapping; many of them show complete, nearly spherical shells, proving that the expanding envelope continues to be well–ordered at great distances ($\sim 10^{16}$ cm) from the star. The 1612 MHz line is pumped by stellar IR photons, and often varies in intensity due to the variability of the central star. The phase lag of these variations, along with the angular size obtained by interferometry, allows the distance to the star to be calculated.

The $J = 1 \rightarrow 0$ rotational transition of CO was first detected from IRC+10°216 in 1970, by Solomon *et al.* (1971). Surveys in the 1970's and 1980's lead to the detection of this line from several hundred evolved stars. Three characteristics of CO emission make it particularly important. First, strong maser emission is never seen from CO; the emission is thermal and often lines of both large and small optical depth can be found when transitions from several isotopic substitutions are observed. The well–ordered nature of the stellar wind, which expands at velocities greatly in excess of the local sound speed, allows simple radiative transfer models based on the Sobolev, or Large Velocity Gradient, approximation to reproduce the observed line–shapes well (Morris 1980). Secondly, CO is composed of the 3rd and 4th most abundant elements in the stellar wind, so the molecular abundance is high. Finally, unlike any of the molecules producing maser emission, CO is present in the outflows of both oxygen–rich and carbon–rich stars.

A revolution in the study of evolved stars followed the 1983 *IRAS* survey (Neugebauer *et al.* 1984). The *IRAS* point source catalog contains nearly a quarter of a million objects, one third of which are stars with circumstellar shells. The envelopes of some of the nearest of these stars were well resolved (see chapter 2). The $\sim$ 1 Jy sensitivity of *IRAS* allowed it to detect a CSS anywhere within our galaxy. In addition to broad–band photometry, *IRAS* obtained low resolution spectra of thousands of the brightest evolved stars, many of which showed the spectral features at 9.8μm and 11.5μm characteristic of dust emission from silicates and silicon carbide, respectively.

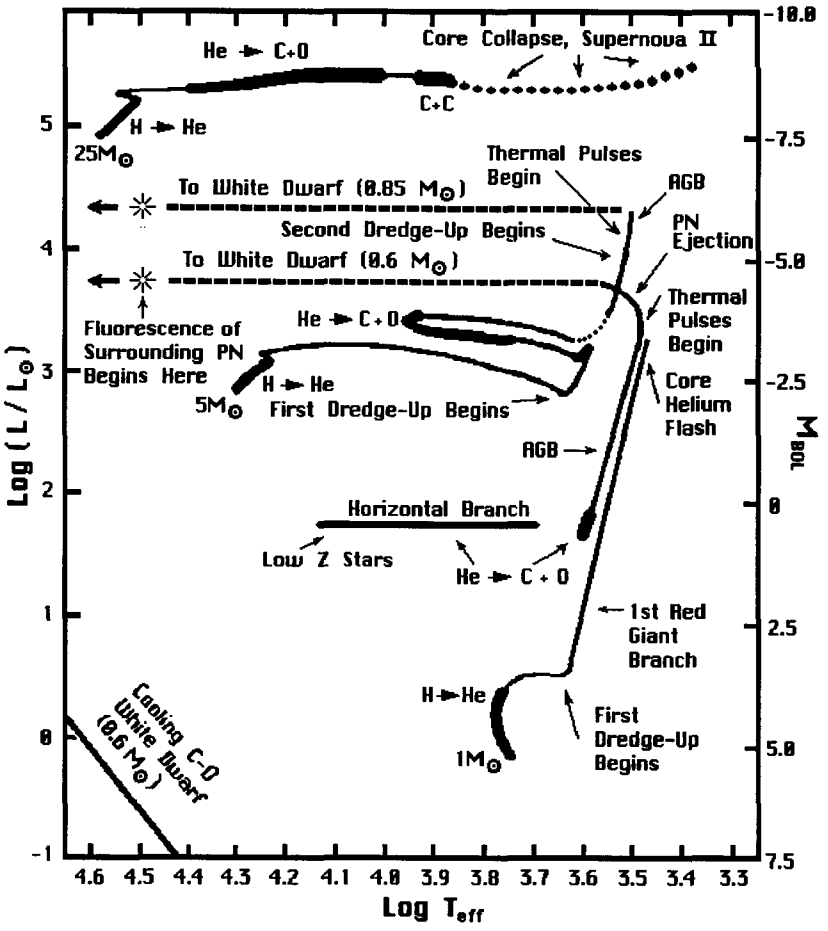

Fig. 1. The main sequence and post main sequence evolution of 3 stars with masses 1 $M_\odot$, 5 $M_\odot$ and 25 $M_\odot$ is sketched on an H–R diagram. The 25 $M_\odot$ star never develops a degenerate C–O core, and hence never passes through the AGB. The thick portions of the evolutionary tracks correspond to periods of slow evolution, when the abundant elements are burned in the core. Adapted from Iben (1985).

2. The Asymptotic Giant Branch

As is the case with many astronomical objects, AGB stars have a name which reveals very little about their nature. The name originated from the distribution of stars on the H–R diagrams of globular clusters. The stars appearing in a region cooler and more luminous than the horizontal branch, asymptotically approaching the red giant branch (RGB) at higher luminosities, were said to be on the asymptotic giant branch. As the theory of post main sequence stellar evolution developed, the name came to be applied to any star with a degenerate core of carbon and oxygen, surrounded by an extensive cool convective envelope. Figure 1, shows the evolutionary paths of

three stars, two of which spend a portion of their lives on the AGB. As the figure shows, the AGB closely approaches the RGB only for low mass stars. Because an AGB star's envelope is convective, it moves nearly vertically on the H–R diagram, closely mimicking a Hayashi track for a pre–main sequence star.

Excellent reviews of the entire post main sequence evolution of intermediate and low mass stars are presented by Iben and Renzini (1983) and Iben (1985). Not all stars pass through the AGB stage; stars with main sequence (MS) masses above 8–9 $M_{\odot}$ burn carbon rather than developing an inert C–O core. It is clear from globular clusters that stars somewhat less massive than the Sun do reach the AGB, and it is difficult to establish a MS mass lower limit for the AGB, because of the extraordinarily long MS lifetimes of stars with masses much below 1 $M_{\odot}$. Within the MS mass range of 1–8 $M_{\odot}$, all stars will pass through the AGB unless a companion disrupts their normal development.

Although the C–O core of an AGB star is inert, hydrogen burning continues at the base of the hydrogen–rich envelope. The helium ashes from the hydrogen burning form a layer just above the C–O core. While the core contributes no energy to the star, Paczinski (1970) found that it is the mass of this core which determines the stellar luminosity. He derived the theoretical result

$$L/L_{\odot} = 5.9 \times 10^4 \, ((M_{core}/M_{\odot}) - 0.5).$$

This luminosity is supplied by the nuclear burning above the core, and the products of the nuclear burning increase the core mass. Thus the rate of core mass growth is proportional to the core mass, implying both the core mass and luminosity grow exponentially. The luminosity predicted by the Paczinski relation allows the time scale for significant changes in the stars' luminosity and structure to be calculated. For a core mass of 0.7 $M_{\odot}$ this evolutionary time scale is about 10^6 years. If energy were the only thing being lost from an AGB star, one would expect that all AGB stars with MS masses greater than about 1.5 $M_{\odot}$ would eventually develop a core more massive than the Chandrasekhar limit, and form a type I supernovae. However the lower mass limit for supernovae is believed to be at least 5 $M_{\odot}$. The most likely explanation for this disparity is that stars must lose $\gtrsim 1$ $M_{\odot}$ after departing from the main sequence, but before the end of the AGB.

If most of this mass loss occurs while the star is on the AGB, then it is constrained by the AGB evolutionary time scale, and must average to $\sim 10^{-6}\ M_{\odot}\mathrm{yr}^{-1}$ over the star's AGB lifetime.

When the AGB core mass exceeds $0.7\ M_{\odot}$, helium fusion becomes possible via the triple α process in the layer between the hydrogen burning shell and the C–O core. This leads to relaxation oscillations, where the hydrogen shell burns until enough helium has accumulated to allow a brief period of intense helium burning. The energy released by this pulse of helium burning lifts and cools the hydrogen envelope, briefly extinguishing hydrogen fusion. After this event, called a "thermal pulse," the ashes from the helium burning increase the mass of the C–O core. Hydrogen burning resumes shortly after the helium burning ceases, and the cycle is started anew. The time between thermal pulses varies from several hundred thousand years for low mass stars, down to a few thousand years for the most massive AGB stars. As the hydrogen envelope is lifted during a thermal pulse, the outer convective zone extends further inward, and can reach material that has undergone nuclear processing, a process called "dredge–up." Because the outer envelope of a red giant is aways convective, this processed material can reach the surface and change the elemental abundances of the photosphere. The most dramatic evidence that this does actually occur was the 1952 discovery by Merrill of the unstable element Technetium in the spectra of red giants believed to be on the AGB. If the convective region reaches material which has been enriched with carbon, perhaps by high temperature CNO processing or helium burning, carbon may in time become more abundant at the surface than oxygen, and the star will be transformed into a carbon star. However the effects of this dredge–up (often called the third dredge–up, because there are two eras before the onset of thermal pulses when the products of nuclear burning can be brought to the surface – see figure 1) are difficult to calculate, as they are sensitive to the mixing length, a free parameter in the theory of convective transport.

Essentially all red stars are variable to some degree. At least some of the AGB stars show spectacular variability in the visible (V) band; V band amplitudes of 10 magnitudes are not uncommon. These stars are the Long Period Variables (LPVs), the most regular of which are called Mira variables. The infrared and bolometric variability of these stars is much more muted, typically only 1 magnitude. Radial velocity variations in spectral lines arising within the photosphere show that large amplitude pulsations are taking place in the envelopes of LPVs. The

period of these oscillations, typically about 1 year, is approximately given by the envelope crossing time of an acoustic wave. Like Cepheid variables, Miras obey a period–luminosity relationship and are very luminous. Thus Miras should be useful distance indicators, particularly for heavily obscured areas, where their high infrared brightness will be particularly helpful.

3. The Circumstellar Shell

As figure 1 shows, some AGB stars should have colors and luminosities indistinguishable from a star of the first red giant branch. However the maximum luminosity for an AGB star exceeds that of a star on the RGB, because of the AGB star's higher core density. Thus the very most luminous red giants (excluding luminosity class 1 supergiants) are believed to be AGB stars. The thick circumstellar shells discussed in §1 only occur around AGB stars; mass loss on the RGB appears to be much more modest. The evolutionary tracks in figure 1 also show that for the more massive AGB stars the luminosity and photospheric color change very little during the AGB phase. Dramatic changes are visible however, if one concentrates on the CSS rather than the photosphere.

Figure 2 shows a two–color diagram produced from the *IRAS* fluxes of stars with and without a CSS. Most of the stars lie within one of two dense clusters of points. The left cluster contains all stars with color temperatures above 2000 K, indicating most of the IR flux arises from the stars' photospheres. For the stars falling within the larger cluster to the right, the [25]–[60] and [12]–[25] color temperatures are in most cases significantly different from each other. While the [25]–[60] colors still often reflect the photospheric temperature, the [12]–[25] color implies a temperature of $\sim$ 500, well below the temperature at which refractory elements will condense to form dust grains. A relatively small number of stars do not fall near either of the two main clusters. Most of these objects are carbon stars, planetary nebulae or non–variable OH/IR stars.

Van der Veen and Habing (1988) found that oxygen–rich Mira variables and OH/IR stars which had high–quality *IRAS* fluxes lie near a curve in the two–color diagram, which is sketched

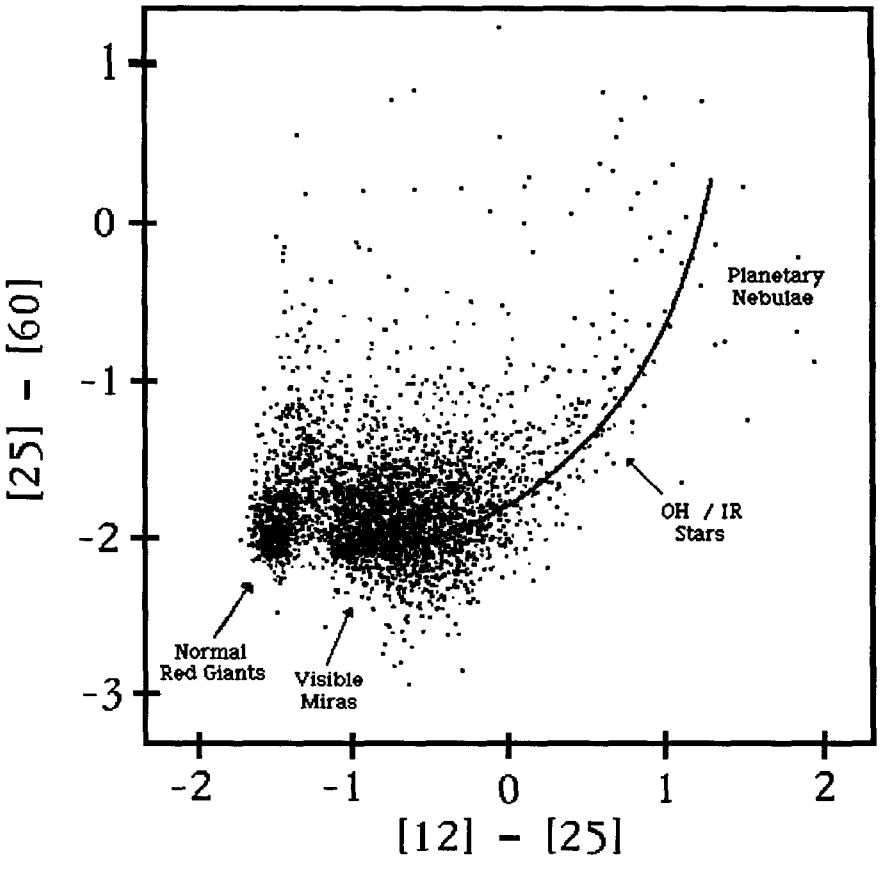

Fig. 2. An *IRAS* color–color diagram for 3800 objects in the *IRAS* Point Source Catalog, with stellar spectra. The colors are defined as

$$[12]-[25]=2.5\log\left(\frac{F_{25\mu m}}{F_{12\mu m}}\right); \qquad [25]-[60]=2.5\log\left(\frac{F_{60\mu m}}{F_{25\mu m}}\right).$$

The line shows an evolutionary track for an oxygen–rich star with an increasingly thick CSS. (Adapted from Van der Veen and Habing, 1988)

in figure 2. These authors argue that this curve represents an evolutionary path for oxygen–rich envelopes, with stars progressing along the curve from left to right. In their evolutionary scheme, stars first develop a thin CSS, which affects the [12]–[25] color but is too optically thin in the far–infrared to change the [25]–[60] color. Thus the star moves nearly horizontally in the two–color diagram. As the star ages, the mass loss rate increases as does the optical depth of the CSS. Eventually the shell has significant optical depth even at 60μm, and the star moves upward on the diagram. Finally the mass loss rate becomes so large that the optical depth of the CSS is well above unity, and the *IRAS* colors start to reflect the lower temperature of the outer regions of the envelope, and the star moves toward the upper end of the curve. Van der Veen and Habing

also point out that both the amplitude and period of the star's infrared variability increase along the evolutionary path they sketched, implying that stronger envelope pulsations accompany the increasing mass loss rate.

The gaseous component of the CSS has a rich chemistry. More than 50 molecular species have been identified in the CSS of the carbon star IRC+10°216, along with many isotopic variants (Olofsson 1992). Several molecules have been mapped in IRC+10°216, with millimeter interferometers. While the size of the emitting region in IRC+10°216 varies from molecule to molecule, the distribution appears in all cases to be nearly spherically symmetric, attesting to the well ordered nature of the velocity field and density distribution of the CSS. It is likely that the temperature, density and velocity distribution is more reliably known for a CSS such as that of IRC+10°216 than for any other type of molecular cloud. This makes the CSS an ideal laboratory for testing cosmochemistry models. In the innermost region of the shell, the temperature and density are high enough that chemical reactions reach thermodynamic equilibrium. As the material moves outward the temperature and density decrease rapidly, freezing in the original molecular mix. Detailed models predict that as expansion continues, some molecules such as SiS are deposited on grains and disappear from view. Others such as HC_3N are broken down by the interstellar UV field into ions or neutral radicals. Because these species are much more reactive than the chemicals initially present, a second wave of chemical reactions occurs, and new species arise in thin spherical shells. Several such shells have been mapped (Bieging and Tafalla, 1993). Figure 3 shows the approximate location of the infrared and radio emission regions of IRC+10°216.

The rate at which material is returned to the interstellar medium from AGB winds is ~ 0.3 $M_\odot \mathrm{yr}^{-1}$ (Knapp and Morris 1985), and is dominated by the contributions of the relatively few stars with the highest mass loss rates ($> 10^{-5}$ $M_\odot \mathrm{yr}^{-1}$). Because of dredge–up, this material is enriched with ^{13}C and ^{14}N from CNO burning, ^{12}C from helium burning, and s-process nuclei produced in the bath of neutrons produced from α particle capture by ^{13}C and ^{22}Ne nuclei. It is likely that AGB stars are the main source of these nuclei.

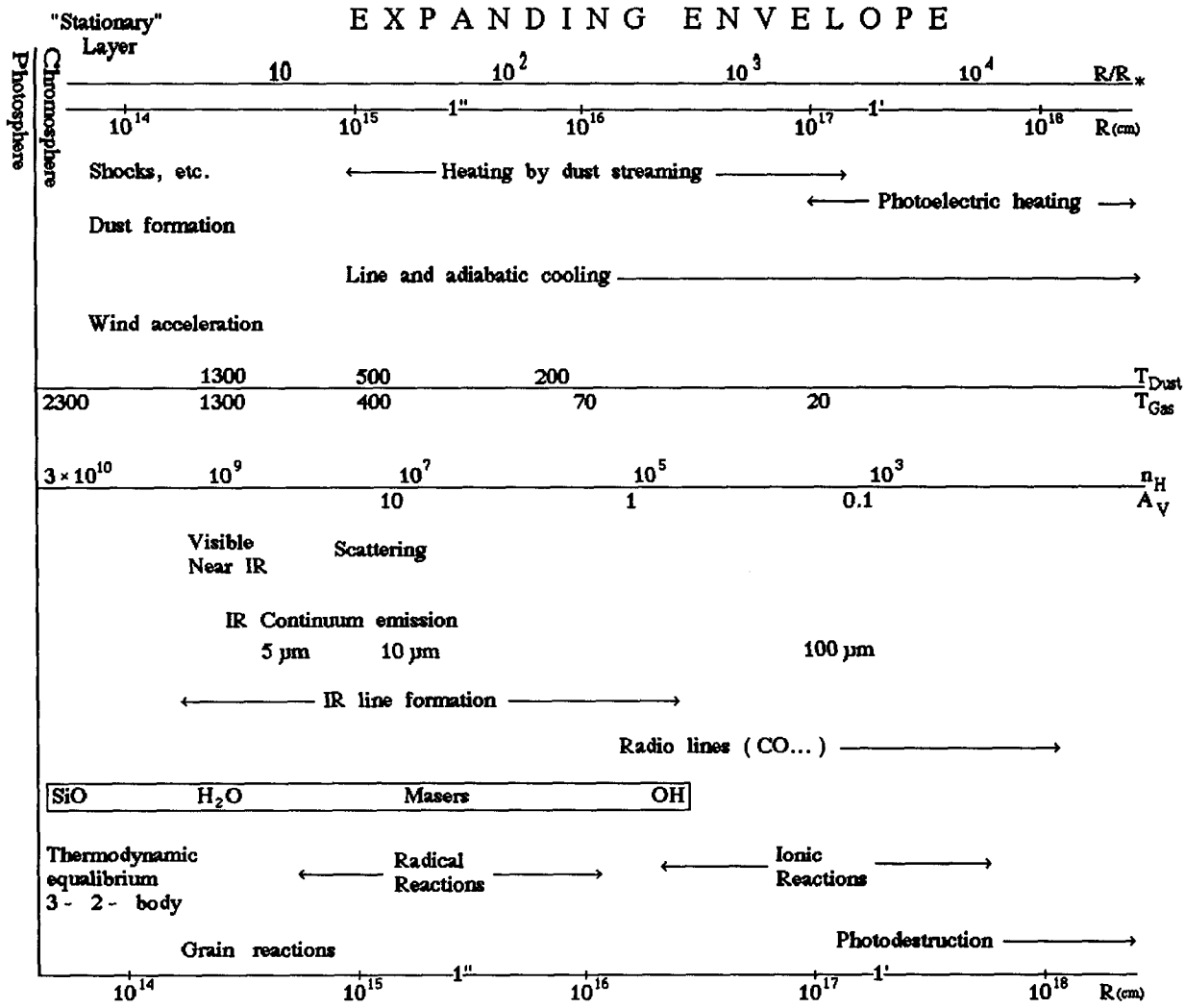

Fig. 3. The structure of the envelope of IRC+10°216 is shown. The locations from which SiO, H_2O and OH maser emission arises in an oxygen-rich shell are shown for comparison. None of these maser lines are present in IRC+10°216. (Adapted from Omont, 1984)

What drives the mass loss from an AGB star? The presence of dust in these stellar winds suggests that radiation pressure is important. When dust forms in the upper atmosphere of a star, it couples to the star's radiation field much more effectively than the gas does, because the size of a dust grain is more comparable to the wavelength of an average stellar photon. If the dust grains are driven outward, momentum can be imparted to the gas by collisions. Salpeter (1974) derived a simple relationship for momentum transfer, which should be obeyed by a radiation driven wind:

$$\dot{M}V_o = \tau L_*/c$$

where $\dot{M}$ is the mass loss rate, V_o is the terminal velocity, and L_* is the stellar luminosity. Knapp *et al.* (1982) examined the mass loss rates derived from radiative transfer models of CO emission, and determined that the Salpeter relation is obeyed for most AGB stars, with $\tau \lesssim 1$. Knapp (1986) further showed that this τ was strongly correlated with the dust optical depth derived independently by modeling the star's infrared spectrum. This strongly suggests that at least for stars with dense shells ($\tau \approx 1$), radiation pressure does drive the expansion. It's worth remembering that there is no reason why τ cannot exceed unity, leading to a rate of momentum increase in the wind larger than the momentum present in the radiation field. This can occur if the envelope is thick enough that a typical stellar photon is scattered or absorbed and reradiated several times before escaping from the shell. However it is unlikely that τ can greatly exceed unity, because photospheric photons reradiated from dust will reflect the dust's lower temperature, and will be redistributed to longer wavelengths. The dust emissivity, (which falls off in the infrared at least as fast as λ^{-1}) ensures that at very long wavelengths the CSS will be optically thin, so reradiated photons have a high escape probability.

4. Unsolved Problems

While there is no longer any doubt that the model proposed by Shklovsky is correct, many unanswered questions remain. Among them are these:

In what mode is the envelope pulsating? There is still no agreement on whether LPVs are pulsating in the primary mode, or a harmonic. The periods of heavily dust enshrouded stars are usually 2 to 3 times longer than those of unobscured Miras. Does a mode change occur which increases the mass loss rate?

How is the gas transported to the region where dust forms? Current models of the gas density for red giants fail by orders of magnitude to predict the density implied by $\dot{M}$ and V_o at the region where the temperature drops below 1000 K, and dust presumably forms (Johnson, 1991). The coincidence of strong envelope pulsations with large mass loss rates in AGB stars

suggests that the pulsation drives the gas, but no quantitative model has been developed. A perhaps related question is whether radiation pressure drives the stellar wind in the cases where $\dot{M}$ is small ($\lesssim 10^{-7}\ M_{\odot}\mathrm{yr}^{-1}$) and the momentum in the wind is far less than what is available in the radiation field. Chapter 3 of this thesis presents evidence that radiation pressure does drive these modest stellar winds.

How does the mass loss rate evolve in time? Several lines of evidence indicate that an AGB star's mass loss rate increases as the star ages. One of them is Van der Veen and Habing's analysis of the *IRAS* two–color diagram mentioned earlier. Also the mass loss rates implied by the strength of CO emission from protoplanetary nebulae such as CRL 618 and CRL 2688, and young planetary nebulae such as NGC 7027 are $10^{-5} \rightarrow 10^{-4}\ M_{\odot}\mathrm{yr}^{-1}$, as high as are seen in any AGB star. But it is not yet clear whether the mass loss rate increases gradually with time, or whether there is an abrupt increase very near the end of the AGB, resulting in the quick ejection of the remainder of the envelope. Chapter 2 presents evidence in favor of an abrupt envelope ejection.

There is evidence from a variety of sources that the mass loss process is occasionally interrupted. Deep optical images of planetary nebulae occasionally show large faint halos arc minutes away from the bright ionized gas (Balick *et al.* 1992); perhaps these are remnants of an earlier episode of mass loss. In the millimeter regime, a map of CO in the carbon star S Sct shows a hollow shell of CO is present rather than a filled envelope (Bergman *et al.* 1993), even though there is currently no internal source of UV emission capable of dissociating the CO. In the infrared, the large scatter in the positions of carbon stars on the *IRAS* two–color diagram has been reproduced by models of dust emission in which the shell has a large inner radius. Willems and de Jong (1988) suggested that the transition from an oxygen–rich to a carbon–rich shell caused the regular envelope pulsations to die out, temporarily halting the mass loss process. However in chapter 2 examples of detached shells surrounding both carbon stars and oxygen rich stars will be presented, implying that the transition to a carbon–rich envelope is not required to cause an interlude of reduced mass loss.

By what mechanism is the last remnant of the envelope ejected? As in the case of IRC+10°216 discussed in §3, the large scale structure of an AGB star's CSS is usually nearly

spherically symmetric. In contrast, protoplanetary and planetary nebulae typically show a pronounced bipolar structure. In addition, both of the best studied protoplanetary nebulae, CRL 618 and CRL 2688 have some molecular material in their envelopes moving at $\sim$ 100 km s^{-1}, far faster than the expansion velocity seen in the shell of any red giant (Gammie *et al.* 1989, and chapter 4). It appears that the last $\sim$ 0.1 $M_{\odot}$ of the envelope is ejected by a different (as yet unidentified) mechanism than the bulk of the CSS.

Where are the brightest carbon stars? In contrast to infrared and radio astronomers, who have usually focused on the nearest AGB stars, workers in the optical regime have concentrated on AGB stars in the Magellanic Clouds. Because the distances to the Magellanic Clouds are well determined, optical surveys have been able to determine the luminosity distribution (N, M_{Bol}) for several classes of AGB stars. Iben (1981) pointed out that extant stellar evolution models produced carbon star luminosity distributions which were extremely poor matches to the observed distribution determined by these optical surveys. In particular, carbon stars were seen at luminosities far lower than predicted by the models, suggesting that dredge–up is much more wide–spread among AGB stars than had been predicted. At the other extreme, virtually no carbon stars more luminous than $M_{Bol} = -6$ are seen, even though the Paczinski core mass – luminosity relation predicts the upper limit should be -7.2. The free parameters in stellar evolution models can be adjusted to produce the observed low–luminosity carbon stars. However the dearth of high–luminosity carbon stars presents a greater challenge. The most probable explanation appears to be that in most cases mass loss terminates the AGB before a star approaches the maximum possible AGB luminosity (Reid, Tinney and Mould 1990). If mass loss strongly influences the luminosity function in the Magellanic Clouds, then the luminosity function derived from those galaxies may not match that of the Milky Way, because the metallicity differences are apt to effect the dust/gas ratio and hence the mass loss rate for a radiation driven wind.

References

Balick, B., Guillermo, G., Frank, A. & Jacoby, G. 1992, ApJ, 392, 582

Bergman, P., Carlstrom, U. & Olofsson, H. 1993, A&A, 268, 685

Bieging, J. H., & Tafalla, M. 1993, AJ, 105, 577

Deutsch, A. J. 1956, ApJ, 123, 210

Gammie, C. F., Knapp, G. R., Young, K., Phillips, T. G., & Falgarone, E., 1989, Astrophys. Space Sci., 345, 87(L)

Herman, J. & Habing, H. J. 1985, Physics Reports, Volume 124, Number 4

Iben, I. 1981, ApJ 246, 278

Iben, I. & Renzini, A. 1983, Ann. Rev. Astron, Astrophys., 21, 271

Iben, I. 1985, Q. Jl R. astr. Soc, 26, 1

Johnson 1991, A&A, 249, 455

Knapp, G. R., Phillips, T. G., Leighton, R. B., Lo, K. Y., Wannier, P. G., Wootten, H. A. & Huggins, P. J. 1982, ApJ, 252, 616

Knapp, G. R., Morris, M. 1985, ApJ 292, 640

Knapp, G. R. 1986, ApJ 311, 731

Morris, M. 1980, ApJ, 236, 823

Neugebauer, G. & Leighton, R. B. 1969, Two Micron Sky Survey, NASA SP-3047

Neugebauer, G. *et al.* 1984, ApJ, 278, L1

Olofsson, H. 1992, Mass Loss of the AGB and Beyond, Proceedings of the 2nd ESO/CTIO Workshop *in press*

Omont, A. 1984, Mass Loss from Red Giants, ed M. Morris and B. Zuckerman, page 269, D. Reidel

Paczinski, B. 1970, Acta Astron., 20, 47

Price, S. D., & Walker, R. G. 1975, AFGL Infrared Sky Survey, (AFGL-TR-75-0373)

Reid, N., Tinney, C. & Mould, J. 1990, ApJ, 348, 98

Salpeter, E., E. 1974, ApJ., 193, 585

Schwarzschild, M., Rabinowitz, I. & Härm, R. 1953, ApJ, 118, 326

Shklovsky, I. S. 1956, Astron. Zh., 33, 315

Solomon, P., Jefferts, K. B., Penzias, A. A. & Wilson, R. W. 1971, ApJ, 163, L53

van der Veen, W. E. C. J., & Habing, H. J. 1988, A&A, 194, 125

Willems, F. J. & de Jong, T. 1988, A&A, 196, 173

Wilson, W. J. & Barret, A. H. 1968, Science, 161, 778

Circumstellar Shells Resolved in IRAS Survey Data

K. Young[1], *T.G. Phillips*[1], *and G.R. Knapp*[2]

[1]California Institute of Technology, Pasadena, CA 91125

[2]Department of Astrophysical Sciences, Princeton University, Princeton, NJ 08544

ABSTRACT

The *IRAS* survey data for 512 red giant stars and young planetary nebulae, most of which have been detected in rotational transitions of CO, were examined. The data for those objects which were not located in highly confused regions of the sky were processed using a computer program which fitted the data to an idealized model of a circumstellar shell. Of these stars 76 were found to have a circumstellar shell (CSS) that is resolved in the 60μm survey data. Some of these stars are also resolved in the 100μm survey data. Of these 76 stars, 40% are carbon stars. Three of the carbon stars, W Pic, RY Dra, and R CrB have shells with radii of 3 pc or more. Only two of the resolved objects detectable in CO, NGC 2346 and IRC+10°216 are surrounded by shells with masses $\gtrsim 1M_{\odot}$. Most of the nearby stars which are resolved are semiregular variables, while most of the nearby unresolved stars are Miras. No evidence was found that the shapes of the shells were distorted by interaction with the ISM. The average dust temperature in the outer region of the shells is $\sim$ 35 K. Using this temperature and the mass–loss rates derived from observations of the inner shell, it is shown that the expansion velocity of the dust cannot greatly exceed that of the gaseous material. Some of the shells appear to be detached from the central star. The distribution of the inner radii of the detached shells indicates that CO is dissociated at a distance of $\sim$ 0.3 pc from the star. Analysis of the colors of the shells resolved in both the 60 and 100μm bands shows that the central star is the dominant dust heating source at radii less than $\sim$ 0.5 pc, whereas an external source dominates beyond $\sim$ 1 pc. Thirteen of the stars found

to be extended are Mira variables. A simple model of the evolution of these shells, involving the interaction of the expelled material with the ISM, suggests that the period during which Mira variables lose mass lasts for $\sim 10^5$ years. The same model indicates that carbon stars shed mass for $\sim 2 \times 10^5$ years. For the largest shells the expansion velocity of the outer shell will typically be lower than the expansion velocity obtained from CO observations, by a factor of 3 – 5.

Subject headings: circumstellar matter — infrared: stars — planetary nebulae: general — stars: late–type — stars: mass loss

1. Introduction

Much of the mass returned to the interstellar medium by stellar evolution processes is shed during the asymptotic giant branch (AGB) stage (Knapp and Morris 1985). AGB stars are cool ($T_{eff} \leq 2000$ K), very luminous ($L_{bol} \sim 10^4\ L_\odot$), and are observed to shed mass copiously, with observed mass–loss rates in the range 10^{-8} to $10^{-4}\ M_\odot\ yr^{-1}$ (Knapp *et al.* 1982). Since the stars are cool, the mass is shed in the form of molecules and dust, and can therefore be studied at radio, millimeter and infrared wavelengths. Studies of the mass shed by evolved stars are important for understanding stellar evolution, e.g., why so few stars ever approach the theoretical peak luminosity for an AGB star (Reid, Tinney and Mould 1990) as well as the formation of planetary nebulae, the initial mass range of the progenitors of Type I supernovae, and the chemical evolution of our Galaxy's interstellar medium. The focus of the work presented here is on measuring the angular extent of the emission from circumstellar dust in these envelopes. Molecular line observations tell us the velocity at which material is expelled from the star, and, together with an estimate of the distance, the envelope extent yields the linear size and age of the envelope. Since the molecular line observations also give estimates of the stellar mass-loss rate, the total envelope mass can be found. We can then obtain a lower limit for the mass lost by these stars (which, given data on a large enough sample of objects, can be used to give an estimate of the total mass returned to the interstellar medium).

At first sight, it might be thought that these goals could be accomplished by mapping the millimeter wavelength molecular line emission, but the sizes of molecular envelopes are truncated by photodissociation (Letzelter *et al.* 1987; Mamon *et al.* 1988). Also, although HI is not photodestroyed in the normal interstellar radiation field, the 21 cm emission from the circumstellar shells is extremely weak, and HI is ubiquitous and strong in the Galactic disk, so that HI observations are of very limited utility for this work (Knapp and Bowers 1988).

The *IRAS* Point Source Catalog (IRAS, 1985; hereafter PSC) contains some 246,000 detections, of which about 81,000 have colors suggesting the presence of circumstellar emission (Olofsson, 1988, van der Veen and Habing 1988). We wished to determine which of these stars had a CSS which had been spatially resolved in the *IRAS* survey. An AGB star with a luminosity of $2 \times 10^4 L_\odot$ and an effective temperature of 2000 K could be as distant as 2.5 kpc, and still have a 60μm flux density above the PSC cutoff of 0.5 Jy. If that same star were obscured by a thick dust shell with a temperature of a few hundred K, it could be detected anywhere within our Galaxy. However, since a typical large CSS is expected to have a radius of about 0.3 pc (Rowan-Robinson *et al.* 1986), it must be no further than 1 kpc to be resolved by the 60" beam *IRAS* provided at 60μm. We therefore needed a way to select the small percentage of AGBs in the PSC which were nearby and had large circumstellar envelopes. Initially we chose to examine only those stars which have been detected in a rotational transition of CO. Such a star must be relatively nearby and have a large envelope, or else telescope beam dilution would prevent detection of its molecular line emission. In addition, the CO observations provide a direct measurement of the envelope's outflow velocity within the region $\lesssim$ 0.1 pc from the star (Olofsson 1989), and an estimate of the star's mass–loss rate. We knew of at least one star, R CrB, which has a very large dust envelope (Gillet *et al.* 1986) but which has not been detected in CO, despite having been examined in several CO surveys (e.g., Wannier *et al.* 1990, Zuckerman and Dyck 1986a). In order to find other such shells, we looked at many additional stars selected by their *IRAS* colors and catalog associations. Stars from this second group will be referred to as the Additional List, and the prescription by which its members where selected is given in the appendix.

We found a total of 76 stars which appear to have CSS shell radii greater than 2' in the *IRAS* 60μm data. The details of how we examined the stars for signs of extended emission, as well tables and figures presenting the results, are also presented in the appendix.

2. Physical Parameters

The angular size may be used to calculate the linear size of the CSS once the distance to the star is known. Table 1 lists the estimated distance and calculated envelope size for each star. The distance estimates were culled from the literature when available. Otherwise, the distances were estimated in one of the following ways. For the Mira variables, the Period-Luminosity-Spectral type relationship (Bowers and Hagen 1984) was used to calculate M_V, then m_V was used along with an estimate of the extinction, to calculate the distance. This technique was analysed by Celis (1981), who estimated that the mean error in the derived distance is 19%. All other stars without published distances were assumed to have $M_K = -8.1$ (Kleinmann 1989). The m_K was obtained from either the 2μm sky survey (TMSS) or the survey of Fouqué *et al.* (1992), and extinction was ignored when the distance was calculated.

If it weren't for the interstellar medium, the age of each CSS could easily be calculated from its size and the expansion velocity obtained from CO observations. However the ISM should appreciably slow the expanding envelope once the density of the expanding shell has decreased to equal the density of the ISM. If the star's envelope is expanding at 15 km $s^{-1}$and the mass–loss rate is $10^{-6} M_\odot yr^{-1}$, equal density will occur at a shell radius of 0.3 pc, assuming an ISM density of 1 H cm^{-3}. The envelope will have expanded to this size after only 2×10^4 years, which is much shorter than the period of time that any star remains on the AGB. Therefore the effect of the ISM on the shell expansion cannot be ignored.

The mean free path for scattering against hydrogen atoms even at a low ISM density of 1 H cm^{-3} is only $\sim 10^{-3}$ pc, so we can assume that the interaction between the ISM and the stellar wind occurs very near the edge of the expanding shell. The shell loses speed as it expands into the ISM and must accelerate the ambient material. Once the outer edge has been slowed by the ISM it will be pushed by material behind it which is still expanding at the original outflow speed.

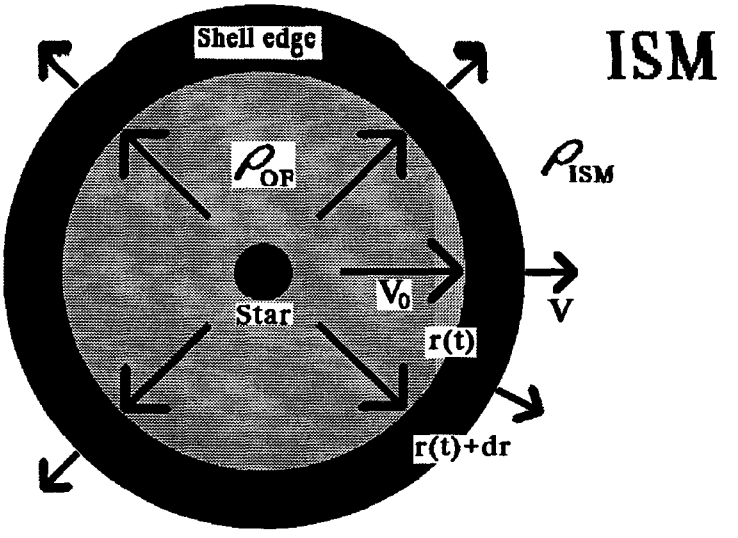

Fig. 1. A dust shell expanding into the ISM. The leading edge of the expanding shell is slowed as it sweeps up material from the ISM. The edge is prevented from slowing to a halt by the pressure of the material behind it, which is still moving at the original speed of v_0.

The rate at which the outer edge expands can easily be calculated. Let p be the total momentum of the expanding envelope edge, moving with a speed of v and having mass m (see Figure 1):

$$F = \frac{dp}{dt} = v\frac{dm}{dt} + m\frac{dv}{dt}. \qquad (1)$$

The material behind the shell edge is still moving with its original expansion velocity v_0, and it exerts a force on the shell edge of

$$F = 4\pi r^2 v_0 \rho_{OF}(v_0 - v)$$

where r is the shell's outer radius. This force acts to maintain the velocity of the expanding shell. During a short time interval of length dt, the shell edge gains material of mass

$$dm = 4\pi r^2 \rho_{OF}(v_0 - v)dt + 4\pi r^2 \rho_{ISM} v dt. \qquad (2)$$

The first term in dm accounts for the stellar wind colliding with the edge from behind, and the second term accounts for the mass of ISM material that is swept up. If the mass–loss rate $\dot{M}$ and outflow speed v_0 are assumed to be constant, then

$$\rho_{OF} = \frac{\dot{M}}{4\pi r^2 v_0}. \qquad (3)$$

With these assumptions equation (2) can be integrated to give the total mass of the shell edge

$$m = 4\pi \int_0^t r^2(\rho_{OF}(v_o - \frac{dr}{dt}) + \rho_{ISM}\frac{dr}{dt})dt = \dot{M}(t - r/v_0) + \frac{4}{3}\pi r^3 \rho_{ISM}. \qquad (4)$$

Substituting equations (2) and (4) into equation (1) gives

$$4\pi r^2 v_0 \rho_{OF}(v_0 - \frac{dr}{dt}) = 4\pi r^2(\rho_{OF}(v_0 - \frac{dr}{dt}) + \rho_{ISM}\frac{dr}{dt})\frac{dr}{dt} + (\dot{M}(t - r/v_0) + \frac{4}{3}\pi r^3 \rho_{ISM})\frac{d^2r}{dt^2}.$$

The above equation can be solved for $d^2r/dt^2 = dv/dt$, yielding equations (5a) and (5b), a system of two coupled differential equations which can be solved to give the shell's radius as a function of time.

$$\frac{dr}{dt} = v \qquad (5a) \qquad \frac{dv}{dt} = \frac{\dot{M}(v_0 - v) - (\dot{M}(1 - v/v_0) + 4\pi r^2 v \rho_{ISM})v}{\dot{M}(t - r/v_0) + \frac{4}{3}\pi r^3 \rho_{ISM}}. \qquad (5b)$$

Equations (5a) and (5b) were numerically integrated to solve for the age of each CO–detected star which was found to be extended. For consistency, the CSS radius from the 60μm data was used in all cases, even if a 100μm radius was available. The results are given in Table 1. The ISM density was assumed to fall off exponentially, in the direction z perpendicular to the Galactic plane, from a value of 2 H cm^{-3} (Spitzer 1978), with a scale height of 100 pc (Mihalas and Binney 1981). As is shown by Figure 2, the expansion rate of the shell edge is not strongly dependent upon ρ_{ISM}; the final size of the shell is reduced by less than a factor of 2 when ρ_{ISM} is increased by a factor of 10. The mass–loss rates were taken from calculations in the literature. These calculations were made by solving the radiative transfer problem for thermal CO emission using the Sobolev approximation (Knapp and Morris 1985), and they

Table 1. — Shell Sizes, Ages and Masses

(1) Name	(2) Distance (pc)	(3) Ref.	(4) Radius Outer	(5) Radius Inner	(6) V_0 ($km\,s^{-1}$)	(7) $10^7 \times \dot{M}$ ($M_\odot\,yr^{-1}$)	(8) Ref. for (6) & (7)	(9) Age (10^3 yr)	(10) Mass ($M_\odot$)	(11) Spectral Type	(12) Class
AQ And	870	17	0.84	< 0.25	...	...	...	...	...	N	SR
R Scl	400	1	0.76	0.13	24.7	71.0	3 [D]	32	0.23	C6II	SRb
CRL 278	250	9	0.37	< 0.07	7.6	1.9	10 [B]	73	0.014	M7III	...
o Cet [A]	100	19	0.06	< 0.03	5.0	11.0	3 [D]	12	0.013	M5e–M9e	Mira
UX And [E]	420	9	0.44	< 0.12	...	...	...	...	...	M6III	SRb
V Eri	310	9	0.73	0.25	13.0	1.5	10 [B]	96	0.014	M5/M6IV	SRc
U Men [E]	490	20	1.9	0.56	...	...	...	...	...	M3	SR
R Dor	60	21	0.12	< 0.02	...	...	...	...	...	M8IIIq:e	SRb
ST Cam	480	2	0.43	< 0.14	10.0	1.6	2	67	0.011	N5	SRb
R Lep	410	1	0.57	< 0.12	20.5	17.0	3 [D]	33	0.057	C6IIe	Mira
W Ori	340	2	0.63	0.21	11.8	1.9	2	96	0.018	C5II	SRb
R Aur	370	3	0.42	< 0.11	10.9	5.3	3 [D]	55	0.029	M7IIIe	Mira
R Oct [E]	500	22	1.5	0.77	...	...	...	...	...	M5.5e	Mira
W Pic	660	1	1.2	0.19	7.0	0.5	1	310	0.016	N	Lb
α Ori [A]	200	3	0.61	< 0.06	15.0	5.6	3 [D]	75	0.042	M2I	SRc
U Ori	240	4	0.48	0.09	7.5	2.7	14	110	0.030	M6.5IIIe	Mira
UU Aur	290	2	0.36	< 0.08	13.4	2.4	5 [D]	43	0.010	CII	SRb
IRC−10°139 [F]	570	9	2.7	0.46	...	...	...	...	...	M1Iab	...
NGC 2346	460	5	0.84	0.20	19.0	100.0	5	57	0.57	C envelope	PN
Y Lyn	330	9	0.41	0.13	5.4	0.73	8 [B]	120	0.008	M5Ib-II	SRc
KK Car [E]	470	9	1.5	0.44	...	...	...	...	...	M3pe	Mira
X Cnc	460	2	1.2	0.16	12.0	2.7	2	170	0.045	CII	SRb
RS Cnc	200	9	0.33	0.06	5.3	0.69	3 [D]	90	0.006	M6IIIase	SRc?
R Leo	120	24	0.13	< 0.03	4.0	0.14	3 [D]	47	0.001	M8IIIe	Mira
Y Hya	510	1	1.4	0.19	10.2	2.0	1	290	0.058	C	SRb
CIT 6 [A]	190	3	0.39	< 0.06	16.9	30.0	3 [D]	26	0.077	C envelope	Mira
U Ant	320	1	0.43	< 0.09	21.2	14.0	1	27	0.038	N	Lb
U Hya	290	1	0.24	0.11	7.9	1.2	1	37	0.004	CII	SRb
VY UMa	520	2	0.46	< 0.15	8.4	1.3	2	64	0.008	C5II	Lb
R Crt	240	9	0.41	0.13	11.0	2.3	10 [B]	88	0.002	M7III	SRb
IRC−30°163E	300	13	0.59	0.20	8.0	1.2	10 [B]	140	0.017	M7III	...
RU Crt	450	9	0.38	< 0.13	...	...	...	...	...	M3	Lb?
BK Vir	280	9	0.45	0.12	4.7	0.48	11 [B]	130	0.006	M7III	SRb
Y UMa	330	9	0.36	0.16	4.7	0.67	11 [B]	92	0.006	M7II-III	SRb
Y CVn	280	2	0.45	0.23	9.0	1.1	2	66	0.007	CIab	SRb
RY Dra	450	2	2.5	0.25	10.0	1.8	2	500	0.090	C	SRb
RT Vir	270	3	0.32	0.08	11.3	2.2	3 [D]	34	0.007	M8III	SRb
SW Vir	210	13	0.70	< 0.06	9.4	3.2	6	110	0.035	M7III	SRb
R Hya	110	19	0.18	0.06	7.5	0.22	8 [B]	42	0.001	M7IIIe	Mira
W Hya	80	19	0.24	< 0.02	9.7	0.20	8 [B]	58	0.001	M8e	SRa
θ Aps [E]	320	21	1.1	< 0.09	...	...	...	...	...	M6.5III	SRb
RX Boo	140	19	0.27	< 0.04	11.5	1.5	3 [D]	32	0.005	M7.5e	SRb
RW Boo [E]	490	9	0.71	0.20	...	...	...	...	...	M5III	SRb
X TrA	300	1	0.36	0.11	9.2	0.9	1	73	0.007	C5	Lb
R CrB [G]	1600	23	4.6	0.70	...	...	...	...	...	G0Iab:pe	R CrB

continued next page

Table 1. — Shell Sizes, Ages and Masses (continued)

(1) Name	(2) Distance (pc)	(3) Ref.	(4) Radius Outer	(5) Inner	(6) V_0 ($km\,s^{-1}$)	(7) $10^7 \times \dot{M}$ ($M_\odot yr^{-1}$)	(8) Ref. for (6) & (7)	(9) Age (10^3 yr)	(10) Mass ($M_\odot$)	(11) Spectral Type	(12) Class
ST Her	290	9	0.48	< 0.08	6.0	0.33	26 [B]	130	0.004	M6s	SRb
X Her	220	9	0.39	< 0.06	8.5	1.4	8 [B]	65	0.009	M8e	SRb
S Dra	430	9	0.96	0.25	8.3	0.61	27 [B]	220	0.013	M6III	SRb
V Pav	460	9	0.51	0.17	16.0	3.1	27 [B]	52	0.016	C+	SRa
NGC 6720 [C]	780	15	1.2	< 0.23	24.0	...	16	...	...	...	PN
δ^2 Lyr	360	21	1.7	0.41	...	...	...	...	...	M4II	SRc?
V Tel [E]	430	9	0.68	0.21	...	...	...	...	...	M7	SRb
V1942 Sgr	630	1	0.59	< 0.18	10.0	1.1	1	110	0.012	CII	Lb
UX Dra	430	2	0.50	< 0.13	6.9	1.8	2	100	0.018	CII	SRa
AQ Sgr	570	1	0.50	0.20	6.0	1.8	6	120	0.021	CII	SRb
R Cyg [A]	420	5	0.59	0.24	11.3	1.6	5	100	0.016	S	Mira
S Pav [E]	210	19	0.42	< 0.06	...	...	...	...	...	M7IIe	SRc
V1943 Sgr	300	7	0.43	< 0.09	8.0	1.9	6	76	0.015	M7III	Lb
X Pav	240	9	0.35	< 0.07	10.5	1.9	18 [B]	37	0.009	Mc	SRa
RZ Sgr	660	9	0.82	0.19	12.5	15.0	27 [B]	72	0.11	Se	SRb
RT Cap	510	1	1.2	0.15	9.1	0.6	1	320	0.019	CII	SRb
T Mic	200	9	0.33	< 0.06	8.1	0.27	27 [B]	83	0.002	M7III	SRb
T Ind	550	1	0.46	< 0.16	5.5	0.4	1	100	0.004	CII	SRb
Y Pav	450	1	0.75	< 0.13	9.4	1.5	1	120	0.017	CII	SRb
S Cep	300	4	0.33	< 0.09	22.4	5.3	10 [B]	20	0.011	CII	Mira
RV Cyg	470	2	0.82	0.21	14.7	5.6	2	100	0.057	CII	SRb
EP Aqr	200	9	0.35	0.09	8.6	2.0	10 [B]	56	0.011	M8III	SRb
PQ Cep	710	13	1.5	0.43	21.7	17.0	12 [B]	110	0.19	C	...
W Peg	270	19	0.57	0.27	6.4	0.68	14	160	0.011	M7e	Mira
SV Peg	320	9	0.44	0.14	11.0	0.76	25 [B]	82	0.006	M	SRa
π^1 Gru	200	7	0.28	< 0.06	14.9	13.0	6	21	0.027	S5	SRb
V PsA	330	7	0.49	0.12	21.0	6.9	6	27	0.019	M7III	SRb
TX Psc	280	1	0.25	< 0.08	12.1	0.7	1 [B]	27	0.002	CII	Lb
RS And [E]	440	9	2.5	0.45	...	...	...	...	...	M7–M10	SRa
R Cas	220	3	0.27	0.06	12.3	5.1	3	29	0.015	M7IIIe	Mira

[A] These results are from processing the small data set provided by the default ADDSCAN parameters. All others used the data set obtained by changing the ADDSCAN search radius to 10'.

[B] The mass–loss rates for these objects were calculated from the CO(1-0) or CO(2-1) line strengths and widths, using formula 9a or 9b from van der Veen and Rugers (1989).

[C] Much of the molecular envelope of NGC 6720 has been dissociated by the central star, therefore observations of CO cannot be used to determine the precursor star's mass–loss rate.

[D] The value for $\dot{M}$ has been rescaled for our estimate of the distance.

[E] Observed, but not detected in a CO(1-0) survey by Nyman *et al.* (1992)

[F] Observed, but not detected in a CO(1-0) survey by Heske (1989)

[G] Observed, but not detected in a CO(2-1) survey by Wannier *et al.* (1990)

Sources — (1) Olofsson *et al.* 1988 (2) Olofsson *et al.* 1987 (3) Knapp and Morris 1985 (4) Using P-L-S relationship from Bowers and Hagen 1984 (5) Knapp 1986 (6) Knapp unpublished (7) Knapp *et al.* 1992 (8) Wannier and Sahai 1986 (9) Using the K magnitude from the IRC

or Fouqué *et al.* 1992, and assuming an absolute K magnitude of -8.1 (Kleinmann 1989) (10) Zuckerman and Dyck 1986a (11) Zuckerman and Dyck 1989 (12) Zuckerman *et al.* 1986 (13) van der Veen and Rugers 1989 (14) An unpublished CO(3-2) spectrum taken at the CSO was used, along with an LVG radiative transfer program (Morris 1980) (15) Huggins and Healy 1986 (16) Leene and Pottasch 1988 (17) Claussen *et al.* 1987 (18) Deguchi *et al.* 1990 (19) Jura and Kleinmann 1992 (20) van den Bergh 1984 (21) Judge and Stencel 1991 (22) Onaka *et al.* 1989 (23) Gillet *et al.* 1986 (24) Gatewood 1992 (25) Zuckerman and Dyck 1986b (26) Margulis *et al.* 1990 (27) Nyman *et al.* 1992

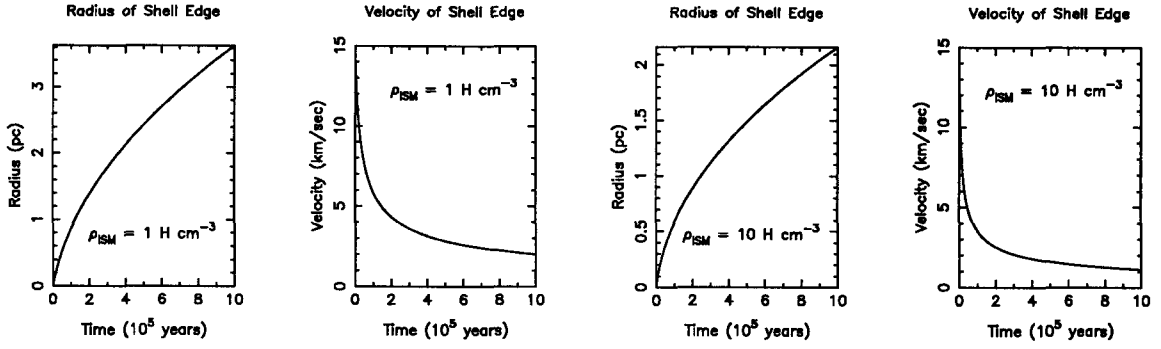

Fig. 2. The results of numerically integrating equations **5a** and **5b** are shown for two values of the ISM density ρ_{ISM}. In both cases $\dot{M} = 10^{-6} M_\odot yr^{-1}$ and $v_0 = 15$ km s^{-1}. The period of copious mass-loss for an AGB star probably lasts for $\sim 5 \times 10^5$ years, and over that period the expansion velocity of the shell edge drops from 15 km s^{-1} to under 3 km s^{-1}. This deceleration would be difficult to detect from molecular line observations. The CO envelope is expected to be truncated at a radius of about 0.3 pc by photodissociation, even for very large mass-loss rates (Mamon *et al.* 1988). If the CSS has expanded beyond the dissociation radius, then the molecular emission lines won't show signs of deceleration because the molecular material will only be present in a region where the ISM has already been swept away. On the other hand, if the CSS has not yet expanded to the dissociation radius, the shell is so small that the velocity of the shell edge will not yet have been significantly reduced.

are not dependent on any measurements of the continuum emission from the CSS. If our assumed distance differed from the value that had been used to calculate $\dot{M}$, we rescaled the value assuming that $\dot{M} \propto D^2$, which is appropriate if, as was usually the case, the molecular envelope was unresolved. The dust was assumed to have been ejected from the star at the terminal velocity derived from the CO profile. The velocity difference between the dust and the gas (the "drift velocity") was ignored, which is apt to have caused us to overestimate the shell's age. While the drift velocity is probably small for optically thick shells with $\dot{M} \geq 2 \times 10^{-5} M_\odot yr^{-1}$ (Gail and Sedlmayr 1985), calculations for the drift velocity in optically thin shells (Berruyer and Frisch

1983, Goldreich and Scoville 1976) predict drift velocities larger than the terminal velocity for the molecular material. Dougados *et al.* (1992) directly determined the dust velocity of the inner $\sim$ 0.01 pc of IRAS 09371 + 1212, by measuring Doppler shifts in the scattered photospheric emission. They found dust velocities 10 – 15 km s^{-1} *lower* than the CO velocity (i.e., a negative drift velocity). While these authors show that the apparent dust velocity could be lowered by a variety of radiative transfer effects, their data certainly do not support large drift velocities. In the outer regions of the envelope it is unlikely that the drift velocity can greatly exceed 20 km s^{-1}, because beyond that velocity the grains will be destroyed by sputtering (Kwok 1975). The fact that extended continuum emission surrounding these stars is visible at all places an upper limit on the magnitude of the drift velocity (see §2.4).

The value for the total shell mass in column (10) of Table 1 is the product of the estimated age multiplied by the mass–loss rate from CO observations. Calculating the mass in this way assumes that $\dot{M}$ is constant over periods comparable with its AGB lifetime, which is almost certainly not true. Evidence suggests that the mass–loss rate increases as the star progresses up the AGB (Iben and Renzini 1983), so our use of the CO–derived mass–loss rate (which samples only material ejected within the last few thousand years) is apt to result in the total mass being overestimated. With the exception of NGC 2346, the estimated masses are strikingly small when one considers that an average star is expected to shed $\sim 1 M_{\odot}$ during its AGB lifetime (Herman and Habing 1985). IRC+10°216 was not included in table 1, because its 60μm *IRAS* data is so anomalous. If we combine IRC+10°216's 100μm size with the distance, expansion velocity and mass–loss rate from Knapp and Morris (1985), we obtain a CSS with a radius of 0.8 pc containing 3 $M_{\odot}$of material. It appears that only IRC+10°216 out of all the red giants in the solar neighborhood, and the planetary nebula NGC 2346, have lost a significant fraction of their total envelope mass. This strongly implies that mass is not lost at a constant rate on the AGB, or even at a gradually increasing rate, but rather most of an AGB star's envelope is ejected during a brief period which may terminate the AGB phase.

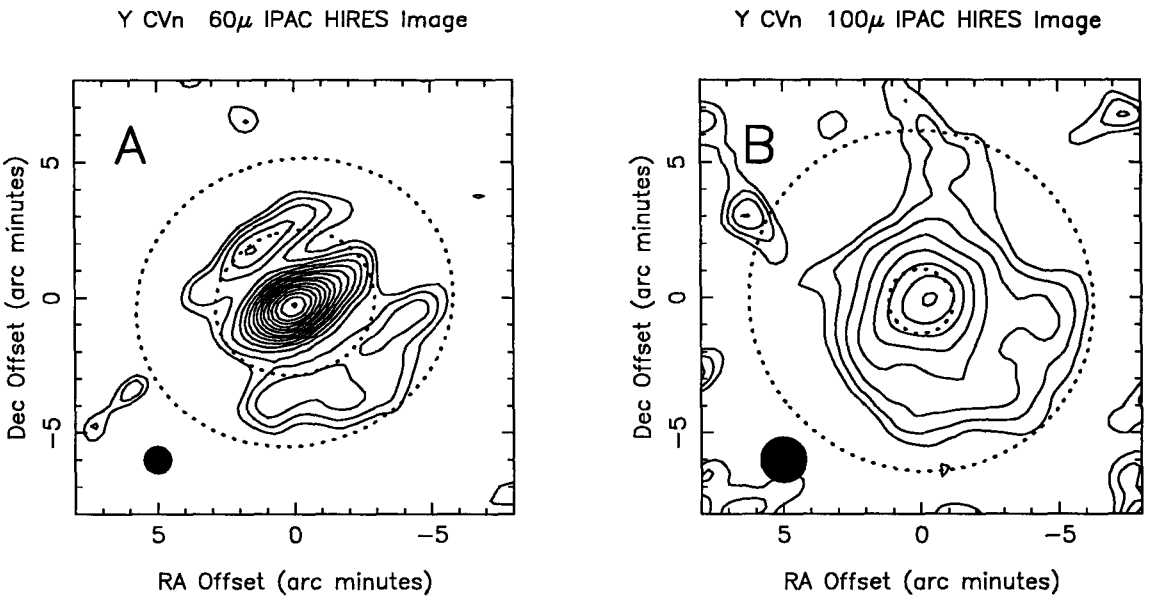

Fig. 3. The results of processing the survey data covering Y CVn with the IPAC HIRES program suite are shown. In figure **A**, the 60μm map, the lowest contour level is 0.45% of the peak intensity, and the contours are logarithmically spaced with ratios of 1.5. The central source appears elongated, however this is almost certainly an artifact caused by the large size of the 60μm detectors in the cross–scan direction. Panel **B** shows the 100μm HIRES map. Here the lowest contour is 2% of peak intensity, and the ratio between successive contours is 1.7. In both figures the inner and outer extents of the dust model fitted by the MFP are shown as dotted lines. The filled circles show the *IRAS* resolution (80% encircled energy).

The average radius of the shells in Table 1 is 0.74 pc. Since this table consists only of those stars which appear to have been resolved, stars with large shells are over–represented. The shells surrounding 28 of the stars are at least twice as large as the maximum size of 0.3 pc predicted by Rowan-Robinson (1986). The mass–loss rates and ages from Table 1 show no correlation.

2.1 Detached Shells

One of the parameters fitted by the MFP was the inner radius of the CSS. Table 3 of the appendix lists these radii in angular units, and the value in pc is given in Table 1 (if the radius is less than the 1' resolution of *IRAS* at 60μm, an upper limit corresponding to 1' is given). Nineteen of the stars have radii larger than 1.5'. These stars may have entered a quiescent period of reduced mass–loss. Figure 3 shows the 60 and 100μm maps produced by analyzing the

Table 2. – CO, OH, H_2O and SiO emission from Oxygen–Rich Shells with Resolved Inner Radii

Name	R_{inner} (pc)	CO	OH 1612	H_2O	SiO	Name	R_{inner} (pc)	CO	OH 1612	H_2O	SiO
RS Cnc	0.06	T				IRC−30°163E	0.20	T		(1)	
R Hya	0.06	T		M	T	RW Boo	0.20				
R Cas	0.06	T		M	M	V Tel	0.21			(1)	
RT Vir	0.08	T		M	T	R Cyg	0.24	T			
U Ori	0.09	T	M	M	T	V Eri	0.25	T			
EP Aqr	0.09	T				S Dra	0.25	T			
V PsA	0.12	T				W Peg	0.27	T		M	T
BK Vir	0.12	T				δ^2 Lyr	0.41	(2)			
Y Lyn	0.13	T				KK Car	0.44			(1)	
R Crt	0.13	T		M	T	RS And	0.45			M	
SV Peg	0.14	T		M		IRC−10°139	0.46				
Y UMa	0.16	T				U Men	0.56			(1)	T
RZ Sgr	0.19	T		(1)		R Oct	0.77			(1)	T

Notes: M = Maser emission, T = Thermal Emission, (1) not in the region covered by the catalog of H_2O masers. (2) We were unable to locate any published detections or non–detections of rotational CO emission from this object.
Sources: CO - see table 1, OH 1612 masers – Hekkert *et al.* (1989), H_2O masers – Cesaroni *et al.* (1988), SiO emission (thermal and maser) Engels and Heske (1989).

survey data for Y CVn with the IPAC HIRES processor (Aumann *et al.* 1990). While the HIRES image shows that the CSS has a more complex structure than the simple dust model used by the MFP, the outer edge of the MFP model dust shell matches the maximum extent of emission in the map quite well. The MFP calculated an inner radius of 2.8' for the 60μm data, and the map also shows a similar inner radius for the extended emission. However the 1.2' inner radius derived from the 100μm data is nearly equal to the resolution of *IRAS* at 100μm, and probably has no physical significance.

If the inner radii reported by the MFP are not spurious, then one would expect those shells with large inner radii to lack the spectral features associated with high–density gas. Maser emission from OH, H_2O and SiO arise from radii of about 10^{16}, 10^{15} and 10^{13} cm, respectively (Herman and Habing 1985). SiO thermal emission also traces higher density material than CO, because of its much larger dipole moment. Table 2 lists which of the oxygen–rich objects with inner radii larger than the *IRAS* diffraction limit have emission from these high–density tracers. All but 2 of the 7 objects with inner radii less than 0.1 pc show one of these lines, while only

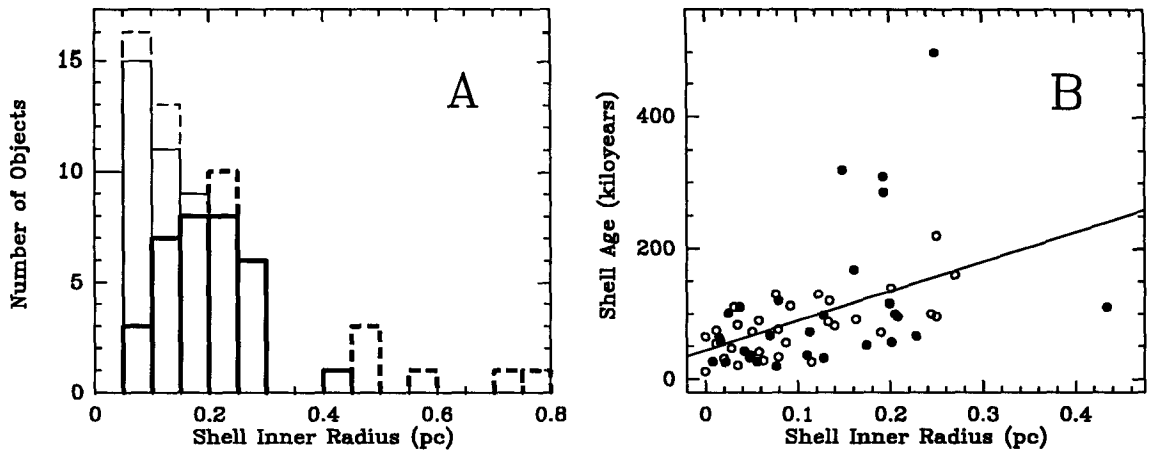

Fig. 4. (A) – A histogram of the inner shell radii is shown. The bold line histogram shows the values for those shells whose inner radii had an angular size of 1' or more, and may have actually been resolved. The thin line histogram shows the values for objects whose fitted inner radii are smaller than the *IRAS* 60μm diffraction limit, and probably have little or no physical significance. Solid lines are used for the objects which have been detected in CO, while a dashed line is used for objects with published non-detections. For the stars with CO emission, the radii are distributed rather uniformly through the range of 0.05 to 0.25 pc and only PQ Cep has an inner radius larger than 0.3 pc. (B) – The calculated age of the dust shells for 59 of the stars in table 1, plotted as a function of the inner shell radius. Carbon stars are plotted as filled circles, oxygen–rich objects are unfilled. NGC 6720, and the stars without CO detections were not included in this plot, because their ages were not calculated. Also shown is the least–squares best fit line. The weak correlation is stronger for the carbon rich envelopes.

6 of the 20 objects with a larger inner radius do. For the shells with inner radii larger than 0.3 pc, even the thermal CO emission is absent. These trends indicate that the inner radii fitted by the MFP are physically significant.

Figure 4A shows a histogram of the CSS inner radii. While the largest number of shells have very small inner radii, those stars whose inner radii were actually resolved have a fairly uniform distribution between 0.05 and 0.25 pc. The distribution falls off dramatically beyond 0.3 pc, and all but 1 of the 7 objects with inner radii larger than 0.3 pc do not have a detectable CO envelope. This suggests that the CO is photodissociated at a radius of 0.25 – 0.30 pc. This is in good agreement with the CO radius calculated by Mamon *et al.* (1988) for stars with very large mass–loss rates ($\dot{M} > 10^{-5} M_{\odot} \mathrm{yr}^{-1}$).

Figure 4B shows the age of 59 of the dust shells from Table 1, plotted as a function of the inner shell radius in parsecs. These two quantities appear to be weakly correlated. The linear

correlation constant, r, for these two variables is 0.48. The probability of r having this high a value if the age and inner shell radius are uncorrelated is less than 0.001 (Young 1962). However, since the age of the shell is strongly correlated with its *outer* radius (r = 0.85), a spurious correlation could occur between the age and the inner radius. This would happen if the assumed dust emission profile, or the MFP itself, had a defect which caused shells with large outer radii to be fitted with large inner radii. Since the outer radii must be larger than the inner radii, the two radii will be correlated even if the MFP is not defective, and this tautologous correlation could give rise to an age – inner radius correlation. There is no correlation between the *IRAS* colors of the object, and the shell's inner radius. This is surprising if the calculated inner radii are correct, since one would expect a detached shell to be cooler, allowing the star's photosphere to dominate the 12 and 25μm bands.

If the weak correlation of age with inner radius is not spurious it suggests that the mass–loss process becomes more episodic as the star loses its atmosphere. For AGB stars, this might occur as a consequence of the thermal pulse cycle. Throughout the thermal pulse phase, the amplitude of the luminosity variation caused by a thermal pulse increases with each successive pulse (Iben and Renzini 1983). Since it is likely that the stellar winds from these stars are driven by radiation pressure, these luminosity variations could modulate the mass–loss rate, and produce shells which appear to be detached from the central star.

2.2 Comparison of Resolved and Unresolved Objects

For the remainder of this paper, unless stated otherwise, we will consider only those stars which have been detected in CO, because they form a more homogeneous group than do the stars from the Additional List. A large fraction of the stars with distances of 500 pc or less appear to be resolved (see appendix). While 7 of the 8 stars with distances less than 200 pc are resolved in the 60μm data, there are many stars within 500 pc which are not. The 33 unresolved stars which are within 500 pc are listed in Table 3. If we adopt Kleinmann's (1989) scale heights of 200 pc for carbon stars and 400 pc for oxygen–rich stars, the total number of stars in our CO–selected list (both resolved and unresolved) as a function of distance is well fit by an exponential disk, out to a distance of 400 pc for the oxygen–rich stars, and 600 pc for the carbon stars. The best–fit

space densities are 110 kpc^{-3} for carbon stars and 270 kpc^{-3} for oxygen–rich stars in the Galactic midplane (here and elsewhere in this paper N stars are grouped with carbon stars and S stars are considered oxygen–rich). Beyond 400 pc our list must be quite incomplete because the number of stars per unit distance drops off rapidly. The fact that the list of resolved stars in Table 1 contains nearly equal numbers of carbon and oxygen–rich objects, even though the oxygen–rich stars are twice as common, is a reflection of the larger average size of the carbon star shells.

The average distance to the unresolved stars is 370 pc. At that distance a CSS with a radius $\geq$ 0.2 pc could be clearly resolved. This is less than 1/3 the average CSS size of the resolved stars listed in table 1. Therefore if the distance estimates for the unresolved stars are not too low by a factor of 3 or more, their shells must either be much smaller on average than those of the resolved stars, or not dense enough to be detected by *IRAS*. If the unresolved stars have shells which are just as large as those of the resolved stars, but less dense, then either the mass–loss rates for these stars must be lower, or the outflow velocity must be higher. However, the average CO velocity for both the unresolved and resolved groups (excluding the resolved stars with distances greater than 500 pc, we shall call this group "the nearby resolved group") is 11 km s^{-1}. Radiative transfer models of the CO emission from evolved stars show that the mass–loss rate is strongly correlated with the expansion velocity (Knapp *et al.* 1982), so it is likely that the mass–loss rates of these two groups are also similar. Therefore the unresolved stars on average should not have less dense envelopes, implying that they must have smaller envelopes than those surrounding the resolved stars. Note, however, that the closest unresolved Miras do have very low expansion velocities, and may have large undetectable shells (see below).

The envelopes surrounding the unresolved objects might be smaller for one of three reasons. The first possible reason is that the ISM surrounding the unresolved objects might be so dense that it confines the ejected material within a relatively small distance from the star. If the unresolved objects are in regions of very high ISM density, then they should cluster more closely about the Galactic plane, but they do not; the average absolute Galactic latitude of the unresolved objects is 29.2°, which is not significantly different than the nearby resolved group's average value of 35.1° and merely reflects the larger average distance of the unresolved objects. The second possible reason is that the CSSs surrounding the unresolved objects have been stripped off by

ram pressure arising from the star's large peculiar velocity. All but 3 of the resolved stars and 2/3 of the unresolved stars within 500 pc are near enough to have measurable proper motions. The proper motion may be combined with the radial velocity from the CO detections to calculate the full three–dimensional velocity of the star, with respect to the local standard of rest ($\vec{v}_{LSR}$). For stars this near the sun, $|\vec{v}_{LSR}|$ should be a good approximation to the speed of the star with respect to its local interstellar medium. For the unresolved stars the average speed is $\overline{|\vec{v}_{LSR}|} = 61.5$ km s^{-1}, which is slightly larger than the value of 54.8 km s^{-1}obtained for the resolved stars. Also the average magnitude of the radial v_{LSR}, which is available from the CO observations for all the stars, is 18.1 km s^{-1}for the unresolved stars and 15.5 km s^{-1}for those which were resolved. While the unresolved stars do appear to be moving $\sim$ 15% faster than the resolved ones, this difference is much less than the standard deviation of the velocities in either sample, and probably is just another reflection of the greater average distance to the unresolved stars. Therefore it does not seem likely that all the unresolved stars have had their envelopes stripped away by ram pressure. The third explanation for the unresolved stars is the simplest – perhaps they simply have not yet grown large enough to be resolved. If this is the case, the close agreement of the average CO expansion velocities in both groups tells us that the unresolved stars must be younger than the resolved ones.

A color–color diagram for these nearby unresolved stars, along with all the stars found to be resolved, is shown in Figure 5. While the stars found to be resolved are divided nearly evenly between carbon stars (27 objects) and oxygen–rich (M) stars (31 objects), only 8 of the 33 unresolved nearby stars are carbon stars. This suggests that the carbon stars have been losing mass for a longer time, on average, than have the M stars. The calculated shell ages in Table 1 provide additional evidence of this. The average age of the carbon star shells is 1.1×10^5 yr, whereas the average age of the oxygen–rich shells is 7.9×10^4 yr.

Table 3. – Stars Within 500 pc Which Are Unresolved

Name	Distance (pc)	Ref.	V_0 ($km\,s^{-1}$)	Ref.	Class	Name	Distance (pc)	Ref.	V_0 ($km\,s^{-1}$)	Ref.	Class
T Cas	360	1	5.2	12	Mira	RV Boo	380	10	8.1	13	SRb
R And	310	2	8.7	2	Mira	CRL 4211 [A]	330	4	20.5	4	...
UY Cet	470	10	8.1	13	SRb	S CrB	300	8	7.8	17	Mira
W And	280	3	11.0	14	Mira	IRAS 15194 – 5115 [A]	400	4	23.3	4	...
R Hor	270	4	6.6	4	Mira	R Ser	330	8	5.6	17	Mira
TW Hor [A]	420	5	5.3	5	SRb	RU Her	370	1	9.2	17	Mira
NML Tau	270	2	22.0	2	Mira	U Her	360	3	11.6	17	Mira
TX Cam	360	2	16.9	15	Mira	g Her	160	9	10.0	15	SRb
S Pic	390	6	11.8	13	Mira	IRC+10°365	500	2	16.7	2	...
Y Tau [A]	480	5	10.7	5	SRa	X Oph	300	1	5.5	17	Mira
V Cam	390	6	12.2	16	Mira	RS CrA	280	7	20.7	19	...
S CMi	480	1	4.1	17	Mira	W Aql	470	2	19.9	2	Mira
R Cnc	310	1	3.4	17	Mira	IRC+80°040	500	10	12.0	20	SRb
CRL 5254 [A]	420	7	12.8	12	...	T Cep	200	1	5.0	16	Mira
R LMi	260	8	6.0	18	Mira	V460 Cyg [A]	440	11	11.4	11	Lb
V Hya [A]	400	2	20.9	2	SRa	CRL 3099 [A]	500	2	10.1	2	...
S Vir	450	8	3.5	17	Mira						

[A] These stars are carbon stars or have carbon–rich envelopes

Sources: (1) Sivagnanam *et al.* 1988 (2) Knapp and Morris 1985 (3) Using P-L-S relationship from Bowers and Hagen 1984 (4) Knapp *et al.* 1989 (5) Olofsson *et al.* 1988 (6) Onaka *et al.* 1989 (7) van der Veen and Rugers 1989 (8) Jura and Kleinmann 1992 (9) Eaton and Johnson 1988 (10) Assuming an absolute K mag. of -8.1 (11) Olofsson *et al.* 1987 (12) Zuckerman and Dyck 1986a (13) Lyman *et al.* 1992 (14) Zuckerman *et al.* 1986 (15) Wannier and Sahai 1986 (16) Zuckerman and Dyck 1989 (17) Young *et al.* 1992 (18) Knapp *et al.* 1982 (19) Zuckerman and Dyck 1986b (20) Knapp (unpublished) (21) Zuckerman and Dyck 1989

The Mira variables in tables 1 and 3 are of particular interest. Since Miras obey a period-luminosity relationship, their distances can be estimated much more accurately than is possible for the other objects in this study. The average age of the shells around the resolved Miras in table 1 is 5.7×10^4 years. The Mira variable with the youngest shell, 1.2×10^4 years old, is Mira itself. W Peg's shell is 1.6×10^5 years old, the oldest of any of the Miras. Evidence that the nearby unresolved Miras do not have less dense shells is provided by the PSC 12μm fluxes. The 12μm emission should arise from the inner portion of the CSS. If the unresolved shells are less dense than those which are resolved, one would expect them to have lower 12μm intensities. However, if we normalize the PSC fluxes by the distance squared, there is no significant difference between the 12μm fluxes of the resolved and unresolved groups.

There are several ways by which we could estimate the lifetime of a Mira, using our age calculations. The simplest way is to take the average age of the resolved Mira shells in Table 1, and assume that on average these stars have lived half of their Mira lifetimes. This yields a lifetime of 1.1×10^5 yr. This is apt to be an overestimate, since an old star has a greater chance of being resolved than does a young star. Some of the nearby unresolved stars in table 3 may be young Miras with small shells. Let's assume for the moment that all the nearby unresolved Miras have shells which are slightly smaller than our resolution threshold. We required the outer radius to be at least 2' in order for the shell to be considered resolved. We can use equations (5a) and (5b) to calculate how long these stars would require to produce a shell of this size. Assuming that these stars do not have large, tenuous shells, this gives the maximum age for each of these Miras. For the 19 unresolved Miras within 500 pc, this maximum age is 3.6×10^4 yr on average. If we now assume that these unresolved stars have lived half of their maximum age, and combine this result with the average ages of the resolved Miras within 500 pc, we obtain an estimated lifetime of 6.5×10^4 yr. This is apt to be an underestimate, because as discussed above, the nearby Miras may have large shells which *IRAS* could not detect. This estimate again suggests that the lifetime of a Mira is $\sim 10^5$ yr, excluding any period before the star begins to lose mass at a detectable rate. This is twice the estimated lifetime obtained by comparing the numbers of Miras and planetary nebulae in our Galaxy (Wood 1990), and the discrepancy may indicate that not all Miras produce planetary nebulae.

Because most of the carbon stars within 600 pc which were processed are resolved (24 out of 38, ignoring IRC+10°216), the ages of these stars can be used to estimate the duration of the carbon star phase for stars in the solar neighborhood. If we assume that these stars are, on average, half–way through the carbon star phase, the average age of 1.1×10^5 yr implies the duration of this phase is about 2×10^5 yr. This result agrees with the carbon star lifetime derived by Claussen *et al.* (1987), who estimated that the carbon star phase lasts for $10^5 \sim 10^6$ yrs. From the distribution of carbon stars in the TMSS, these authors deduce that carbon stars had main–sequence masses between 1.2 $M_\odot$and 1.6 $M_\odot$. They obtained their upper limit age by dividing the envelope mass that must be shed ($\sim 0.8\ M_\odot$) by the average mass–loss rate ($\geq 2 \times 10^{-7} M_\odot \mathrm{yr}^{-1}$). Their lower limit is set by the birthrate of the main–sequence F stars they

believe evolve into carbon stars. On the other hand our estimate is an order of magnitude longer than the lifetime of 2×10^4 yr calculated by Willems and de Jong (1988). Even if the interaction of the CSS with the ISM is ignored, and the age is calculated by simply dividing the CSS size by the molecular expansion velocity, and all of the unresolved stars are assumed to have an age of 0 yr, the average age is 6.1×10^4 yr, implying a carbon star lifetime of 1.2×10^5 yr. One potential source of error in our calculation is that the molecular velocity has been used, rather than the unknown dust expansion velocity. However, the dust velocity would have to be at least 5 times as large as the molecular velocity, requiring an average drift velocity of ≥ 80 km s^{-1} to force the lifetime calculated here to match that of Willems and de Jong. A drift velocity this large will result in grain sputtering, and also implies a dust density which is too low to produce the flux detected by *IRAS* at a reasonable temperature (see §2.4). Bringing our estimate for the carbon star lifetime into agreement with Willems and de Jong would require that all or most of the CSS material at large radii is oxygen–rich. It is not clear whether the composition of the dust at large radii can be determined spectroscopically. While a few carbon stars do show the 9.7μm silicate feature in their IRAS low–resolution spectra (Willems and de Jong 1986), probably arising from material expelled when the star had an oxygen–rich envelope, the overwhelming majority do not. Willems and de Jong (1986) estimate that the silicate feature will disappear $\sim$ 100 years after the abundance of carbon exceeds that of oxygen, but van der Veen and Habing (1988) report that about 30% of stars in region V of their *IRAS* two–color diagram, which is populated by stars with detached shells, show the 9.7μm feature in absorption. It seems unlikely that such a large fraction of these stars would exhibit this spectral feature if it disappeared only 100 years after the cessation of mass–loss.

Not surprisingly, the resolved stars have redder $[100\mu\text{m}-60\mu\text{m}] \equiv \log_{10}(100\mu\text{m flux}/60\mu\text{m flux})$ colors on average than do the unresolved objects. Only one of the stars with $[100\mu\text{m} - 60\mu\text{m}] < -0.54$ was resolved, while all but one of the stars with $[100\mu\text{m} - 60\mu\text{m}] > -0.37$ (including NGC 6720 and NGC 2346 which are not shown in Figure 5) were resolved. However, many of the extended stars have *bluer* $[25\mu\text{m} - 12\mu\text{m}]$ colors than the nearby unresolved stars. All but one of the objects with $[25\mu\text{m} - 12\mu\text{m}] < -0.475$ were found to be extended. A $[25\mu\text{m} - 12\mu\text{m}]$ value less than -0.56 corresponds to a temperature of 2000 K or more, and indicates that there

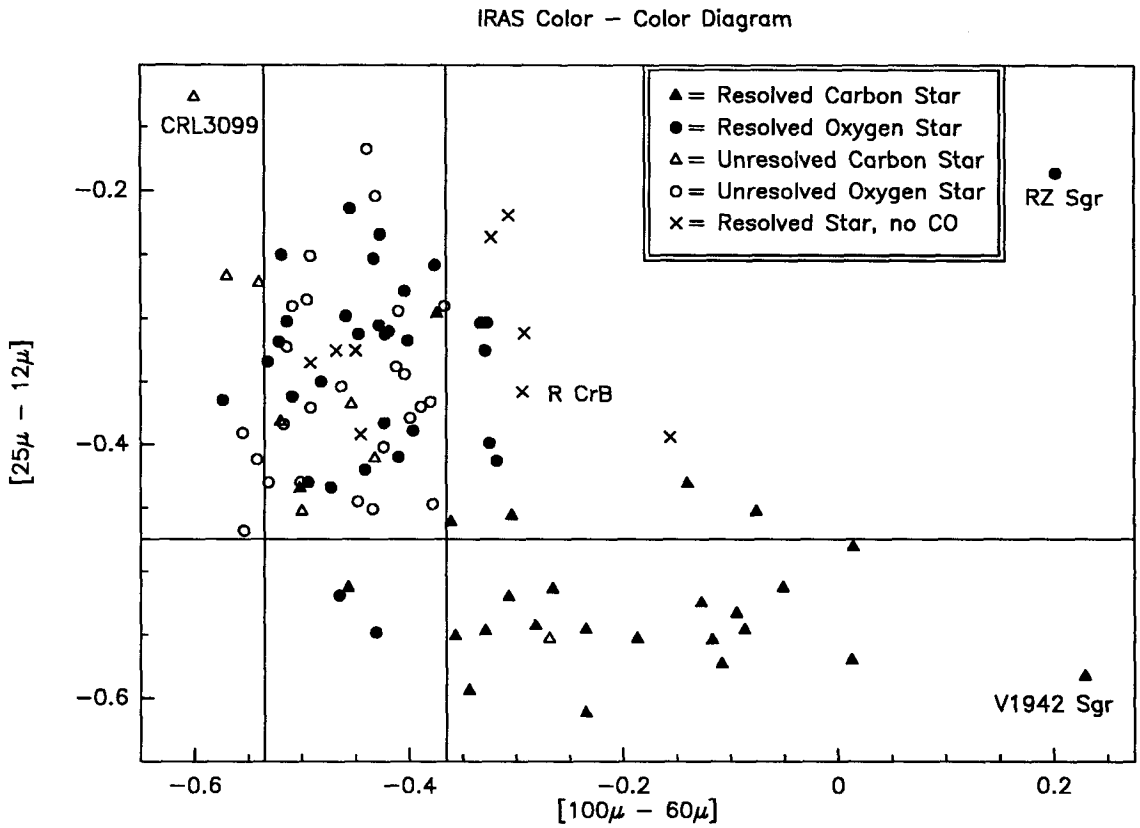

Fig. 5. An *IRAS* two color diagram is shown for all extended objects (*filled symbols*), including those beyond 500 pc, along with objects within 500 pc which were not found by the MFP to be extended (*opensymbols*). No color corrections have been applied to the fluxes from the PSC. Not shown are two planetary nebulae with very blue [25-12] colors, NGC 6720 and NGC 2346. IRAS 09372+1212, Y Hya, and IRC−10°139 are not shown because of problems with one or more of the *IRAS* fluxes for these objects.

is very little dust close to the star. If the resolved objects are older than the unresolved objects, their bluer [25μm – 12μm] color is additional evidence that the mass–loss process is increasingly episodic as the star ages. With the exception of the S star RZ Sgr, the objects with the reddest [100μm – 60μm] colors are all carbon stars. This 100μm excess has been noted by several authors, and has been analyzed by Egan and Leung (1991), who modeled the IR emission from carbon stars and found that a large ($\sim$ 1 pc) detached outer shell is required to produce the *IRAS* 25, 60 and 100μm fluxes.

One final difference between the nearby resolved and unresolved groups is the much higher percentage of semiregular variables in the resolved group. The percentage of Miras and semiregulars is 58% and 21%, respectively, in the unresolved group, but 25% and 63% in the nearby

resolved group. Semiregulars are more common in the nearby resolved group even if the oxygen–rich or carbon stars are considered separately, or if the SRc stars (which are supergiants not on the AGB) are eliminated, or if all the unresolved stars of unknown type are counted as semiregulars. The prevalence of semiregular variables in the resolved group is surprising; these variables have a much smaller average amplitude of variation than do Miras, and at least among Mira variables the mass–loss rate is positively correlated with the amplitude of the star (Whitelock *et al.* 1987).

There are three simple effects that could cause the semiregular variables to have larger shells than the Miras; their shells could be expanding more rapidly, they could have higher mass–loss rates producing denser, more easily detected shells, or they could have been losing mass for a longer time than the Miras. If the velocity from the CO observations is a good indication of the dust expansion velocity, then the resolved semiregulars are not expanding faster than the resolved Miras, because the two groups have nearly identical average CO velocities. The average mass–loss rate for resolved semiregulars is only about half the average value for the resolved Miras, so their shells should be *less* dense, on average. It is conceivable that the semiregulars have larger shells because their lower mass–loss rates allow the dust to decouple from the gas at a smaller radius, and thereby develop a larger drift velocity. However, this would imply that the size of a dust shell should be anticorrelated with the mass–loss rate (if the mass–loss rate is constant). Instead, the shell sizes and mass–loss rates in Table 1 show a weak (and probably insignificant) positive correlation. The most likely explanation seems to be that the semiregular variables have on average been losing mass longer than have the Miras.

2.3 The Interaction of the Shells with the ISM

With the exception of R CrB, the resolved stars are all less distant than 1 kpc, and most are within 500 pc. Being this nearby, almost all of these objects have measurable proper motions, which allows us to calculate ($\vec{v}_{LSR}$). Borkowski and Sarazin (1990) have found that the envelopes of planetary nebulae with large velocities relative to the local ISM are often distorted by the ISM ram pressure. The simple model fitted by the MFP includes this effect only insofar as the model is ellipsoidal. Distortion caused by the ISM might increase the eccentricity of the fitted shell. Any distortion should be most easily seen in larger shells which, for a given $\dot{M}$ and v_0, will have

less dense outer edges more easily deformed by the ISM ram pressure. However, no correlation was found between the eccentricity of the shell and the shell size. Because ram pressure increases quadratically with the star's velocity with respect to the ISM, and since this velocity will nearly equal $\vec{v}_{LSR}$ in the solar neighborhood, the shells of stars with large $|\vec{v}_{LSR}|$ should suffer the greatest distortion, but no such correlation is seen. The shells of stars near the Galactic plane are no more eccentric than those located far from the plane, where the ISM density should be less. Finally, there is no correlation between $\dot{M}$ and the eccentricity. We therefore find no evidence in this study that the shape of the CSS is distorted as a result of ram pressure from the surrounding ISM. Perhaps the eccentricity caused by bipolar outflow dominates any effect of ram pressure from the ISM.

2.4 The Dust Temperature

The estimated shell masses from Table 1 can be combined with the extended emission flux values from appendix Table 3, to calculate mean temperatures for the resolved region of the dust shells. Hildebrand (1983) showed that for spherical dust grains

$$M_{shell} = \frac{F(\nu)D^2}{B(\nu,T)} \frac{4/3a\rho}{Q(\nu)} \left[\frac{M_{gas}}{M_{dust}}\right] \qquad (6)$$

where

M_{shell} = the mass of the resolved portion of the dust shell

$F(\nu)$ = the 60μm flux from the resolved region

D = the distance to the star

$B(\nu,T)$ = the Planck function at frequency ν and temperature T

a = the radius of a dust grain.

ρ = the density of the dust material, assumed here to be 3 gm cm^{-3}

$Q(\nu)$ = the emissivity of the dust at frequency ν

$[M_{gas}/M_{dust}]$ = the gas to dust mass ratio, assumed here to be 100

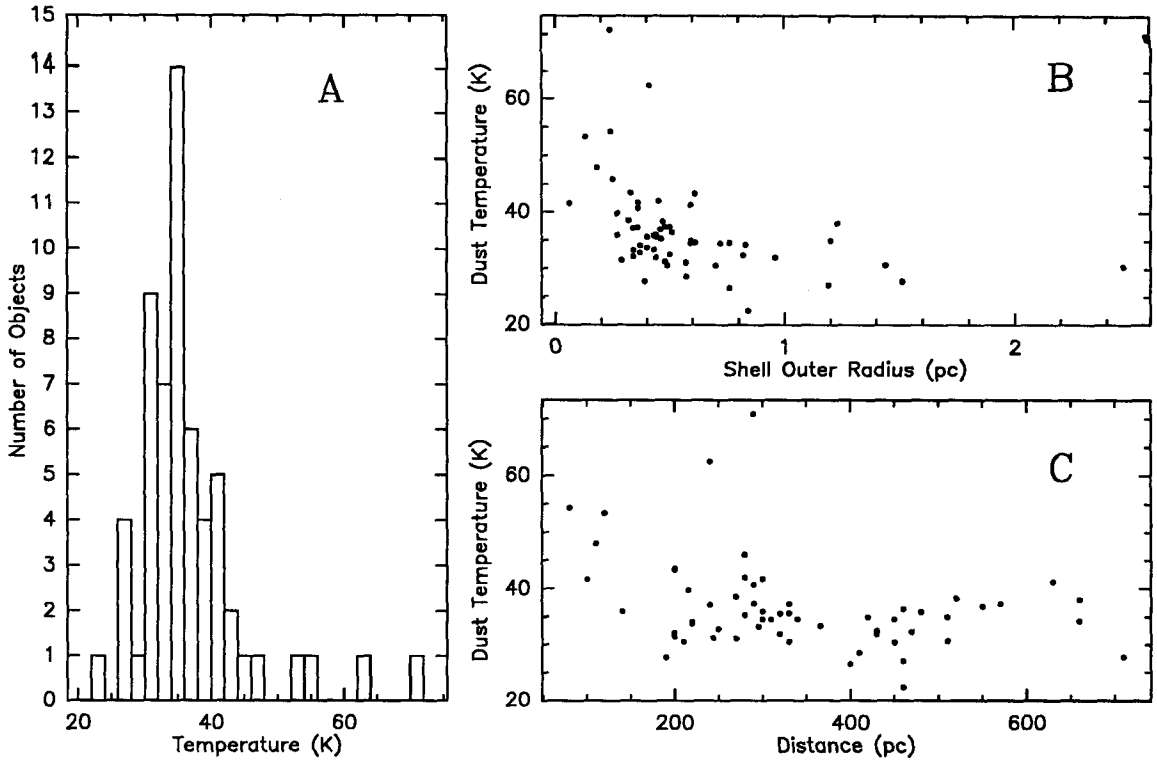

Fig. 6. Figure **A** shows a histogram of calculated dust temperatures. Four of the shells, those of R Leo (53 K), W Hya (54 K), R Crt (63 K) and U Hya (71 K) seem to be significantly warmer than average. **B** shows the distribution of calculated shell temperatures as a function of the shells' outer radii. Note that the warmest shells are much smaller than average, therefore the average temperature of the dust should be higher. **C** shows the calculated shell temperatures as a function of distance. All of the warmest shells are also closer than average, allowing material nearer the star to be resolved.

An iterative procedure was used to find a temperature which satisfied equation (6), for each resolved shell except that of NGC 6720, for which no mass–loss rate was available. The mass of the material within a radius of 1' was subtracted from the mass listed in Table 1 to produce an estimate of the mass of the resolved region. The dust grains were assumed to have radii of 0.1μm, and a 60μm emissivity of 0.0046 was used. This emissivity was obtained by interpolating values tabulated by Draine (1987). The emissivities of graphite spheres and spheres of "astronomical silicate" differ negligibly at 60μm. The 60μm flux values from appendix Table 3 were multiplied by 1.03, to color correct them for a 40 K blackbody.

Figure 6A shows a histogram of the temperatures calculated by solving equation (6). The average and median temperatures are 37 and 35 K, respectively. The average outer radius for these shells is 0.57 pc. Collison and Fix (1991) modeled the temperature profiles of axisymmetric

circumstellar dust shells by solving the radiative transfer problem. They found that all temperature profiles exhibited the same basic shape

$$T(r) = T_0\left(\frac{r_0}{r}\right)^{0.4} e^{-\xi(1-r_0/r)} \approx T_0\left(\frac{r_0}{r}\right)^{0.4} e^{-\xi} \qquad (r \gg r_0) \qquad (7)$$

where r_0 is the radius at which dust condenses with a temperature of T_0, and ξ ranges from 0.48 near the pole to 0.86 near the equator of their model shells. Equation (7) implies that the temperature at large r is not strongly dependent upon r, so the average temperature of 37 K obtained by solving equation (6) should be a good estimate of the temperature at 1/2 the average outer radius (0.29 pc). This temperature is in fair agreement with the value of 30 K obtained from equation (7) with T_0 = 1000 K, r_0 = 50 AU, ξ = 0.67 (these are typical values for T_0 and r_0 from the models of Collison and Fix; this value of ξ is the average of the polar and equatorial values), and r = 0.29 pc.

Figure 7 shows the radial dependence of $I_{60\mu m}/I_{100\mu m}$ for the stars which were found to be extended in the 100μm data. IRC+10°216 was not included, because of the low reliability of its 60μm model parameters. This ratio decreases for all the stars from a radius of 0.1 pc to a radius $\approx$ 0.5 pc. Assuming there is no radial gradient in the grain emissivity, this decrease must arise from a decrease in dust temperature. The dust within this region must be heated either by radiation from the central star, or by collisions with the expelled gas. The data become progressively more noisy as the edges of the envelopes are approached, but the four stars (V Eri, W Pic, RY Dra, and R CrB) with the largest envelopes show that $I_{60\mu m}/I_{100\mu m}$ stops decreasing at a radius of about 0.9 pc. The nearly constant ratio beyond 0.9 pc indicates that in the outer envelope the dust is externally heated.

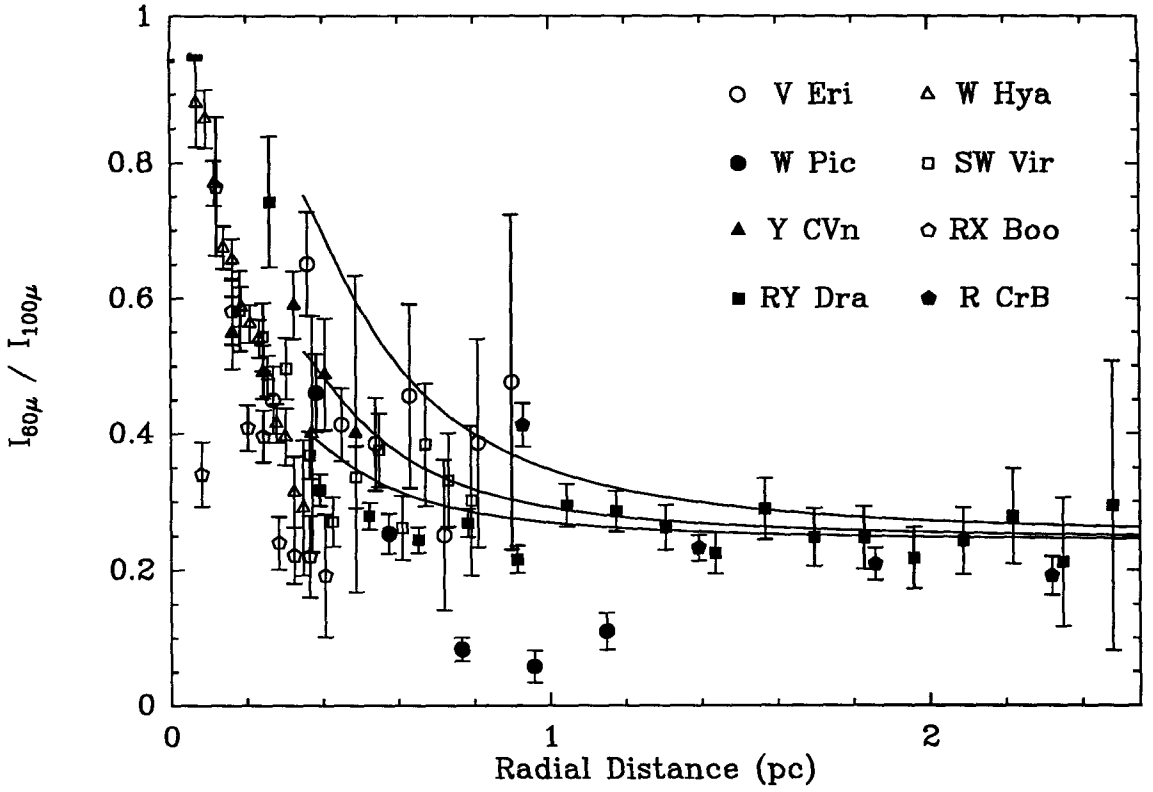

Fig. 7. The radial dependence of the ratio of the 60 and 100μm brightness is shown for the stars which are extended in the 100μm data. In this figure, the raw CRDD data have been summed after baseline removal in 1' wide annular bins of increasing radial distance from the central star. Filled symbols, for W Pic, Y CVn, RY Dra and R CrB, represent carbon star data. Data at radii < 2' are not shown. Several points from radii less than 0.2 pc with $I_{60\mu m}/I_{100\mu m} > 1.0$ are not shown. The error bars represent the value of

$$\sigma(60\mu m/100\mu m) \equiv \left(\frac{1}{I_{100\mu m}}\right)\sqrt{\frac{\sigma^2_{60\mu m}}{N_{60\mu m}} + \frac{I^2_{60\mu m}\sigma^2_{100\mu m}}{I^2_{100\mu m}N_{100\mu m}}}$$

where $\sigma_{60\mu m}$ and $\sigma_{100\mu m}$ are the standard deviations in $I_{60\mu m}$ and $I_{100\mu m}$, and $N_{60\mu m}$ and $N_{100\mu m}$ are the numbers of points in the annular bins. For clarity of the figure, the very substantial error bars for the abscissa are not shown. The curves are from the model of Gillet *et al.* (see text).

These temperature gradient regimes have been noted separately in earlier work. Hawkins (1990) presented *IRAS* 60 and 100μm maps of W Hya obtained from the same survey data used here, and also found it to be extended in both bands. The maps show the CSS has a radius of 15' – 20'. This is in fair agreement with the 10' 60μm and 15' 100μm sizes for this object listed in appendix Table 3, obtained from the MFP. Hawkins compared the 60 and 100μm data, and

derived a dust temperature of $\sim$ 40 K in the outer envelope, in good agreement with the average temperature of 37 K obtained by solving equation (6). He found that $I_{60\mu m}/I_{100\mu m}$ decreases radially and showed that this is consistent with radiative heating of the dust by W Hya. Though not remarked upon by the author, the Hawkins data also indicate $I_{60\mu m}/I_{100\mu m}$ no longer decreases beyond a radius of 0.33 pc (assuming the distance used here, 80 pc, rather than 115 pc used by Hawkins). For R CrB, Gillet *et al.* (1986) found that $I_{60\mu m}/I_{100\mu m}$ is constant across the entire 18' diameter shell, excluding an unresolved central hot-spot which covers the inner 1 pc radius of the shell. The dust temperature inferred by the authors is 25 K – 30 K. Both of these earlier works, plus the results in Figure 7, indicate that within the central $\sim$ 0.5 pc the dust is heated primarily by the central stars' radiation, while an external heat source dominates beyond about 1 pc.

Gillet *et al.* (1986) developed a model for the radial temperature profile and infrared brightness of an envelope heated by both its central star and an external heat source, the effects of which are constant throughout the envelope. This model was used to produce the three curves shown in figure 7. The three curves represent the expected value of $I_{60\mu m}/I_{100\mu m}$ for stars of $10^4 L_\odot$(upper curve), $5 \times 10^3 L_\odot$, and $3 \times 10^3 L_\odot$(lowest curve). In all three cases the central star was assumed to be at a distance of 340 pc and emit as a 2500 K black body, the dust emissivity $\propto \lambda^{-1}$, and the external heating rate is equivalent to that of a $10^4 L_\odot$star at a radius of 0.9 pc. The curves are truncated at 0.4 pc (4'), because at smaller radii the value of $I_{60\mu m}/I_{100\mu m}$ becomes very sensitive to the orientation of the *IRAS* detector with respect to the central star. Lowering the exponent of the dust emissivity (m) below -1 causes $I_{60\mu m}/I_{100\mu m}$ to increase, for a fixed rate of external heating. By calculating models with no external heating we can place a lower limit on the value of m by requiring $I_{60\mu m}/I_{100\mu m}$ to match the data at large radii. For a $10^4 L_\odot$ model, m cannot go below -1.4, and for a $3 \times 10^3 L_\odot$ model m must be greater than -1.6, to match the color near 1 pc. It should be emphasized that changing m cannot remove the need for an external heat source, because central heating cannot produce the flat color distribution seen beyond 1 pc.

In §3.5 it was shown that our results indicate that the carbon star phase of evolution lasts substantially longer than the lifetime estimate of Willems and de Jong (1988). One way in which our results could be brought into agreement with those of Willems and de Jong is by assuming

that the dust has a substantially larger terminal velocity than the molecular material. This is by no means excluded by the results of some of the models of dust acceleration which can be found in the literature. For example Wickramasinghe (1972) calculated that the dust should typically be accelerated to a terminal velocity of several thousand km s^{-1}! However if the dust is expanding at a much higher velocity than the molecular material, then equation (3) tells us that the density of the dust in the CSS must be less than the value that the molecular expansion velocity and the dust/gas ratio near the star would suggest. This means that we must obtain the far–infrared fluxes measured by *IRAS* from a much smaller total amount of solid material. If we assume the dust velocity is 5 times that of the CO (the minimum increase required to make our carbon star age estimates consistent with Willems and de Jong's lifetime estimate), then equation (6) must be solved with a correspondingly smaller effective dust/gas ratio. This increases the average estimated dust temperature from 37 K to 50 K, which does not agree as well with the 30 K predicted by equation (7), or the temperatures implied by $I_{60\mu m}/I_{100\mu m}$.

3. Notes on Particular Objects

W Pictoris: The 18.4' radius of the 100μm emission surrounding this star (appendix Figure 18D) is the second largest of any of the CSSs presented here (after R CrB), corresponding to 3.5 pc (assuming a distance of 660 pc). The 60μm emission (appendix Figure 6B) covers a much smaller area, however no well–defined outer edge is seen in the 60μm emission, suggesting noise may be obscuring emission from beyond a radius of $\sim 7'$. The size of the 100μm envelope is so large, it is questionable whether the extended emission is actually associated with the star. The extended emission at both 60 and 100μm is well centered on the star's position, and the MFP reported the emission arises from a a nearly circular region with an aspect ratio of 0.96 in both bands. The object is at a fairly high Galactic latitude ($b^{II} = -31$), however its PSC CIRR2 flag is 4, indicating the field may be contaminated by infrared cirrus. The CIRR1 flag, which is a count of the objects within 30' which were detected by *IRAS* only in the 100μm band and are apt to be cirrus structures, is 0. A search of the SIMBAD and NED databases revealed no objects within 20' of W Pic which could produce the 100μm emission.

Assuming the 100μm emission is circumstellar in origin, the mass–loss rate and outflow

velocities derived from CO observations (Olofsson *et al.* 1988) imply that near the outer edge the CSS has a density of only 4×10^{-3} H cm^{-3}. Even at this star's distance of 330 pc above the Galactic plane, the surrounding ISM should be dense enough that the CSS would require more than 10^6 years to expand to 3.5 pc. It therefore seems likely that in order for the CSS to reach this size, either W Pic must lie in a region of very low ISM density, or its mass–loss rate must have been much greater in the past, or our distance estimate must be much too high.

RY Draconis: This object is surrounded by the third most extensive region of emission of all those examined. If the extended emission is circumstellar, the radius is 2.9 pc (assuming a distance of 450 pc and using the 100μm size). As with W Pic, the size is so large, it is possible that the extended emission arises from a chance alignment with an object not associated with the star. RY Dra has a high Galactic latitude (b^{II} = 51°), so it is unlikely that this region is contaminated by infrared cirrus. Also, the PSC CIRR1 and CIRR2 flags are 0 and 3 respectively, indicating the region is relatively free of cirrus contamination. We obtained 2° × 2° FRESCO (IPAC 1989) images centered on RY Dra. They reveal very little cirrus contamination at 60μm. There is cirrus emission visible in the 100μm image, but it is neither as intense nor as large as the extended emission surrounding RY Dra. A search of the SIMBAD and NED databases revealed only two cataloged objects within 20' of RY Dra; SAO 15949, a 10th magnitude F2 star 9' away and IRAS F12532+6600, a faint galaxy 17' away whose 60μm flux is 2.5 mJy, and which was undetected at 100μm. Neither of these objects could be responsible for the extended emission around RY Dra.

RY Dra differs from W Pic in that the size and shapes of the 60 and 100μm regions are very similar (see appendix Figures 10B and 19C). Throughout most of the extended emission, $I_{60\mu m}/I_{100\mu m} \approx 0.25$ which is near the middle of the range for infrared cirrus clouds (Low *et al.* 1984). If the extended emission is circumstellar in origin, the temperature of the dust shell is nearly constant throughout the outer envelope. As with W Pic, the CO–derived mass–loss rate and outflow velocity (Olofsson *et al.* 1987) imply a very low density near the outer edge of the CSS, again indicating that either the surrounding ISM has a very low density, or the star's mass–loss rate was greater in the past.

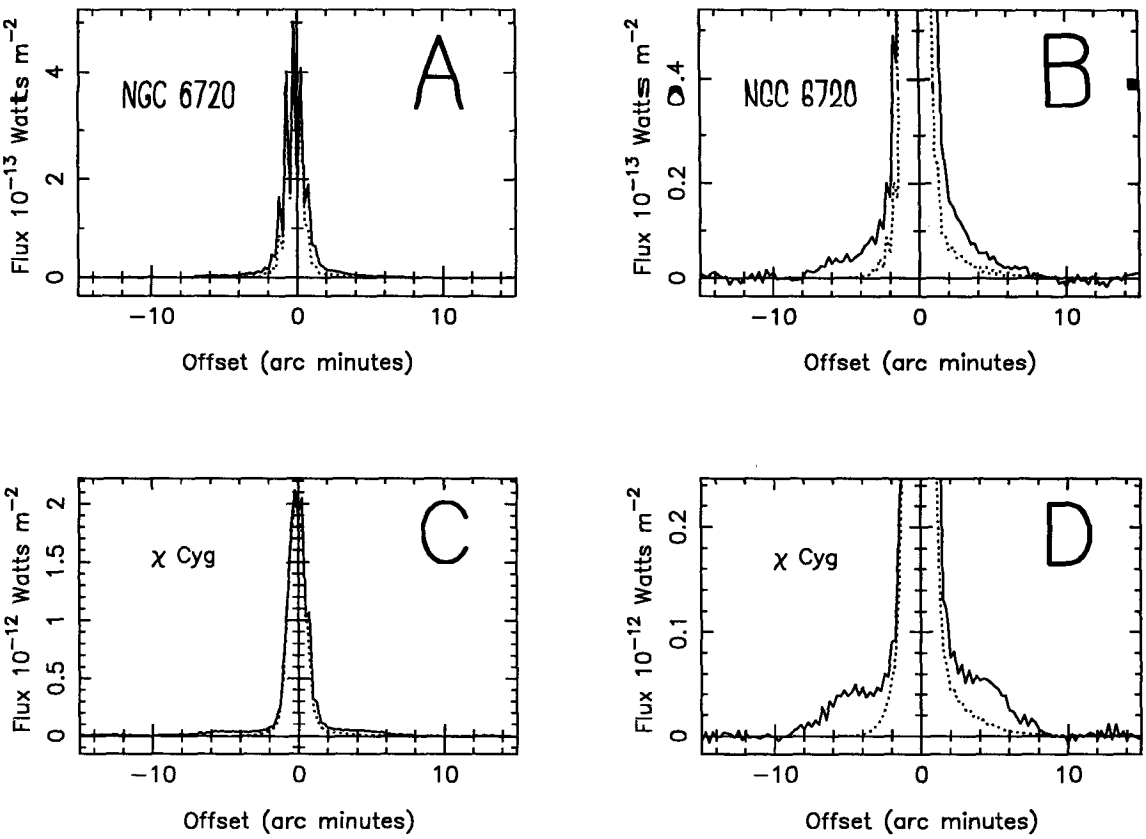

Fig. 8. (**A**) The solid line shows the 60μm data for NGC 6720, binned as in Fig. 1. The dotted line shows the best–fit point source for these data. (**B**) The same data show in **A**, but with an expanded vertical scale. Note that emission is seen several arc minutes further from the source than can be explained by the detector's point spread function alone. (**C**) shows the binned data for χ Cygni (*solidline*) and the best–fit point source (*dottedline*). The extended emission region is very flat, suggesting the CSS is hollow. (**D**) is the same data as in **C** plotted with an expanded vertical scale.

NGC 6720 (the Ring Nebula): Hawkins and Zuckerman (1991 hereafter HZ) also analyzed the survey data for this object, by performing a one–dimensional deconvolution. The results they obtained differ significantly from those presented here. The 60μm diameter they obtained is 50", far smaller than the 10' diameter we obtained. The source of this disagreement is shown in Figures 8A and 8B. The HZ diameter is a Full Width at Half Maximum, whereas the MFP reports a size at zero intensity. Since the extended emission is very weak, it has very little effect on the FWHM. However, HZ also examined the individual detector scans in an attempt to find low level emission which might arise from a weak infrared halo, and found none. We believe that because our program fit a model to all the scans passing near the object, it lowered the noise floor by averaging, and this allowed us to detect extended emission that is too faint to be seen in individual scans.

χ Cygni: This object is not listed in Table 1 or appendix Table 3, because its PSC CIRR2 flag is 5, which indicates the field may be contaminated by infrared cirrus. Nevertheless, this object does appear to be extended (see Figure 8C and 8D), and the 60μm survey scans covering the object have reasonably flat baselines. Unfortunately the 100μm scans show abundant evidence of cirrus contamination. The 60μm shell has a radius of 7', and it is strikingly flat-topped, implying that the shell is detached, with an inner radius of 3.5'. If a distance of 115 pc (Stein 1991) is adopted, the inner and outer radii are 0.12 and 0.23 pc respectively, and the shell age obtained by solving equations (5a and (5b) is 3.5×10^4 years. Further evidence that χ Cygni has a detached shell is provided by its *IRAS* [12-25] and [25-60] colors, which correspond to a temperature of 2000–2500 K. This indicates most of the infrared radiation from this star arises from the star's photosphere. This is in sharp contrast to the situation for most of the AGB stars with detectable molecular emission, the colors of which usually indicate the presence of dust at a temperature below 1000 K. Had this star not been rejected due to its CIRR2 flag (which is only 1 unit above the rejection threshold), it would have been the best example of a detached shell in the entire sample. However χ Cygni is located only 7 pc above the Galactic plane, so the detached shell might be composed of swept–up ISM material, and may not indicate that the star's mass–loss rate was greater in some past era. χ Cygni is not listed in the *IRAS* small scale structure catalog.

4. Conclusions

The *IRAS* survey data for 512 red giant stars were processed using a simple model–fitting program. This program was developed to detect the presence of low intensity extended emission surrounding a bright unresolved source. Of these stars, 76 were found to have shells which are resolved in the *IRAS* 60μm data. The average shell radius is 0.74 pc. Forty percent of the 76 resolved stars have carbon–rich envelopes. A model for the interaction of the expanding shell with the surrounding ISM was developed. This model predicts that the edges of the largest shells (those with radii > 1 pc) will be expanding at much lower speeds than the inner envelope, where the CO emission arises. From examining the resolved envelopes we conclude the following:

1) Most of the CSSs, including many surrounding stars which have been losing mass for $\sim 10^5$ yr, have small total masses. Yet NGC 2346 and IRC+10°216 are surrounded by much more

massive envelopes, implying that duration of the "superwind" is only a small fraction of star's AGB lifetime.

2) The average age for the shells surrounding the 13 Mira–type stars which are extended is 6×10^4 yr. This suggests that the period during which these stars lose mass lasts for $\sim 10^5$ yr. The oldest shell found surrounds W Peg, and the youngest surrounds Mira itself.

3) Some shells appear to be detached from the central star, and have resolved inner radii.

4) Most of the shells with inner radii of 0.25 pc or less have detectable CO emission, while most with inner radii larger than 0.3 pc (such as R CrB) do not. The simplest explanation for this is that CO is destroyed by the interstellar UV field at a radius of about 0.3 pc.

5) Although all but one of the 8 stars less distant than 200 pc are resolved in the *IRAS* 60μm data, 33 stars within 500 pc with CO envelopes, were not. These stars probably have younger CSSs than those which were resolved.

6) Almost all the carbon stars with distances of 500 pc or less have resolved shells, while only 1/2 of the oxygen–rich stars do. The resolved carbon star shells also are older on average than the oxygen–rich ones. These facts imply that carbon stars have been losing mass for a longer period, on average, than oxygen–rich red giants. The average age of these nearby carbon stars is 1.1×10^5 yr, which indicates the lifetime of an average carbon star is $\sim 2 \times 10^5$ yr.

7) Most of the nearby unresolved stars from the CO selected list are Mira variables, while most of the nearby resolved stars are semiregular variables. The simplest explanation for this is that the semiregular variables have been losing mass for a longer period than the Miras.

8) Radiative transfer models and the value of $I_{60\mu m}/I_{100\mu m}$ allow the average dust temperature in the outer regions of a CSS to be estimated. The typical value obtained is about 35 K. This provides a constraint on the value of the dust drift velocity, because a very large drift velocity results in a low dust density in the outer shell which in turn requires a high dust temperature to produce the 60 and 100μm fluxes measured by *IRAS*. The radial dependence of $I_{60\mu m}/I_{100\mu m}$ suggests that an external heat source supplies most of the thermal energy to the dust beyond a radius of 1 pc.

We would like to thank the staff of IPAC for their help; particularly Linda Fulmer and Mehrdad Moshir, for patiently describing the *IRAS* data; Helen Hanson, Rosanne Hernandez and Hilary Hope, who cheerfully and quickly processed dozens of requests for CRDD data and Joe Mazzarella for help using IPAC's CATSCAN database system, which was used to select the stars on the Additional List. Nicolas Mauron, Robert Stencel and Wendy Bauer contributed many helpful comments after reading an early draft of this paper. Finally the contribution of an anonymous referee, whose comments resulted in many improvements and the removal of a great deal of chaff, is gratefully acknowledged. This work was supported by NASA contract NAG 5-1153 and NSF contract #AST 90-15755.

Appendix

Data–Processing Procedure, Results and Confidence Tests

1. Introduction

In this appendix we will: 1) explain how the *IRAS* survey data were examined for evidence of spatially extended structure, 2) list those objects we were able to classify as resolved or unresolved, as well as those we could not classify and 3) present tests of the reliability of our results.

The primary goal of the *IRAS* project was to survey the entire sky at 4 infrared wavelengths. While some specific objects were studied individually by the satellite, most of the sky was only observed as part of the all–sky survey. The overriding consideration in the design of the survey was to ensure the reliability of the derived data products; the Point Source Catalog, the Small-Scale Structure Catalog (IRAS 1985, hereafter SSSC), the Atlas of Low–Resolution Spectra (Olnon *et al.* 1986) and the maps of total sky brightness. A major difficulty in ensuring the integrity of these products was that the unprocessed survey data is contaminated with "detections" caused by cosmic rays, Earth–orbiting debris and minor denizens of the solar system. In order to recognize and reject these spurious detections, the survey was designed to observe each position in the sky several times. For this reason, the *IRAS* survey data for a particular object consists of one or more sets of detector scans passing near the object's position.

Because the *IRAS* survey was designed to produce reliable measurements of new objects, rather than to carry out detailed studies of well–known objects, there are several characteristics of the survey data which make it difficult to produce high–resolution images from the scans. The individual *IRAS* detectors were larger than the telescope's diffraction pattern, particularly in the direction parallel to the satellite's rotation axis (the "cross-scan" direction). Only by analyzing the data from several detectors, whose paths on the sky partially overlap, can information about

source structure on spatial scales near the instrument's diffraction limit be recovered. Also, the detectors' outputs were passed through low–pass filters with cutoff frequencies well below the frequencies required for Nyquist sampling when the satellite was scanning the sky at the survey rate.

Several earlier investigations of the spatial information contained in the *IRAS* data have been published. Bauer and Stencel (1992) measured the widths of the individual 60μm scans of 9 nearby Mira variables, at 10% of maximum intensity. All of these stars also appear in our list of candidate objects and, with one exception (IRC+10°216), we are in agreement regarding which stars were and were not resolved. Stencel *et al.* (1988, 1989) summed all the 60μm scans passing near 111 stars, and measured the width of each star's composite profile at 10% and 5% of maximum, to search for extended emission. They found that one-fourth of their objects were resolved. Because Stencel *et al.* focused exclusively on supergiant stars of spectral types F0 through M5, very few of the stars they examined appear in our list objects. Hawkins (1989, 1990) published fully deconvolved maps of several AGB stars, most of which also appear in our list.

Instead of deconvolving the *IRAS* data and producing a map, we fitted a model of a point source surrounded by dust to the data. There were two reasons for doing this. First, the sky coverage of *IRAS* data is nonuniform. If the star is very near one of the ecliptic poles, the survey data usually contains scans approaching the star from several different position angles. For these sources the effective point spread function for the survey is nearly circular (Moshir *et al.* 1989) and it should be possible to construct a map of the circumstellar material. More commonly, the survey data consists of several sets of scans, all approaching the star with very nearly identical position angles. This fact, combined with the saturation which may occur as soon as the star's image falls upon the detector, makes it difficult to construct a two–dimensional map of the material surrounding the star. On the other hand, since the detectors are extended in the cross scan direction, and since the distance of closest approach of each detector to the star's position varies, some two–dimensional information is contained in the survey data even if each detector approaches with the same position angle. The second reason for fitting a model, rather than producing an image, is that this approach directly gives values for the physically important parameters, such as the size and intensity of the dust shell's emission.

The data were fitted to a model consisting of an ellipsoidal envelope, at a single temperature throughout, with an unresolved point source at its center. Two of the axes of the ellipse were constrained to be perpendicular to the line of sight, and the semiminor axis was forced to be equal in length to the third axis, which lies along the line of sight. The emission is proportional to the column density of the dust, and the density of the dust is assumed to decrease linearly with the square of the distance from the star, but at differing rates along the different axes of the ellipsoid. The intensity of emission from the dust alone at position *(x,y)* is

$$I(x,y) = \frac{C}{\sqrt{k^2x^2+y^2}} \arctan\left(\sqrt{\frac{b^2-k^2x^2-y^2}{k^2x^2+y^2}}\right)$$

where

x	= the distance from the model center along the semimajor axis
y	= the distance from the model center along the semiminor axis
C	= a constant proportional to the rate of mass–loss in dust (a model parameter)
k	= the ratio of the minor axis length to the major axis length (a model parameter)
b	= the semiminor axis length (a model parameter).

Since the formula above gives an infinite result at (0,0), the model assumes that the emission from dust reaches a constant value along lines of sight intersecting some inner radius where either the envelope is terminated, or the dust becomes optically thick. This inner radius is another parameter fitted by the model–fitting program (MFP).

In addition to the parameters C, k and b of the dust model above, the model includes the intensity of the star, the Right Ascension (RA) and Declination (Dec) offsets of the model from the position given to ADDSCAN (an IPAC program which originally extracted the data), and a position angle in the sky of the major axis of the envelope, as parameters to be determined.

The model is fitted by minimizing the function

$$\text{error} = \sum_{i=1}^{N_D} \sum_{j=1}^{N_{S_i}} \sum_{k=1}^{N_{P_{ij}}} \left| \frac{y_{ijk} - y_{ijk}(\vec{a})}{\sigma_i} \right|$$

where

N_D = the number of *IRAS* detectors for a particular band

N_{S_i} = the number of scans for this source from detector *i*

$N_{P_{ij}}$ = the number of points in the j^{th} scan of the i^{th} detector

y_{ijk} = the k^{th} data point from the j^{th} scan of the i^{th} detector

σ_i = the noise level of the i^{th} detector relative to other detectors

$\vec{a}$ = a vector composed of the eight model parameters.

$y_{ijk}(\vec{a})$ is a two–dimensional integral of the model intensity at the sky position corresponding to y_{ijk} multiplied by the response function for the i^{th} detector

$$y_{ijk}(\vec{a}) = \int_{-S_i}^{S_i} \int_{-T_i}^{T_i} I(\vec{a}, s, t)\, R_i(s,t)\, ds\, dt.$$

The limits in the integral above correspond to the spatial extent of the i^{th} detector, which for the 60μm detectors is $\pm$3.0' in the in-scan direction and $\pm$3.3' in the cross-scan direction. $R_i(s,t)$, the two–dimensional response function of the i^{th} detector, is calculated from the Moshir response functions (Moshir 1989). These response functions were derived from a set of 32 Additional Observations (AOs) of the planetary nebula NGC 6543. The functions do not perfectly represent the point spread function of the *IRAS* detectors during survey observations, for two reasons. The first reason is that NGC 6543 was slightly resolved by *IRAS*. The second reason is that when the AO data were taken, the satellite scanned the sky more slowly than it did during survey observations. Since the detector outputs were passed through low–pass filters, and since the detectors themselves were hysteretic, the response functions derived from AOs are less extended on the sky than a point source observed at the survey scan rate would be. Since the first problem makes the templates too large on the sky, and the second makes them too small, the problems cancel each other to some extent. Tests, described below, were performed

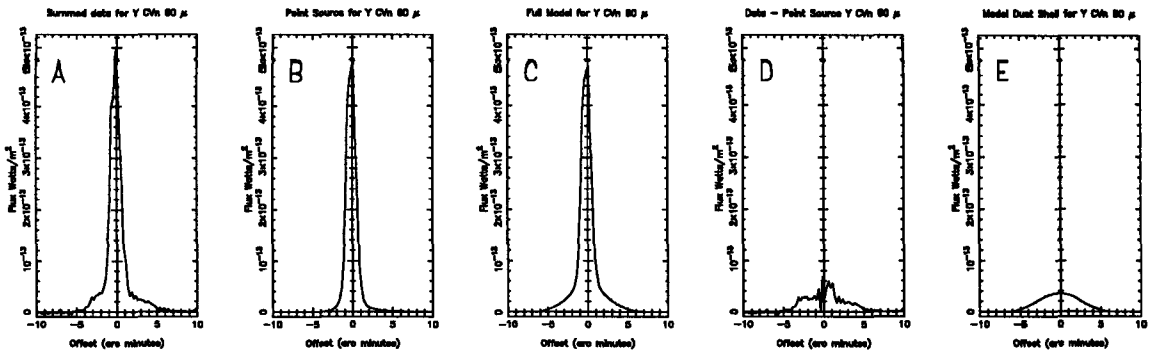

Fig. 1. **(A)** All the scans for the source Y CVn, averaged together. To produce this plot the data points were averaged in bins 15" wide. The bin in which to place a data point was determined by the distance of the point from the source, in the in-scan direction. **(B)** Results from the first pass of the model–fitting program (MFP) are shown. Synthetic data were produced by calculating the flux predicted by the model for each point at which a measurement was taken. The model used in this plot consisted of the MFP's best fit for the first three parameters: point source intensity, and RA and Dec offsets. **(C)** The results of the second pass of the MFP are shown. Synthetic data were produced, using the MFP's final best fit for both the point source and dust shell. **(D)** This plot shows the residual flux remaining after the best fit point source is subtracted from the data. Some residual flux remains, from a resolved dust shell. **(E)** The rightmost plot shows synthetic data for the dust shell only.

to judge how well the Moshir functions mimicked the shape of a point source observed during the survey. We calculated $y_{ijk}(\vec{a})$ by Simpson's rule integration. The function *error* was minimized in the eight–dimensional space of model parameters by a direction set algorithm (Press 1986). The integrals were calculated to a precision of 5%, and the direction set algorithm was iterated until an iteration passed during which none of the model parameters changed by as much as 5%.

The absolute value of the deviation of the model from the data was minimized, rather than the square of the deviation, which is a more common figure of merit. This approach was taken because the noise in *IRAS* data is very non-Gaussian. Radiation hits and emission from dust near the satellite produced frequent spikes in the data, which have a noticable effect on the MFP if the square of the deviation is used as the figure of merit.

2. Data–Processing Steps

Of the four *IRAS* bands, dust emission is visible primarily in the 60 and 100μm data, where the emission from the central star is less dominant. The 60μm data were analysed first, because

the 60μm data yield higher resolution and are much less effected by infrared cirrus emission. Each star's data set was produced by the default ADDSCAN processing, and consists of all scans in which the star passes within 1.7' of the detector center.

The first step in processing the data was to subtract a linear baseline from the Calibrated Raw Detector Data (CRDD). The baseline is fitted to 2 windows 15' away from the star's position. If one of the windows contained emission from another source, then the windows were moved further from the source to regions showing no emission. Obvious noise spikes were also removed at this point.

The first pass of the MFP tried to fit just three of the model's eight parameters: the point source intensity, and the right ascension and declination offsets. After these three parameters had been determined, the MFP minimized the *error* function with respect to six parameters: point source intensity, dust shell density, radius at which dust becomes optically thick, semimajor axis length, aspect ratio, and position angle. The point source intensity had to be redetermined in this second fitting loop, because the first loop might have overestimated the intensity of the point source by ignoring the contribution from the resolved region. If MFP reported that the CSS extended as far as 15' from the star, the baseline windows were moved further from the central position and the data were reprocessed. Figure 1 compares the results of the two passes of the MFP to the CRDD data, for the case of the carbon star Y CVn.

For those objects which the MFP indicated were extended, the MFP was run a second time. For this run a larger data set was used, consisting of all scans which passed within 10' of the star's position. Figure 2 shows the increased coverage afforded by this larger data set, again for Y CVn. In the case of Y CVn, as with most of the stars, all the scans approached the star from nearly the same position angle. As a result of this, the extent of the dust in the direction perpendicular to the scans (the cross-scan direction) was very poorly constrained by the small data set. The larger data set allowed the size of the shell in the cross-scan direction to be determined much more accurately. This second 60μm processing pass was not performed for the four brightest resolved sources: CIT 6, α Ori, o Cet, and IRC+10°216. The CRDD data for these four objects shows optical cross–talk caused by the telescope's secondary support spider. None of these objects showed optical cross–talk in the 100μm band, except IRC+10°216 which showed it only weakly.

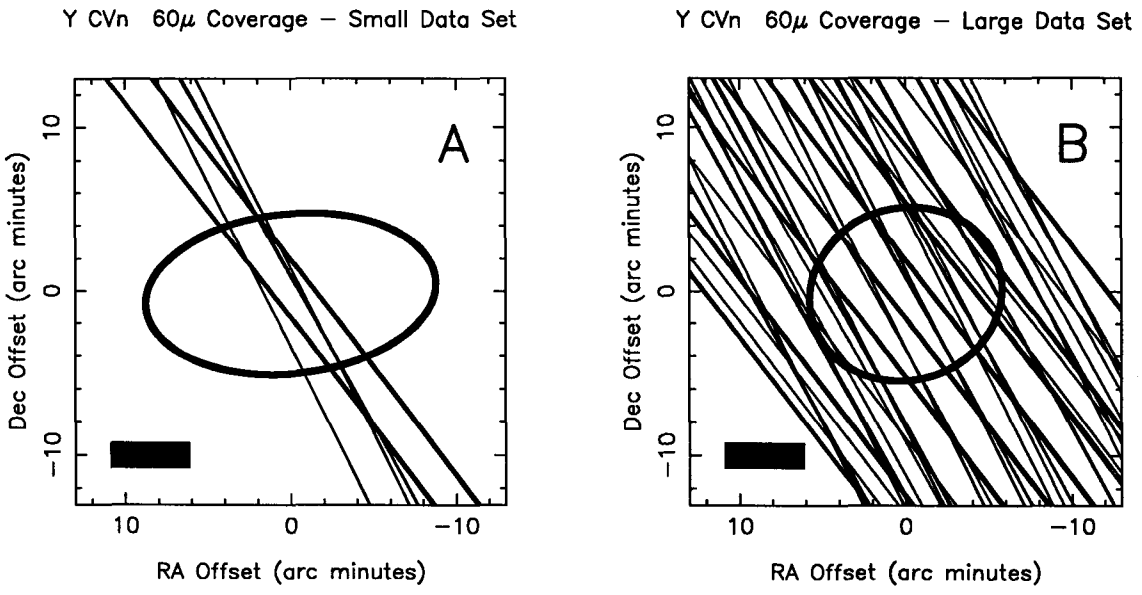

Fig. 2. Figure **A** shows the coverage of the source Y CVn, using the default ADDSCAN selection criteria which selects all scans passing within 1.7' of the source. Each line represents the path on the sky of an *IRAS* detector, and some lines overlap. The ellipse plotted is the size and shape of the CSS, determined from these 10 scans. Since all the passes approached the source from nearly the same angle, the size of the dust shell in the orthogonal direction is poorly constrained. Figure **B** shows the increased coverage when all 56 scans which passed within 10' are used, along with the shape of the CSS derived from those scans. Even though all scans still approach from about the same angle, the size of the dust shell is now well constrained in all directions, and the CSS is seen to be nearly circular. In both figures, the black box shows the size of the largest *IRAS* 60μm detector.

3. Results

The initial list of objects processed consisted of all the evolved stars for which a detection of emission in a rotational line of CO had appeared in the literature (by 1989). Four of these stars fell within the small areas of the sky not covered by the *IRAS* survey. Sixty six of these stars were either near other sources or imbedded in regions of extended emission, resulting in badly curved baselines. These stars were rejected. The data for the remaining 213 stars were processed by the MFP. The calculations consumed more than 1 CPU year on a VAX 11/750 computer. 152 of these stars did not appear to be extended. Five of the stars which did appear extended had a CIRR2 value greater than 4 in the PSC, suggesting the region may have been contaminated by cirrus. These stars were also rejected.

The example of R CrB, which was very clearly resolved by *IRAS* (Gillet *et al.* 1986), yet has not been detected in CO, lead us to look for additional stars which might have been resolved. In an effort to find other such objects, all objects listed in the PSC matching the following criteria were examined:

PSC CIRR2 flag < 5

and

[((12μm flux / 25μm flux) < 3.7 and
60μm flux > 2.0 Jy and
all 4 PSC fluxes have quality flags > 1 and
Spectral type, if available, later than K and
(an association in
the General Catalog of Variable Stars or
the General Catalog of Cool Carbon Stars or
the General Catalog of S Stars))

or

(an association in the SSSC within 120" and
a SSSC 60 or 100μm flux > 0 and
a SSSC Cir flag < 5 and
(12μm flux / 25μm flux) < 4.0 and
Spectral type, if available, later than K and
no extragalactic associations)]

or

a Mira variable within 500 pc (using distance estimates from Jura and Kleinmann (1992) if available, otherwise using the Bowers and Hagen (1984) P–L–S relationship)

An additional 235 stars matched the above criteria. This group of objects will be referred to as the "Additional Objects." Of them, 116 had bad baselines, and 95 appeared to be unresolved.

Table 1 lists all the stars from the CO selected list that were rejected, along with those which were not found to be extended. Table 2 does the same for the Additional Objects.

Table 1. - Stars from the CO List Which Were Examined and Rejected

Stars not observed during *IRAS* survey				
IRC−10°236	NGC 7027	IRC+40°483	IRC+00°509	
Stars with curved baselines				
IRAS 00210+6221	OH 127.8 − 0.0	OH 141.7 + 3.5	U Ari	U Cam
RX Lep	IRC−10°139	S Aur	S Ori	M 1 − 7
M 1 − 8	RY Mon	W CMa	IRC−20°131	NGC 6072
RS Sco	RR Sco	IRAS 17217-3916	IRAS 17371-3021	OH 0.9 + 1.3
TW Oph	OH 11.4 + 6.6	NGC 6445	IRAS 17581-1744	VX Sgr
NGC 6563	M 4 − 9	CRL 2154	IRAS 18248-0839	IRAS 18269-1257
OH 17.7 − 2.0	OH 26.5 + 0.6	IRC+00°365	IRAS 18424+0346	R Sct
OH 30.1 − 0.7	S Sct	OH 32.8 − 0.3	OH 39.7 + 1.5	IRC+10°401
V Aql	R Aql	IRAS 19068+0544	OH 44.8 − 2.3	Vy2 − 2
RT Aql	IRAS 19477+2401	IRAS 20028+3910	IRAS 20435+3825	IRAS 20532+5554
IRAS 21003+4801	V1549 Cyg	IRAS 21147+5110	IRAS 21223+5114	IRAS 21282+5050
IC 5117	IRAS 21318+5631	IRC+40°485	RU Cyg	IRAS 21449+4950
M 2 − 51	OH 104.9 + 2.5	CRL 2985	CRL2999	CRL 3011
IRC+60°427				
Stars which were processed, but did not appear to be extended				
IRC+40°004	T Cas	R And	IRC+10°011	IRC+30°021
IRC+60°041	Z Psc	CRL 190	S Cas	W And
IRAS 02152+2822	R For	CRL 341	CIT 4	IRC−30°023
R Hor	IRAS 03074-8732	TW Hor	CRL 482	OH 138.0 + 7.3
IRC+50°096	CRL 5102	NML Tau	IRC+60°144	CRL 618
IRAS 04530+4427	TX Cam	IRC+50°137	NSV 1835	IRAS 05136+4712
IRC+60°154	CRL 809	IRC+70°066	Y Tau	IRC+40°149
V Cam	CRL 865	TU Gem	CRL 933	CRL 935
CRL 954	IRC+60°169	CRL 971	IRC−20°101	GX Mon
CL Mon	R Vol	CRL 1085	IRAS 07134+1005	VY CMa
IRAS 07217-1246	S CMi	M 1 − 16	NGC 2440	OH 231.8 + 4.2
IRAS 07582-1933	IRAS 08045-1524	IRAS 08074-3615	CRL 1235	R Cnc
CRL 5250	W Cnc	CRL 5254	X Hya	IRAS 09371+1212
R LMi	IW Hya	X Vel	V Hya	IRAS 11308-1020
RU Vir	S Vir	CRL 4211	S CrB	IRAS 15194-5115
WX Ser	V CrB	R Ser	CRL 1822	RU Her
IRAS 16105-4205	U Her	g Her	M 2 − 9	CPD−56
CRL 1922	V463 Sco	NGC 6302	CRL 6815S	IRC+20°326
MW Her	CRL 5379	HD 161796	89 Her	T Dra
FX Ser	CRL 2135	CRL 2155	T Lyr	CRL 2199
IRC+10°365	X Oph	IRC+20°370	IRC+10°374	IRAS 18467-4802
CRL 2259	IRC−30°398	RS Cra	V3880 Sgr	IRC−30°404
CRL 2343	W Aql	CRL 2362	IRC−10°502	IRC+10°420
CRL 2417	M1 − 92	IRAS 19346+1209	IRAS 19454+2920	GY Aql
IRAS 19475+3119	IRAS 19500-1709	CRL 2477	RR Aql	CRL 2494
Z Cyg	IRC−10°529	NSV 12961	IRC+80°040	V Cyg
CRL 2646	IRAS 20541-6549	CRL 2686	CRL 2688	IRC+00°499
UU Peg	CRL 5625S	IRAS 21373+4540	V460 Cyg	RT Cep
IRAS 21489+5301	IRAS 21554+6204	TW Peg	CRL 2901	IRAS 22272+5435
IRAS 22303+5950	CRL 3068	CRL 3099	IRAS 23268+6854	IRAS 23279+5336
IRC+40°540	IRAS 23321+6545			
Stars which appeared to be extended, with a PSC CIRR2 flag > 4				
IRAS 05104+2055	RS Lib	χ Cyg	T Cep	μ Cep [A]

[A] Although it is located in a region contaminated by cirrus, it is likely that μ Cep is truly resolved in the *IRAS* data (Stencel *et al.* 1988, Hawkins 1989)

Table 2. – Stars from the Additional Objects List Which Were Examined and Rejected

Stars with curved baselines				
PK 118 + 02.1	VX And	CE And	TT Per	S Per
SS Cep	BE Cam	BR Eri	RS Eri	IR Per
BZ Tau	DV Tau	RT Ori	V883 Ori	S Col
TV Gem	CRL 5188	CR Gem	FX Mon	NP Pup
BM Gem	RX Cnc	Z Cnc	FK Hya	RV Hya
SZ Car	SAO 238059	IRAS 10308 – 6122	BI Car	IRAS 10501 – 5556
AF Leo	C 1882	S Crt	Z UMa	TZ Vir
BB Cru	TV Cen	AA Cru	SS Vir	V497 Cen
V744 Cen	WY Boo	AQ Cen	C 2147	UZ Cir
Y Cen	GI Lup	S Ser	R Cir	RV Tra
Z Sco	NSV 7459	SS Nor	C 2336	V594 Her
R UMi	AF Sco	AH Dra	V850 Oph	TU Sco
V617 Sco	V522 Oph	IRC−20°360	C 2451	V492 Sco
TY Dra	RU Sco	BG Oph	V762 Sgr	V438 Sco
OP Her	AU Her	EK CrA	WY Her	IRC−10°392
V1804 Sgr	V529 Her	V1014 Oph	IRC+10°356	TW Lyr
SS Tel	V348 Sgr	AM CrA	V2059 Sgr	SU Sgr
RX Tel	V1256 Sgr	RY Sgr	YZ Dra	V859 Aql
DI Sgr	V464 Aql	RR Sgr	V468 Cyg	RX Sge
CRL 2492	V718 Cyg	GN Cyg	AE Cap	V372 Cyg
RS Del	AI Cyg	V570 Cyg	RX Vul	UX Cyg
RS Cap	PK 97 + 3.1	VV Cep	SS Peg	AB Aqr
DG Cep	RX Lac	BC And	SV Aqr	PZ Cas
RT Cas				
Stars which were processed, but did not appear to be extended				
SY Scl	S Scl	T Cet	T And	UY Cet
TU And	RW And	ST Psc	R Psc	SV Psc
UZ Cet	RY Cet	R Cet	R Tri	W Hor
T Ari	Z Eri	X Hor	RR Eri	U Hor
UU Eri	T Cam	R Cae	SY Men	T Lep
S Pic	U Dor	RT Lep	TW And	S Lep
CRL 915	U Lyn	X Gem	L2 Pup	SV Lyn
RZ UMa	FZ Hya	RT Hya	AK Hya	CRL 5252
EY Hya	RT Cnc	FF Hya	R UMa	ST UMa
C 1886	AZ UMa	T Crv	NSV 5868	U CVn
T Com	R CVn	AY Vir	RW CVn	RU Hya
U UMi	RS Vir	V Boo	RV Boo	Y Lib
S UMi	CRL 1788	BG Ser	RS CrB	AT Dra
RY CrB	TV Dra	U Tel	Nova Aql 1919	CH Cyg
V2234 Sgr	R Tel	RT Sgr	Y Tel	U Mic
TZ Aql	Y Aqr	U Del	W Aqr	S Ind
V Mic	R Gru	UU Tuc	DZ Aqr	S Gru
RV Peg	R Peg	Y Scl	S Peg	BU And
R Aqr	EY And	S Phe	Z Peg	W Cet

Figures 4 through 16 show the results of the MFP for the 78 stars that appeared extended in the 60μm data, and for IRC+10°216 which appeared extended, but badly saturated the detectors. Three plots are shown for each star. The first plot shows the average of all the survey scans passing within 1' of the star's position. To produce this plot, the distance in the scan direction of the detector's center from the star's position was used to select the bin in which each data point would be averaged. There were 4 bins per arcminute. The second plot, labeled "DATA," shows these same averaged scans after the point source, fitted by the MFP, has been subtracted. The third plot, labeled "MODEL," shows synthetic averaged data. This plot was constructed by calculating the predicted flux from the extended portion of the model, at every point where data were actually measured. A bar is plotted under both the "DATA" and "MODEL" plots, the length of which is the "diameter" of the CSS, defined as the geometric mean of the shell's major and minor axes.

4. Tests for Reliability of the Results

One can easily imagine problems that might cause the MFP to fit a spurious resolved component to the data. For example, if the satellite pointing reconstruction was poor for some proper subset of the scans covering a particular star, then the peak intensities for those scans would not appear to fall at the star's true position. If all the scans for the star were then summed via ADDSCAN, the star's detection profile would be artificially broadened. In order to verify that our results were not badly contaminated by such errors, several tests were performed to determine whether or not the extended emission reported by the MFP was real. The first test was to run the MFP using data for sources that should not be resolved. Figure 17 shows the results of running the MFP on the 60μm data for 6 galaxies which were unresolved at all *IRAS* wavelengths (Soifer 1989). Except for the case of NGC 2966 (Figure 17C), the data for each of these galaxies is well approximated by the point source that the MFP fitted. When the model point source is subtracted from the NGC 2966 data, the fit is seen to be quite poor at small offset values. This defect, which is also seen in many of the stellar cases, probably arises from small errors in the position reconstruction of individual survey scans. While the MFP fitted a position offset to the data set as a whole, no attempt was made to correct for position errors on

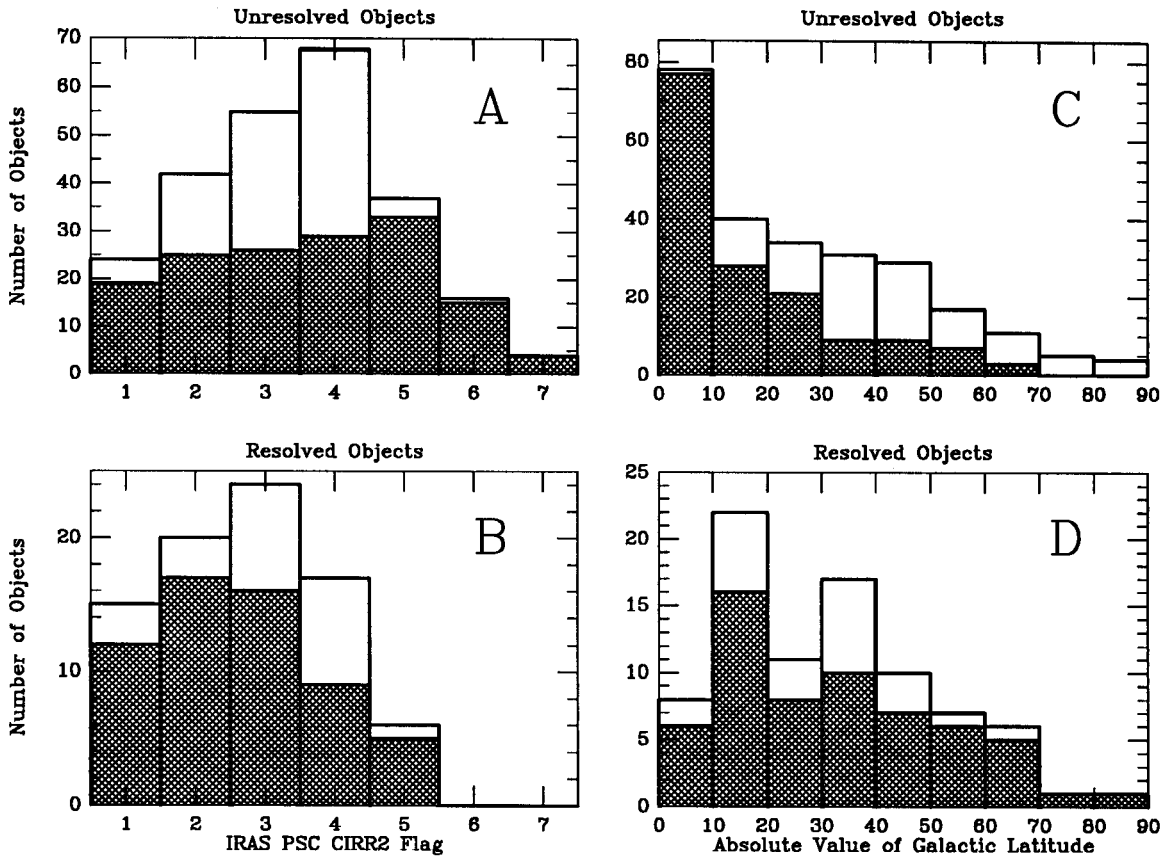

Fig. 3. **A** and **B** show the distributions of the PSC CIRR2 flag for the resolved and unresolved objects respectively. We judged 248 objects to be unresolved, however only 246 of these appear in the PSC (two failed to meet the strict confirmation criteria, even though individual *IRAS* observations show a strong detection). One resolved object, Y Hya, does not appear in the PSC and hence has no CIRR2 flag. **C** and **D** show the distribution of Galactic latitudes among the unresolved and resolved objects. These two plots contain the objects which do not appear in the PSC. In all four plots the data from the CO selected sample are presented in the shaded regions.

a scan by scan basis. Because we were searching for extended structure, corresponding to low spatial frequencies in the data, small position errors could not greatly affect our results. This is confirmed by the fact that in none of the galaxy test cases, including NGC 2966, did the MFP fit a significant extended component.

Although the infrared cirrus emission was detected primarily at 100μm, it occasionally was seen at 60μm. If the area around the star being examined is contaminated by infrared cirrus emission, then the MFP might fit a dust shell to this emission even though it is not circumstellar in origin. A value greater than 4 for the PSC CIRR2 flag indicates the source is in a region which

may be contaminated by cirrus emission. Figure 3A shows the CIRR2 flag distribution of all objects which the MFP reported were unresolved. The average CIRR2 value for this group is 3.5. Figure 3B shows the distribution for the objects which appeared to be resolved, including those with CIRR2 flags greater than 4. For this group, the average value is 2.7. On average, the objects which appear to be extended are in regions which are less apt to be contaminated with cirrus emission than are the unresolved objects, so it is unlikely that the extended emission reported by the MFP was caused by infrared cirrus.

Figures 3C and 3D show the distribution of absolute Galactic latitudes, $|b^{II}|$, for the unresolved and resolved groups respectively. The unresolved objects are clustered nearer to the Galactic plane than are the resolved ones, as one would expect if the resolved objects are less distant. The average $|b^{II}|$ value of the resolved group is 31.3°. If the resolved objects were distributed randomly about the sky, $|b^{II}|$ would average to 32.7°. This close agreement suggests that the average distance to the resolved objects is less than 1 kpc, the half thickness of the Galactic disk. The greater clustering of the unresolved objects about the Galactic plane explains the higher average CIRR2 value for that group.

As a final test, a function was defined to discriminate between cases where the MFP found significant amounts of extended emission, and those where it did not. The "Quality Function" is defined as

$$Q.F. = \frac{Q_0 F_{extended}}{F_{unresolved} R_{outer}^2}$$

where

$F_{extended}$ = The flux the model predicts from beyond 1' from the point source

$F_{unresolved}$ = The flux the model predicts from within 1 arc minute

R_{outer} = The geometric mean of the dust shell's semimajor and semiminor axes

Q_0 = The normalization constant

The ratio of the two fluxes in *Q.F.* gives a measure of the fraction of the total flux arising from the resolved region of the CSS. The division by R_{outer}^2 is included to discriminate against

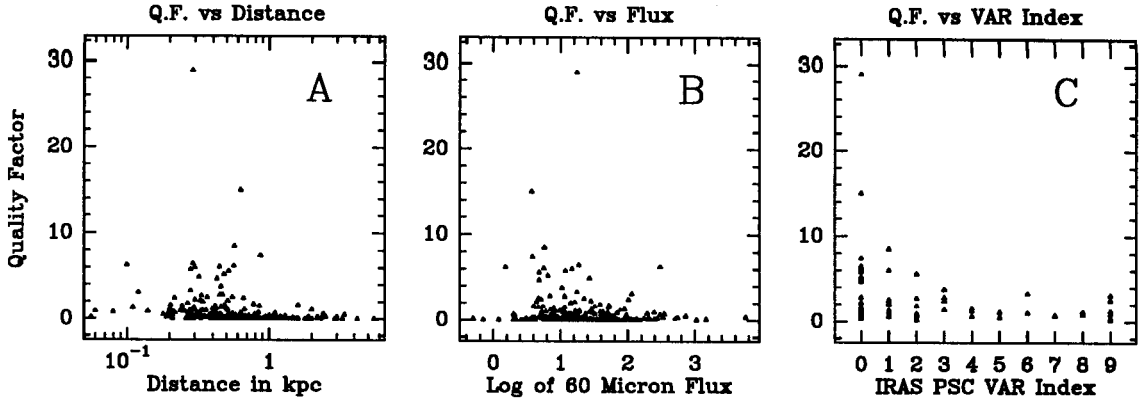

Fig. 21. The distribution of "Quality Factor" values as a function of distance, 60μm flux, and the *IRAS* PSC variability index. Higher values of $Q \triangleright F \triangleright$ correspond to sources that have been resolved. In Figures A&B, the $Q \triangleright F \triangleright$ is shown for all 263 stars which were processed by the MFP and which have CIRR2 values of 4 or less. The average $Q \triangleright F \triangleright$ value is 0.87, and many symbols overlap. Figure A does not include the stars IRAS 03074–8732, W Hor, T Com NSV 5868, NSV 1835, V2234 Sgr, NSV 12961, and IRAS 20541–6549, because no distance estimates were available for these stars. Z Cen is also not shown (see text). 49 of the stars shown in Figure A are at distances of 1 kpc or more. The star at 1.6 kpc with a $Q \triangleright F \triangleright$ greater than 1 is R CrB. Figure C, which includes only the 74 stars which were judged to be extended, shows the distribution of the PSC variability index amongst these objects.

model results predicting low intensity emission from a very large area, which is apt to be caused by slight curvature in the scan baselines. The *Q.F.* function is normalized so that a spherical CSS with a radius of 5' and $F_{unresolved}/F_{extended} = 10$ will have a *Q.F.* value of 1. Values substantially less than 1 indicate the star is not resolved.

Figure 21 shows the values of *Q.F.* for each star processed by the MFP, with a CIRR2 flag of 4 or less. In Figure 21A, the *Q.F.* values are displayed as a function of the distance to the source. Except for the case of R CrB, all of the large values of *Q.F.* come from objects less than 1 kpc away. This implies that the extended emission found by the MFP arises from a real shell around a nearby object, and is not a spurious feature of the data or the detector templates. Figure 21B shows the *Q.F.* values as a function of 60μm flux. Above average *Q.F.* values were obtained for sources differing by more than a factor of 1,000 in 60μm flux, therefore the extended emission is not just an artifact caused by the templates matching either very weak or very strong sources poorly. Many of the objects in Figure 21B with 60μm flux values below 10.0 Jy have large *Q.F.* values. The average *Q.F.* value for these 101 objects is 0.91. To check whether some defect in the

MFP caused all faint objects to have high *Q.F.* values, the data for 45 unresolved galaxies with flux values below 10 Jy were processed. The average *Q.F.* for these galaxies was 0.18, which is less than the *Q.F.* value for any of the objects we claim are resolved. Figure 21C shows the *Q.F.* values as a function of the PSC VAR index, which is defined as 10 times the probability that a source is variable in the 12 or 25μm bands. Above average *Q.F.* values are seen at all VAR index values, and the highest values are found for the stars which showed the least evidence of variability (there is, of course, no doubt that *all* of these objects, except the planetary nebulae, are long–period variables; the limited duration of the *IRAS* survey meant that most of them were only observed a few times, over a interval of less than one pulsation period). It therefore seems unlikely that intensity fluctuations caused by source variability confused the MFP, and caused it to fit a spurious resolved component.

While these reliability tests give us confidence that most of the extended emission we have found is circumstellar in origin, we cannot be certain in any individual case that the emission is truly associated with the star. The extended emission that was found surrounding any of the Additional Objects should be regarded with particular skepticism. A case in point is Z Cen, which the MFP found to be extended. This object is a Type I supernova in a nearby galaxy. It is very unlikely that the extended emission is related to the supernova, and even the association of the *un*resolved emission with the supernova is questionable.

60 Micron Results

Table 3 shows the model parameters for the 78 stars found to be extended in the 60μm data. While all stars with Q.F. > 1.5 are included in this table, stars with Q.F. ≈ 1 were included only if the extended model appeared to fit the CRDD data appreciably better than a point source did. The fluxes quoted are not color corrected, and were converted from the raw units of W m^{-2} to Janskys by assuming a flat energy spectrum $\nu F_\nu = 1$. The radii given in Table 3 are the geometric means of the major and minor axes of the best fit ellipsoidal shell.

100 Micron Results

At first glance, the 100μm data would seem to hold the most promise for detecting extended emission. The cool outer regions of the CSS should radiate most strongly around 100μm, even if the dust emissivity has a wavelength dependence as strong as λ^{-2}. In addition, the warm inner unresolved region will be relatively less dominant at 100μm than at 60μm. Unfortunately there are problems with the 100μm survey data that more than offset these advantages.

By far the worst problem with the 100μm data is the contamination of much of the sky by infrared cirrus. When the 100μm data for the 78 stars which were resolved in the 60μm data were examined, most of the scans were strongly curved, presumably due to infrared cirrus. In these cases even when the individual scans showed extended emission surrounding the star, it was impossible to find regions of the scan which were clearly free of emission that could be used to calculate the scan's baseline. The results of the MFP depend very strongly on the position of the scans' baselines, therefore if no baselines could be calculated, the scans could not be used. Only 16 of these 78 stars are in regions so free of cirrus emission that baselines could be calculated and the 100μm data could be processed with the MFP. In all cases except RY Dra all scans passing within 10' of the star's position were analysed. For RY Dra, all scans passing within 25' were used.

As an initial test, 100μm data for several unresolved galaxies were processed with the MFP. The MFP found almost all of them to be slightly resolved. This indicated that the 100μm detector response functions did not fit the survey data as well as the 60μm functions did. The cause of this is apt to be the fact that the 100μm data stream was passed through a 1.5 Hz low–pass filter (the filter for the 60μm data rolled off at 3 Hz). At the survey scan rate of 3.85' s^{-1}, this severe filtering significantly broadened the response to a point source beyond the 44" diffraction limit. The response functions were derived from pointed observations taken at 1/2 the survey scan rate, and therefore did not suffer as great a broadening. In order to compensate for this mis–match, the 100μm response functions were stretched in the in–scan direction until the MFP reported that the test galaxies were unresolved. The required stretch factor was 16%. Even after the response functions had been modified in this way, comparison of the CRDD data with simulated data produced with the response functions showed that the 100μm response functions did not fit the

data as well as the 60μm functions did. For this reason only the stars with dramatically extended CSSs or very high signal/noise will be considered to have been resolved in the 100μm data. These stars are listed in Table 3, and the MFP results are shown in Figures 18 through 20.

All the stars found to be resolved in the 100μm band show a larger shell in the 100μm data than in the 60μm data, though in some cases the difference is quite small. Since the model derived by the MFP is convolved with the detector response functions before it is compared with the data, the larger 100μm size is not an artifact of the telescope's poorer resolution at 100μm. It is likely that the size difference arises from a radial temperature gradient in the envelope. A similar systematic difference in the 60 and 100μm sizes was found by Hawkins and Zuckerman (1991), who deconvolved the IRAS data for the strongest infrared planetary nebulae. Three of the objects resolved in both 60 and 100μm appear at least 50% larger in the 100μm data (W Pic, W Hya and RX Boo). It is likely that for these objects the outer extent of the model 60μm shell only reflects the point at which emission falls below the detectors' noise level, rather than the true extent of the shell. Because these three objects represent almost half of the objects for which we have good data in both FIR bands, we suspect that many of the 60μm outer radii for the other stars listed in Table 3 also are smaller than the full extent of the CSSs.

Table 3.
Model Results for Stars Found to be Extended

60μm Results									
Name	R_{outer} (arcmin)	R_{inner} (arcmin)	F_{ps} (Jy)	F_{ext} (Jy)	Name	R_{outer} (arcmin)	R_{inner} (arcmin)	F_{ps} (Jy)	F_{ext} (Jy)
AQ And [B,H]	3.3	0.5	3.8	1.7	SW Vir	11.4	0.5	57.4	12.2
R Scl	6.5	1.1	60.4	6.1	R Hya	5.7	1.8	106.4	21.4
CRL 278	5.1	0.7	45.3	5.5	Z Cen [H,I]	6.7	2.1	33.5	3.1
o Cet [F]	2.2	0.0	287.0	89.1	W Hya	10.5	0.7	216.2	76.5
UX And [H]	3.6	0.7	13.3	1.3	θ Aps [H]	12.3	0.3	59.5	12.2
V Eri [A]	8.0	2.8	25.5	5.4	RX Boo	6.6	0.5	75.9	12.1
U Men [H]	13.6	3.9	27.5	3.6	RW Boo [H]	5.0	1.4	6.2	1.2
R Dor [H]	6.8	0.3	267.3	49.8	X TrA [C]	4.1	1.3	15.4	9.2
ST Cam	3.1	0.5	7.1	2.0	R CrB [H]	9.8	1.5	4.5	3.1
R Lep	4.8	0.4	28.8	2.7	ST Her [H]	5.7	0.9	18.8	2.9
W Ori	6.2	2.1	15.8	5.9	X Her	6.2	0.0	43.9	5.7
R Aur	4.0	0.1	24.7	5.7	S Dra [H]	7.7	2.0	13.6	1.5
R Oct [H]	10.1	5.3	7.8	5.6	V Pav [C,H]	3.8	1.3	11.3	3.7
W Pic	6.4	1.0	5.6	2.6	NGC 6720 [B]	5.4	0.1	55.1	13.7
α Ori [F]	10.5	0.2	302.9	165.2	δ^2 Lyr [H]	16.5	3.9	9.3	11.0
U Ori [C]	6.7	1.3	43.1	8.9	V Tel [H]	5.5	1.7	11.6	1.9
CRL 5185 [G,H]	10.4	0.5	578.1	148.5	V1942 Sgr [A]	3.2	0.2	2.7	3.2
UU Aur [C]	4.3	0.5	18.2	11.8	UX Dra [B]	4.0	0.2	5.0	2.1
IRC−10°139 [H]	16.7	2.8	1.8	22.2	AQ Sgr [B]	3.0	1.2	6.0	3.4
NGC 2346	6.3	1.5	8.4	2.2	R Cyg	4.8	2.0	13.5	3.6
Y Lyn [C]	4.2	1.4	12.2	3.1	S Pav [H]	6.8	0.9	31.6	5.3
KK Car [H]	10.7	3.2	7.4	8.6	V1943 Sgr	5.0	0.9	29.7	7.7
X Cnc	8.9	1.2	7.6	1.2	X Pav	4.9	0.7	54.7	8.9
RS Cnc	5.8	1.0	36.7	4.0	RZ Sgr [C,H]	4.3	1.0	10.4	7.7
R Leo	3.8	0.8	127.0	29.0	RT Cap	8.1	1.0	5.1	3.1
IRC+10°216 [D,F]	6.6	0.0	6048.3	441.9	T Mic [H]	5.6	0.6	34.6	7.7
Y Hya	9.7	1.3	8.3	3.6	T Ind	2.9	0.8	5.1	0.6
CIT 6 [F]	7.0	0.4	300.4	13.8	Y Pav [B]	5.8	0.6	7.2	3.0
U Ant [A]	4.7	0.6	28.6	15.4	S Cep	3.9	0.9	32.2	3.2
U Hya [A]	2.9	1.3	12.5	48.3	RV Cyg [A]	6.0	1.5	12.1	6.0
VY UMa [B]	3.1	0.1	4.4	1.7	EP Aqr	5.9	1.5	55.1	5.8
R Crt	5.9	1.9	59.5	9.2	PQ Cep [C]	7.3	2.1	10.1	2.6
IRC−30°163E	6.8	2.3	33.9	7.1	W Peg [H]	7.3	3.4	14.3	2.6
RU Crt [H]	2.9	0.2	5.1	1.7	SV Peg	4.7	1.5	26.9	1.2
BK Vir	5.6	1.5	21.0	3.1	π^1 Gru	4.9	0.6	89.4	11.3
Y UMa	3.8	1.7	16.4	2.9	V PsA	5.1	1.2	19.8	2.4
Y CVn [B]	5.5	2.8	19.0	10.7	TX Psc	3.1	0.1	11.8	4.5
RY Dra	18.9	1.9	8.8	6.9	RS And [H]	19.3	3.5	10.4	5.1
RT Vir	4.1	1.0	40.7	6.3	R Cas [C]	4.3	1.0	116.5	27.0

coninued next page

Table 3 (Continued)

100μm Results									
Name	R_{outer} (arcmin)	R_{inner} (arcmin)	F_{ps} (Jy)	F_{ext} (Jy)	Name	R_{outer} (arcmin)	R_{inner} (arcmin)	F_{ps} (Jy)	F_{ext} (Jy)
V Eri [A]	8.9	1.0	5.6	7.5	RY Dra	22.1	5.3	4.4	31.1
U Men	18.7	7.3	7.8	13.2	SW Vir	15.0	4.7	15.4	23.5
R Dor	18.0	3.8	84.0	39.5	W Hya	15.0	2.4	72.0	65.1
W Pic	18.4	4.1	3.6	23.8	θ Aps	11.7	4.8	16.8	20.3
CRL 5185	16.7	0.2	414.9	462.1	RX Boo	12.6	4.8	25.1	16.6
KK Car	15.5	2.7	2.5	59.9	R CrB	13.0	1.0	1.2	9.1
IRC+10°216	9.5	0.7	865.8	256.0	δ^2 Lyr	16.9	6.8	2.7	28.1
Y CVn [B]	6.3	1.2	5.9	11.0					

[A]These objects are listed as extended at 60 and 100μm in the SSSC

[B]These objects are listed as extended at 60μm in the SSSC

[C]These objects are listed as extended at 100μm in the SSSC

[D]IRC+10°216 saturated the 60μm detector and produced strong optical cross–talk in the 60μm band. The windows used to fit a baseline before processing were not free of these effects, and the 60μm results given by the MFP are probably spurious. The 100μm data are largely free of these effects.

[E]NGC 6720 is listed as extended at 12 and 25μm in the SSSC

[F]These values were obtained from fits to the small data set provided by the default ADDSCAN search radius of 1.7'. The data obtained using 10' search radius were not used, because they showed signs of optical cross–talk.

[G] CRL 5185 is listed as extended at all 4 *IRAS* bands in the SSSC. It is associated with the HII region S 270. The extended emission is apt to be associated with the surrounding molecular cloud.

[H] These stars are from the Additional Objects list.

[I] Z Cen is a type I supernova which erupted in NGC 5253 during 1895. It is likely that the extended emission seen is due to the galaxy it is embedded in, rather than a circumstellar shell.

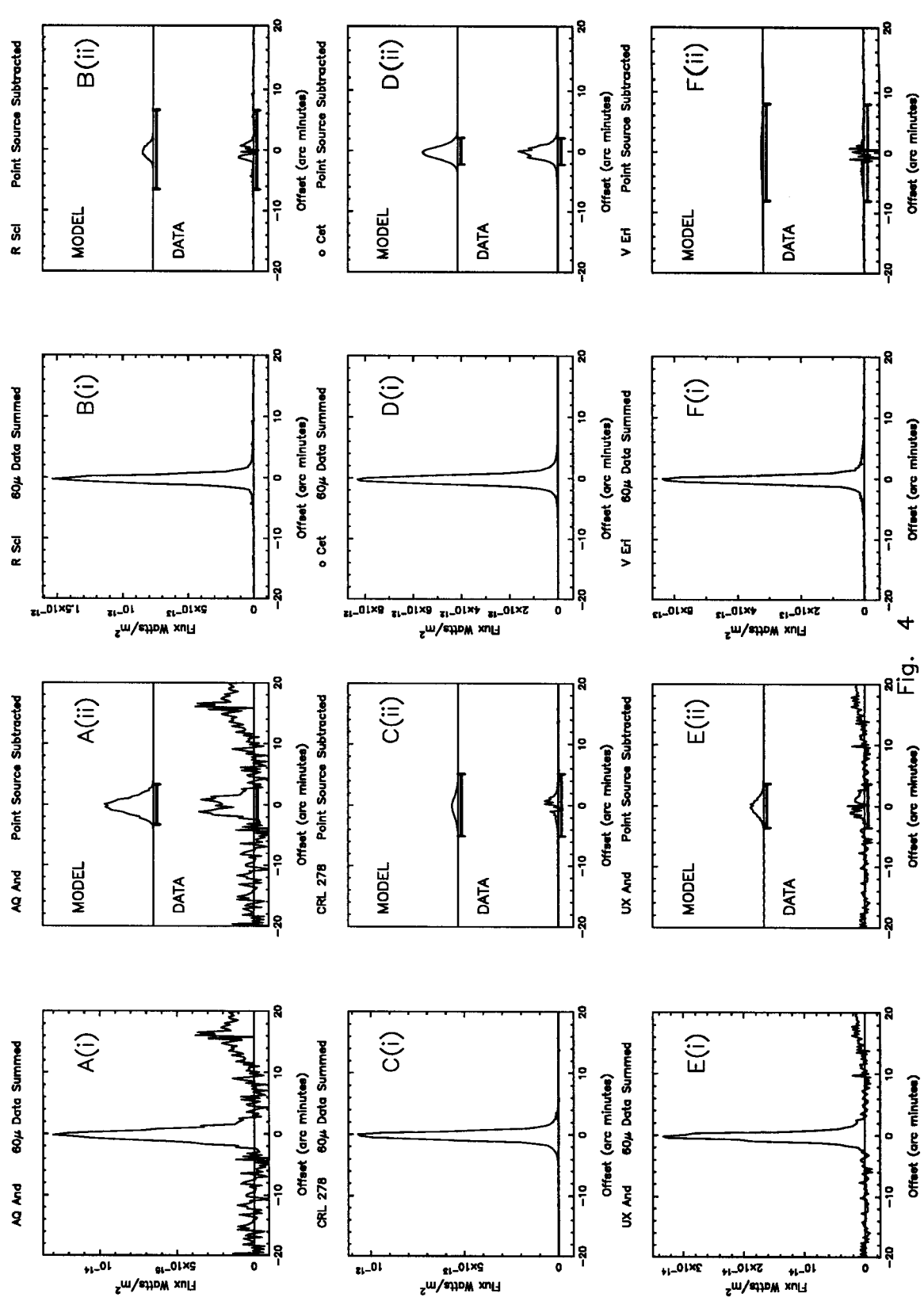
AQ And 60μ Data Summed
A(i)
Flux Watts/m²
Offset (arc minutes)
AQ And Point Source Subtracted
A(ii)
MODEL
DATA
CRL 278 60μ Data Summed
C(i)
CRL 278 Point Source Subtracted
C(ii)
UX And 60μ Data Summed
E(i)
UX And Point Source Subtracted
E(ii)
R Scl 60μ Data Summed
B(i)
R Scl Point Source Subtracted
B(ii)
o Cet 60μ Data Summed
D(i)
o Cet Point Source Subtracted
D(ii)
V Eri 60μ Data Summed
F(i)
V Eri Point Source Subtracted
F(ii)

Fig. 4

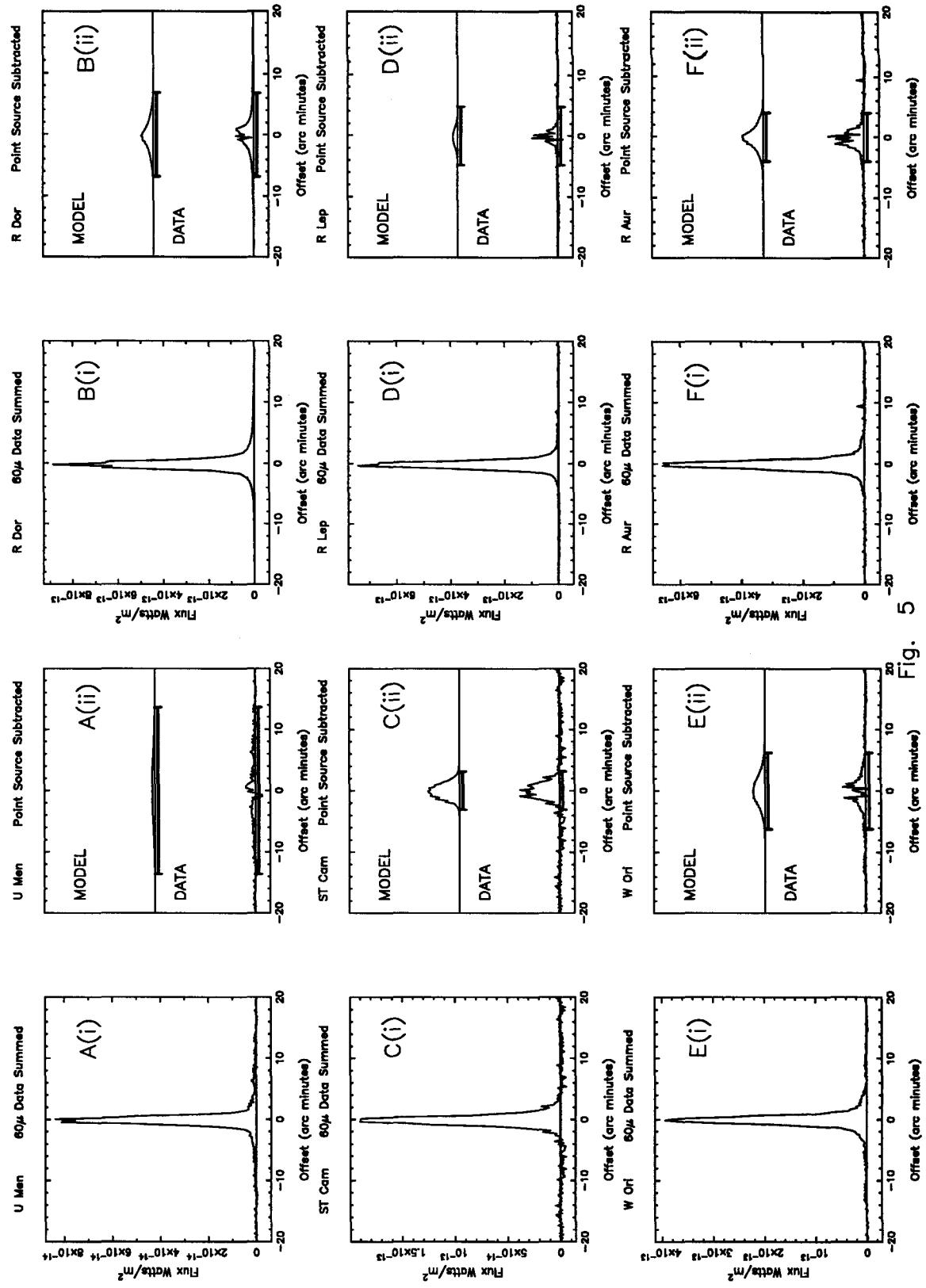
U Men 60μ Data Summed
A(i)
Flux Watts/m²
Offset (arc minutes)
U Men Point Source Subtracted
A(ii)
MODEL
DATA
Offset (arc minutes)
R Dor 60μ Data Summed
B(i)
Flux Watts/m²
Offset (arc minutes)
R Dor Point Source Subtracted
B(ii)
MODEL
DATA
Offset (arc minutes)
ST Cam 60μ Data Summed
C(i)
Flux Watts/m²
Offset (arc minutes)
ST Cam Point Source Subtracted
C(ii)
MODEL
DATA
Offset (arc minutes)
R Lep 60μ Data Summed
D(i)
Flux Watts/m²
Offset (arc minutes)
R Lep Point Source Subtracted
D(ii)
MODEL
DATA
Offset (arc minutes)
W Ori 60μ Data Summed
E(i)
Flux Watts/m²
Offset (arc minutes)
W Ori Point Source Subtracted
E(ii)
MODEL
DATA
Offset (arc minutes)
R Aur 60μ Data Summed
F(i)
Flux Watts/m²
Offset (arc minutes)
R Aur Point Source Subtracted
F(ii)
MODEL
DATA
Offset (arc minutes)

Fig. 5

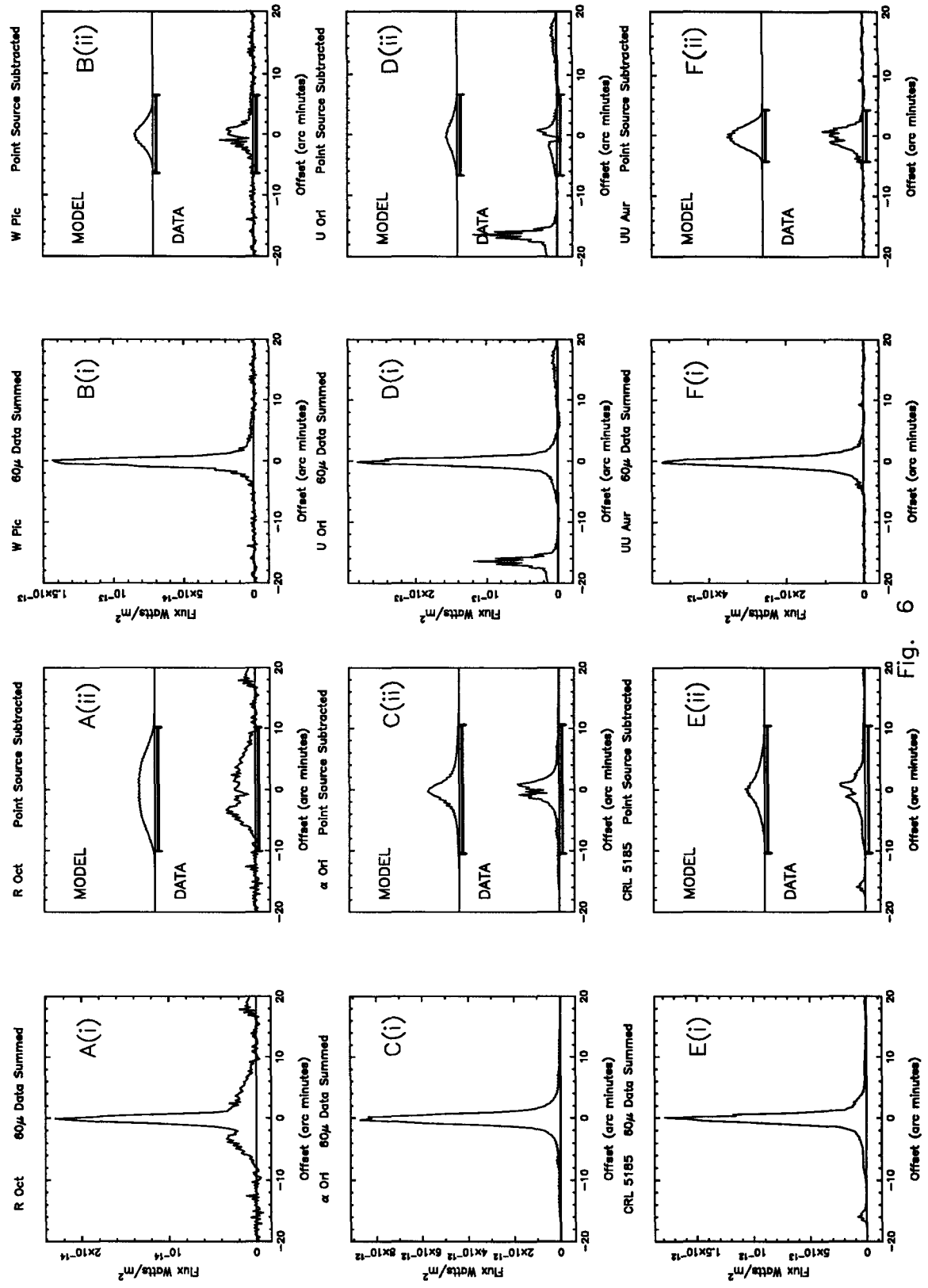
R Oct 60μ Data Summed
A(i)
α Ori 60μ Data Summed
C(i)
CRL 5185 60μ Data Summed
E(i)
R Oct Point Source Subtracted
A(ii)
MODEL
DATA
α Ori Point Source Subtracted
C(ii)
CRL 5185 Point Source Subtracted
E(ii)
W Pic 60μ Data Summed
B(i)
U Ori 60μ Data Summed
D(i)
UU Aur 60μ Data Summed
F(i)
W Pic Point Source Subtracted
B(ii)
U Ori Point Source Subtracted
D(ii)
UU Aur Point Source Subtracted
F(ii)
Flux Watts/m²
Offset (arc minutes)

Fig. 6

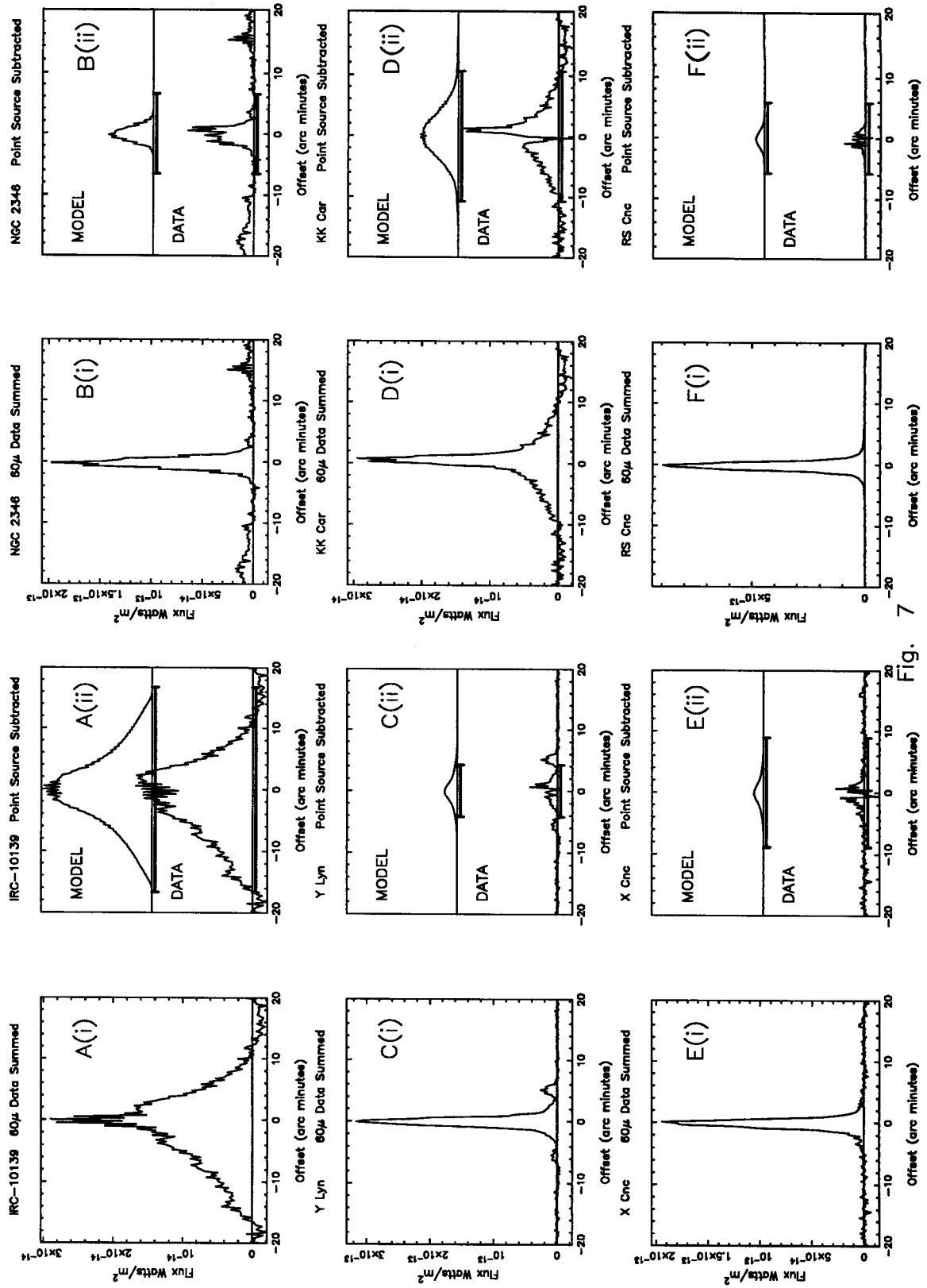
IRC−10139 60μ Data Summed
A(i)
Flux Watts/m²
Offset (arc minutes)
IRC−10139 Point Source Subtracted
A(ii)
MODEL
DATA
Y Lyn 60μ Data Summed
C(i)
Y Lyn Point Source Subtracted
C(ii)
X Cnc 60μ Data Summed
E(i)
X Cnc Point Source Subtracted
E(ii)
NGC 2346 60μ Data Summed
B(i)
KK Car 60μ Data Summed
D(i)
RS Cnc 60μ Data Summed
F(i)
NGC 2346 Point Source Subtracted
B(ii)
KK Car Point Source Subtracted
D(ii)
RS Cnc Point Source Subtracted
F(ii)

Fig. 7

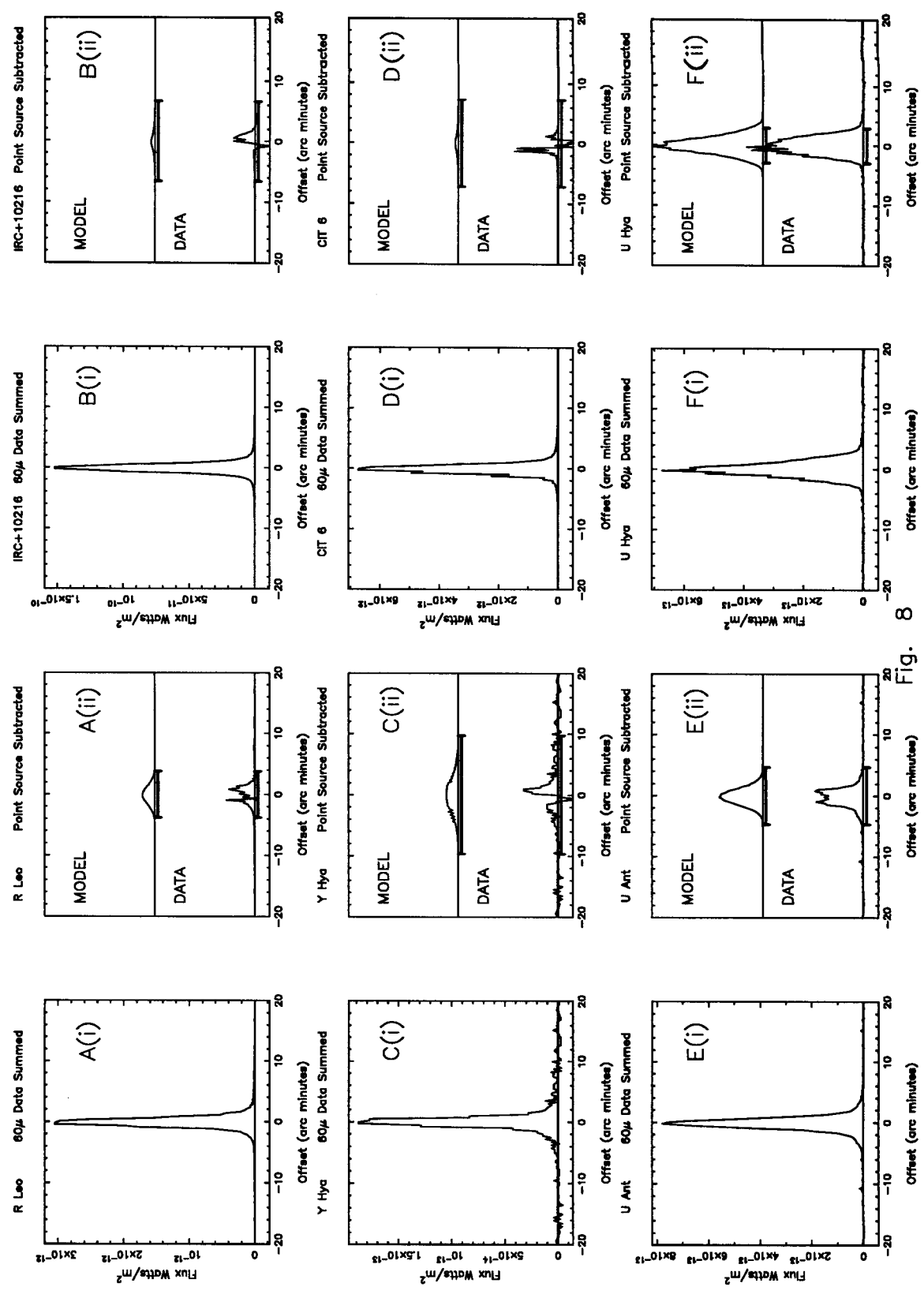
R Leo 60μ Data Summed
A(i)
R Leo Point Source Subtracted
MODEL
A(ii)
DATA
IRC+10216 60μ Data Summed
B(i)
IRC+10216 Point Source Subtracted
MODEL
B(ii)
DATA
Y Hya 60μ Data Summed
C(i)
Y Hya Point Source Subtracted
MODEL
C(ii)
DATA
CIT 6 60μ Data Summed
D(i)
CIT 6 Point Source Subtracted
MODEL
D(ii)
DATA
U Ant 60μ Data Summed
E(i)
U Ant Point Source Subtracted
MODEL
E(ii)
DATA
U Hya 60μ Data Summed
F(i)
U Hya Point Source Subtracted
MODEL
F(ii)
DATA
Flux Watts/m²
Offset (arc minutes)

Fig. 8

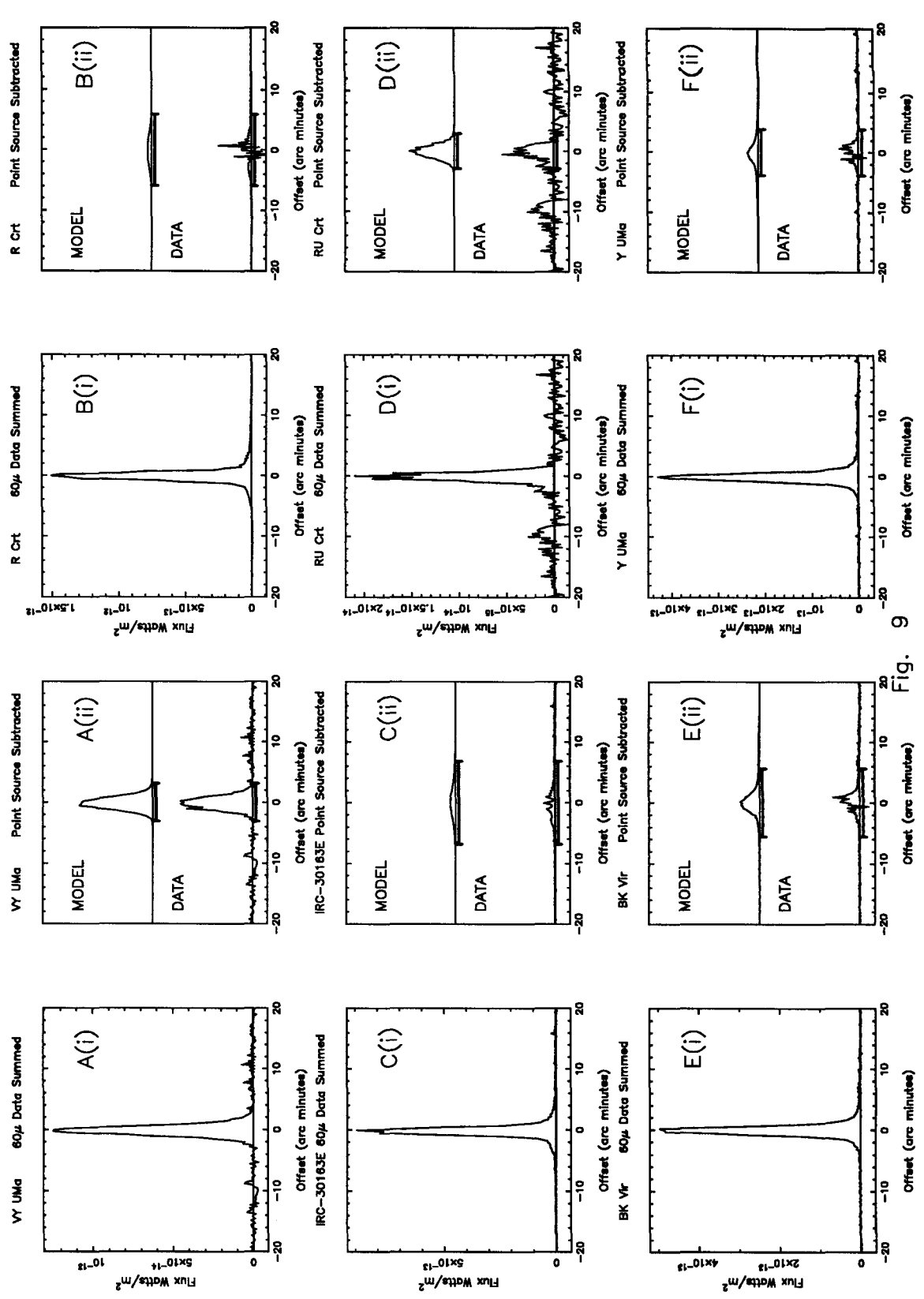
VY UMa 60μ Data Summed
A(i)
Flux Watts/m²
Offset (arc minutes)
VY UMa Point Source Subtracted
A(ii)
MODEL
DATA
IRC-30183E 60μ Data Summed
C(i)
IRC-30183E Point Source Subtracted
C(ii)
BK Vir 60μ Data Summed
E(i)
BK Vir Point Source Subtracted
E(ii)
R Crt 60μ Data Summed
B(i)
R Crt Point Source Subtracted
B(ii)
RU Crt 60μ Data Summed
D(i)
RU Crt Point Source Subtracted
D(ii)
Y UMa 60μ Data Summed
F(i)
Y UMa Point Source Subtracted
F(ii)

Fig. 9

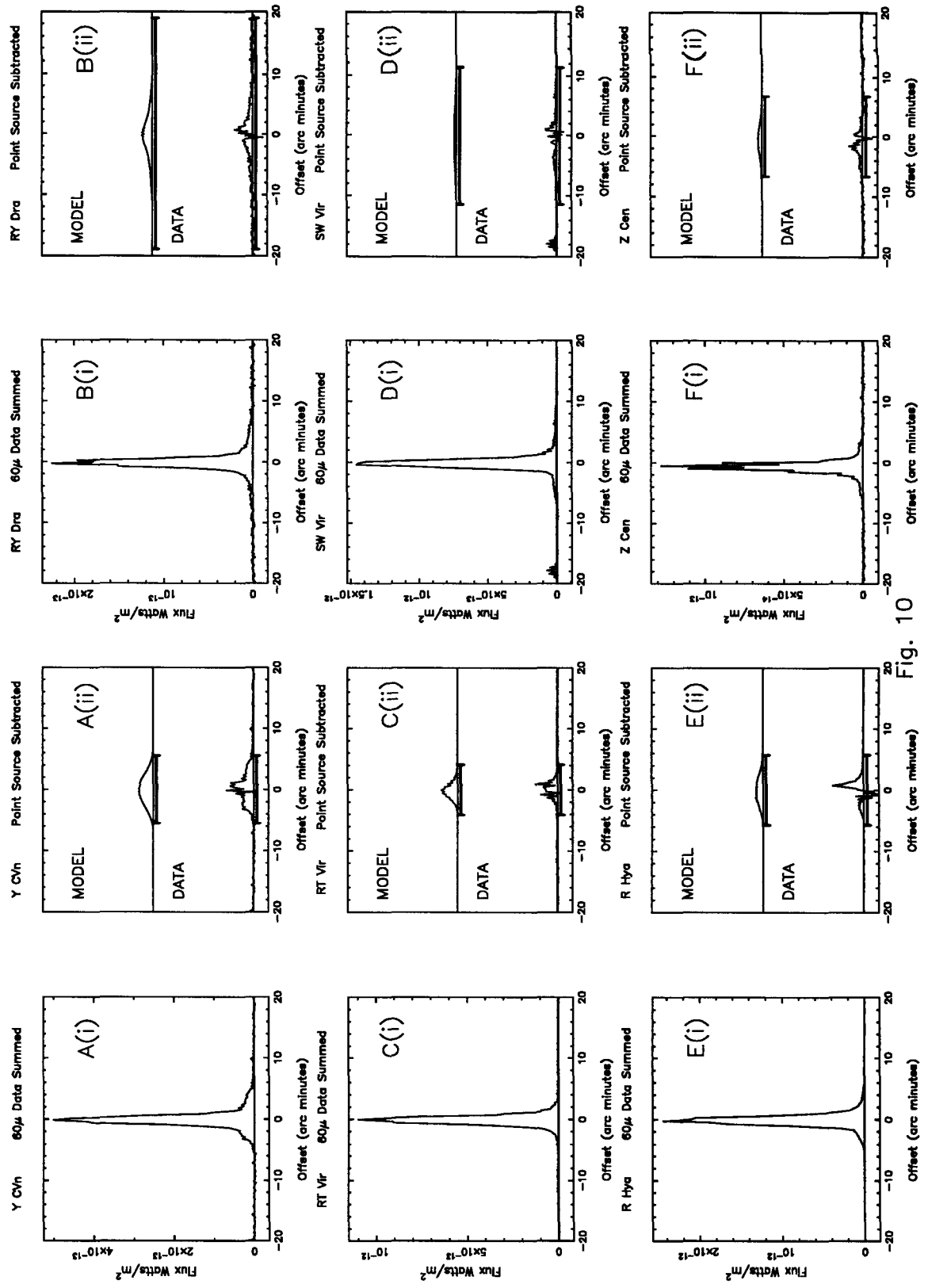
Y CVn 60μ Data Summed
A(i)
Flux Watts/m²
Offset (arc minutes)
Y CVn Point Source Subtracted
A(ii)
MODEL
DATA
RY Dra 60μ Data Summed
B(i)
RY Dra Point Source Subtracted
B(ii)
RT Vir 60μ Data Summed
C(i)
RT Vir Point Source Subtracted
C(ii)
SW Vir 60μ Data Summed
D(i)
SW Vir Point Source Subtracted
D(ii)
R Hya 60μ Data Summed
E(i)
R Hya Point Source Subtracted
E(ii)
Z Cen 60μ Data Summed
F(i)
Z Cen Point Source Subtracted
F(ii)

Fig. 10

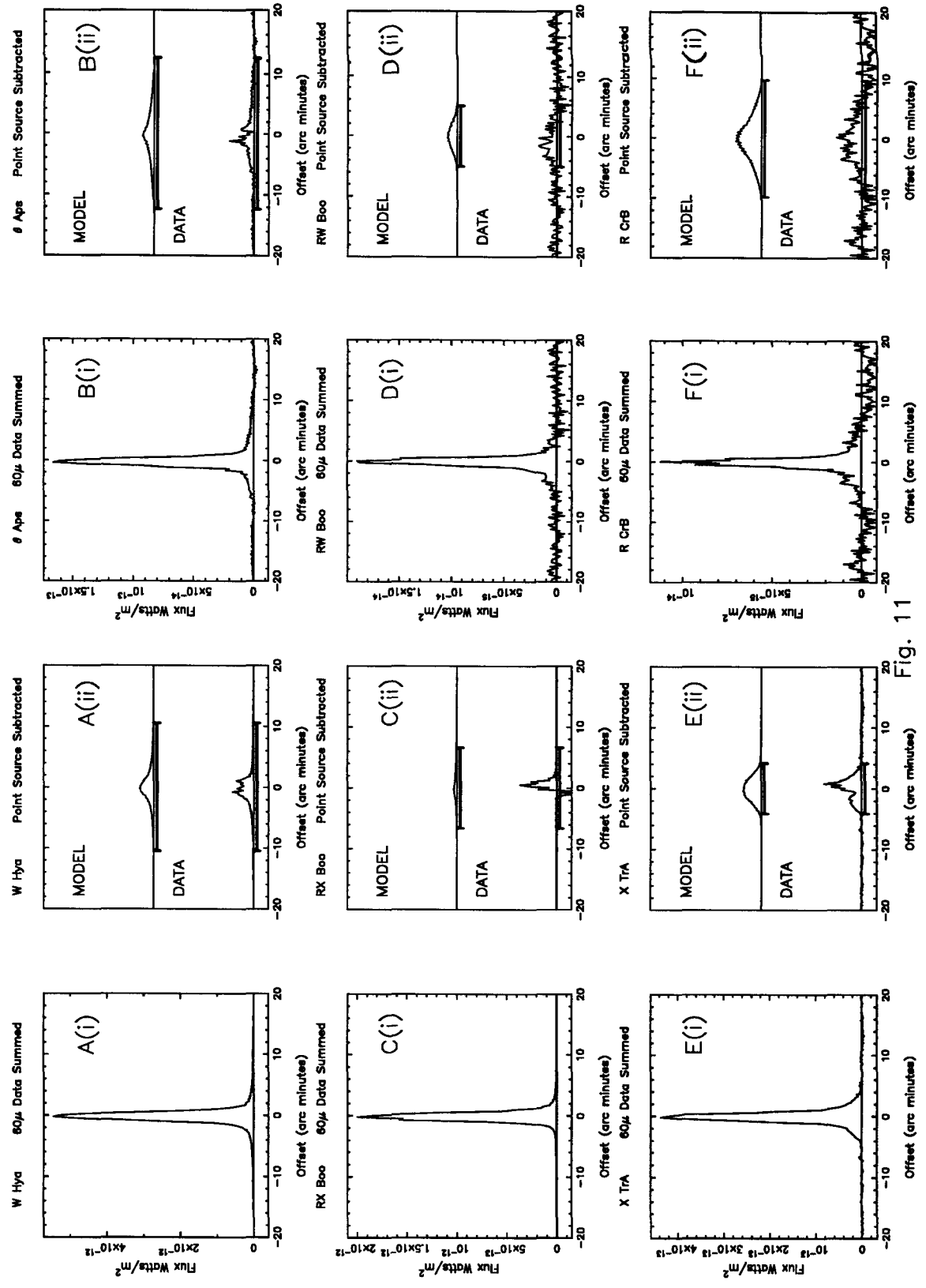
W Hya 60μ Data Summed
A(i)
Flux Watts/m²
Offset (arc minutes)
W Hya Point Source Subtracted
A(ii)
MODEL
DATA
θ Aps 60μ Data Summed
B(i)
θ Aps Point Source Subtracted
B(ii)
RX Boo 60μ Data Summed
C(i)
RX Boo Point Source Subtracted
C(ii)
RW Boo 60μ Data Summed
D(i)
RW Boo Point Source Subtracted
D(ii)
X TrA 60μ Data Summed
E(i)
X TrA Point Source Subtracted
E(ii)
R CrB 60μ Data Summed
F(i)
R CrB Point Source Subtracted
F(ii)

Fig. 11

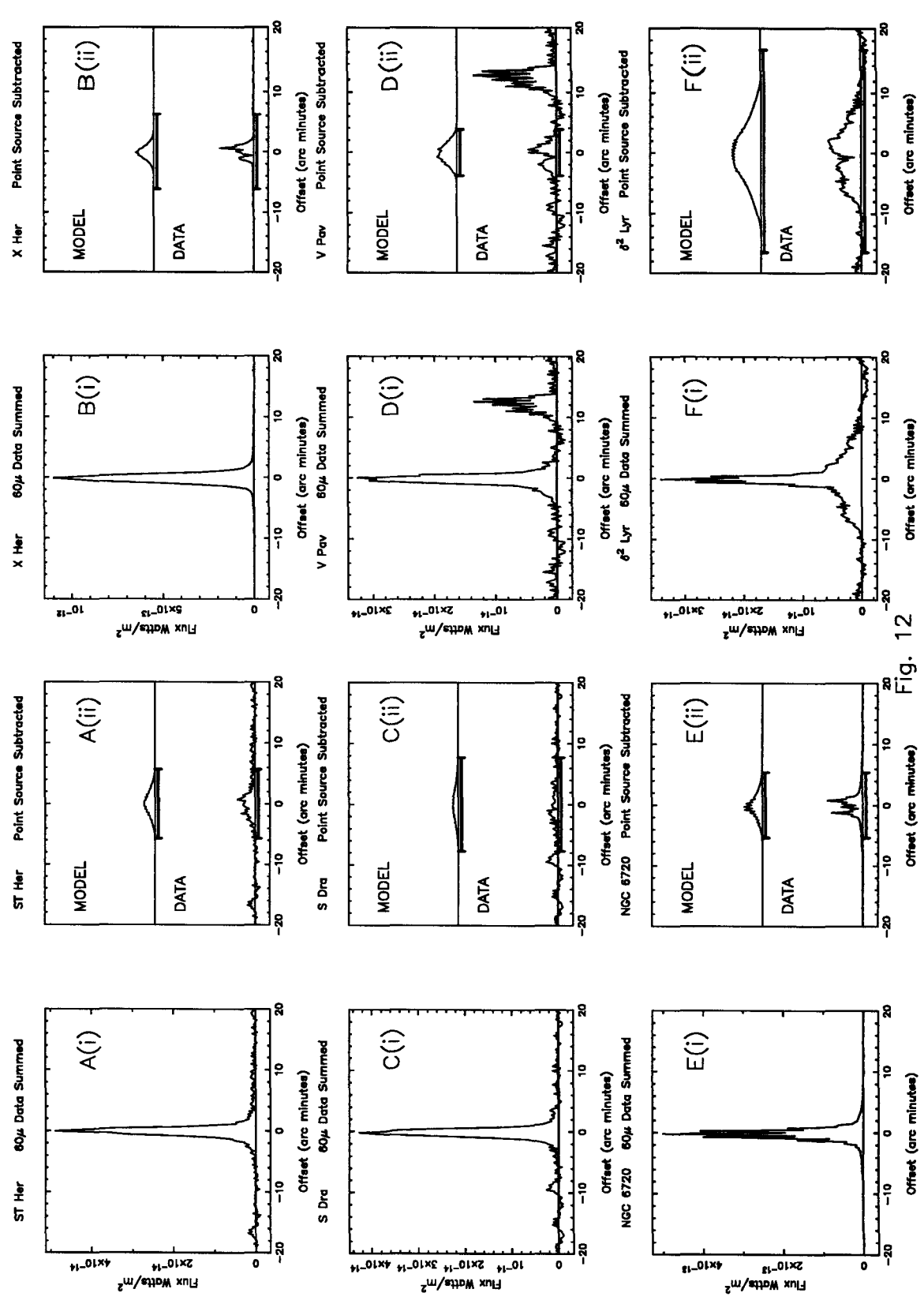
ST Her 60μ Data Summed
A(i)
Flux Watts/m²
Offset (arc minutes)
S Dra 60μ Data Summed
C(i)
Offset (arc minutes)
NGC 6720 60μ Data Summed
E(i)
Offset (arc minutes)
ST Her Point Source Subtracted
MODEL
DATA
A(ii)
Offset (arc minutes)
S Dra Point Source Subtracted
MODEL
DATA
C(ii)
Offset (arc minutes)
NGC 6720 Point Source Subtracted
MODEL
DATA
E(ii)
Offset (arc minutes)
X Her 60μ Data Summed
B(i)
Flux Watts/m²
Offset (arc minutes)
V Pav 60μ Data Summed
D(i)
Offset (arc minutes)
δ² Lyr 60μ Data Summed
F(i)
Offset (arc minutes)
X Her Point Source Subtracted
MODEL
DATA
B(ii)
Offset (arc minutes)
V Pav Point Source Subtracted
MODEL
DATA
D(ii)
Offset (arc minutes)
δ² Lyr Point Source Subtracted
MODEL
DATA
F(ii)
Offset (arc minutes)

Fig. 12

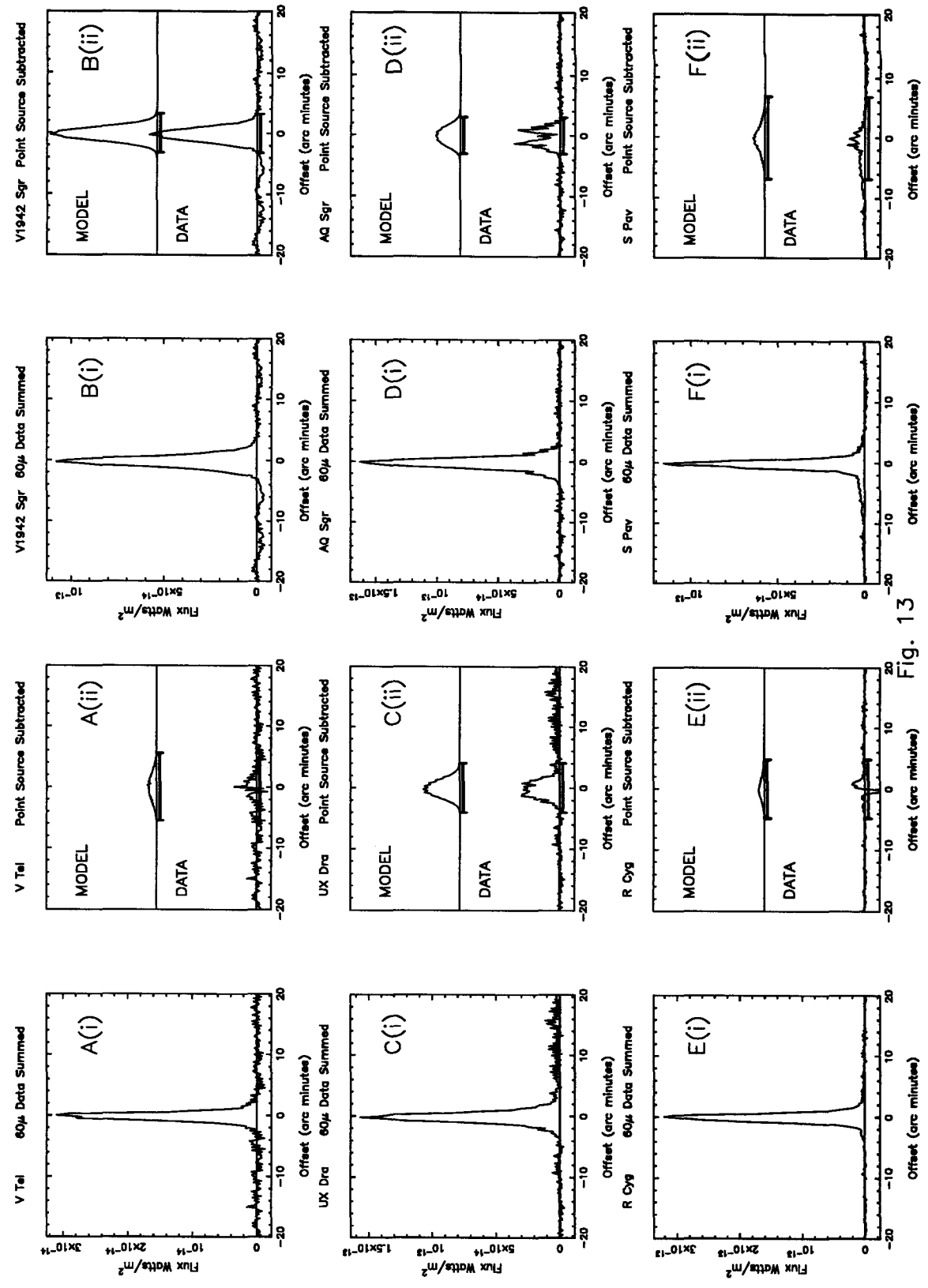
V Tel 60μ Data Summed
A(i)
Flux Watts/m²
Offset (arc minutes)
V Tel Point Source Subtracted
A(ii)
MODEL
DATA
UX Dra 60μ Data Summed
C(i)
UX Dra Point Source Subtracted
C(ii)
R Cyg 60μ Data Summed
E(i)
R Cyg Point Source Subtracted
E(ii)
V1942 Sgr 60μ Data Summed
B(i)
V1942 Sgr Point Source Subtracted
B(ii)
AQ Sgr 60μ Data Summed
D(i)
AQ Sgr Point Source Subtracted
D(ii)
S Pav 60μ Data Summed
F(i)
S Pav Point Source Subtracted
F(ii)

Fig. 13

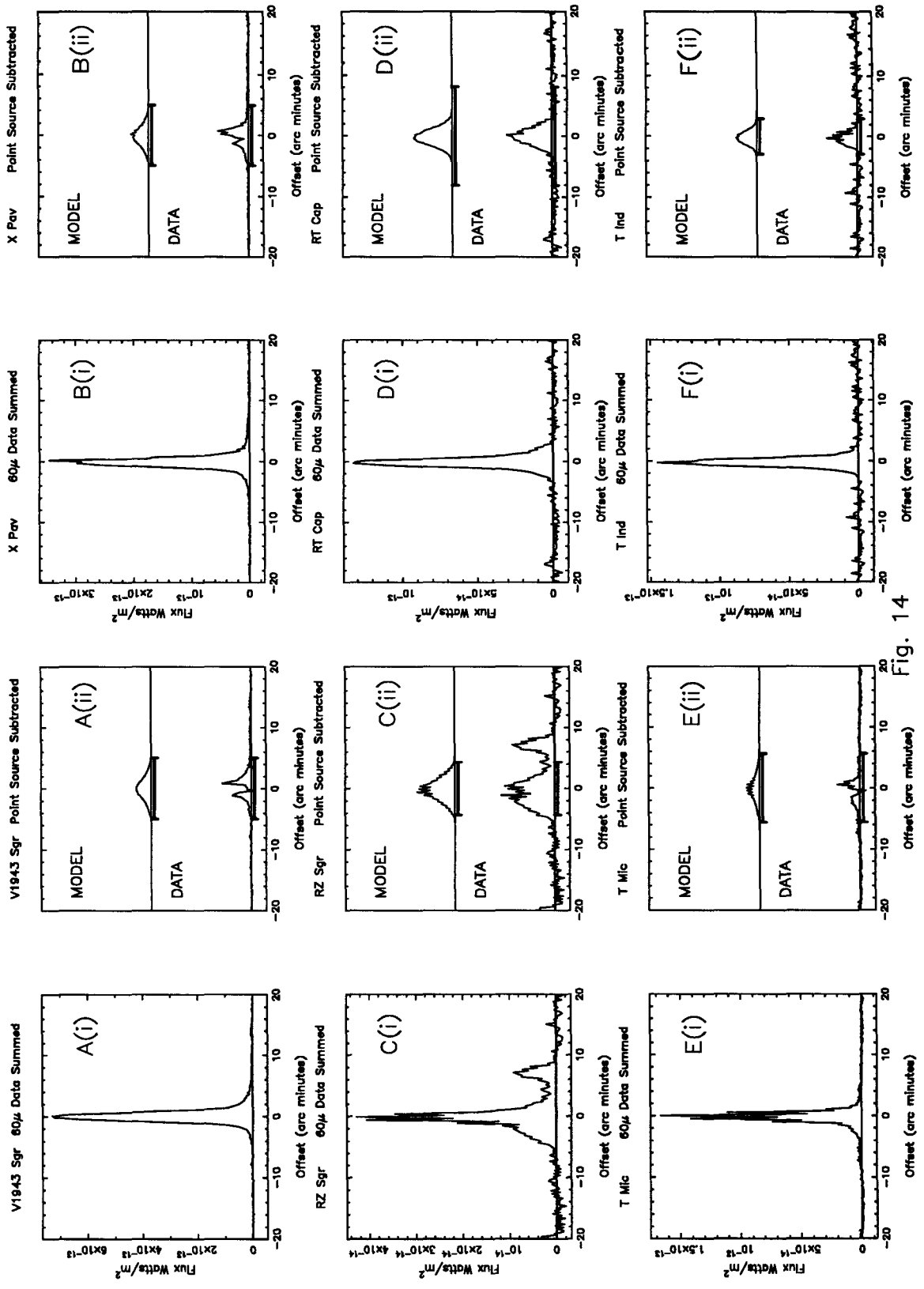
V1943 Sgr 60μ Data Summed
A(i)
Flux Watts/m²
Offset (arc minutes)
V1943 Sgr Point Source Subtracted
A(ii)
MODEL
DATA
X Pav 60μ Data Summed
B(i)
X Pav Point Source Subtracted
B(ii)
RZ Sgr 60μ Data Summed
C(i)
RZ Sgr Point Source Subtracted
C(ii)
RT Cap 60μ Data Summed
D(i)
RT Cap Point Source Subtracted
D(ii)
T Mic 60μ Data Summed
E(i)
T Mic Point Source Subtracted
E(ii)
T Ind 60μ Data Summed
F(i)
T Ind Point Source Subtracted
F(ii)

Fig. 14

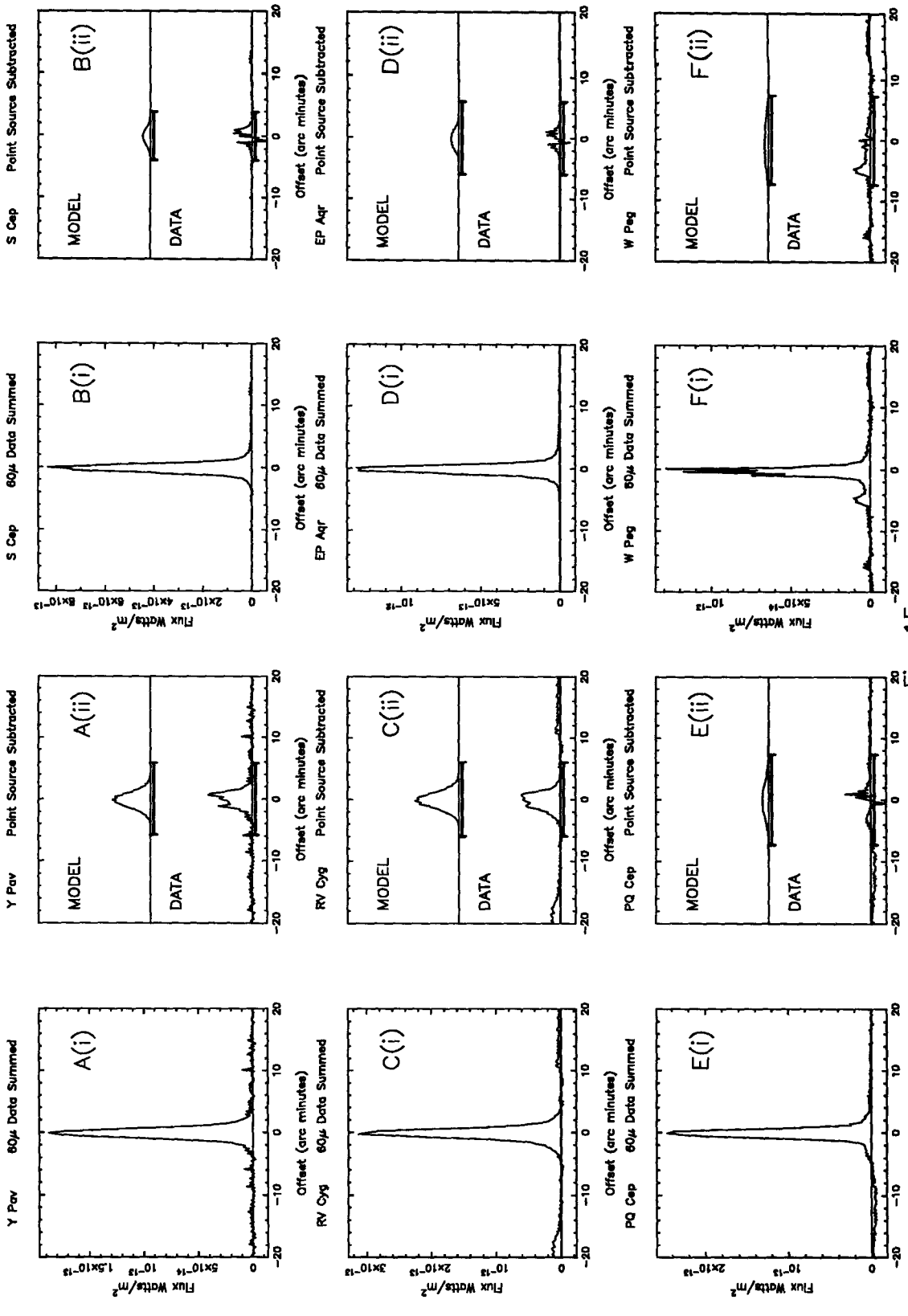
Y Pav 80μ Data Summed
A(i)
Flux Watts/m²
Offset (arc minutes)
Y Pav Point Source Subtracted
MODEL
A(ii)
DATA
RV Cyg 80μ Data Summed
C(i)
RV Cyg Point Source Subtracted
MODEL
C(ii)
DATA
PQ Cep 80μ Data Summed
E(i)
PQ Cep Point Source Subtracted
MODEL
E(ii)
DATA
S Cep 80μ Data Summed
B(i)
S Cep Point Source Subtracted
MODEL
B(ii)
DATA
EP Aqr 80μ Data Summed
D(i)
EP Aqr Point Source Subtracted
MODEL
D(ii)
DATA
W Peg 80μ Data Summed
F(i)
W Peg Point Source Subtracted
MODEL
F(ii)
DATA

Fig. 15

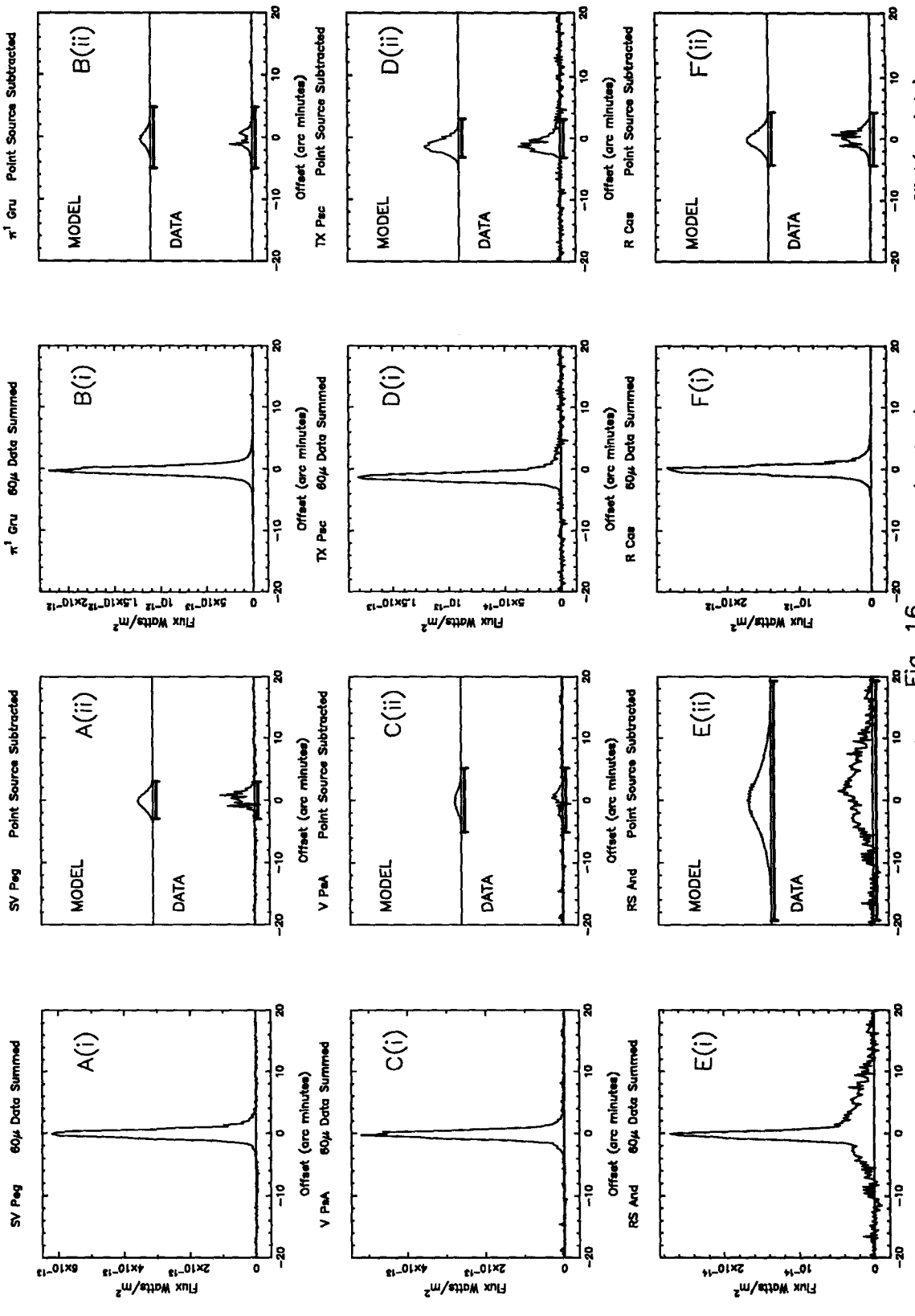
SV Peg 60μ Data Summed
A(i)
Flux Watts/m²
Offset (arc minutes)
SV Peg Point Source Subtracted
MODEL
DATA
A(ii)
V PsA 60μ Data Summed
C(i)
V PsA Point Source Subtracted
C(ii)
RS And 60μ Data Summed
E(i)
RS And Point Source Subtracted
E(ii)
π¹ Gru 60μ Data Summed
B(i)
π¹ Gru Point Source Subtracted
B(ii)
TX Pac 60μ Data Summed
D(i)
TX Pac Point Source Subtracted
D(ii)
R Cas 60μ Data Summed
F(i)
R Cas Point Source Subtracted
F(ii)

Fig. 16

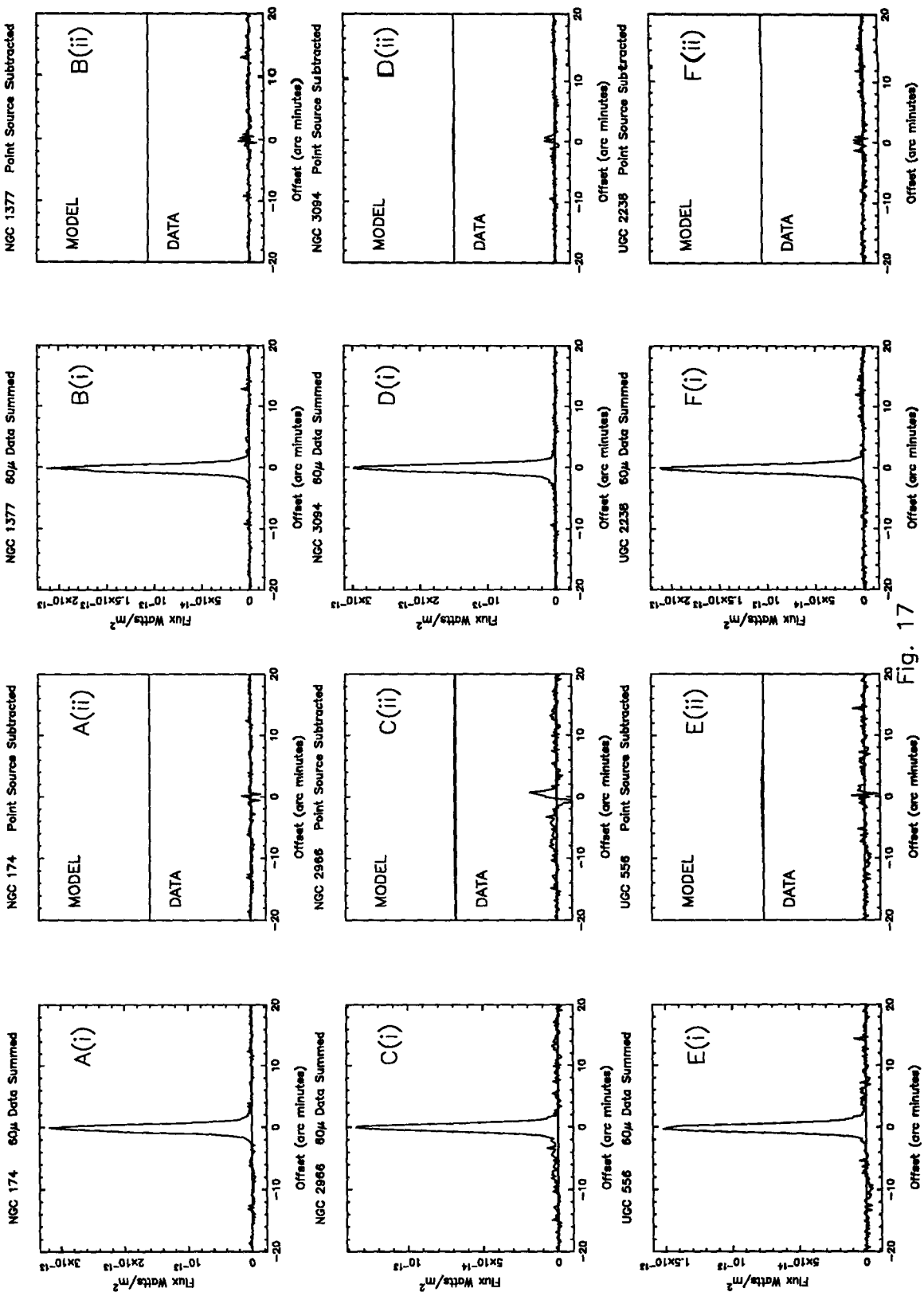
NGC 174 60μ Data Summed
A(i)
Flux Watts/m²
Offset (arc minutes)
NGC 174 Point Source Subtracted
MODEL
A(ii)
DATA
Offset (arc minutes)
NGC 1377 60μ Data Summed
B(i)
Offset (arc minutes)
NGC 1377 Point Source Subtracted
MODEL
B(ii)
DATA
Offset (arc minutes)
NGC 2966 60μ Data Summed
C(i)
Offset (arc minutes)
NGC 2966 Point Source Subtracted
MODEL
C(ii)
DATA
Offset (arc minutes)
NGC 3994 60μ Data Summed
D(i)
Offset (arc minutes)
NGC 3994 Point Source Subtracted
MODEL
D(ii)
DATA
Offset (arc minutes)
UGC 556 60μ Data Summed
E(i)
Offset (arc minutes)
UGC 556 Point Source Subtracted
MODEL
E(ii)
DATA
Offset (arc minutes)
UGC 2238 60μ Data Summed
F(i)
Offset (arc minutes)
UGC 2238 Point Source Subtracted
MODEL
F(ii)
DATA
Offset (arc minutes)

Fig. 17

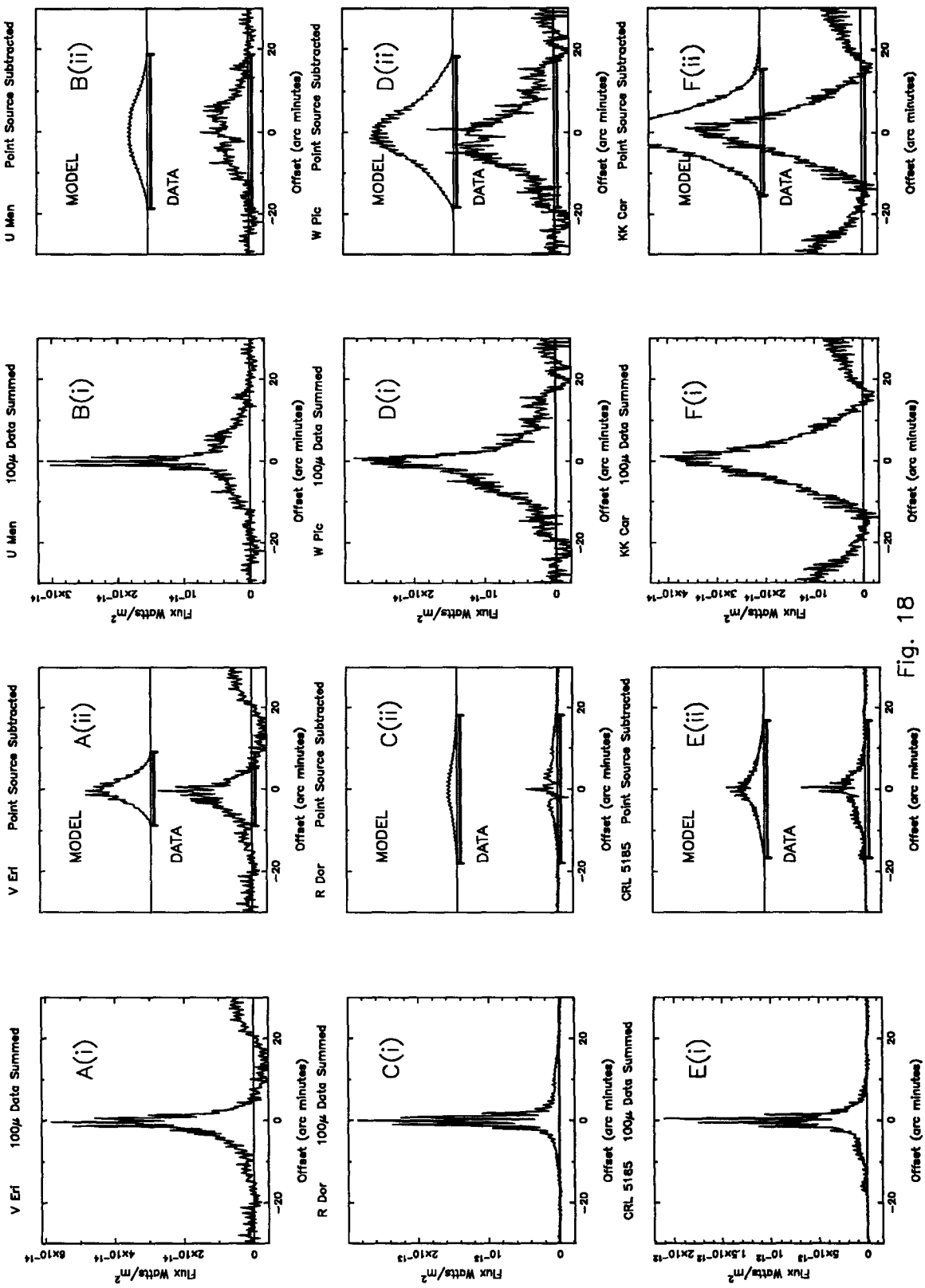
V Eri 100μ Data Summed
A(i)
Flux Watts/m²
Offset (arc minutes)
R Dor 100μ Data Summed
C(i)
CRL 5185 100μ Data Summed
E(i)
V Eri Point Source Subtracted
MODEL
DATA
A(ii)
R Dor Point Source Subtracted
C(ii)
CRL 5185 Point Source Subtracted
U Men 100μ Data Summed
B(i)
W Pic 100μ Data Summed
D(i)
KK Car 100μ Data Summed
F(i)
U Men Point Source Subtracted
B(ii)
W Pic Point Source Subtracted
D(ii)
KK Car Point Source Subtracted
F(ii)

Fig. 18

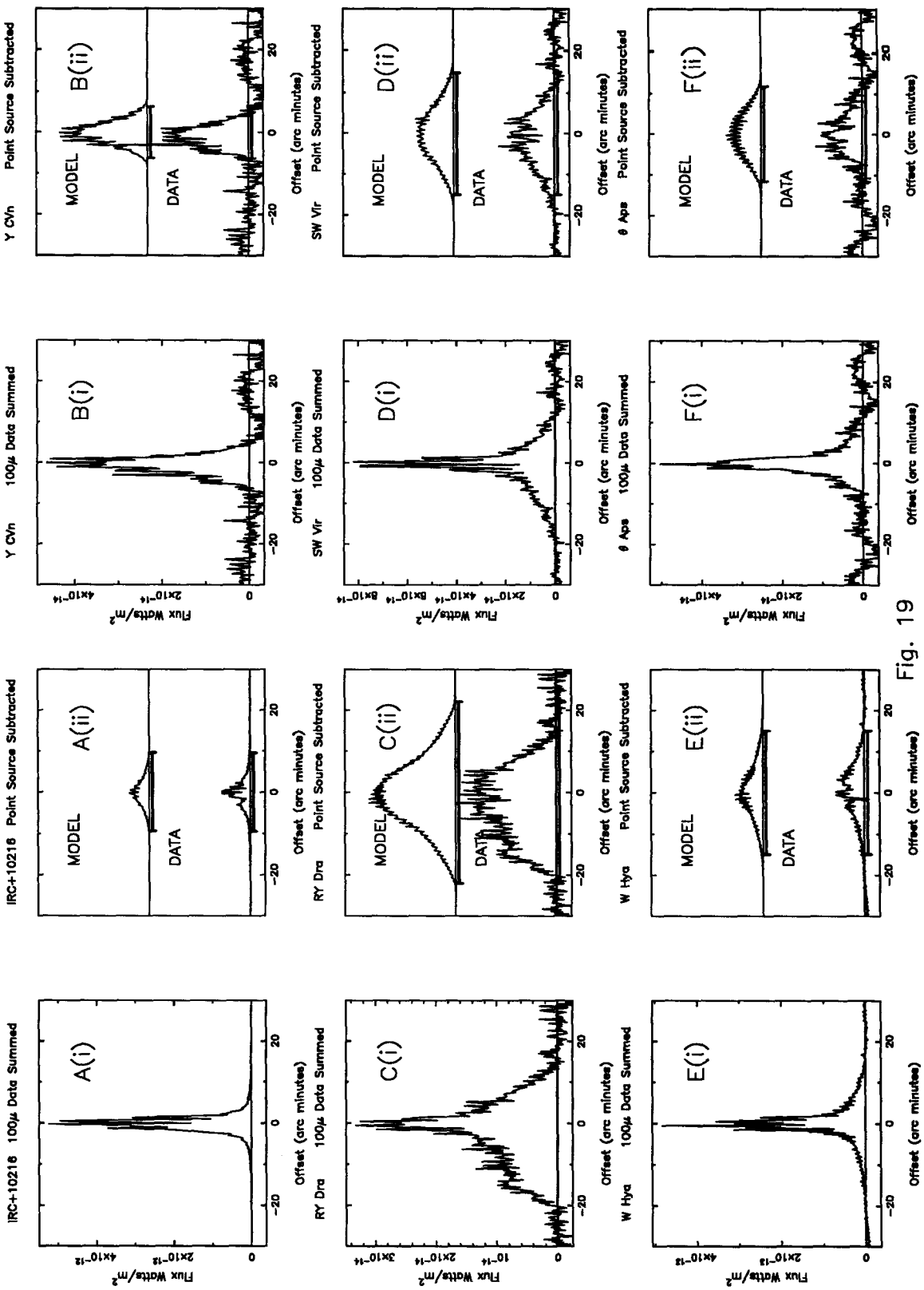
IRC+10216 100μ Data Summed
A(i)
Flux Watts/m²
Offset (arc minutes)
IRC+10216 Point Source Subtracted
A(ii)
MODEL
DATA
RY Dra 100μ Data Summed
C(i)
RY Dra Point Source Subtracted
C(ii)
W Hya 100μ Data Summed
E(i)
W Hya Point Source Subtracted
E(ii)
Y CVn 100μ Data Summed
B(i)
Y CVn Point Source Subtracted
B(ii)
SW Vir 100μ Data Summed
D(i)
SW Vir Point Source Subtracted
D(ii)
θ Aps 100μ Data Summed
F(i)
θ Aps Point Source Subtracted
F(ii)

Fig. 19

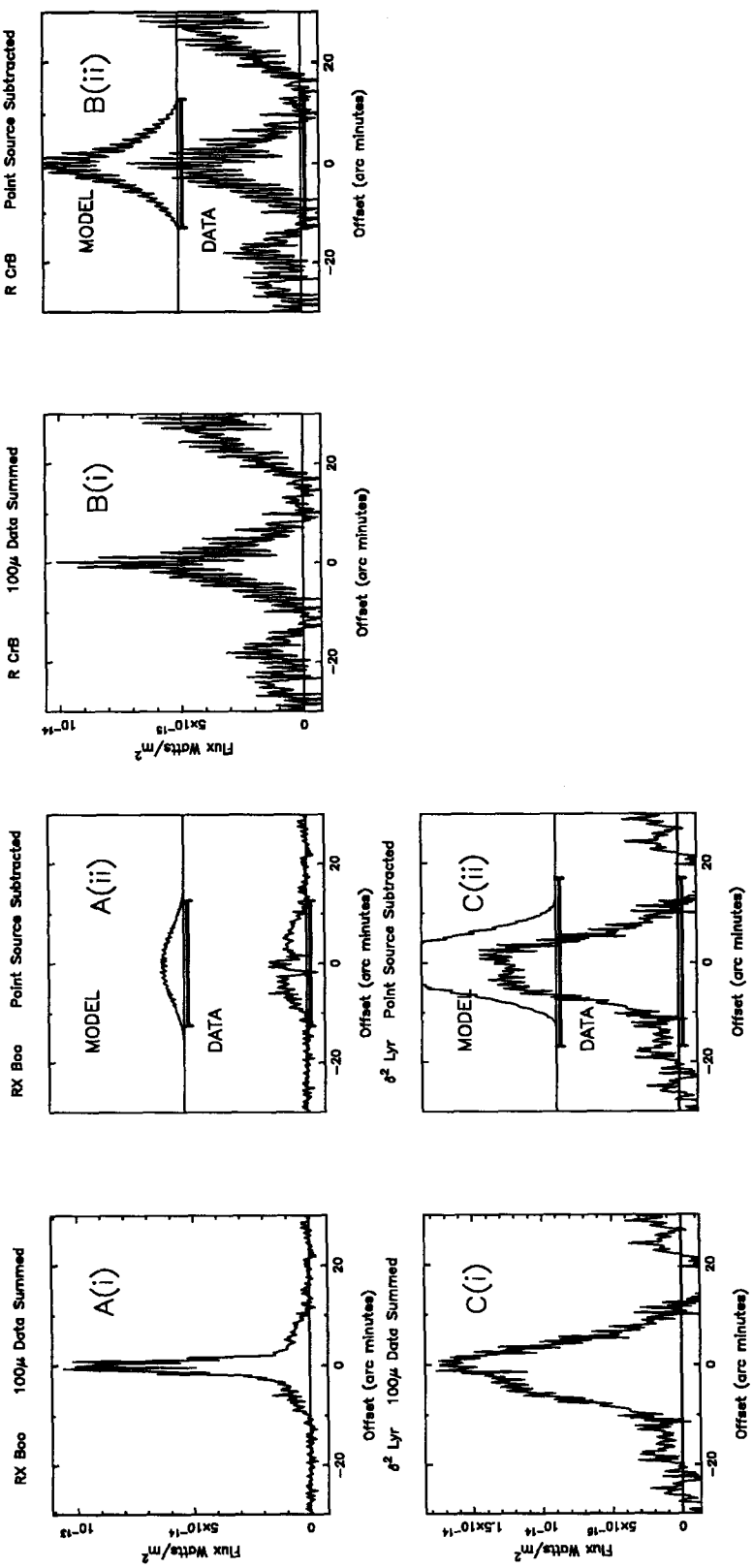
RX Boo 100μ Data Summed
A(i)
Flux Watts/m²
Offset (arc minutes)
RX Boo Point Source Subtracted
MODEL
A(ii)
DATA
Offset (arc minutes)
δ² Lyr 100μ Data Summed
C(i)
Flux Watts/m²
Offset (arc minutes)
δ² Lyr Point Source Subtracted
MODEL
C(ii)
DATA
Offset (arc minutes)
R CrB 100μ Data Summed
B(i)
Flux Watts/m²
Offset (arc minutes)
R CrB Point Source Subtracted
MODEL
B(ii)
DATA
Offset (arc minutes)

Fig. 20

References

Aumann, H.H., Fowler, J.W., & Melnyk, M. 1990, AJ, 99, 1674

Bauer, W.H., & Stencel, R.E. 1992, Proceedings of Seventh Cambridge Workshop on Cool Stars, Stellar Systems, and the Sun. ASP Conference Series, Vol 26, pp. 478-480, (San Francisco: ASP)

Berruyer, N. & Frisch, H. 1983, A&A, 126, 269

Borkowski, K.J. & Sarazin, C.L. 1990, ApJ, 360, 173

Bowers, P.F. & Hagen, W. 1984, ApJ, 285, 637

Celis, L.S. 1981, A&A, 99, 58

Cesaroni, R., Palgi, F., Felli, M., Catarzi, M., Comoretto, G., Di Francos, Giovanardi, C. & Palla, F. 1988, A&AS 76, 445

Claussen, M.J., Kleinmann, S.G., Joyce, R.R. & Jura, M. 1987, ApJS, 65, 385

Collison, A.J. & Fix, J.D. 1991, ApJ, 368, 545

Deguchi, S., Nakada, Y. & Sahai, R. 1990, A&A, 230, 339

Dougados, C., Rouan, D. & Léna, P. 1992, A&A, 253, 464

Draine, B.T. 1987, unpublished supplement to Draine & Lee (1984)

Draine, B.T. & Lee, H.M. 1984, ApJ, 285, 89

Eaton, J.A. & Johnson, H.R. 1988, ApJ 325, 355

Egan, M. P., & Leung, C. M. 1991, ApJ, 383, 314

Engels, D. & Heske, A. 1989, A&AS 81, 323

Fouqué, P., Le Bertre, T., Epchtein, N., Guglielmo, F., & Kerschbaum, F. 1992, A&AS, 93, 151

Gail, H. P. & Sedlmayr, E. 1985, A&A, 148, 183

Gatewood, G. 1992, PSAP, 104, 23

Gillet, F.C., Backman, D.E., Beichman, C. & Neugebauer, G. 1986, ApJ, 310, 842.

Goldreich, P. & Scoville, N. 1976, ApJ, 205, 144

Hawkins, G.W. 1989, BAAS, 21, 1112

Hawkins, G.W. 1990, A&A, 229, L5

Hawkins, G.W. & Zuckerman, B. 1991, ApJ, 374, 227

Hekkert, P.L., Versteege–Hensel, H.A., Habing, H.J. & Wiertz, M., 1989, A&AS 78, 399

Herman, J. & Habing H.J. 1985, Physics Reports, Vol. 124, No. 4

Heske, A. 1989, A&A, 208, 77

Hildebrand, H. 1983, Q. Jl. R. astr. Soc., 24, 267

Huggins, P.J & Healy, A.P. 1986, MNRAS, 220, P33

Iben, I. & Renzini, A. 1983, ARA&A, 21, 271

IPAC, User's Guide 1989

IRAS, Point Source Catalog 1985, Joint *IRAS* Working Group (Washington: GPO)

IRAS, Small–Scale Structure Catalog 1985, Joint *IRAS* Working Group (Washington: GPO)

Judge, P.G., & Stencel, R.E. 1991, ApJ, 371, 357

Jura, M & Kleinmann, S.G. 1992, ApJS, 79, 105

Kleinmann, S.G. 1989, Evolution of Peculiar Red Giant Stars, IAU Colloquium 106, Cambridge University Press

Knapp, G.R., Phillips, T.G., Leighton, R.B., Lo, K.Y., Wannier, P.G., & Wootten, H.A. 1982, ApJ, 252, 616

Knapp, G.R. & Morris, M. 1985, ApJ, 292, 640

Knapp, G.R. 1986, ApJ, 311, 731

Knapp, G.R. & Bowers, P.F. 1988, ApJ, 332, 299

Knapp, G.R., Sutin, B.M., Phillips, T.G., Ellison, B.N., Keene, J.B, Leighton, R.B., Masson, C.R., Steiger, W., Veidt, B. & Young, K. 1989, ApJ, 336, 822

Kwok, S. 1975, ApJ, 198, 583

Leene, A. & Pottasch, S.R. 1988, A&A, 202, 203

Letzelter, E., Eidelsberg, M., Rostas, F., Breton, J, & Thiebelmont, B. 1987, *Chem. Phys.* 114, 273

Low F.J. *et al.* 1984, ApJ, 278, L19

Mamon, G.A., Glassgold, A.E. & Huggins, P.J. 1988, ApJ, 328, 797

Margulis, M., Van Blerkom, D.J., Snell, R.L., Kleinmann, S.G. 1990, ApJ, 361, 673

Mihalas, D. & Binney, J. 1981, Galactic Astronomy, W. H. Freeman

Morris, M. 1980, ApJ, 236, 823

Moshir, M., *et al* 1989, Explanatory Supplement to the IRAS Faint Source Survey, preprint

Nyman, L.Å., Booth, R.S., Calström, U., Habing, H.J., Heske, A., Sahai, R., Stark, R., van der Veen, W.E.C.J. & Winnberg, A. 1992, A&AS, 93, 121

Olnon, F.M., Raimond, E., & IRAS Science Team 1986, A&AS, 65, 607

Olofsson, H. 1988, Space Science Reviews, 47, 145

Olofsson, H. 1989, Evolution of Peculiar Red Giant Stars, IAU Colloquium 106, Cambridge University Press

Olofsson, H., Eriksson, K. & Gustafsson, B. 1987, A&A, 183, L13

Olofsson, H., Eriksson, K. & Gustafsson, B. 1988, A&A, 196, L1

Onaka, T., de Jong, T. & Willems, F.J. 1989, A&A, 218, 169

Press, W.H., Flannery, B.P., Teukolsky, S.A. & Vetterling, W.A. 1986, Numerical Recipes, Cambridge University Press

Reid, N., Tinney, C. & Mould, J. 1990, ApJ, 348, 98

Rowan-Robinson, M., Lock, T.D., Walker, D.W. & Harris, S. 1986, MNRAS, 222, 273

Sivagnanam, P., Le Squeren, A.M. & Foy, F. 1988, A&A, 206, 285

Soifer, B.T. 1989, *private communication*

Spitzer, L. 1978, Physical Processes in the Interstellar Medium, (New York: Wiley)

Stein, J. W. 1991, ApJ 377, 669

Stencel, R. E., Pesce, J. E., & Bauer, W. H. 1988, AJ, 95, 141

Stencel, R. E., Pesce, J. E., & Bauer, W. H. 1989, AJ, 97, 1120

van den Bergh, S. 1984, Astrophys. Space Sci., 102, 295

van der Veen, W. E. C. J., & Habing, H. J. 1988, A&A, 194, 125

van der Veen, W. E. C. J. & Rugers, M. 1989, A&A, 226, 183

Wannier, P. G. & Sahai, R. 1986, ApJ, 311, 335

Wannier, P. G., Sahai, R., Andersson, B–G & Johnson, H. R., 1990, ApJ, 358, 251

Whitelock, P. A., Pottasch, S. R., & Feast, M. W. 1987, Late Stages of Stellar Evolution, (Dordrecht: Reidel)

Wickramasinghe, N. C. 1972, NMRAS, 159, 269

Willems, F. J., & de Jong, T. 1986, ApJ, 309, L39

Willems, F. J., & de Jong, T. 1988, A&A, 196, 173

Wood, P. R. 1990, From Miras to Planetary Nebulae: Which Path for Stellar Evolution?, (Paris: Éditions Frontières)

Young, H. D. 1962, Statistical Treatment of Experimental Data, (New York: McGraw-Hill)

Young, K. *et al.* 1992 *in preparation*

Zuckerman, B. & Dyck, H.M. 1986a, ApJ, 304, 394

Zuckerman, B. & Dyck, H.M. 1986b, ApJ, 311, 345

Zuckerman, B. & Dyck, H.M. 1989, A&A, 209, 119

Zuckerman, B., Dyck, H.M. & Claussen, M.J. 1986, ApJ, 304, 401

Addendum

The Prevalence of Semiregular Variables

A surprising result of this survey was the high percentage of semiregular variables among the resolved stars. Because all mira variables within 500 pc were included in the candidate list, while members of no other type of star were included merely because of proximity, the small percentage of miras in the resolved group (17%, when heavily enshrouded stars such as IRC+10°216 and CIT 6 are included) may actually be higher than an unbiased survey would have found. While most miras are oxygen–rich, the majority of semiregulars are carbon stars. However the list of resolved objects contains nearly twice as many oxygen–rich semiregulars as carbon–rich. Semiregular variables would be much more common in the resolved list even if only oxygen–rich envelopes were considered. For the shells with resolved inner radii, the average inner radius for semiregulars (0.20 pc, excluding the SRc supergiants) is not significantly different from the average for miras with resolved inner radii (0.28 pc). This casts doubt on the model of Willems and de Jong (1988), which proposes that detached shells are created when stars which have been pulsating regularly switch to an erratic pulsation mode.

The Shell Evolution Model

The anonymous referee of the ApJ paper which forms chapter 2 of this thesis offered the following criticism of the shell expansion model (see equations 1 through 5b). While the gas will definitely be slowed by the ram pressure of the ISM, it is not clear that the dust would be. The drift velocity ensures that the dust will outrun the gas, and contact the ISM first. Assuming spherical dust grains 10^{-5} cm in radius, the mean free path of a dust grain once the ISM is reached will be $3 \times 10^{9}\ n^{-1}$ cm, where n is the ambient density of the ISM. If n = 0.1 cm^{-3}, such a dust grain would encounter only 2% of its mass while traveling 1 pc. Thus the dust would not be immediately slowed by the ISM. In response to the referee's comment, it was pointed out that while the dust will outrun the gas in which it condensed, it will encounter any gas that had

previously been ejected from the star. This gas will have been slowed by the ISM. If 0.1 $M_{\odot}$ of material has been lost, and if the shell has expanded to a radius of 0.3 pc, then a spherical dust particle 10^{-5} cm in radius will collide with 1.7×10^{9} particles (assuming the gas is in the form of H_2) as it passes through the previously ejected circumstellar gas. The mass of this swept–up gas would be 3/4 as large as the mass of the dust grain (assuming the grain has the density of quartz), so the grain would be appreciably slowed. If the grain is nonspherical, as is very likely, then its surface area per unit mass will be higher, and it will be slowed even more effectively. Therefore while the dust lost very early in the mass loss era will move into the ISM quite freely, dust ejected at later epochs will be slowed by the circumstellar gas which has already been slowed by the ISM. Mass loss on the 1st Red Giant Branch is non-negligible, and it is likely that $\gtrsim 0.1$ $M_{\odot}$ is lost even before the star reaches the AGB (Groenewegen and de Jong, 1993).

It could be argued that the shell expansion model should not have been used, because no evidence has been presented showing that the ISM has actually affected these circumstellar shells in any way. Indeed, Hawkins (1989) argued that dust envelope surrounding W Hya has expanded virtually unimpeded into the rarified gas ($n < 0.1 cm^{-3}$) of the local "bubble" in the ISM. However the the local bubble only extends $\sim$ 100 pc from the sun (Cox and Reynolds, 1987); most of the stars found to be extended in this survey are not within the bubble. On scales larger than 100 pc, the filling factor of such low density hot gas may is very uncertain, but may be $\sim$ 10% (Slavin and Cox, 1992). Thus most of the stars examined should reside in regions with densities ≥ 0.1 cm^{-3}.

Consider for the moment only those objects on the CO–selected list. A positive correlation exists between the size of the CSS (S) and the star's distance from the galactic plane. The coefficient of linear correlation (r) between S and |z| is 0.42, giving a confidence level in excess of 99.8% that the two quantities are not independent. This correlation could be evidence that the ISM does retard the expansion of the CSS, and the greater average ISM density near the plane retards the shell growth more effectively than does the more rarified ISM at large |z|. Unfortunately, a completely spurious correlation of this kind could arise from two causes. First, there are selection effects. All stars had to have outer radii of 2' or more in order to be considered resolved. This introduces a distance dependent lower–limit to the sizes of the shells, which will

produce a spurious S, |z| correlation. At the distance of NGC 6720, the most distant object in our list of resolved objects which has been detected in CO, a CSS would have to have a radius of at least 0.45 pc to appear resolved. Another selection effect arises from our list of candidate objects, which contained only those stars which have been detected in thermal CO emission lines. Many small shells with low mass loss rates may have been missed at large distances, which tend have large values of |z| as well.

The second potential source for a spurious correlation arises from errors in the estimated distances to these objects. If we over–estimate the distance to an object, we will also over–estimate its size and distance from the galactic plane. If the distances are systematically in error by a constant multiplicative factor, then the errors won't produce a correlation, but if the fractional error in the estimated distance is itself a function of distance, or if there is a random component to the estimate's error, then a spurious correlation may be seen. In order to investigate the sensitivity of the S, |z| correlation to distance errors, a program was written to simulate the data. Stars were placed at random positions in a disk, with an exponential scale height of 300 pc. Each star was surrounded by a CSS with an age between 0 and 5×10^5 yr, and an expansion velocity between 0 and 30 km s^{-1} having no correlation with |z|. Shells too small to be resolved by *IRAS* were rejected, thereby simulating the first of the two selection effects mentioned above. The program calculated the effect on S and |z| of using erroneous distance values. The errors were assumed to follow a gaussian distribution. When the program was run using the correct distances, a small correlation was seen ($r = 0.12$) which arose from the angular size selection effect. Introducing significant distance errors did produce a stronger correlation, and the 99.8% confidence level was reached when the variance of the error distribution was 95%. In other words, if the distance we are using for an object is typically incorrect by a factor of ~ 2 (excluding any constant systematic error), these errors will produce the S – |z| correlation we see. Because our list of objects contains several types of objects, whose distances were estimated in a variety of ways, it is difficult to say whether the values for the distance we have used are this uncertain or not. If we examine only the Mira variables, the class for which we probably have the best distance estimates, an S, |z| correlation still appears.

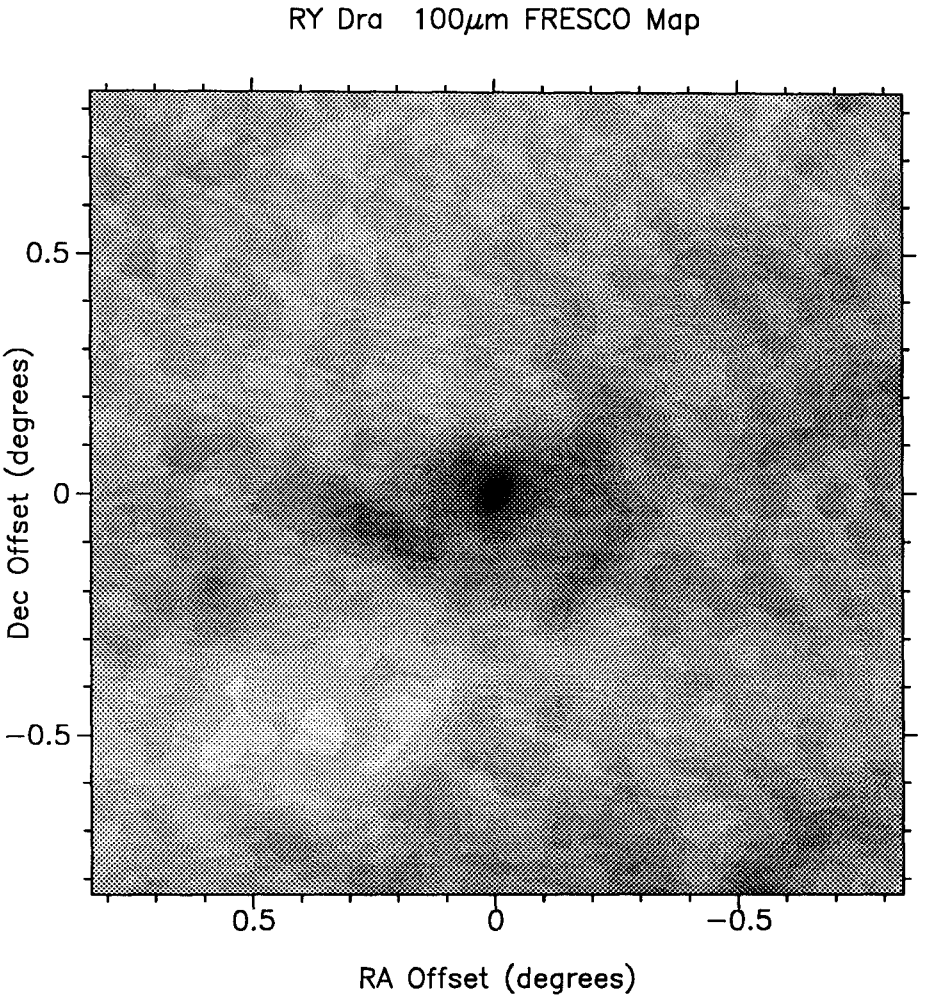

Fig. 1. A 100μm map of RY Dra is shown. The IPAC FRESCO program was used to produce this image. FRESCO makes no attempt to deconvolve the image. Thus the elliptical shape of the central peak is an artifact of the detector's rectangular shape. RY Dra has the 3rd largest shell found in the survey. The shape of the shell suggests the star is traveling toward the south–west, and a bow–shock has formed at the leading edge.

The confidence level drops to 96%, and because our list of resolved CO–detected objects contains only 9 Miras, this confidence level can be raised or lowered dramatically by removing a single object from the list. To reproduce this degree of correlation, our model requires a typical error of 40% in the estimated distance. Finally, the distribution of S as a function of x and y (the objects' coordinates projected onto the galactic plane) was examined. For the Miras, S shows a much weaker correlation with |x| and |y| than with |z|. If the S, |z| correlation is merely a reflection of errors in the estimated distance, then a roughly equal degree of correlation should be seen in the x and y directions. The larger set of all 54 resolved CO–list objects shows only a very weak

correlation of S with |x|, but its correlation with |y| is comparable to that with |z|. In summary, it appears likely that the S, |z| correlation we see is real, but that errors in the adopted values for the distances significantly increase the degree to which these quantities appear related.

A final morsel of evidence that the ISM does affect the growth of the CSS is shown in figure 1. The shell of RY Dra, the third largest found in the survey, appears to have been distorted by the motion of the star through the ISM. Note also the limb–brightening, which suggests that material does collect along the outer edge of the shell, as our shell evolution model predicts. Because the peculiar velocities of these stars are often larger than the outflow velocity of the ejected material, a model containing a bow–shock would probably be more realistic than the ellipsoidal model that we fitted to the *IRAS* data.

Additional tests

A few additional tests were performed which were not included in the journal articles (Chapter 2 and its appendix), but which will be mentioned here for the sake of completeness.

Several tests not listed in the appendix were performed in order to verify the proper operation of the MFP. The 60μ data for NGC 6543 were processed. NGC 6543 is the object that was used to produce the detector templates used by the MFP, thus whatever the true structure of NGC 6543, it should appear unresolved to the MFP. As expected, the MFP did not find extended emission surrounding this object. The data for one star, TX Psc, was obtained twice from IPAC, once using the correct coordinates, and once using coordinates with were deliberately chosen to be several arc minutes from the star's true position. The MFP correctly fit offsets to the erroneous position, effectively determining the star's true position. Finally, test data was generated using the detector templates and two model stars, one with and one without a large CSS. Gaussian noise was added to the test scans, which were then processed by the MFP. The parameters of the test objects were correctly determined.

The model used in the MFP assumes that the extended portion of the CSS is isothermal, which is certainly not true. It was originally hoped that once the MFP had identified the stars with resolved circumstellar shells, a more sophisticated computer model could be used to analyze the

data without this assumption, and the temperature profile in the dust shell could be determined. Such a program was written (MFP2), but the results were disappointing for a reason which in retrospect should have been obvious. In MFP2, the isothermal condition was dropped, and the program attempted to fit a power-law temperature profile $T(r) = T_o r^{-\alpha}$. T_o and α were added to the list of model parameters to be adjusted. The initial value was $\alpha = 0.5$. Once the program was modified in this way, there was no need to have a separate unresolved component as the original MFP did, because the extended dust model now produced a very sharp peak as $r \rightarrow 0$. Unfortunately, because the unresolved emission was so strong, the fitting of the dust shell now became totally dominated by the unresolved emission. Worse yet, many different combinations of inner radius, T_o and α could fit the unresolved emission equally well. This prevented MFP2 from converging, and no useful results were obtained from MFP2.

References

Cox, D. P., Reynolds, R. J. 1987, Ann. Rev. Astron. Astrophys., 25, 303

Groenewegen, M. A. T., & de Jong, T. 1993, A&A, 267, 410

Hawkins, G. W. 1989, A&A, L5

Willems, F. J. & de Jong, T. 1988, A&A, 196, 173

Slavin, J. D. & Cox, D. P. 1992, ApJ, 392, 131

A CO(3–2) Survey of Nearby Mira Variables

K. Young

California Institute of Technology, Pasadena, CA 91125

ABSTRACT

A survey of CO(3–2) emission from optically visible oxygen–rich Mira variable stars within 500 pc of the sun was conducted. A molecular envelope was detected surrounding 36 of the 66 stars examined. Some of the detected stars have lower outflow velocities than any previously detected. The average terminal velocity of the ejected material was 7.0 $\mathrm{km\,s^{-1}}$, about half the value found in Miras selected by infrared criteria. None of the stars with spectral types earlier than M 5.5 were detected. The terminal velocity increases as the temperature of the stellar photosphere decreases, as would be expected for a radiation driven wind. Mass loss rates for the detected objects were calculated, and it was found that there is no correlation between the infrared color of a Mira variable, and its mass loss rate. The mass loss rate is correlated with the far infrared luminosity, although a few stars appear to have extensive dust envelopes without any detectable molecular wind. A power–law relationship is found to hold between the mass loss rate and the terminal velocity of the ejected material. This relationship indicates that the dust envelope should be optically thick in the near infrared and visible regions of the spectrum when the outflow velocity is $\gtrsim 18\ \mathrm{km\,s^{-1}}$. At the low end of the range of outflow velocities seen, the dust drift velocity may be high enough to lead to the destruction of the grains via sputtering. Some of the stars which were detected were re–observed in the CO(4–3) transition. A comparison of the outflow velocities obtained from these observations with those obtained by other investigators at lower frequencies shows no evidence for gradual acceleration of the outer molecular envelope, though there is evidence of discrete shells expanding at significantly different velocities in some cases.

Subject headings: stars: mass–loss — stars: evolution — stars: Late–type, stars: variable

1. Introduction

Over the last 25 years the new infrared surveys, particularly the Two–Micron Sky Survey (Neugebauer and Leighton 1969, hereafter TMSS), the Air Force Geophysical Laboratory survey (Price and Walker 1975, hereafter AFGL), and the *IRAS* Point Source Catalog (Neugebauer *et al.* 1984, hereafter PSC), have revealed the presence of tens of thousands of cool stars surrounded by dusty envelopes. After each of these surveys was completed, observers examined the most prominent of the newly detected objects in the radio regime, and were frequently able to detect molecular line emission from molecules such as OH, HCN and CO. From this confluence of infrared and radio data arose a compelling model for mass loss in highly evolved stars. According to this model, dust condenses in the outer envelope of a cool red giant star. This dust is then accelerated by radiation pressure to a velocity of $\sim$ 15 km s^{-1}. The dust in turn accelerates gaseous material by colliding with it (see a review by Olofsson 1988).

This paper presents the results of a survey of Mira variables with distances of 500 pc or less, which were selected without regard to their infrared characteristics. There are several reasons for carrying out such a survey. First, it is possible that the radiation pressure mechanism described above is not the only one driving mass loss from red giant stars. Mechanisms which do not require the formation of dust, such as radial pulsations (Wood 1979), momentum transfer from Alfvén waves (Hartmann and MacGregor 1980) or from sound waves (Fusi–Pecci and Renzini 1975, Pijpers and Hearn 1989) have been proposed for driving AGB winds. Finding a large, expanding molecular envelope surrounding a highly evolved star without a massive dust envelope would be strong evidence for an alternative mass loss mechanism. Secondly, because previous surveys tended to concentrate on the very strongest infrared sources, stars with small, but detectable, mass loss rates may be under–represented in their compilations of detections. The final reason for surveying nearby Miras is that they obey a period – luminosity relationship. This allows their distances to be estimated more accurately than many of the other types of stars which have been detected in the surveys of bright infrared objects. The derived values of many important physical parameters, including the absolute luminosity and the mass loss rate, are sensitive to errors in the estimated distance.

Examining the CO(3–2) line, rather than a lower J transition, offers several advantages. The first is that higher J transitions have higher critical densities for collisional excitation. For this reason the emission from molecular clouds is less extensive, and the spectra of Miras near the Galactic plane are less apt to be contaminated by galactic emission. Secondly, the antenna temperature of the 3–2 line will in general be higher than in the lower J lines (Morris 1980). While the rotational transitions above 3–2 may have even higher brightness temperatures, particularly for optically thin envelopes, the earth's atmosphere is much less transparent where these transitions are found, even on high mountain sites. The 3–2 line may therefore allow the most sensitive ground–based searches for cool circumstellar envelopes. Finally, for those objects which have already been detected in lower J surveys, the availability of spectra covering several CO transitions allows the models of molecular excitation to be better constrained, and variations of the CO envelope at different radii can be studied (van der Veen and Olofsson 1989).

2. Observations

The candidate objects for this survey where selected from the *Revised Catalog of Spectra of Mira Variables of Types Me and Se* (hereafter RCMV) (Keenan *et al.* 1974). The spectral types and periods of the stars were used to calculate an absolute visual magnitude, using the formulae derived by Celis (1980). This calculated absolute magnitude was used with the apparent magnitude, to calculate the star's distance. The star's sky position and distance were then used to calculate the amount of absorption, using Parenago's formula with coefficients from Sharov (1964). Finally the amount of absorption was used to derive a new distance estimate. This process of estimating the distance was iterated until it converged. Distances to a smaller set of stars were calculated in this way by Celis (1981), who estimated the mean error in derived distance values to be 19 %. However distances to many of these stars were later calculated by Jura and Kleinmann (1992) using infrared data, and their distance estimates differ from those of Celis by 50% on average. 79 of the stars in the RCMV were found to have a distance of 500 pc or less. 66 of these stars were observed.

All observations presented here were made at the Caltech Submillimeter Observatory,* (CSO) on Mauna Kea, Hawaii. Data were taken during January, May and August of 1990, and during February through August of 1991. The $^{12}C^{16}O(3–2)$ line at 345.796 GHz was observed with an SIS receiver (Ellison 1987) having a double sideband temperature of about 200 K. A 1024 channel AOS spectrometer was used, which has a total bandwidth of 500 MHz and a velocity resolution of 0.9 $km\,s^{-1}$. In most cases, scans were taken while position switching at 0.05 Hz between the source position and 2 off–source positions located 3 arc minutes away in azimuth. For weak objects at low galactic latitudes, the scans used 4 off-source positions spaced symmetrically about the source, and 30 arc seconds away (1.5 beam widths), in order to remove any contamination from extended galactic emission. For those stars which appear in the SAO catalog, SAO coordinates and proper motions were used. For the remainder of the stars, coordinates were obtained from the *IRAS* PSC. Table 1 lists the names, coordinates and on–source integration times for the stars. For the stars which had not previously been detected in a rotational transition of CO, the radial velocity used for receiver tuning was obtained from the RCMV. If the star showed only weak CO emission ($T_{mb} \leq 200$ mK), it was re–observed on at least one additional night in order to confirm the detection. Two of the stars which were not detected, R Car and R Cen, never rise above 10 degrees from the horizon when observed at the CSO. Since telescope pointing can be problematic at very low elevations, the pointing was checked after these two stars were observed by observing the strong source IRC+10°216 as it passed through an elevation of 10 degrees. Both the CO(3–2) and CS(7–6) transitions were seen, indicating that errors in pointing were not responsible for these non–detections.

In April and May of 1993, sixteen of the stars with strong CO(3–2) emission were examined again with a second SIS receiver (Walker *et al.* 1992), tuned to the CO(4–3) line at 461.041 GHz, where it had a double sideband temperature of $\sim$ 250 K. The system temperature was $\sim$ 2500 K, allowing lines as weak as 0.1 K to be detected in an hour of integration. Because the LSR velocity of each of the stars was known from the CO(3–2) profile, a narrower AOS spectrometer having a total bandwidth of 50 MHz, was used for most of these observations,

---

* The CSO is operated by the California Institute of Technology under funding from the National Science Foundation, Contract #AST–9015755.

Table 1. – Survey Star Positions, Integration Times and Spectrum Noise Levels

Nondetections are listed in parenthesis

Star	R.A. (1950)	Decl. (1950)	Time (min.)	rms (mK)	Star	R.A. (1950)	Decl. (1950)	Time (min.)	rms (mK)
(S Scl)	00 12 51.11	−32 19 22.5	27.2	74	(R CVn) [A,D]	13 46 48.10	39 47 28.0	51.8	26
(T And)	00 19 46.43	26 43 10.3	7.1	149	(R Cen)	14 12 56.90	−59 40 55.2	34.9	144
T Cas	00 20 31.50	55 30 56.0	23.3	86	(U UMi) [A]	14 16 13.40	67 01 29.0	16.8	38
(TU And) [A]	00 29 44.70	25 45 12.0	13.6	81	(S Boo)	14 21 12.40	54 02 12.4	14.2	59
W And	02 14 22.70	44 04 26.0	8.4	62	(R Boo)	14 34 59.27	26 57 09.4	22.0	60
o Cet	02 16 49.04	−03 12 13.4	5.2	173	(Y Lib) [A]	15 09 02.50	−05 49 27.0	11.7	63
T Ari [C]	02 45 32.04	17 18 07.2	108.7	15	S CrB [C]	15 19 21.53	31 32 46.5	9.1	68
R Hor	02 52 13.00	−50 05 32.0	3.9	249	CO(4–3)			63.4	104
U Ari [A,C]	03 08 16.20	14 36 40.0	31.7	38	RS Lib [A,C]	15 21 24.30	−22 44 06.0	24.6	41
S Pic [A]	05 09 37.20	−48 34 00.0	50.5	48	CO(4–3)			25.9	118
R Aur	05 13 15.26	53 31 56.6	8.7	93	(S UMi) [A]	15 31 24.10	78 47 54.0	19.4	84
CO(4–3)			31.1	137	(T Nor)	15 40 11.71	−54 49 44.8	31.7	134
(W Aur) [A,B,C]	05 23 31.20	36 51 40.0	28.5	39	R Ser [C]	15 48 23.24	15 17 02.7	24.6	30
S Ori [B,C]	05 26 32.68	−04 43 51.7	14.2	42	(CO(4–3))			64.7	85
U Aur	05 38 53.50	32 00 57.0	12.9	81	(Z Sco) [A]	16 03 04.10	−21 35 55.0	6.5	71
CO(4–3)			47.9	67	RU Her [A,C]	16 08 08.60	25 11 59.0	14.2	65
U Ori	05 52 51.00	20 10 06.2	16.8	78	CO(4–3)			64.7	128
CO(4–3)			60.8	106	U Her [C]	16 23 34.86	19 00 18.0	12.9	56
(V Mon)	06 20 11.69	−02 10 07.0	19.4	36	CO(4–3)			24.6	107
(X Gem) [A,B]	06 43 55.20	30 19 53.0	40.1	21	(S Her)	16 49 37.14	15 01 27.8	19.4	56
(Y Mon) [A]	06 54 05.80	11 18 33.0	50.5	80	RS Sco [B,C]	16 51 59.82	−45 01 22.9	29.1	39
(RS Mon) [A]	07 04 49.30	05 03 58.0	50.5	127	RR Sco [B,C]	16 53 26.31	−30 30 08.3	31.1	27
S CMi [A]	07 30 00.00	08 25 35.0	18.1	29	(R Oph)	17 04 53.43	−16 01 39.5	24.6	44
R Cnc [C]	08 13 48.54	11 52 52.6	14.9	44	X Oph [B]	18 35 57.51	08 47 19.7	8.4	71
W Cnc [A,C]	09 06 57.90	25 27 06.0	78.9	20	R Aql	19 03 57.70	08 09 08.0	3.2	102
(R Car)	09 30 59.21	−62 34 01.1	29.1	234	CO(4–3)			19.4	304
X Hya [C]	09 33 06.92	−14 28 03.5	45.3	23	RT Aql [A,B,C]	19 35 39.70	11 36 24.0	19.4	38
R LMi	09 42 34.40	34 44 35.0	10.4	51	χ Cyg	19 48 38.30	32 47 08.0	6.5	156
CO(4–3)			63.4	91	CO(4–3)			19.4	244
R Leo	09 44 52.23	11 39 41.9	16.9	41	(RR Sgr) [A]	19 52 50.20	−29 19 21.0	9.1	60
CO(4–3)			43.2	109	Z Cyg [A,C]	20 00 02.60	49 54 07.0	23.3	29
(R UMa) [A]	10 41 07.30	69 02 19.0	19.4	57	T Cep [A]	21 08 53.30	68 17 12.0	12.9	90
(X Cen) [A]	11 46 41.10	−41 28 47.0	34.9	39	(S Lac)	22 26 49.37	40 03 34.3	13.6	113
(R Crv)	12 17 02.32	−18 58 41.7	19.4	65	R Peg	23 04 08.23	10 16 21.5	27.2	42
(R Vir)	12 35 57.67	07 15 47.0	16.8	74	W Peg [A]	23 17 22.70	26 00 18.0	9.7	66
R Hya	13 26 58.40	−23 01 27.0	10.4	81	(S Peg)	23 18 00.95	08 38 42.1	13.6	77
CO(4–3)			20.7	268	(R Aqr)	23 41 14.18	−15 33 41.8	72.5	30
S Vir [A,C]	13 30 22.80	−06 56 18.0	23.9	39	R Cas	23 55 51.68	51 06 36.4	5.2	84
CO(4–3)			32.4	84	CO(4–3)			15.5	400
W Hya	13 46 12.50	−28 07 11.0	5.8	129	(Z Peg) [A]	23 57 33.20	25 36 29.0	18.8	66
CO(4–3)			16.8	406	(W Cet)	23 59 33.64	−14 57 15.2	45.3	27

[A]Coordinates for these objects are from the *IRAS* PSC.

[B]Four off-source positions spaced symmetrically 30 arc seconds away from the source position were used when these objects objects were observed, in order to minimize contamination from extended galactic emission, if any.

[C]These objects showed only weak CO emission, so they were observed and the detection was confirmed on at least 1 additional night.

[D]R CVn was marginally detected when initially observed, but was not detected when re–observed for confirmation.

providing much greater velocity resolution. The 500 MHz spectrometer was used for R Cas, because its emission covered too large a velocity range to fit comfortably into the 50 MHz backend. All but one of the sixteen stars were detected in this higher transition.

3. Calibration

The receiver was sensitive to radiation in both sidebands, which were separated by 2.8 GHz. Indeed, when CO(3–2) was located in the upper sideband, ^{29}SiO(8–7) was detected in the lower sideband for several objects (χ Cyg, R Leo and especially W Hya). The relative sensitivity of the receiver to the two sidebands is difficult to determine, and it changes when the receiver's mechanical tuning structures are moved. For this reason, the carbon star IRC+10°216 was observed whenever the receiver was mechanically retuned, to assess its sensitivity to the signal sideband. Corrected for the main beam efficiency as measured on planets, the average value of T_{mb} for IRC+10°216 for all tunings was 24 K. The value of T_{mb} for IRC+10°216 is apt to be constant even if the central star's luminosity varies, since the rotational levels of CO in the envelope are populated primarily through collisions (Kwan and Hill 1977). For this reason, the temperature scales for each observation were scaled by the factor required to yield a T_{mb} of 24.0 K for IRC+10°216. Because the CO(4–3) observations were all made with a single receiver tuning, the sensitivity to the signal sidebands should be constant for those observations. For the CO(4–3) observations the antenna temperature was corrected for the main beam coupling efficiency, which was measured to be 60% on both Jupiter and Mars.

4. Analysis

Linear baselines were fitted to regions of the spectra judged to be free of emission, and were then subtracted from the spectra. For those objects which were detected, a model line profile was fitted to the data. The model (Morris 1984) assumes that CO is expelled from the central star in a spherical shell, at a nearly constant velocity (which is much larger than either the thermal or turbulent velocities). The line's temperature profile T(v) has the form

$$T(v) = T_{mb} W \left(\frac{\exp(-\beta^2 W)}{\exp(-\beta^2)}\right)\left(\frac{1-\exp(-\alpha/W)}{1-\exp(-\alpha)}\right) \quad \text{where} \quad W = 1 - \left(\frac{v - V_{LSR}}{V_o}\right)^2. \quad (1)$$

In the above equations T_{mb} is the line's temperature at the systemic velocity V_{LSR}, and V_o is the outflow velocity of the CO. α is related to the optical depth of the CO transition; large values correspond to high optical depths and give rise to parabolic line–shapes. Small values indicate that the transition is optically thin, and give rise to flat–topped lines. β is the ratio of the size of the source to that of the telescope's beam. Large values of β give rise to profiles with "horns" at $V_{LSR} \pm V_o$ on optically thin lines, or somewhat flattened parabolae in the optically thick case. Because none of the spectra showed very pronounced horns, and most of them are too noisy to allow discrimination between a flattened parabola and a perfect one, for the purposes of profile fitting all sources are assumed to be completely unresolved ($\beta = 0$). The remaining 4 parameters were adjusted for their least–squares best fit. Table 2 lists which stars were detected, the results of the profile analysis, and the 95% confidence limits on the derived parameters. The values of V_o have been corrected for the broadening caused by the 0.9 km s^{-1} resolution of the 500 MHz AOS, by assuming V_o and the velocity resolution add in quadrature. No such correction was applied to the CO(4–3) line fits (except for that of R Cas), because the more narrow 50 MHz AOS used for those observations did not broaden the lines measurably. Figures 1a–d and 2a–b show the CO(3–2) and CO(4–3) spectra of the detected stars, along with the fitted profiles.

Three of the stars; T Ari, R Cnc and RR Sco, have outflow velocities of less than 4 km s^{-1}, lower than any evolved star previously detected in CO (to the author's knowledge).

Table 2. – Line Fit Results

Star	T_{mb} (K)	Area K km s^{-1}	(α)	V_{LSR} (km s^{-1})	V_o (km s^{-1})
T Cas	0.84 ± 0.05	13.8	0.8	-9.3 ± 0.2	10.5 ± 0.5
W And	0.49 ± 0.05	5.8	> 4	-36.7 ± 0.3	8.9 ± 0.5
o Cet	9.69 ± 0.15	62.0	> 4	46.5 ± 0.0	4.8 ± 0.0
T Ari	0.08 ± 0.01	0.4	1.4	-0.8 ± 0.3	2.7 ± 0.7
R Hor	2.55 ± 0.18	18.7	1.9	35.7 ± 0.2	5.2 ± 0.3
U Ari	0.24 ± 0.03	1.4	1.3	-55.3 ± 0.2	4.0 ± 0.3
S Pic	0.27 ± 0.03	4.3	2.5	-0.9 ± 0.5	11.6 ± 1.0
R Aur	1.03 ± 0.06	13.3	> 4	-3.4 ± 0.2	9.6 ± 0.5
(4–3)	0.90 ± 0.04	11.4	> 4	-1.0 ± 0.2	10.0 ± 0.3
S Ori	0.37 ± 0.03	2.8	> 4	14.5 ± 0.2	5.7 ± 0.5
U Aur	0.34 ± 0.03	5.9	0.1	7.0 ± 0.5	9.2 ± 0.5
(4–3)	0.17 ± 0.02	2.2	3.8	6.8 ± 0.5	9.8 ± 0.8
U Ori	0.91 ± 0.06	9.1	> 4	-37.5 ± 0.2	7.5 ± 0.3
(4–3)	0.72 ± 0.04	5.8	> 4	-37.9 ± 0.2	6.5 ± 0.3
S CMi	0.26 ± 0.02	1.7	1.7	51.7 ± 0.2	4.7 ± 0.3
R Cnc	0.36 ± 0.03	2.2	0.3	15.0 ± 0.2	3.5 ± 0.3
W Cnc	0.08 ± 0.02	0.6	0.1	36.8 ± 0.2	4.2 ± 0.5
X Hya	0.08 ± 0.01	0.7	1.1	26.2 ± 0.5	5.9 ± 1.1
R LMi	0.68 ± 0.02	7.9	> 4	1.3 ± 0.2	8.7 ± 0.3
(4–3)	0.63 ± 0.02	7.1	> 4	0.6 ± 0.2	8.5 ± 0.2
R Leo	3.06 ± 0.02	30.3	> 4	-0.4 ± 0.0	7.4 ± 0.0
(4–3)	2.82 ± 0.04	28.1	3.5	-0.4 ± 0.0	7.4 ± 0.1
R Hya	2.09 ± 0.05	30.3	2.3	-10.1 ± 0.2	10.5 ± 0.2
(4–3)	4.60 ± 0.11	46.1	> 4	-10.0 ± 0.1	8.2 ± 0.1
S Vir	0.35 ± 0.03	2.1	2.3	9.8 ± 0.2	4.4 ± 0.5
(4–3)	0.35 ± 0.04	2.3	> 4	10.1 ± 0.2	5.7 ± 0.4
W Hya	1.75 ± 0.06	24.4	0.3	39.9 ± 0.2	8.0 ± 0.2
(4–3)	3.14 ± 0.09	40.3	1.0	41.0 ± 0.1	8.4 ± 0.2
S CrB	0.73 ± 0.03	7.5	> 4	1.5 ± 0.2	7.7 ± 0.3
(4–3)	0.60 ± 0.04	4.9	> 4	1.4 ± 0.2	6.3 ± 0.3
RS Lib	0.29 ± 0.03	2.0	1.7	7.8 ± 0.3	4.9 ± 0.5
(4–3)	0.45 ± 0.06	3.1	> 4	7.6 ± 0.3	5.5 ± 0.5
R Ser	0.31 ± 0.02	2.1	> 4	31.7 ± 0.3	5.1 ± 0.5
(4–3)			*not detected*		
RU Her	0.65 ± 0.03	7.8	> 4	-11.4 ± 0.3	8.9 ± 0.3
(4–3)	0.53 ± 0.04	5.7	1.1	-11.1 ± 0.2	7.2 ± 0.4
U Her	0.39 ± 0.03	6.0	> 4	-13.7 ± 0.5	11.5 ± 0.6
(4–3)	0.36 ± 0.02	4.9	0.1	-13.7 ± 0.1	7.4 ± 0.2
RS Sco	0.29 ± 0.03	1.9	> 4	6.5 ± 0.3	5.0 ± 0.3
RR Sco	0.16 ± 0.02	0.7	> 4	-28.9 ± 0.3	3.1 ± 0.5
X Oph	0.27 ± 0.05	2.4	1.3	-55.0 ± 0.5	6.1 ± 0.9
R Aql	2.90 ± 0.05	36.9	> 4	46.0 ± 0.2	9.5 ± 0.2
(4–3)	3.09 ± 0.09	36.9	> 4	47.1 ± 0.1	9.2 ± 0.2

continued next page

Table 2. – Line Fit Results (continued)

Star	T_{mb} (K)	Area K km s^{-1}	(α)	V_{LSR} (km s^{-1})	V_o (km s^{-1})
RT Aql	0.18 ± 0.02	1.6	> 4	-28.6 ± 0.5	6.6 ± 0.6
χ Cyg	3.93 ± 0.08	52.1	> 4	7.8 ± 0.2	9.9 ± 0.2
(4–3)	4.03 ± 0.07	52.7	1.4	9.9 ± 0.1	9.0 ± 0.1
Z Cyg	0.22 ± 0.02	1.2	> 4	-147.7 ± 0.2	4.0 ± 0.3
T Cep	1.22 ± 0.06	7.8	> 4	-3.0 ± 0.2	4.8 ± 0.3
R Peg	0.19 ± 0.02	2.1	> 4	22.7 ± 0.5	8.3 ± 0.8
W Peg	0.26 ± 0.03	3.0	1.2	-15.5 ± 0.5	7.7 ± 0.9
R Cas	3.86 ± 0.03	71.6	0.9	23.7 ± 0.0	12.1 ± 0.2
(4–3)	6.01 ± 0.29	102.4	> 4	25.6 ± 0.2	13.3 ± 0.3

The average outflow velocity is only 7.0 km s^{-1}. This is substantially below the value found in previous surveys in which candidates were selected by infrared criteria. For example the survey by Nyman *et al.* (1992) used *IRAS* color criteria to select candidates. Their survey detected 20 oxygen–rich Miras, with an average outflow velocity of 13.3 km s^{-1}. Zuckerman and Dyck (1986a, 1986b, 1989, Zuckernam, Dyck and Claussen 1986) surveyed the evolved stars with the largest fluxes in the AFGL and *IRAS* catalogs; among their detections were 14 oxygen–rich Miras with an average outflow velocity of 11.3 km s^{-1}.

4.1 Detections and Nondetections

The characteristic that best discriminates between the stars which were detected and those which weren't is the spectral type's decimal subtype (Yerkes system), taken from the RCMV. As figure 3 shows, the detection percentage is a steep and nearly monotonic function of the subtype. None of the 13 stars examined with subtypes below 5.5 were detected, while all 4 with subtypes greater than 7 were. An attempt was made to find an infrared color index which divided the stars cleanly into detected and nondetected groups. All colors of the form

$$C = \frac{f_I^{\lambda(1)} f_K^{\lambda(2)} f_{4\mu}^{\lambda(3)} f_{11\mu}^{\lambda(4)} f_{12\mu}^{\lambda(5)} f_{25\mu}^{\lambda(6)} f_{60\mu}^{\lambda(7)} f_{100\mu}^{\lambda(8)}}{f_I^{\lambda(9)} f_K^{\lambda(10)} f_{4\mu}^{\lambda(11)} f_{11\mu}^{\lambda(12)} f_{12\mu}^{\lambda(13)} f_{25\mu}^{\lambda(14)} f_{60\mu}^{\lambda(15)} f_{100\mu}^{\lambda(16)}}$$

were examined, where f_I and f_K are the I and K band fluxes from the TMSS catalog, $f_{4\mu}$ and $f_{11\mu}$ are from the AFGL catalog, the four long wavelength fluxes are from the *IRAS* PSC and $0 \leq \lambda(n) \leq 2$. No color of this form was found to be able to predict which stars would be

detectable in all cases, although several of these colors were nearly able to do so. Also, no color was a more reliable indicator of detectability than the *IRAS* 25μ flux alone. Three of the undetected stars; R Aqr, R Car and R Cen, were consistently included among the detected stars by all the colors and fluxes which most reliably discriminated between detectable and not detectable sources. R Aqr is a symbiotic variable, and this might explain its lack of detectable CO emission. R Cen and R Car are normal Miras however, and the lack of CO surrounding these stars is intriguing. Both have larger fluxes in all four *IRAS* bands than many of the stars which were detected, indicating that they do have substantial dust shells. As neither of these stars rise above 10 degrees from the southern horizon, it's tempting to dismiss their nondetection as a result of poor instrument performance at low elevations. However Nyman *et al.* (1992) also observed R Car from the southern hemisphere (at SEST), and they too did not detect it. The *V* band amplitudes of R Car and R Cen, 6.0 and 6.5 mag. respectively (Eggen 1992), are fairly low for Mira variables, but they are as large or larger than several of the detected stars. However at visual band maximum the spectral types of R Car and R Cen, M5e and M4.5e respectively (RCMV), are earlier than any of the detected objects. Perhaps the hotter photospheres of these two stars prevents the dust forming near enough to the star to allow efficient dust–gas momentum coupling and mass loss. Alternatively, these stars may be losing mass at rates comparable to cooler Miras, but carbon monoxide might not be fully associated in their photospheres. It would be surprising if R Car and R Cen had strong winds with no CO, because a CO envelope has been detected surrounding α Ori (Knapp *et al.* 1982) which has an even warmer photosphere (M2Iab).

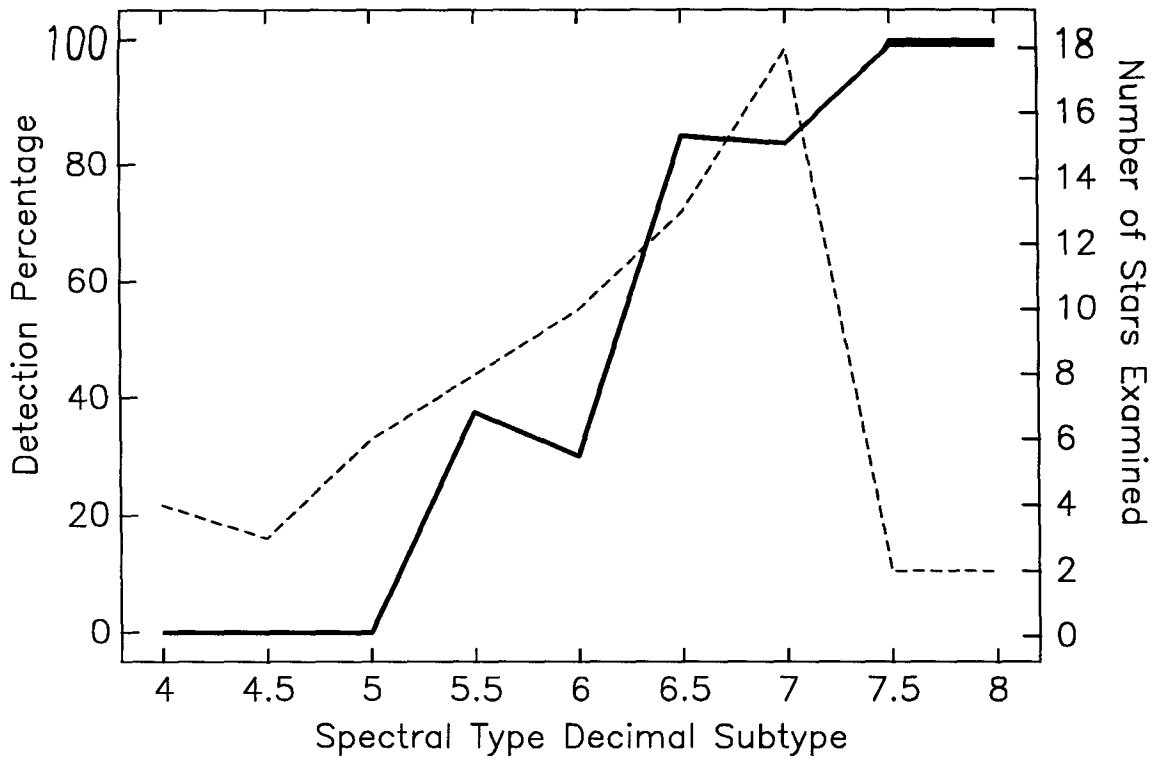

Fig. 3. The horizontal axis denotes the decimal subtype of the star's spectral type at visual maximum. A value of 5.5 could denote a spectral type of either M5.5 or S5.5. The bold line shows the percentage of stars detected. The dashed line shows the number of stars examined for each spectral type.

4.2 Mass Loss Rates

After the line profile parameters had been calculated, an artificial CO(3–2) profile was calculated using a Large Velocity Gradient (LVG) radiative transfer program (Morris 1980). The mass loss rate was adjusted until the peak T_{mb} of the artificial profile matched that of the parameterized profile. The CO envelope was assumed to be truncated by photodissociation, and this radius was calculated using the photodissociation rate of Mamon *et al.* (1988). Table 3 lists the calculated absolute magnitudes, distances, mass loss rates ($\dot{M}$) and the outer radii of the CO envelopes for the stars which were detected. The highest (R Cas: $2.4 \times 10^{-6} M_{\odot} \mathrm{yr}^{-1}$) and lowest (T Ari and RR Sco: $5 \times 10^{-9} M_{\odot} \mathrm{yr}^{-1}$) mass loss rates differ by nearly 3 orders of magnitude. The star's distance, luminosity and fractional abundance of CO were input parameters to the LVG model, and the sensitivity of the calculated value of $\dot{M}$ to errors in these parameters was investigated by varying the parameters by their estimated 1σ uncertainties, and recalculating $\dot{M}$.

Errors in the star's estimated luminosity and distance are not independent, because the distance was calculated using the luminosity provided by the period-spectral type-luminosity relationship (PSLR). If a particular star is actually more luminous than the PSLR indicates it is, it provides more infrared radiation to excite CO, which leads to increased CO(3–2) radiation from a given amount of CO. Increasing the estimated luminosity of the star decreases the value of $\dot{M}$ calculated by the LVG model, because less molecular material is needed to produce the same line strength. However if the star's luminosity has been underestimated, then its derived distance will also be too low. Increasing the distance estimate given to the LVG increases the calculated value of $\dot{M}$, because less of the CO(3–2) radiation from a given amount of CO will arrive at the telescope. Therefore the errors in $\dot{M}$ introduced by errors in the luminosity and distance will have opposite signs. The net effect is that varying the luminosity by ± 0.4 magnitudes, the mean spread in the PSLR (Celis 1981), changes the derived distances by (+20%,–17%) and $\dot{M}$ by $\pm 23\%$, on average. The $\dot{M}$ values shown in Table 3 were calculated with the assumption $f = [CO]/[H_2] = 3 \times 10^{-4}$, as would be the case if hydrogen and carbon were present in the solar abundance ratio, and half of the carbon was incorporated into CO molecules. Decreasing f to 2×10^{-4} increases $\dot{M}$ by 39% on average, while increasing f to 4×10^{-4} on average decreases $\dot{M}$ by 21%. If errors in the estimated luminosity and f are independent, then they should add in quadrature, and the uncertainty in the calculated value of $\dot{M}$ arising from these two sources is $\pm$ 60%. Error estimates for the value of $\dot{M}$ for individuals stars, using the range of parameters discussed above, are given in Table 3.

Table 3. – Calculated Luminosities, Distances and Mass Loss Rates

Star	M_V	Distance (pc)	$\dot{M}$ (10^{-8} $M_\odot yr^{-1}$)	R_{Max} (10^{16} cm)	Star	M_V	Distance (pc)	$\dot{M}$ (10^{-8} $M_\odot yr^{-1}$)	R_{Max} (10^{16} cm)
T Cas	-0.54	350	92. ± 30	16.	W Hya	-0.12	80 [A]	15. ± 6	7.5
W And	-0.16	280	28. ± 10	9.7	(4-3)			21. ± 8	
o Cet	-1.84	100 [A]	30. ± 10	14.	S CrB	-0.83	310 [A]	29. ± 10	11.
T Ari	-1.63	350	0.5 ± 0.2	2.4	(4-3)			11. ± 4	
R Hor	-0.98	190	23. ± 9	12.	RS Lib	-0.11	210	3.1 ± 1	3.5
U Ari	-1.44	710 [A]	5.4 ± 2	6.3	(4-3)			3.5 ± 1	
S Pic	-0.77	440	49. ± 20	11.	R Ser	-1.35	330 [A]	3.7 ± 1	4.7
R Aur	-1.11	450	130. ± 50	20.	RU Her	-0.89	410	62. ± 20	14.
(4-3)			113. ± 40		(4-3)			28. ± 10	
S Ori	-0.75	480	17. ± 6	9.4	U Her	-0.72	360	49. ± 20	11.
U Aur	-0.71	500	52. ± 20	13.	(4-3)			14. ± 5	
(4-3)			24. ± 9		RS Sco	-1.03	300	1.8 ± 0.7	4.3
U Ori	-0.90	240	23. ± 8	9.5	RR Sco	-0.96	200	0.5 ± 0.2	2.2
			9.1 ± 3		X Oph	-0.80	270	3.7 ± 1	4.2
S CMi	-0.52	340	3.4 ± 1	4.6	R Aql	-0.67	190	90. ± 30	17.
R Cnc	-0.88	300	1.9 ± 0.7	4.0	(4-3)			76. ± 30	
W Cnc	-1.61	720 [A]	2.6 ± 1	4.3	RT Aql	-0.52	450	8.5 ± 3	6.2
X Hya	-0.16	400	2.5 ± 0.9	3.6	χ Cyg	-0.29	115 [C]	68. ± 20	14.
R LMi	-0.47	260 [A]	30. ± 10	10.	(4-3)			46. ± 20	
(4-3)			23. ± 9		Z Cyg	-1.11	490	3.3 ± 1	5.0
R Leo	-0.46	120 [B]	34. ± 10	12.	T Cep	-0.94	220	8.2 ± 3	7.2
(4-3)			25. ± 9		R Peg	-0.74	380 [A]	10. ± 4	6.1
R Hya	-0.76	110 [A]	35. ± 10	10.	W Peg	0.03	270 [A]	8.1 ± 3	5.6
(4-3)			39. ± 20		R Cas	-0.78	230	240. ± 90	24.
S Vir	-1.87	450	4.6 ± 2	5.6	(4-3)			360. ± 100	
(4-3)			5.7 ± 2						

[A]Distance from Jura and Kleinmann 1992, [B]Distance from Gatewood 1992

[C]Distance from Stein 1991

Figure 4 shows a log–log plot of the calculated mass loss rates versus the outflow velocity. There's an obvious strong correlation, indicating a power–law relationship holds between these quantities. The best–fit power–law is

$$\dot{M} \approx 2.43 \times 10^{-10}\ V_{o\ (km\,s^{-1})}^{3.35}\ M_\odot yr^{-1}. \qquad (2)$$

Ironically, the star which deviates most strongly from this relationship is Mira itself! The most likely reason for this is that Mira's true outflow velocity is substantially larger than the

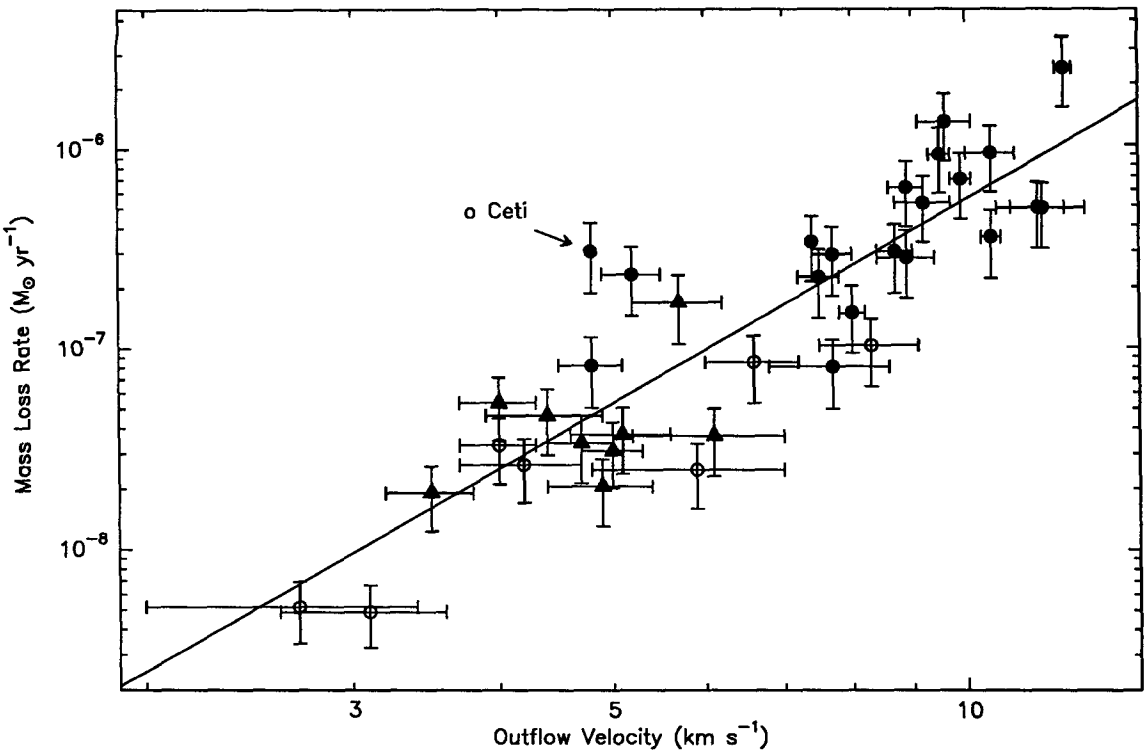

Fig. 4. A Log-Log plot of mass loss rate as a function of outflow velocity is shown for the 36 Mira stars which were detected. The line shown is the linear least-squares best fit to the data (equation 2). Filled circles indicate stars with integrated CO(3–2) line intensities of 3 K km s^{-1} or greater, which lie above line D in figure 5. Open circles represent stars which fall below line C in figure 5.

4.8 km s^{-1} found by fitting equation 1 to the data. The wings of Mira's CO(3–2) profile extend to about 10 km s^{-1} from the line center (Knapp 1993). Plotting Mira in figure 4 with a higher expansion velocity would move it closer to the locus of points, but the peculiar high velocity wings on the 3–2 profile indicate that the simple spherical, constant expansion velocity LVG model used to calculate $\dot{M}$ is too simplistic for this star.

It is important to recognize that selection effects could influence the appearance of figure 4 and hence equation 2. For example, for any given peak antenna temperature T_D, in a noisy spectrum one is more apt to recognize a narrow line with a peak temperature of T_d than a wide line with the same peak temperature. Very wide, weak lines are apt to be overlooked or incorrectly attributed to instrument baseline irregularities, leading to false *non*detections. In this way one could end up with a list of detections in which all the least intense lines, which for a given distance indicate a low mass loss rate, have small outflow velocities. Figure 5 shows the line

area as a function of expansion velocity, on a log–log plot. If we assume that the weakest lines are unresolved and optically thin, then the line area is approximately given by twice the product of the peak antenna temperature and the expansion velocity. If one could detect all lines above some threshold antenna temperature, regardless of the line width (i.e., if this selection effect were absent), then the points in figure 5 should all lie on or above some line with a slope of 1. If the selection effect has influenced the survey, then one would expect the points to be bounded by a line with a slope greater than 1. For instance, if the threshold detection temperature were proportional to the expansion velocity, then the points should be bounded by a line with slope 2. In fact, the points all lie on or above line A in figure 5, which has a slope of 0.7. However, there are no points near line A with large expansion velocities, and if one star (X Hya) is rejected, the points seem to be bounded more closely by line B, which has a slope of 1.8. Thus the sample is probably too small to allow the importance of this selection effect to be quantitatively assessed. A reasonable guess would be that the 7 points falling below line C on figure 5, which has a slope of 1, represent stars with antenna temperatures which might not have been recognized as detections, had their outflow velocities been higher. In figure 4, these 7 stars are represented by open circles, and it is clear that the line produced by equation 2 is still a good fit to the data even if these points are rejected. Above 3 K km s^{-1} (line D in figure 5), there is no correlation at all between line area and outflow velocity. Figure 4 shows that even if only those points lying within this uncorrelated region of figure 5 are used, there is still a correlation between $\dot{M}$ and V_o .

Van der Veen and Habing (1988) showed that oxygen rich Miras and OH/IR stars fall along a broad track on an *IRAS* two–color diagram constructed from the PSC 12, 25 and 60μ fluxes. They further showed that as one moves along this path from the warmer to the cooler end, stars with increasingly large mass loss rates are found. These authors interpret this as an evolutionary progression. Figure 6 shows such a two–color diagram for the stars in this survey. Surprisingly, the detected and nondetected stars are not well segregated and the mass loss rate seems unrelated to either of the colors. Though not shown in figure 6, colors involving the *IRAS* 100μ flux were also examined and they too appeared uncorrelated with the mass loss rate. It has been shown that for highly obscured stars the mass loss rate is strongly dependent on

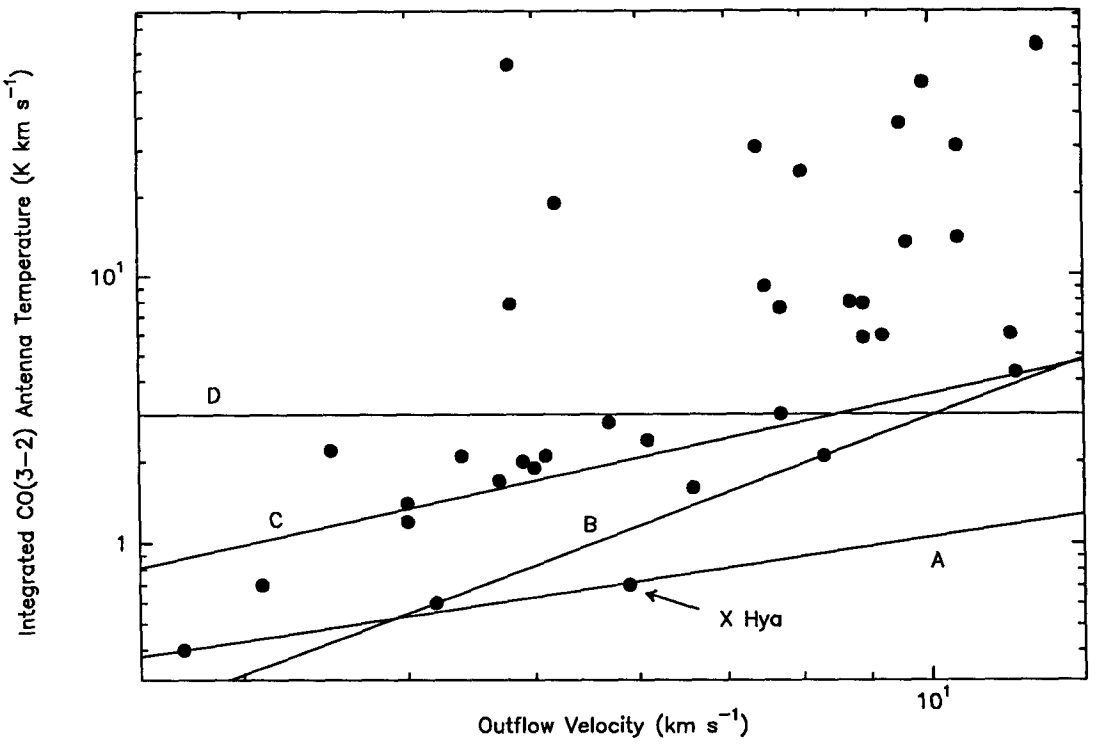

Fig. 5. The CO(3-2) line area, as a function of outflow velocity, is shown. Above 3 K km s^{-1} there is no correlation.

IRAS color, and empirical formulae have been constructed to give mass loss estimates based on these colors (van der Veen 1989). The results presented here show that such formulae are not applicable to stars with visible photospheres and low values of $\dot{M}$. On the other hand, figure 7 shows that the mass loss rates in table 3 do correlate with all four *IRAS* fluxes if they are normalized to a common distance, although the correlation with 100μm flux is very weak. The correlation is strongest with the 60μ flux. Such a correlation should be viewed with caution, because errors in the stellar distance estimate influence both the calculated mass loss rate and the distance normalized flux in the same manor, and can produce a spurious correlation. However neither $\dot{M}$ nor the 60μm luminosity shows any correlation with distance (see figures 7E and 7F), therefore it seems likely that the correlation of $\dot{M}$ with infrared luminosity is real.

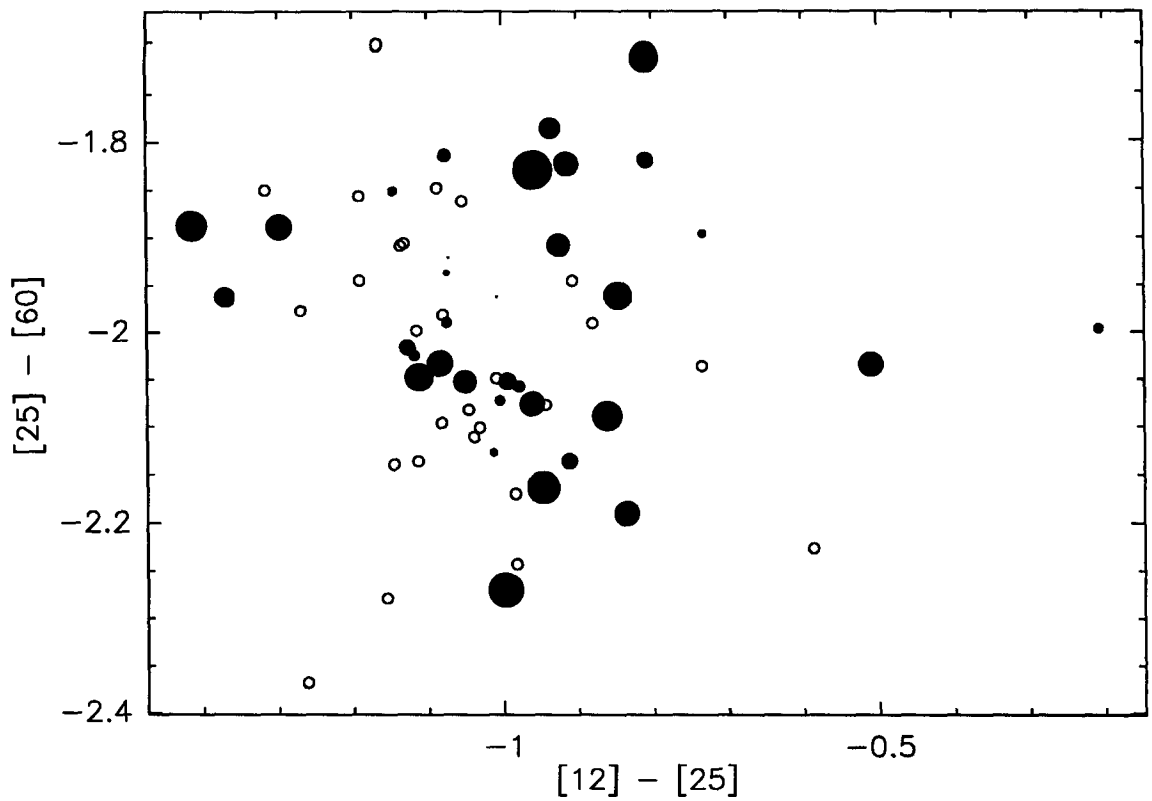

Fig. 6. An *IRAS* two-color diagram, for the detected and nondetected stars is shown. The abscissa is $2.5\log_{10}(F_{25\mu}/F_{12\mu})$ and the ordinate is $2.5\log_{10}(F_{60\mu}/F_{25\mu})$. Open circles represent nondetections, filled circles represent detections. The size of the filled circles is proportional to the log of the mass loss rate listed in table 3. Five survey stars with poor quality 12, 25, or 60μ fluxes in the PSC (RS Mon, R Cen, T Nor, RS Sco and R Aqr) have not been included in this plot.

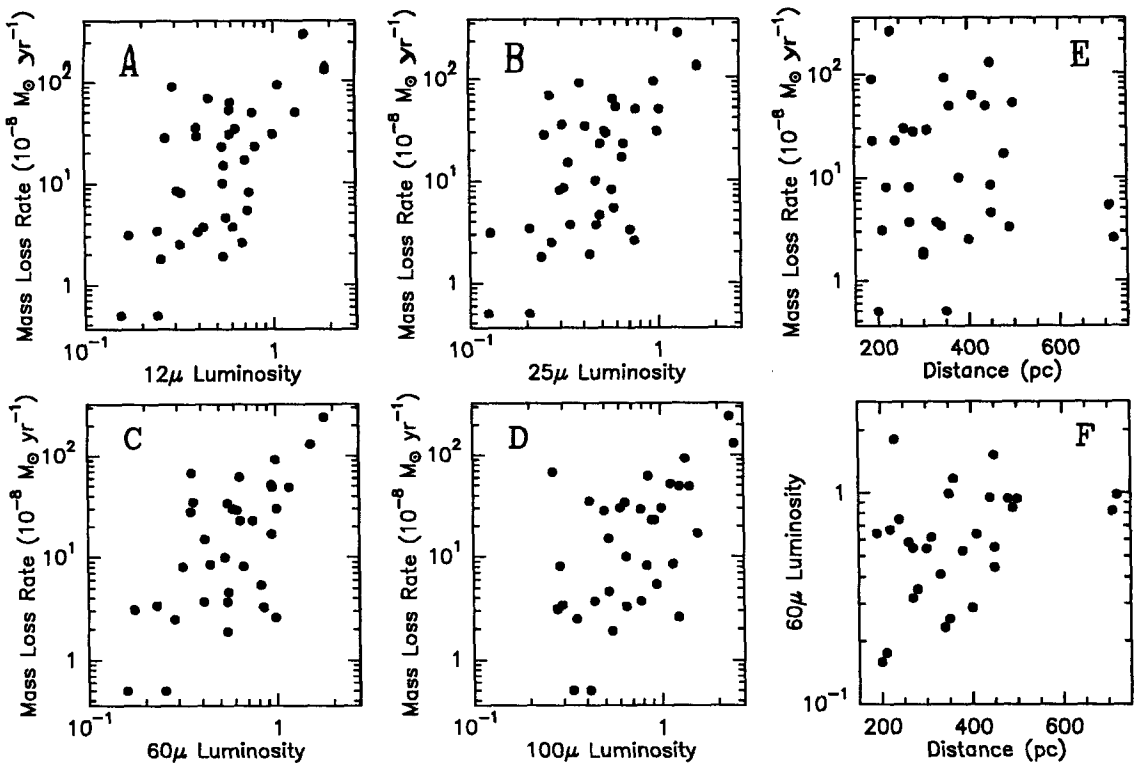

Fig. 7. Figures **A** through **D** show the mass loss rate as a function of far infrared luminosity (calculated as flux × distance^2) plotted for each of the *IRAS* bands. Stars with poorly determined *IRAS* fluxes are not included. In each case, the luminosity has been normalized to that of o Ceti. Figures **E** and **F** show there is no correlation between the calculated mass loss rates and 60μm luminosity, implying that these quantities aren't dominated by the effects of errors in the distance estimates.

4.3 The Wind Velocity

There is general agreement that the copious mass loss from heavily dust enshrouded stars, such as the OH/IR stars, is driven by radiation pressure on dust grains. However there is no such consensus on the cause of the much more modest mass loss seen in visible Miras. Netzer and Elitzur (1993) solved the equations of motion for dust and gas in a radiation driven wind, and concluded that there is a lower limit of $\sim 10^{-7}\ M_\odot \mathrm{yr}^{-1}$ for radiation driven mass loss, well below many of the values of $\dot{M}$ in table 3. Fusi–Pecci and Renzini (1975) showed that acoustic energy could drive mass loss in red giant stars. Yet the increase in outflow velocity at later spectral types shown in figures 8A&B is what would be expected in a radiation driven wind. Netzer and Elitzur (1993) show that for a such a wind, if the terminal velocity of the gas

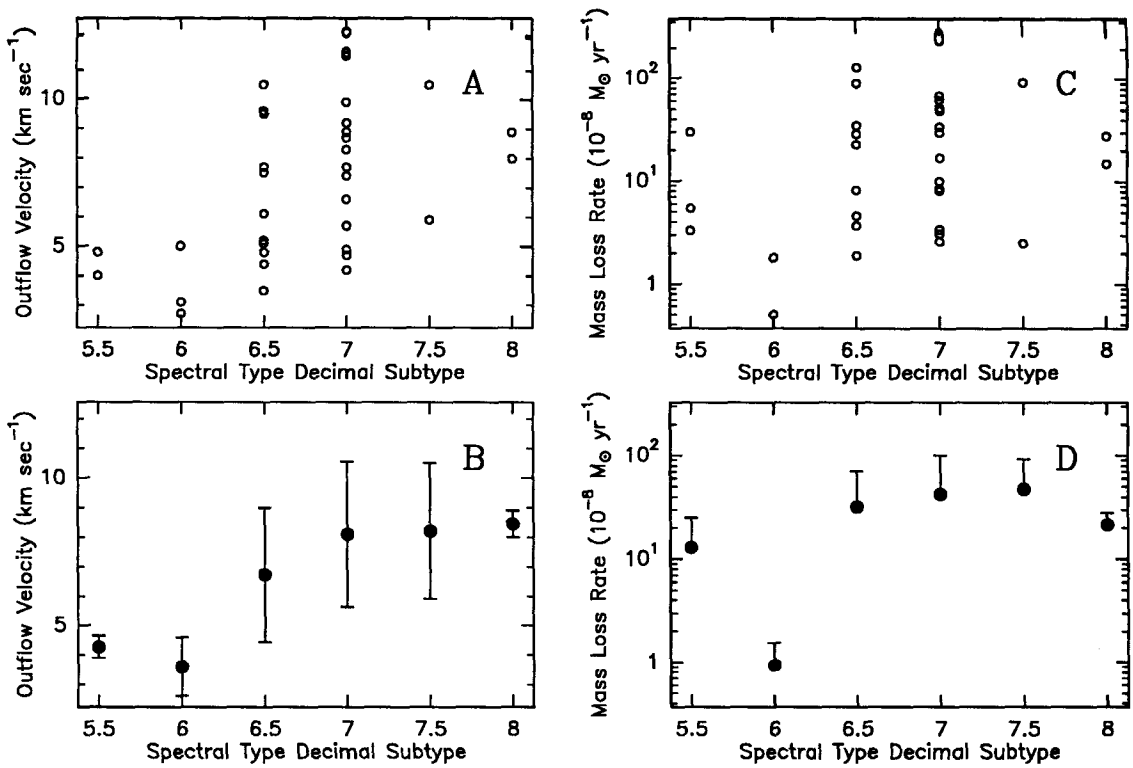

Fig. 8. (**A**) shows the distribution of CO(3–2) outflow velocities as a function of decimal spectral subtype at V band maximum. (**B**) shows the averages of the points in plot A. The error bars indicate the standard deviation. (**C**) shows the mass loss rates from table 3 as a function of decimal subtype, and (**D**) once again shows the averages.

greatly exceeds the initial velocity that the gas has at the base of the acceleration region, then $V_o \propto R_o^{-1/2}$ where R_o is the distance at which dust forms. Thus cooler stars, which should allow dust to form at smaller radii, will have higher values of V_o. The absence of detectable CO emission from the stars with spectral types earlier than M5.5 indicates that either such stars have extremely low mass loss rates or that they have mass loss rates similar to the cooler stars, but the gas is atomic. Knapp *et al.* (1993) looked for the 609μm line of C I in the envelope of Mira (spectral type M5.5) but did not detect it. Thus it would be surprising if large amounts of atomic carbon would be seen surrounding Miras with only slightly warmer photospheres. It seems more likely that these warmer Miras have very low mass loss rates. These warm Miras may inhibit the formation of dust throughout the region where the gas density is high enough to support a significant mass loss rate. It therefore appears that the results of this survey support radiation pressure on grains as the driving mechanism for even low mass loss rates. It is surprising however, that $\dot{M}$ is not correlated with spectral type (figures 8C&D).

One of the strongest pieces of evidence that the winds from AGB stars are driven by radiation pressure is the fact that the momentum present in the wind is almost always less than or comparable to the momentum available in the radiation field (Knapp *et al.* 1982). Assuming radiation pressure drives the wind, the rate of increase of the wind's mechanical momentum ($\dot{M}V_o$) can exceed the momentum available from the star's radiation (L_*/c) only if the light is scattered in an optically thick dust envelope. All of the stars in this survey must have optically thin dust envelopes, because the photospheres are still visible. If we assume that all Miras have a luminosity of about 3400 $L_\odot$ (the average of the oxygen Miras in the LMC survey of Feast *et al.* 1989), and if we use equation 2 to estimate the mass loss rate, then there is a maximum value of V_o , V_{max}, for which $\dot{M}V_o < L_*/c$. This value is 18 km s^{-1}. Because equation 2 is such a strong function of V_o , V_{max} is rather insensitive to the assumed Mira luminosity; if the true luminosities of Mira variables ranged from 10^3 to 10^4 $L_\odot$, this would only introduce a range of $\pm 40\%$ in V_{max}. It seems therefore that any AGB star losing mass by the same mechanism as these Miras will be obscured by an optically thick envelope if V_o is $\gtrsim$ 18 km s^{-1}.

In the standard radiation driven model of the wind, the dust feels the radiation pressure, and propels the gas outward via collisions. Thus the dust must be moving though the gas, at a velocity called the "drift velocity," for which Goldreich and Scoville (1976) derived the expression

$$v_d \approx \left(\frac{QL_*V_o}{\dot{M}c}\right)^{1/2} \qquad (3)$$

where Q is the momentum coupling constant between the radiation field and the dust. If we assume that the dust consists of silicate spheres with radii of 0.1μ, and the radiation field is that of a 2000 K black body, equation 3 becomes

$$v_d \approx \left(\frac{3Q_{ext}L_*V_o}{2\dot{M}c}\right)^{1/2} = \left(\frac{3 \times 0.023 \times 3400L_\odot \times V_o}{2\dot{M}c}\right)^{1/2}$$

where Q_{ext}, the dust extinction efficiency, has been taken from a tabulation by Draine (1987). Substituting equation 2 for $\dot{M}$ gives

$$v_d \approx 67 \times V_o^{-1.18} \approx \frac{67}{V_o} \quad \text{km s}^{-1} . \qquad (4)$$

At V_o = 3 km s^{-1}, this gives a drift velocity of 20 km s^{-1}, which is the velocity above which significant ablation of dust by sputtering is believed to occur (Wickramasignhe 1972; Kwok 1975). The lowest expansion velocity for any of the stars in this survey is that of T Ari, 2.7 km s^{-1}. While the assumption of uniform spherical grains used to derive equation 4 is a crude approximation at best, this result provides a possible explanation for why no Miras have outflow velocities significantly below 3 km s^{-1}.

Although the CO emission lines from these stars presents a radiative transfer problem which is too complex to be solved analytically, it is likely that in all cases the emission from higher J transitions arises from a region closer to the star than does a low J transition. In the case of a large mass loss rate ($\dot{M} \gtrsim 10^{-5} M_{\odot} \mathrm{yr}^{-1}$), this is because the rotational levels are populated by collisions (Morris 1980, Schönberg 1988), which tends to force the partition function to reflect a single temperature at a given radial distance. This temperature will decrease with increasing distance from the star, so the Boltzman factor will allow high J levels to be populated only at small radii. For low mass loss rates, collisional excitation is less important than radiative pumping via the CO vibrational transitions near 4.6μ (Morris 1980, Schönberg 1988). Although infrared absorption and subsequent decay can either increase or decrease J, the branching ratios of the transitions insure that an increase in J is more likely, therefore the net effect of infrared pumping is to increase the population of the higher J transitions. However the spontaneous decay rate of a rotational transition is proportional to J^3, and as J increases the pump rate must increase also to maintain a significant population. This means that as J increases infrared pumping will only be effective at smaller radii, again implying that high J emission arises from small radial distances. Assuming the CO rotational ladder can be characterised by a temperature distribution of the form $T(r) \propto r^{-\alpha}$, Van der Veen and Olofsson (1989) derived an expression giving the approximate relative locations from which the different rotational emission lines arise

$$\frac{R_{J \rightarrow J-1}}{R_{1 \rightarrow 0}} = \left(\frac{2}{J(J+1)} \right)^{1/\alpha}.$$

If α = 0.7 (Kwan and Linke 1982), this implies the CO(4–3) probes the stellar wind at a radius only $\sim 1/25$ as large as CO(1–0), and reflects the conditions in the wind only a few hundred AU from the star.

Table 4 lists the outflow velocities, culled from the literature, for the stars in this survey which had previously been detected at a lower J transition. One must be cautious in comparing the outflow velocities obtained by different authors who no doubt processed their data with different algorithms. Even for the very strong source Mira, the velocities obtained for a single transition, CO(2–1), show considerable scatter (Knapp and Morris 1985: 5.0 km s^{-1}; Zuckerman and Dyck 1986a: 4.6 km s^{-1}; Zuckerman, Dyck and Claussen 1986: 8.3 km s^{-1}; Zuckermann and Dyck 1989: 4.3 km s^{-1}). However if the gaseous component of the wind is still being accelerated at radii greater than a few hundred AU, the value obtained for V_o should on average be lower as increasingly high transitions are examined. Table 4 shows no evidence of this. On the other hand, it is hard to believe that differing data processing algorithms and low signal to noise account for all the scatter seen in these tabulated velocities. Compare, for example, the CO(3–2) and CO(4–3) profiles of U Her, shown in figures 1c and 2b. Table 2 lists the fitted outflow velocities for these two profiles as 11.5 and 7.4 km s^{-1} respectively. While neither profile is of such high quality that the zero intensity points can easily be distinguished with high precision, the line fitting routine found exactly the same systemic velocity for both profiles (–13.7 km s^{-1}). If the differing outflow velocities merely reflect poor signal-to-noise, then one also would expect at least some disagreement between the fitted systemic velocities. The profiles of some of the brighter sources in figures 1 and 2, such as Mira and R Hya, are poorly fit by the template function. This too might be an indication of a more complicated envelope velocity structure than isotropic outflow at a nearly constant velocity. Many studies have indicated that discrete shells are present in the winds of AGB stars (David and Papoular 1992 and references therein); perhaps shells from different mass loss episodes are ejected with significantly different terminal velocities. If this is the case, the validity of mass loss rates derived from radiative transfer models which assume a small dispersion in the wind velocity would be called into question. It would be interesting to obtain very high signal-to-noise spectra of several CO transitions for a few bright stars, to assess how constant the outflow velocity is.

Two groups have recently studied the acceleration of the SiO in oxygen–rich red giants, including χ Cygni. Lucas *et al.* (1992) mapped SiO(2–1) using the IRAM interferometer, and concluded that the gaseous component of the envelope had attained only 1/2 of its terminal

velocity at a distance of 330 AU from the star, and only 3/4 at a distance of 730 AU. In contrast Sahai and Bieging (1993) mapped the same spectral line in several of the same objects using the BIMA array, and concluded that the acceleration zone was only 1/10 as large as Lucas *et al.* had deduced. The results presented here, which show no systematic decrease in the the outflow velocity as higher J transitions of CO are observed, argue in favor of the Sahai and Bieging model.

Table 4. – Comparison of Outflow Velocity Measurements for Previously Detected Stars

	CO Rotational Transition					CO Rotational Transition			
Star	1–0	2–1	3–2	4–3	Star	1–0	2–1	3–2	4–3
T Cas	10.5 [A]	5.2 [B]	10.5	...	R Leo	4.0 [E]	6.5 [H]	7.4	7.4
W And	11.0 [C]	...	8.9	...	R Hya	...	7.2 [B]	10.5	8.2
o Cet	10.0 [D]	5.0 [E]	4.8	...	W Hya	...	8.8 [B]	8.0	8.4
R Hor	5.4 [D]	6.6 [F]	5.2	...	R Aql	...	10.1 [I]	9.5	9.2
S Pic	11.8 [D]	...	11.6	...	χ Cyg	10.2 [E]	...	9.9	9.0
R Aur	11.1 [D]	...	9.6	10.0	T Cep	...	5.0 [J]	4.8	...
U Ori	5.8 [G]	...	7.5	6.5	R Cas	14.3 [D]	...	12.1	13.3
R LMi	6.5 [D]	6.0 [H]	8.7	8.5					

Sources: (A) Knapp, 1986; (B) Zuckerman and Dyck, 1986a; (C) Zuckerman, Dyck and Claussen, 1986; (D) Nyman *et al.* , 1992; (E) Knapp and Morris, 1985; (F) Knapp and Sutin, 1989; (G) Kastner, Zuckerman, Dyck and Sopka, 1989; (H) Knapp *et al.* 1982; (I) Wannier and Sahai, 1986; (J) Zuckerman and Dyck, 1989

5. Conclusions

A survey of stars from the RCMV within 500 pc was conducted; of the 66 stars examined 36 were detected. The survey data led to the following conclusions:

1) A Mira's spectral type is the best predictor of whether an extensive CO envelope exists or not. None of the stars examined with spectral types earlier than M5.5 were detected, all of those later than M7 were.

2) For the relatively low mass loss rates of these Miras there is no correlation between far infrared color and the mass loss rate indicated by the CO emission, in contrast to the findings of CO surveys containing heavily obscured stars. The far infrared luminosity is, however, correlated to the mass loss rate.

3) Two stars, R Cen and R Car, appear to have extensive dust envelopes, yet were not detected in CO(3–2). Because these stars are near the southern limit of the sky observable from the CSO, it would be useful to examine these stars carefully from an observatory in the southern hemisphere. It would also be interesting to search for atomic carbon emission from these stars, to see if the lack of CO is caused by the stars' relatively warm photospheres, rather than an undetectablely low mass loss rate.

4) The outflow velocity increases as stars with cooler photospheres are examined, as would be expected if radiation pressure on dust grains drives the stellar wind.

5) The mass loss rate is strongly correlated to the outflow velocity. A power–law relationship holds between these two quantities over almost 3 orders of magnitude in $\dot{M}$.

6) At the low end of the observed outflow velocities (~ 3 km s^{-1}), the dust drift velocity may be large enough to cause the destruction of the dust grains though dust–gas collisions.

7) At the high end of the observed outflow velocities (~ 12 km s^{-1}), the momentum in the wind is beginning to approach the total amount of momentum available in the radiation field. At velocities $\gtrsim 18$ km s^{-1}, the power–law $V_o - \dot{M}$ relationship indicates that all the momentum in the radiation field will be transferred to the wind; this can only occur if the dust envelope is optically thick in the visible and near infrared.

8) An examination of the outflow velocities obtained at differing CO rotational transitions shows no general trend in V_o as high J transitions are observed. The outflow velocity does appear significantly different in different CO transitions for some of the stars. This, in addition to the peculiarities in the shapes of some of the spectra, suggests that shells expanding at different velocities may co–exist in some cases.

I am greatly indebted to the staff of the CSO for their help and support during the numerous observing runs over which these data were collected. Jill Knapp, Tom Phillips and Antony Schinckel provided helpful suggestions to improve an early version of this paper. This work was supported by NSF contract #AST 90–15755.

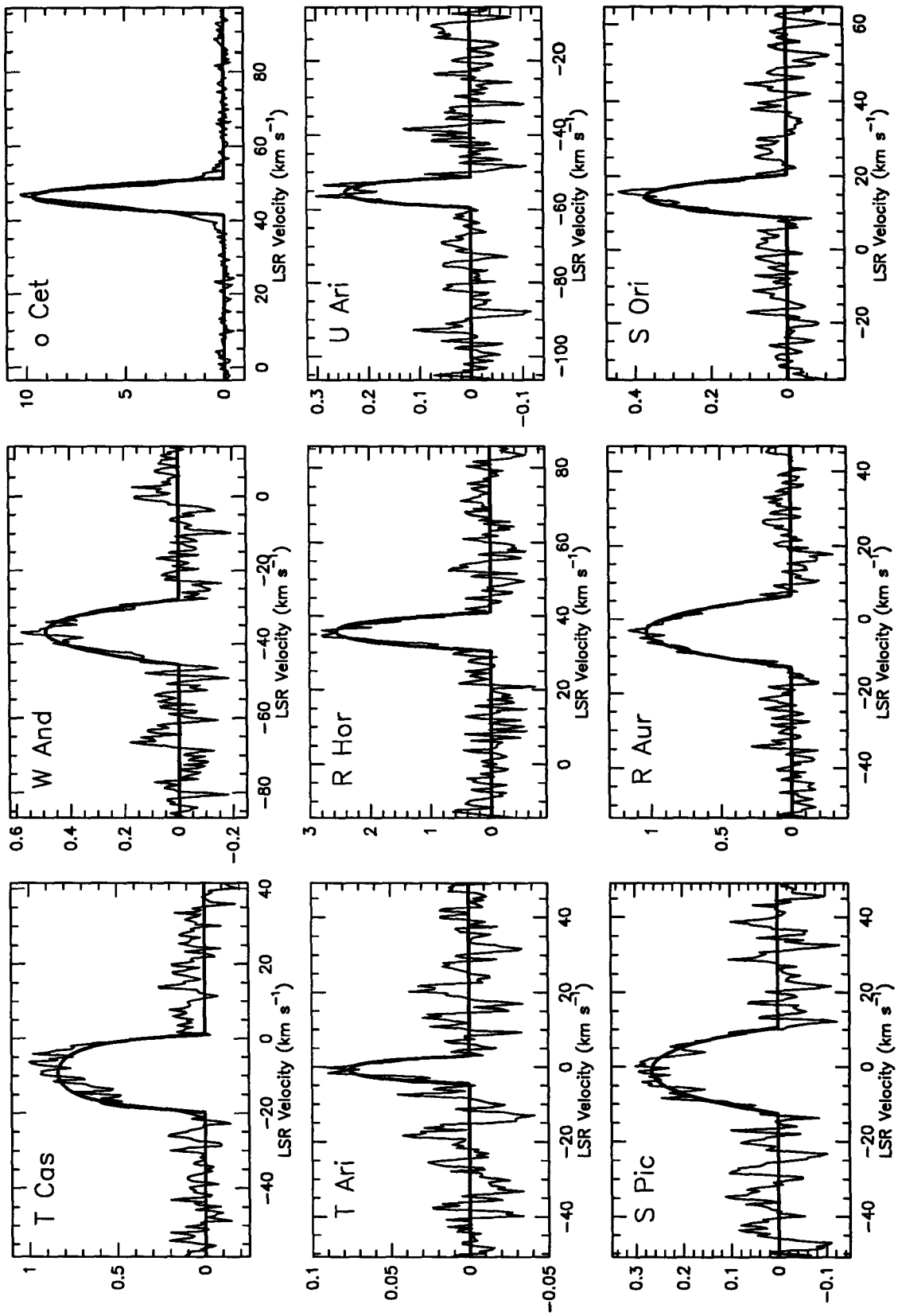
o Cet
W And
U Ari
T Cas
R Hor
S Ori
T Ari
R Aur
S Pic
LSR Velocity (km s^{-1})

Figure 1a

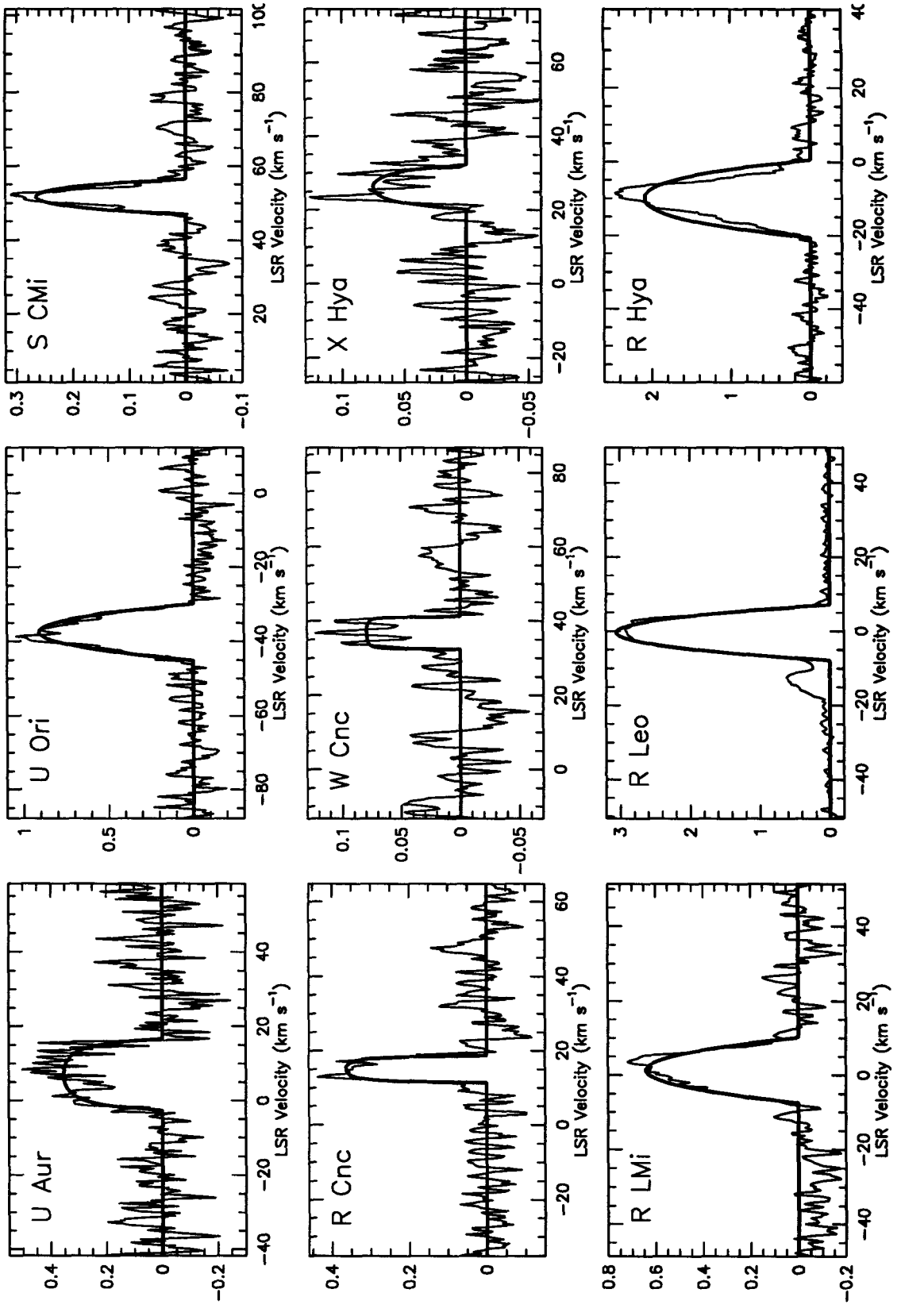
U Aur
U Ori
S CMi
R Cnc
W Cnc
X Hya
R LMi
R Leo
R Hya
LSR Velocity (km s^{-1})

Figure 1b

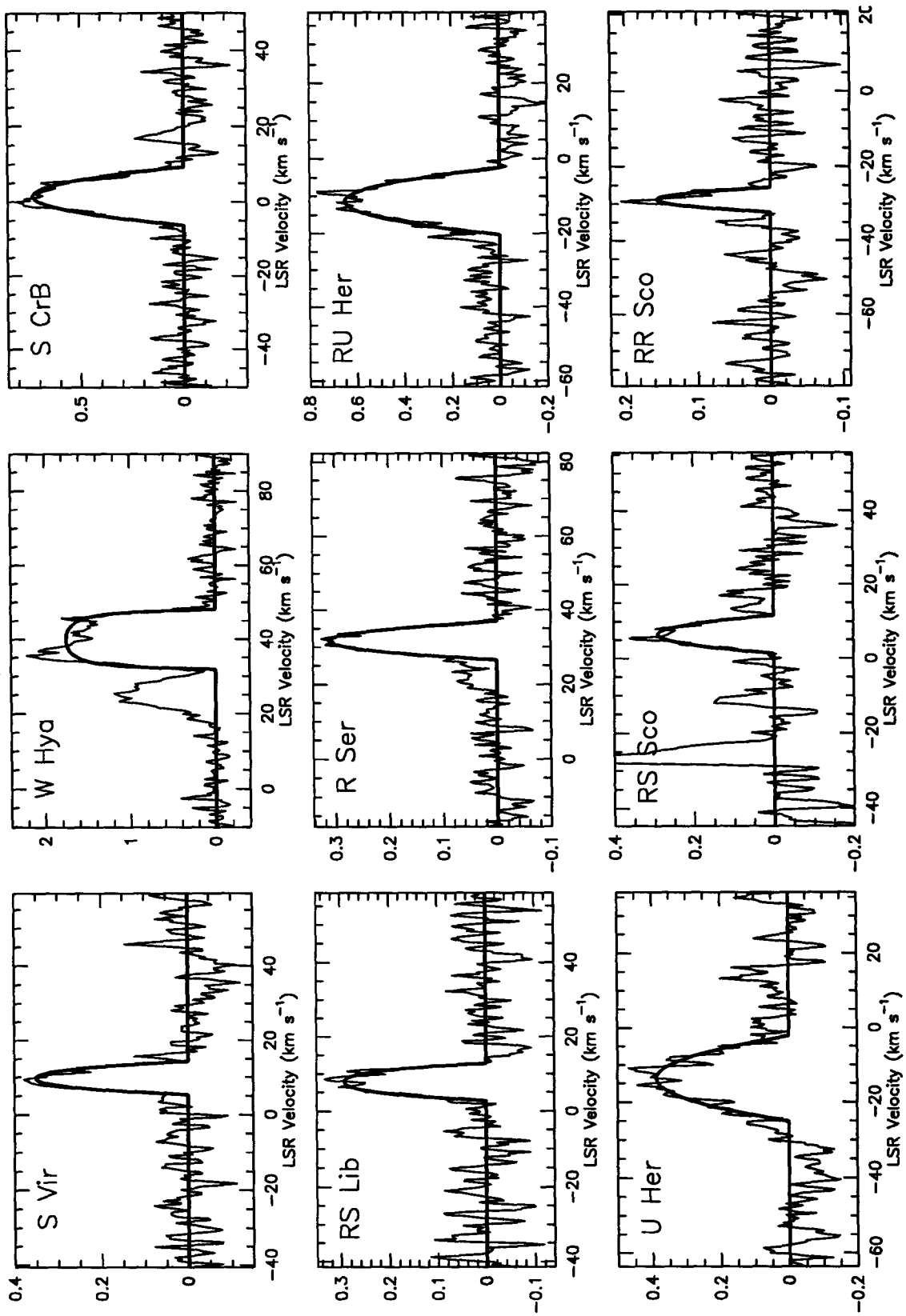
S Vir
W Hya
S CrB
RS Lib
R Ser
RU Her
U Her
RS Sco
RR Sco
LSR Velocity (km s^{-1})

Figure 1c

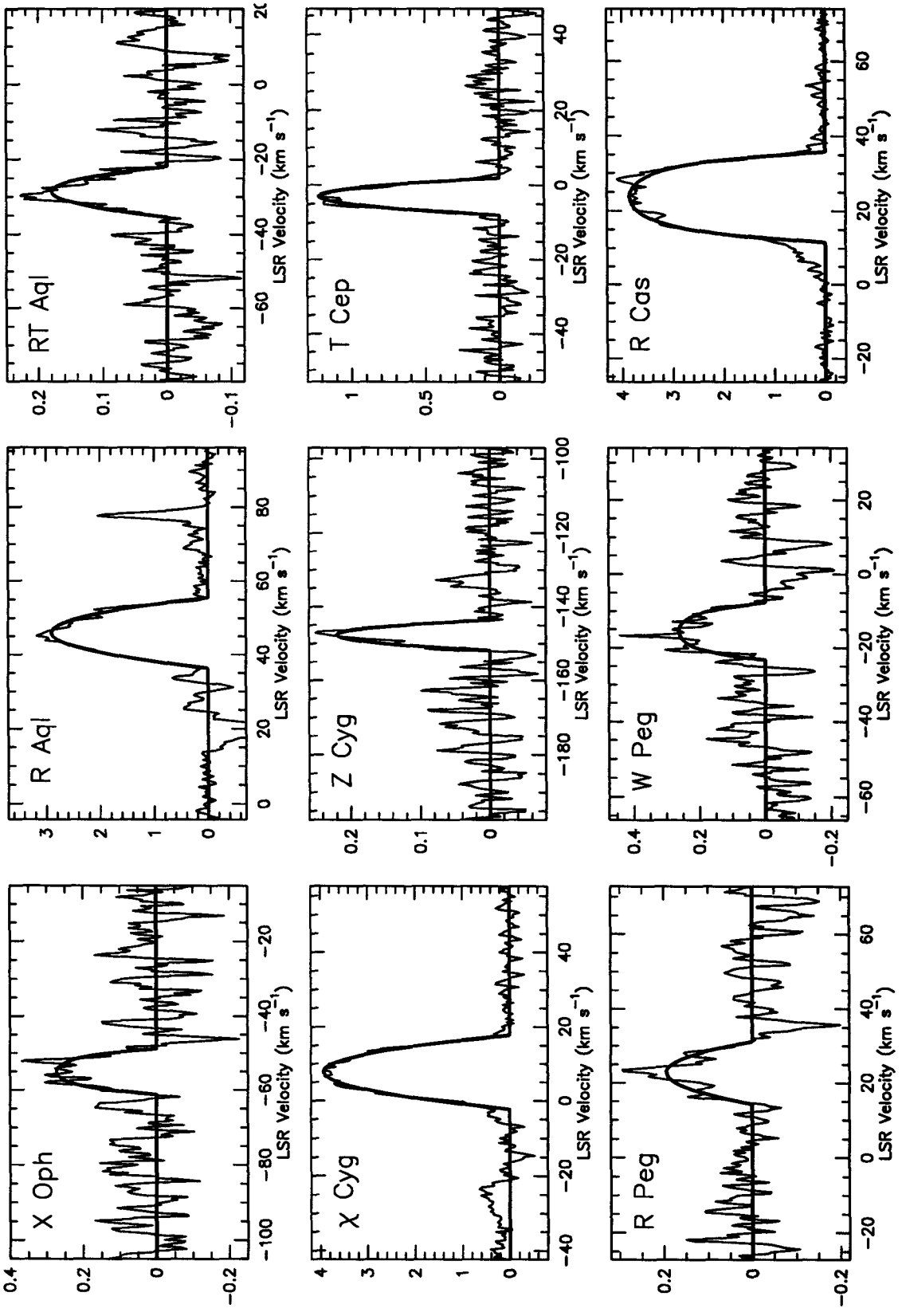
X Oph
R Aql
RT Aql
χ Cyg
Z Cyg
T Cep
R Peg
W Peg
R Cas
LSR Velocity (km s⁻¹)

Figure 1d

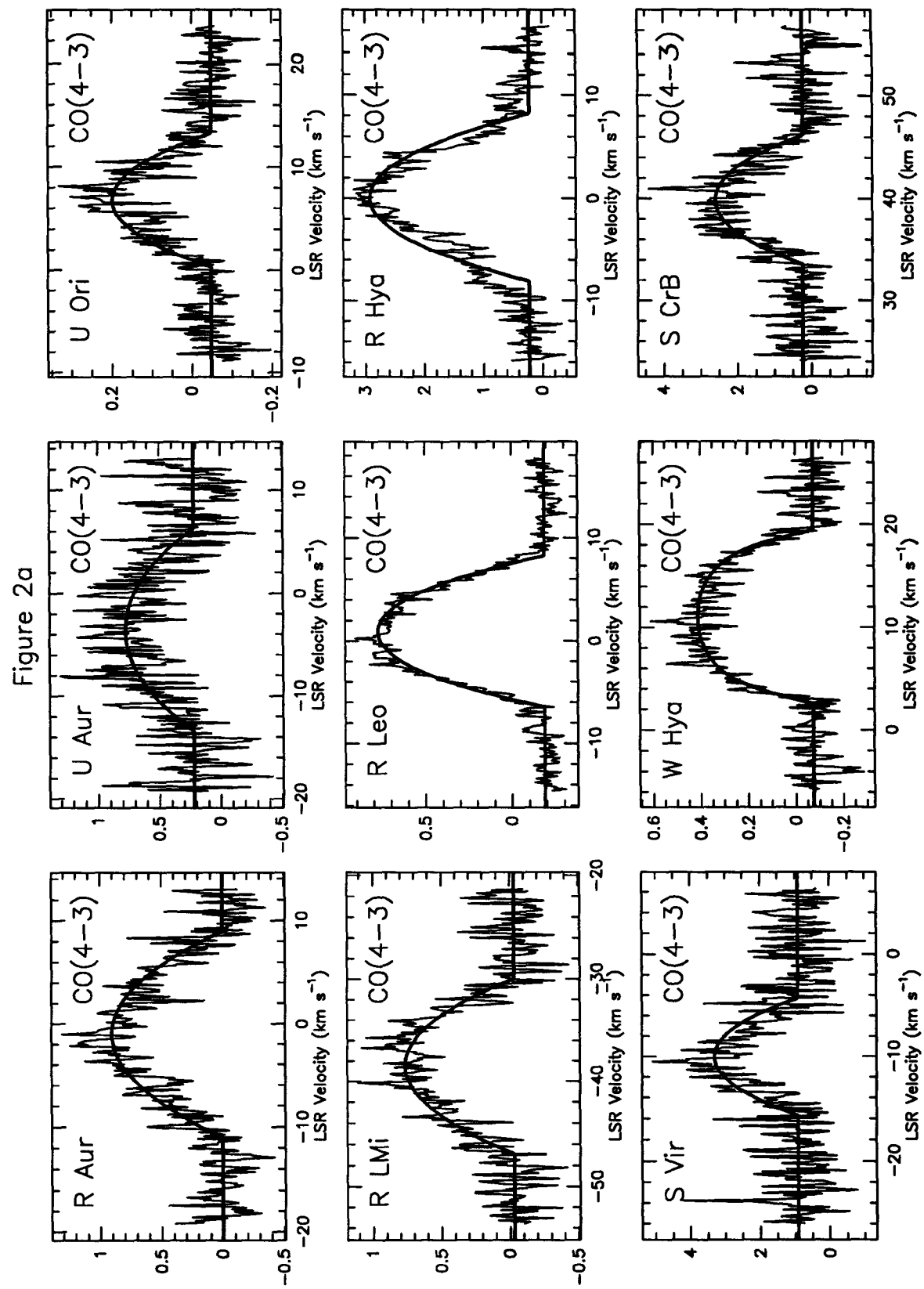
R Aur
CO(4–3)
U Aur
CO(4–3)
U Ori
CO(4–3)
R LMi
CO(4–3)
R Leo
CO(4–3)
R Hya
CO(4–3)
S Vir
CO(4–3)
W Hya
CO(4–3)
S CrB
CO(4–3)
LSR Velocity (km s^{-1})

Figure 2a

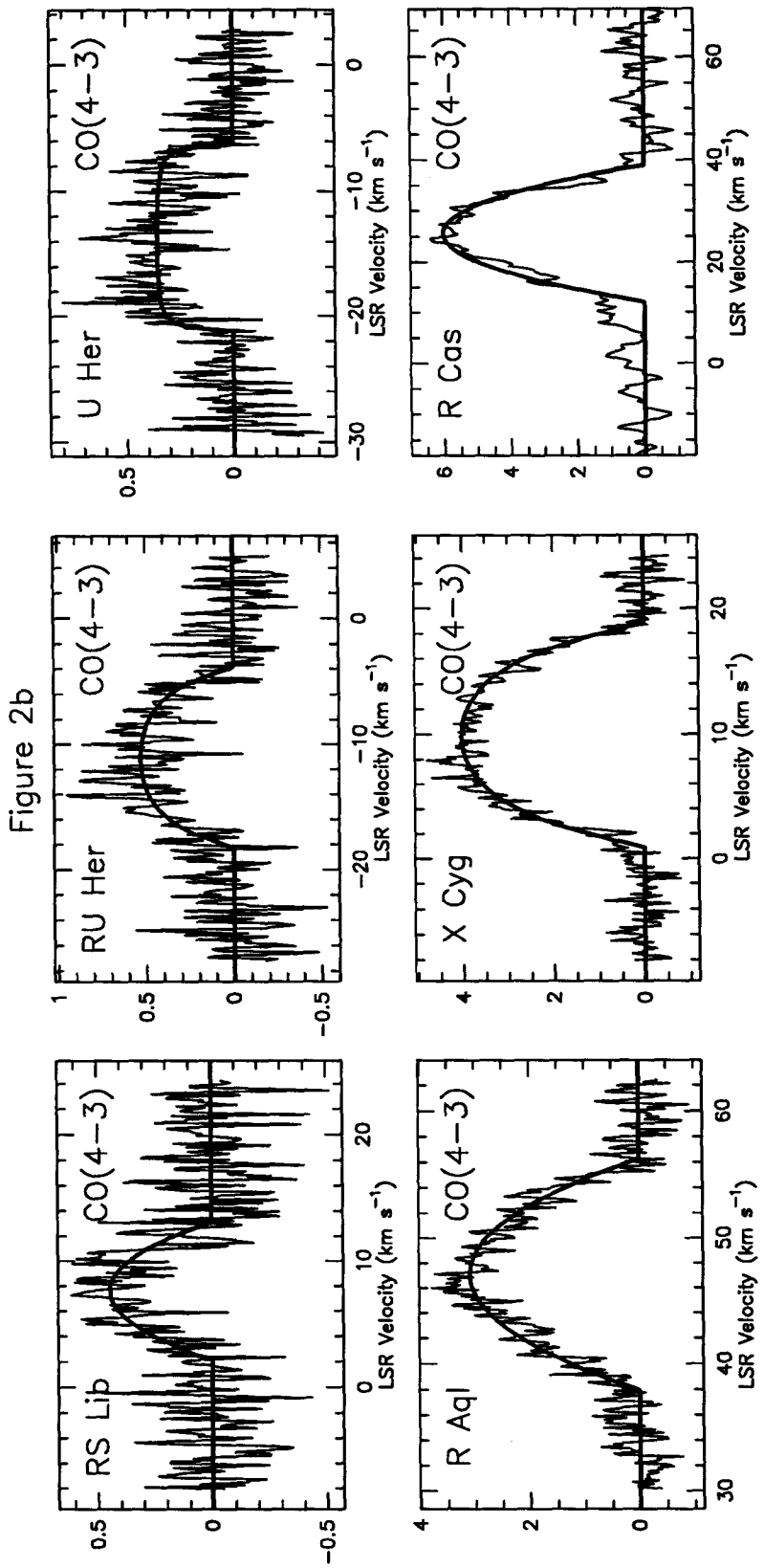
RS Lib
CO(4−3)
RU Her
CO(4−3)
U Her
CO(4−3)
R Aql
CO(4−3)
X Cyg
CO(4−3)
R Cas
CO(4−3)
LSR Velocity (km s⁻¹)

Figure 2b

References

Celis, L. S. 1980, A&A, 89, 145

Celis, L. S. 1981, A&A, 99, 58

David, P. & Papoular, R. 1992, A&A, 265, 195

Draine, B. T. 1987, unpublished supplement to Draine & Lee (1984)

Draine, B. T. & Lee, H. M. 1984, ApJ, 285, 89

Eggen, O. J. 1992, AJ, 104, 275

Ellison, B. N., & Miller, R. E. 1987, Int'l J. IR & MM Waves, Vol. 8, No. 6, 609

Feast, M. W., Glass, I. S., Whitelock, P. A., & Catchpole, R. M. 1989, MNRAS, 241, 375

Fusi-Pecci, F. & Renzini, A. 1975, A&A, 39, 413

Gatewood, G. 1992, PASP, 104, 23

Goldreich, P., & Scoville, N. 1976, ApJ, 205, 144

Hartmann, L., & MacGregor, K. B. 1980, ApJ, 242, 260

Jura, M & Kleinmann, S.G. 1992, ApJS, 79, 105

Kastner, J. H., Zuckerman, B., Dyck, H. M., & Sopka, R. J. 1989, From Miras to Planetary Nebulae: Which Path for Stellar Evolution?, ed M. O. Mennessier & A. Omont, page 143, Editions Frontières

Keenan, P. C., Garrison, R. F. & Deutsch, A. J. 1974, ApJ Supp. Ser., 28, 271

Knapp, G. R., Phillips, T. G., Leighton, R. B., Lo, K. Y., Wannier, P. G., Wootten, H. A. & Huggins, P. J. 1982, ApJ, 252, 616

Knapp, G. R. & Morris, M. 1985, ApJ, 292, 640

Knapp, G. R. 1986, ApJ 311, 731

Knapp, G. R. & Sutin, B. M. 1989, ApJ, 336, 822

Knapp, G. R. 1993, *in preparation*

Kwan, J., & Hill, F. 1977, ApJ, 215, 781

Kwan, J. & Linke, R. A. 1982, ApJ, 254, 587

Kwok, S. 1975, ApJ, 198, 583

Lucas, R., Bujarrabel, V., Guilloteau, S., Bachiller, R., Baudry, A., Cernicharo, J., Delannoy, J., Forveille, T., Gu/'elin, M & Radford, S. J. E 1992, A&A, 262, 491

Mamon, G. A., Glassgold, A. E., & Huggins, P. J. 1988, ApJ, 328, 797

Morris, M. 1980, ApJ, 236, 823

Morris, M. 1984, Mass Loss from Red Giants, ed M. Morris and B. Zuckerman, page 129, D. Reidel

Netzer, N. & Elitzur, M. 1993 ApJ, 410, 701

Neugebauer, G., & Leighton, R. B. 1969, Two–Micron Sky Survey, (NASA SP-3047) (TMSS)

Neugebauer, G. *et al.* 1984, ApJ (Letters), 278, L1 (PSC)

Nyman, L. A., Booth, R. S., Carlström, U., Habing, H. J., Heske, A., Sahai, R., Stark, R. van der Veen, W. E. C. J., and Winnberg, A. 1992, A&A Supp. Ser., 93, 121

Olofsson, H. 1988, Space Science Reviews, 47, 145

Pijpers, F. P. & Hearn, A. G. 1989, A&A, 209, 198

Price, S. D., & Walker, R. G. 1975, AFGL Infrared Sky Survey, (AFGL-TR-75-0373)

Sahai, R. & Bieging, J. H. 1993, AJ, 105, 595

Schönberg, K. 1988, A&A, 195, 198

Sharov, A. S. 1964, Soviet Astron., 7, No. 5, 689

Stein, J. W. 1991, ApJ 377, 669

van der Veen, W. E. C. J., & Habing, H. J. 1988, A&A, 194, 125

van der Veen, W. E. C. J., & Olofsson, H. 1989, From Miras to Planetary Nebulae: Which Path for Stellar Evolution?, ed M. O. Mennessier & A. Omont, page 143, Editions Frontières

van der Veen, W. E. C. J. 1989, A&A, 210, 127

Walker, C. K., Kooi, J. W., Chan, M., LeDuc, H. G., Schaffer, P. L., Carlstrom, J. E., & Phillips, T. G. 1992, Int'l J. IR & mm Waves, 13 (6), 785

Wannier, P. G. & Sahai, R. 1986, 311, 335

Wickramasinghe, N. C. 1972, NMRAS, 159, 269

Wood, P.R. 1979, ApJ, 227, 220

Zuckerman, B. & Dyck, H. M. 1986a, ApJ, 304, 394

Zuckerman, B. & Dyck, H. M. 1986b, ApJ, 311, 345

Zuckerman, B. & Dyck, H. M. 1989, A&A, 209, 119

Zuckerman, B., Dyck, H. M. & Claussen, M. J. 1986, ApJ, 304, 401

Zuckerman, B. & Dyck, H. M. 1989, A&A, 209, 119

The Multiple Molecular Winds of CRL 2688

K. Young[1], *E. Serabyn*[1], *T.G. Phillips*[1], *G.R. Knapp*[2], *R. Güsten*[3] *and A. Schulz*[3]

[1]California Institute of Technology, Pasadena, CA 91125

[2]Department of Astrophysical Sciences, Princeton University, Princeton, NJ 08544

[3]MPI für Radioastronomie, Auf dem Hügel 69, D-5300 Bonn 1, F.R.G.

ABSTRACT

Three rotational transitions of $^{12}C^{16}O$, two of $^{13}C^{16}O$ and one of $^{1}H^{12}C^{14}N$ were observed toward the protoplanetary nebula CRL 2688. The spectra reveal a previously undetected wing of emission representing an outflow velocity of about 100 km s^{-1}. The mechanical momentum in this wind appears to be too large to be supplied by radiation pressure. Also observed is an absorption feature which is on the blue–shifted side of the spectrum with respect to the systemic velocity. This feature is interpreted as due to the low–velocity wind absorbing radiation from higher velocity gas nearer the star. High resolution spectra of this absorption feature show that its blue edge is very sharp, providing a tight constraint on the turbulent velocity of the low–velocity stellar wind.

Subject headings: stars: mass–loss — stars: evolution — stars: post–asymptotic giant branch (post–AGB) — ISM: individual (CRL 2688)

1. Introduction

CRL 2688, the Egg Nebula, is believed to be a protoplanetary nebula (PPNe) (Rodriguez 1987), nearing the end of the copious mass loss phase which terminates the asymptotic giant branch (AGB) phase of evolution. Most of the mass lost during the AGB stage is ejected at a low

velocity, typically 15 km s^{-1}. This low velocity wind is probably driven by radiation pressure on dust, which can condense in the atmosphere of a cool red giant star (see a review by Olofsson 1988). Optically, CRL 2688 is a highly polarized double–lobed nebula. These optical lobes scatter the light from the central star, and reveal that the star's spectral type is F5 1a, with some anomalous features arising from short carbon–chain molecules (Crampton *et al.* 1975). Between these two optical lobes is a small infrared source with a temperature of 150 K (Ney *et al.* 1975). This infrared source is extended, and its position and orientation suggest that it is a torus of dust surrounding the hidden star. The fact that both of the optical lobes are visible suggests that we must be nearly in the plane of the torus. CRL 618, another probable PPNe, has an even hotter photosphere with a spectral type of B0 (Westbrook *et al.* 1975). These elevated temperatures show that both of these objects have moved off the AGB, and are in the process of uncovering their white dwarf cores. Since it is unlikely that grains can continue to condense in such hot atmospheres, the mechanism by which the final portion of the extended atmosphere is expelled probably differs from the mechanism operating on the AGB. Evidence is accumulating that the material expelled by PPNe is ejected at a much higher velocity than the material lost while the star was on the AGB. H_2 emission at a outflow velocity of 125 km s^{-1} has been detected surrounding CRL 618 (Burton and Geballe 1986), as well as CO emission with a velocity in excess of 190 km s^{-1} (Gammie *et al.* 1989; Cernicharo *et al.* 1990).

Another interesting feature of CRL 2688's molecular spectra is the presence of a deep absorption dip (Smith *et al.* 1990; Kawabe *et al.* 1987). This feature is probably caused by the low velocity wind absorbing radiation from the high velocity material closer to the star. We have obtained high velocity resolution spectra of this absorption feature which show that it has a very steep blue edge which is smeared out in low resolution spectra. The shape of this absorption feature allows the amount of turbulence in the expanding envelope to be calculated. This quantity is an important input parameter to radiative transfer models of CRL 2688 because it determines the local line width of a volume element in the envelope. If this line width is much less than 1 km s^{-1}, infrared pumping of the rotational–vibrational lines is hindered by large optical depths in the infrared lines along the radial direction (Morris and Alcock 1977). The amount of turbulence in the envelope can also constrain models of the innermost regions of the envelope, where the

bipolar morphology probably arises. Morris (1981) proposed that the bipolar morphology of CRL 2688 was the result of an interacting binary system. The orbital motions of a close binary might increase the turbulence in the molecular outflow above the value found in the envelope of an isolated red giant star. Finally, the corotation of the molecular envelope with the central star, which was proposed by Bieging and Nguyen-Quang-Rieu (1988), could affect the shape of this absorption feature.

2. Observations

All observations presented here were made at the Caltech Submillimeter Observatory* (CSO) on Mauna Kea, Hawaii. The ^{12}CO(2–1) line was observed in June 1989 (figures 1A and 3A) with an SIS receiver (Ellison 1987), having a double sideband temperature of about 100 K. Two 1024 channel AOS backends were used, one having a total bandwidth of 500 MHz, and the other having a total bandwidth of 50 MHz. The ^{12}CO(3–2) transition was observed (figures 1B, 2A and 3B) with an SIS receiver (Ellison 1989), having a double sideband temperature of about 200 K. Once again two backends were used; the 500 MHz in May 1989, and the 50 MHz in June 1990. A spectrum of the ^{12}CO(4–3) transition was obtained in October 1990 (figure 1C), using a Schottky diode receiver built by the Max Plank Institute für Radioastronomie (Keen *et al.* 1986) with a double sideband temperature of 1150 K, and the 500 MHz backend. Finally spectra of the ^{13}CO(2–1), ^{13}CO(3–2) and HCN(4–3) transitions were taken in April of 1991 using the same SIS receivers, and the 500 MHz AOS. Table 1 gives the details of these integrations.

The coordinates used for CRL 2688 were $\alpha_{1950} = 21^h00^m20.0^s$, $\delta_{1950} = 36^d29^m44.0^s$ for all the observations except for those of the CO(4–3) transition, where $\alpha_{1950} = 21^h00^m19.7^s$, $\delta_{1950} = 36^d29^m45.0^s$ was used. For the five lower frequency lines, the pointing was checked and adjusted by taking test scans in a 5–point cross centered on the source. For the CO(4–3) spectrum, Mars was used as the pointing reference. Scans where taken while position switching at 0.05 Hz between the source and 2 off-source positions located 3 arc minutes away in azimuth, on either side of the source.

---

* The CSO is operated by the California Institute of Technology under funding from the National Science Foundation, Contract #AST–9015755.

Table 1.

Figure	Transition	Freq. (GHz)	Res. (arc sec)	Main Beam Eff.	Velocity Res. ($km\,s^{-1}$)	T_{sys} SSB (K)	Integration Time (min.)	rms noise (mK)
1A	$^{12}CO(2-1)$	230.538	32	0.72	1.3	520	26	20
1B	$^{12}CO(3-2)$	345.796	21	0.60	0.85	570	22	19
1C	$^{12}CO(4-3)$	461.041	15	0.50	0.64	9000	16	260
1D	$^{13}CO(2-1)$	220.399	33	0.72	1.3	755	25	15
1E	$^{13}CO(3-2)$	330.588	22	0.60	0.89	1800	28	26
1F	HCN(4–3)	354.505 *	20	0.60	0.83	1400	19	45
3A	$^{12}CO(2-1)$	230.538	32	0.72	0.20	440	33	53
3B	$^{12}CO(3-2)$	345.796	21	0.60	0.13	430	23	62

* The frequency given is the strength weighted average of the six hyperfine levels which make up the HCN(4–3) transition. The frequencies of the individual levels are given in the table below. They were calculated using spectral constants measured by DeLucia and Gordy (1969).

Hyperfine Levels of the HCN(4–3) Sextet

Transition	Frequency (GHz)	Relative Strength	Velocity Shift ($km\,s^{-1}$)
$F = 5 \rightarrow 4$	354.505518	0.4074	0.039
$F = 4 \rightarrow 4$	354.503861	0.0208	-1.364
$F = 4 \rightarrow 3$	354.505472	0.3125	0.000
$F = 3 \rightarrow 4$	354.505837	0.0003	0.309
$F = 3 \rightarrow 3$	354.507449	0.0208	1.673
$F = 3 \rightarrow 2$	354.505361	0.2381	-0.094

When viewed on an expanded temperature scale, the CO(3–2) spectrum shows a low intensity feature between LSR velocities –160 and 40 $km\,s^{-1}$ (figure 2A). A broad, weak feature like this might arise from instrumental imperfections, so the 18 scans making up this spectrum were interleaved with scans taken 20 arc minutes away from the source. The combined off-source scans (figure 2B) show that the AOS baseline was flat over the region in question at the time of the observations. Even though the off-source scans were flat, the high velocity wings in the on-source scans could still be spurious, if an instrumental defect existed which produced broad wings around any strong line. To eliminate this possibility, a CO(3–2) profile of CIT 6, with signal–to–noise comparable to figure 1B, was obtained. No broad wings appeared in the

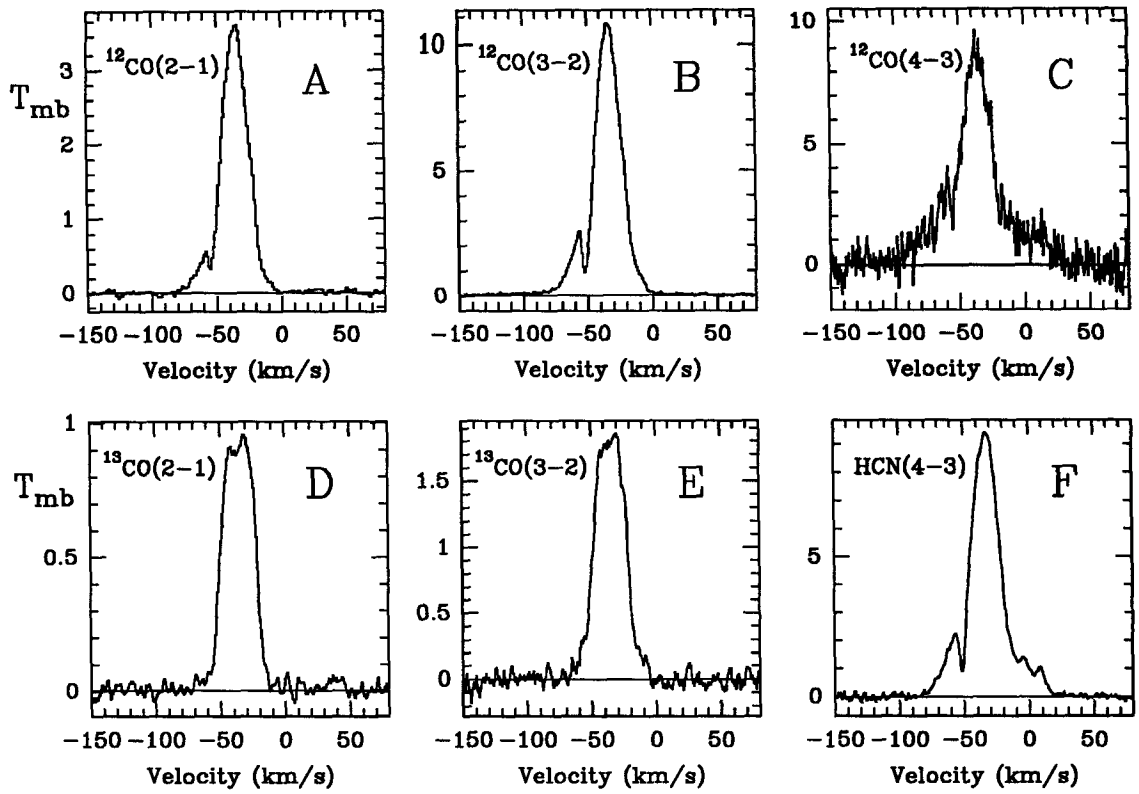

Fig. 1. Spectra for five molecular transitions of CO and one of HCN. The wide wing can be seen in the ^{12}CO(4–3) and ^{12}CO(3–2) spectra. In figure 2 it is shown with an expanded temperature scale. The self–absorption feature, at –55 km s^{-1} is visible in all three ^{12}CO spectra, but neither ^{13}CO spectrum. Figure 3 shows this feature with higher spectral resolution.

CIT 6 spectrum. It is therefore very unlikely that the broad wings shown in figure 2A arose from an instrumental defect.

The spectra were calibrated by placing an absorber at a temperature of 280 K into the telescope's beam. Linear baselines were fitted to the regions of the 500 MHz spectra judged free of emission, and subtracted from the data. No baselines were removed from the 50 MHz spectra, because there was no region free of emission. Finally the spectra were corrected for the coupling of the receiver to the telescope by dividing them by the telescope's main beam efficiency, which was determined from planetary measurements. All temperatures presented here are therefore on the main beam brightness scale (T_{mb}).

3. Analysis

The ^{12}CO(3–2) spectrum (figures 1B and 2A) has the highest signal-to-noise of the three transitions observed. In it can be seen three velocity components. The first, a low velocity wind (LVW), has a very nearly parabolic profile characteristic of unresolved, optically thick emission. It is centered at –33.3 km s^{-1}, and the outflow velocity is 18.0 km s^{-1}. The peak main beam temperatures for the ^{12}CO(3–2) and ^{12}CO(4–3) transitions, 10.8 and 9.1 K respectively, are similar. However the ^{12}CO(2-1) peak temperature is only 3.4 K. These values suggest that the region where the LVW feature arises is resolved by the ^{12}CO(3–2) and ^{12}CO(4–3) beams, but not by the ^{12}CO(2–1) beam. The profiles of the LVW in both the ^{13}CO(2-1) and ^{13}CO(3-2) spectra are flat topped, indicating that the envelope is optically thin in these transitions (Morris 1980). Comparison of the temperatures of the main and isotopically substituted lines at the systemic velocity allows the optical depth of the LVW to be calculated. Assuming a ^{12}CO/^{13}CO ratio of 20 (Wannier and Sahai 1987; Sopka *et al.* 1989), the optical depth of the LVW is 4.0 in ^{12}CO(3–2) and 6.6 in ^{12}CO(2–1).

The second component, a moderate velocity wind (MVW), cuts off at a velocity of – 73 km s^{-1} on the blue edge of the ^{12}CO(3–2) transition, giving an outflow velocity of $\sim$ 40 km s^{-1}. The red wing of the MVW is weaker than the blue wing in all transitions, and falls to zero intensity at –2 km s^{-1} in the ^{12}CO(3–2) spectrum. The blue wing of the HCN(4–3) profile's MVW resembles that of ^{12}CO(3–2) very closely, while its red wing, which shows two small peaks not seen in any of the CO spectra, extends to 20 km s^{-1}, and resembles the red wing seen in the CO(4–3) profile. Although the HCN(4–3) transition has six components due to hyperfine structure, the frequency difference between the highest and lowest frequency components corresponds to a velocity difference of only 3 km s^{-1}. Therefore the hyperfine structure cannot be responsible for much of the 100 km s^{-1} width of the HCN profile. The "peak" main beam temperature of the MVW feature, measured at – 57 km s^{-1} (just to the left of the self–absorption dip), is 0.6, 2.6 and 3.6 for the ^{12}CO(2–1), ^{12}CO(3–2) and ^{12}CO(4–3) transitions. The ratios of the peak MVW temperature to that of the LVW are 0.16, 0.24 and 0.40 for the three transitions. This increase in the relative strength of the MVW as the telescope's beam shrinks indicates that the MVW arises from a smaller region than the LVW, and is

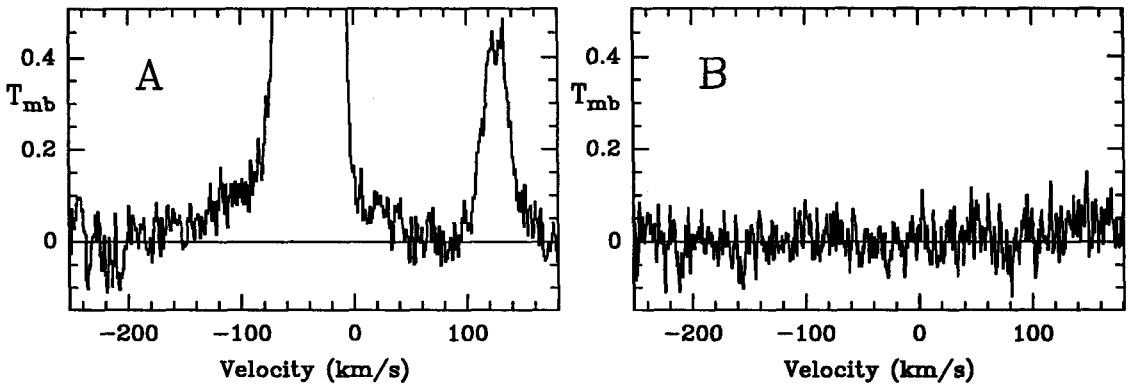

Fig. 2. (A) – Weak high velocity emission in the $^{12}CO(3–2)$ spectrum from figure 1B is shown with an expanded vertical scale. The high velocity emission extends from about −160 to 50 km s^{-1}. The line at 125 km s^{-1} is $HC_3N(38–37)$. (B) – Sum of 16 scans taken at a position 20 arc minutes away from the source, in order to check the baseline stability. These scans were interleaved in time with the on-source scans which were summed to produce plot A.

probably not resolved by either the $^{12}CO(2–1)$ or $^{12}CO(3–2)$ beams. The MVW is clearly visible in the $^{13}CO(3–2)$ spectrum, and its blue wing is marginally detected in the $^{13}CO(2–1)$ spectrum. The MVW's $^{13}CO(3–2)$ profile appears to cover a smaller velocity range than its $^{12}CO(3–2)$ profile, suggesting that the optical depth of both transitions decreases as the velocity extrema are approached. Comparison of the main beam temperatures of ^{12}CO and ^{13}CO at – 57 km s^{-1} yields a maximum MVW optical depth of 2.1 for $^{12}CO(2–1)$ and 2.3 for $^{12}CO(3–2)$, once again using $^{12}CO/^{13}CO = 20$.

Finally, on an expanded scale, figure 2A shows a third component, a high velocity wind (HVW) in the $^{12}CO(3–2)$ profile. The HVW extends over a velocity range of -160 ± 20 to 40 ± 10 km s^{-1}, which implies the outflow velocity of this material is 100 ± 10 km s^{-1}. The shape of the HVW profile is triangular, as is that of the HVW surrounding CRL 618 (Gammie *et al.* 1989; Cernicharo *et al.* 1990), suggesting that the same acceleration mechanism may be at work in both cases. This shape is not apt to arise from a spherical envelope of gas expanding at a constant velocity (cf Morris *et al.* 1985).

The $^{12}CO(2–1)$ spectrum shows the LVW and MVW clearly, but not the HVW. The $^{12}CO(4–3)$ and HCN(4–3) spectra show emission with a total extent intermediate between the extents of the MVW and the HVW, with an outflow velocity of at least 60 km s^{-1}.

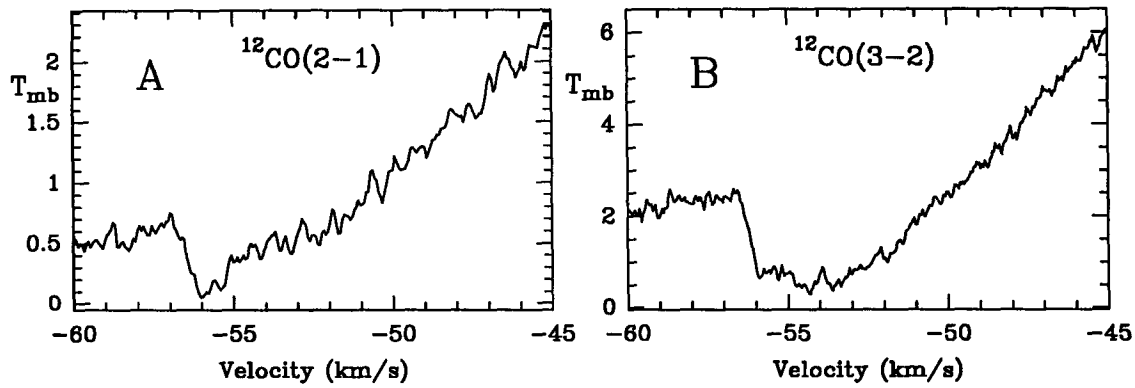

Fig. 3. (A) The self–absorption dip in the ^{12}CO(2–1) transition. (B) The self–absorption dip in the ^{12}CO(3–2) transition. The blue edge of this feature has a width of only 0.5 km s^{-1}.

Figure 3 shows CRL 2688's absorption feature, with the increased velocity resolution provided by the 50 MHz AOS. The depth of the absorption feature in the ^{12}CO(2–1) transition (figure 3A) is much greater than it appears in the low resolution spectrum (figure 1A), and at a velocity of –56.0 km s^{-1} T_{mb} drops nearly to 0. Both the ^{12}CO(2–1) and ^{12}CO(3–2) absorption features (the latter shown in figure 3B) have very steep blue edges. The edge of the ^{12}CO(3–2) feature is only 0.5 km s^{-1} wide. The frequency resolution of the 50 MHz AOS was measured by examining a calibration oscillator, which produced a peak with a full width at half maximum corresponding to 0.13 km s^{-1} at the frequency of ^{12}CO(3–2).

4. A Model for the Absorption Feature

The absorption feature probably arises when radiation from the MVW is absorbed by the LVW, since it lies at the cut off velocity of the LVW's profile. The absorbing LVW gas must be situated between the observer and the MVW, since absorption is only seen on the blue - shifted side of the line. A simple model that could give rise to this feature is shown in figure 4(i). In this model the MVW and LVW arise in separate, concentric spherical regions.

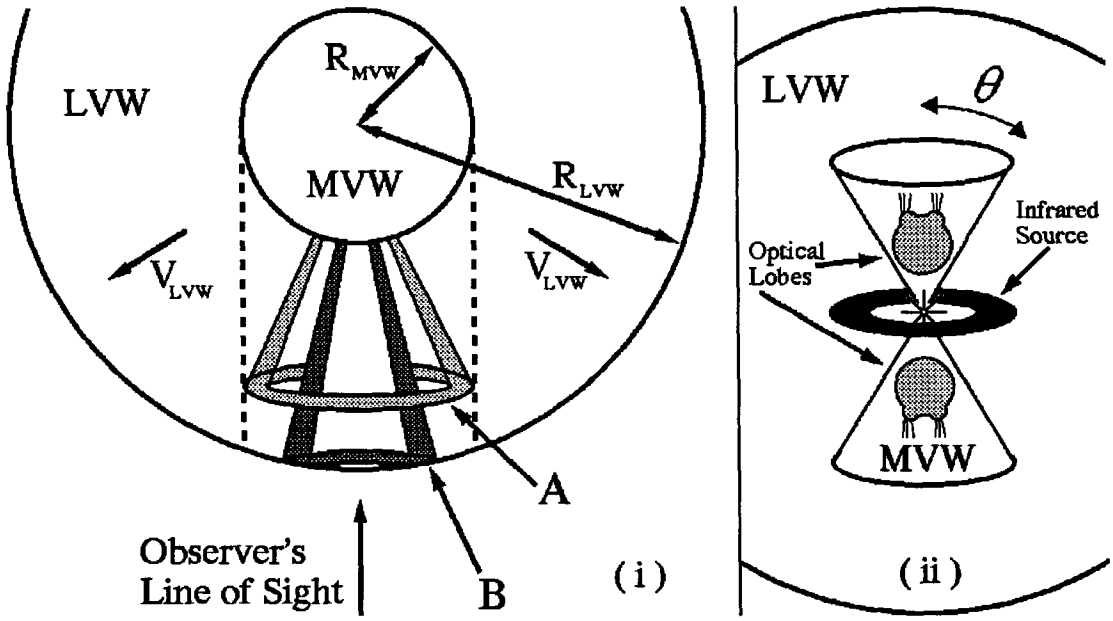

Fig. 4. **(i)** – The model for the absorption feature is shown. Broad line emission from the MVW region is absorbed by the surrounding LVW region. The LVW is assumed to be expanding at a constant velocity, so all material within a cone with axis of symmetry along the observer's line of sight has the same radial velocity. Cone **A** is an example of a cone containing material with a radial velocity less than V_c (see equation 1). Cones of this type are truncated by a cylinder of radius R_{MVW}. Material in cone **B** has a radial velocity greater than V_c. Such cones are truncated when they reach the edge of the LVW envelope. **(ii)** – Here an alternative geometry is shown, with the MVW gas occupying two conical regions, rather than a complete sphere as in (i). The conic axes are assumed to coincide with the axis defined by the optical nebula. θ measures the opening angle of the cones, relative to this axis. Figure (i) corresponds to the case $\theta = 90°$. If the observer is located in the equatorial plane of the object, then dm(v)/dv has the form of equations 2a–c, regardless of the value of θ.

The material in the inner MVW region emits radiation which can be absorbed by the outer LVW envelope. If the thermal and turbulent velocities are small when compared to V_{LVW}, then all the material within a truncated cone, such as either of the ones shown in figure 4(i), will have the same radial velocity. If the MVW region is unresolved by the telescope, then all the material within the cone contributes to the absorption seen at the central position. Let v be the radial velocity offset from CRL 2688's LSR velocity. If the partition of CO among the low J states is the same at all positions where LVW gas is present, the depth of the absorption feature at a given velocity v will be determined by the mass present within the cone with that radial velocity. The absorbing cones fall into two categories. Cones with small |v| (e.g., cone A in figure 4(i))

all have a base radius equal to the radius of the MVW region (R_{MVW}). Cones with $|v| \approx V_{LVW}$ (e.g., cone B) will have smaller base radii, because they will be truncated at the outer radius of the LVW (R_{LVW}). The value of v at which the transition between these two regimes occurs is

$$V_c = V_{LVW}\sqrt{1 - \left(\frac{R_{MVW}}{R_{LVW}}\right)^2} \; . \qquad (1)$$

Let us assume that during the period when the LVW was formed, CRL 2688 was expelling material at a constant rate. The density of CO will then fall off as $1/r^2$. If the outer radius of the MVW is also the inner radius of the LVW, and if ρ_0 is the density of CO at that radius, then $\rho_0 R_{MVW}^2/r^2$ is the density at radius r within the LVW region. All radiation in a velocity interval of width dv centered at v will be absorbed by material of mass dm(v) given by

$$\frac{dm(v)}{dv} = 0 \qquad \text{for} \quad 0 < v \quad \text{and for} \quad v < -V_{LVW} \qquad (2a)$$

$$\frac{dm(v)}{dv} = \frac{2\pi\rho_0 R_{MVW}^3}{V_{LVW}} \left(\frac{1}{\sqrt{1 - \left(\frac{v}{V_{LVW}}\right)^2}} - 1 \right) \qquad \text{for} \quad -V_c \le v \le 0 \qquad (2b)$$

$$\frac{dm(v)}{dv} = \frac{2\pi\rho_0 R_{MVW}^2 (R_{LVW} - R_{MVW})}{V_{LVW}} \qquad \text{for} \quad -V_{LVW} \le v < -V_c \; . \qquad (2c)$$

Equation 2c is constant for all values of v. Because of this the absorption feature has a width comparable to the velocity range over which equation 2c holds. This range of velocities is itself determined by V_c, which is a function of R_{MVW}/R_{LVW}. Therefore the width of the absorption feature allows the relative sizes of the MVW and LVW regions to be determined, even if neither one can be resolved by the telescope.

In order to compare this model with the observations in figure 3B, a model of the emission being absorbed is needed. The profile of the emission from the MVW will be approximated by

a gaussian function centered at the systemic velocity, V_{LSR}. For simplicity, all velocity structure within the MVW will be ignored. The profile of the LVW emission will be assumed to be parabolic. If line(v) is a function giving the profile of the line in the absence of absorption, and if we ignore re-emission of the absorbed radiation, the profile with absorption is given by

$$\text{profile(v)} = \text{line(v)} \exp\left(C\frac{\text{dm(v)}}{\text{dv}}\right)$$

where C is a constant.

There is a discontinuity in the equations above for dm(v)/dv at $v = V_{LVW}$. This is the blue edge of the absorption feature. Figure 3B shows that the blue edge is very sharp, but not discontinuous. The total width of the blue edge is 0.5 km s^{-1}. This finite width is caused by a combination of instrumental resolution, thermal broadening and turbulent motion within the LVW.

Figure 5 shows the absorption model given in equations 2a through 2c compared with the 50 MHz AOS data for the ^{12}CO(3–2) line. In order to produce a blue edge with a finite width, the analytic expressions for dm(v)/dv were convolved with a gaussian function. The model parameters were fitted in a least-squares sense, using Powell's direction set method of minimization (Press *et al.* 1988). Table 2 lists the parameters and their best fit values. The rms difference between the model and data is 0.18 K.

Table 2.

Parameter Number	Description	Best Fit Value
1	Maximum Optical Depth of Absorption Line	1.7
2	R_{MVW}/R_{LVW}	0.52
3	V_{LVW}	22.8 km s^{-1}
4	Peak T_{mb} from LVW Emission	4.9 K
5	Full Width at Half Maximum of MVW Profile	44.0 km s^{-1}
6	Peak T_{mb} from MVW Emission	5.3 K
7	V_{LSR} of CRL 2688	−33.3 km s^{-1}
8	Full Width at Half Maximum of Convolved Gaussian	0.58 km s^{-1}

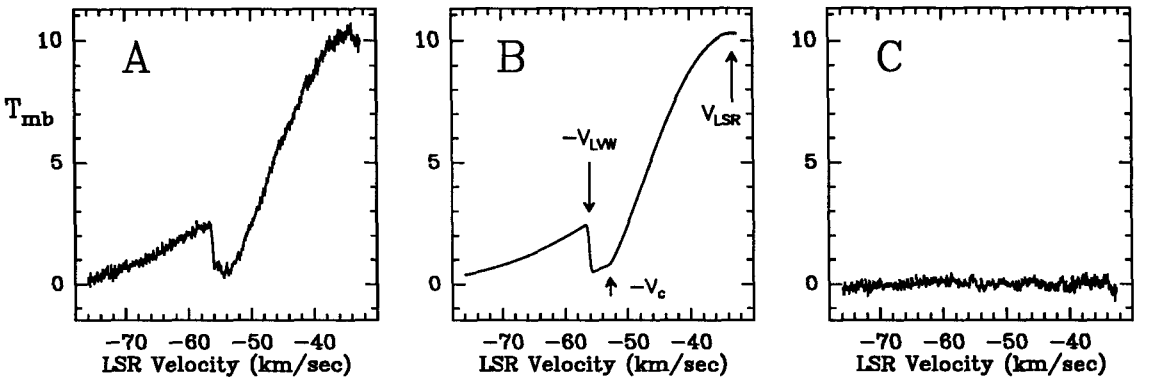

Fig. 5. (A) – The full 50 MHz ^{12}CO(3–2) spectrum. (B) – The model spectrum using the best fit parameters. (C) – The residuals: A – B.

Taking the frequency resolution of the 50 MHz AOS into account, the gaussian broadening of the best fit model is 0.56 km s^{-1}. If all of this broadening were due to the LVW's thermal velocity, the implied temperature would be 190 K. Since CRL 2688's central infrared source has a temperature of only 150 K (Ney *et al.* 1975), it is very unlikely that the gas temperature could be so high. Truong-Bach *et al.* (1990) obtained a value of $\sim$ 15 K for the temperature of the outer envelope by solving the radiative transfer problem using the large velocity gradient approximation. If the temperature of the LVW region is $\sim$ 15 K, then most of the broadening must be due to large scale turbulent motion.

5. Discussion

(a) The High Velocity Wind

The fast wind in CRL 618 seen in the ^{12}CO(3–2) transition (Gammie *et al.* 1989) has a velocity of $\sim$ 190 km s^{-1}, about twice the value of the HVW from CRL 2688. The map of the HVW from CRL 618 made by Cernicharo *et al.* shows that the HVW is bipolar, and slightly tilted along the line of sight. If the HVW surrounding CRL 2688 is also bipolar, then some of the difference between the expansion velocities may be due to differing angles of inclination of the outflows with respect to our line of sight. The optical nebulosities of both these objects have a bipolar morphology. If the bipolar axes of the optical nebulae and HVWs agree, then the deprojected velocities of the HVWs can be calculated. An emission line study of the CRL 618

nebula gave an inclination of 45° (Carsenty and Solf 1982). Monte Carlo simulations of scattering by dust in the reflection nebula centered on CRL 2688 (Yusef-Zadeh 1984) yielded an inclination angle of 16° for the equatorial plane. Using these inclinations, the deprojected outflow velocities are 270 km s^{-1} for CRL 618, and 360 km s^{-1} for CRL 2688.

The CO(3–2) spectrum of CRL 618 (Gammie *et al.* 1989) shows a narrow self–absorption dip at the blue–shifted edge of that object's LVW feature, as do the CO(2–1), HCO^+(3–2), and HC_3N(25–24) spectra of Cernicharo *et al.* (1990). These absorption features may arise from the LVW material absorbing radiation from CRL 618's HVW. However the very deep absorption feature seen in the Cernicharo *et al.* HCO^+(1–0) profile passes below $T_{mb} = 0$, and must arise from absorption by the LVW of CRL 618's underlying continuum emission. Absorption of the continuum could also be responsible for the weaker absorption dips seen in the other molecular transitions. One might expect to see a similar absorption dip at the blue edge of the MVW feature in CRL 2688's CO(3–2) profile. No such feature is seen (see figure 2A). The lack of such a feature could indicate that the MVW is not situated between the observer and the HVW. A more likely explanation is that the optical depth of the MVW feature at its velocity extrema is too low to produce self–absorption. The latter interpretation is supported by the MVW's optically thin ^{13}CO(3–2) profile, which extends over a smaller velocity range than does the optically thicker ^{12}CO(3–2) profile (see figures 1B and 1E).

The CRL 2688 HVW is considerably less conspicuous than that of CRL 618. In the spectra of Gammie *et al.* (1989), the ratio of the peak main beam temperature of the CRL 618 HVW to that of its LVW is 0.127, while the ratio for CRL 2688 is 0.018. CRL 618 has already developed an HII region (Kwok and Bignell 1984), but CRL 2688 has not (Spergel *et al.* 1983). CRL 618's photosphere (spectral type B0) is hotter than that of CRL 2688 (spectral type F5). These facts all suggest that CRL 2688 left the AGB more recently than CRL 618.

Gammie *et al.* (1989) used the Large Velocity Gradient (LVG) model of Morris (1980) to estimate the mass and size of the HVW from CRL 618 . The model assumes spherical symmetry and that both the mass loss rate and outflow velocity are constant. The data presented here showing the HVW from CRL 2688 were modeled using the same LVG code. Table 3 shows the best–fit parameters for both stars. The shape of the HVW profiles, and the relative strengths

of the $^{12}CO(3–2)$ and $^{12}CO(2–1)$ transitions, suggest that in both cases the HVW is unresolved by the CSO's $^{12}CO(3\text{-}2)$ beam, and therefore have $r \leq 10''$. However the estimates of the radii presented in Table 3 are very poorly constrained.

Table 3.

Object	Distance (pc)	R_{HVW} (10^{15} cm)	V_{HVW} ($km\,s^{-1}$)	M ($M_\odot$)	$\dot{M}$ ($10^{-4}M_\odot$/yr)	$\dot{M}V_{HVW}$ (10^{29} gm cm / sec^2)
CRL 618	1300	100	200	0.1	7	9
CRL 2688	1000	5	100	0.016	10	6

Knapp *et al.* (1982) showed that radiation pressure was adequate to explain the mass loss rates observed in most evolved stars. If a stellar wind is driven by radiation pressure, then the rate of momentum transfer to the wind must be less than or equal to the momentum of the star's radiation

$$\dot{M}V \leq L_*/c\ .$$

For the PPNes CRL 618 and CRL 2688, the momentum in the LVW appears to exceed the momentum available in the radiation field by a factor of 7 (Knapp *et al.* 1982; Knapp 1986). This might be due to a decrease in the brightness of the central star as it leaves the AGB. However the values of $\dot{M}V_{HVW}$ in Table 3 exceed the value available from radiation pressure by a factor of about 100, even assuming the central stars have the theoretical maximum luminosity for an AGB star, $5 \times 10^4 L_\odot$ (Iben and Renzini 1983). Therefore it seems unlikely that radiation pressure drives the HVW.

Cernicharo *et al.* (1990) suggest two possible mechanisms for the acceleration of the HVW from CRL 618. One, originally proposed by Morris (1987), is for acceleration to occur via an interaction with a small orbiting companion star. The second method proposed is that the shock front from the PPNe's small HII region accelerates and dissociates the dense material in the LVW. This material then recombines to form molecules, traveling at a high velocity. However the absence of an HII region associated with CRL 2688 shows that the HVW can form in the absence

of a high speed ionized wind. There is currently no clearly favored mechanism for producing the HVW.

(b) The Absorption Dip at –55 km s^{-1} and the MVW Feature

The absorption model gives a value of 0.52 for the ratio of the radius of the MVW region to that of the LVW. Truong-Bach *et al.* (1990) calculated that the CO envelope would be truncated by photodissociation at a radius of 3×10^{17} cm. Using this value as R_{LVW} gives $R_{MVW} = 1.5 \times 10^{17}$ cm. Assuming a distance of 1 kpc (Ney *et al.* 1975), the angular diameter of the MVW would be 20". Truong-Bach *et al.* argue that published detections and non-detections of this feature from a variety of telescopes suggest that the MVW region cannot have a diameter of more than 15". However one of the observations used by these authors to constrain the size of the MVW region was the non-detection of the absorption dip in the ^{12}CO(2–1) spectrum obtained by Heiligman *et al.* (1986). Truong-Bach *et al.* suggest that this non-detection was caused by the large beam of the NRAO 12m telescope. The ^{12}CO(2–1) profiles presented here, taken with a 10.4m telescope and a correspondingly bigger beam, clearly show the absorption feature, implying the feature is masked by noise in the Heiligman *et al.* spectrum.

The Morris LVG code was used to calculate the mass loss rates for both the MVW and the LVW. It showed that it is not possible to match the observed intensities of the LVW component if all the LVW gas is located further than R_{MVW} from the star. If the LVW gas is confined within $R_{LVW} = 3 \times 10^{17}$ cm and the MVW is confined within $R_{MVW} = 1.5 \times 10^{17}$ cm, then the LVG model which best reproduces the observed line profiles has a total mass loss rate of $1.5 \times 10^{-4} M_{\odot}$/yr. This agrees well with the value of $1.7 \times 10^{-4} M_{\odot}$/yr found by Truong-Bach *et al.* (1990). To produce the MVW profile, half of the gas within R_{MVW} must have the MVW velocity. The total mass in the MVW is $0.1 M_{\odot}$, and that of the LVW is $0.7 M_{\odot}$. Additional evidence that some of the LVW gas must be located inside R_{MVW} is provided by a comparison of the ^{12}CO(3–2) and ^{13}CO(3–2) profiles, which yields an optical depth for the main line of 4.0, while the best-fit model results presented in table 2 give a maximum optical depth in the absorption feature of only 1.7. Therefore the model shown in figure 4(i) is at best only an approximation to the true source geometry. If the MVW region is optically thick, two other source geometries would give rise to

an absorption feature with an identical shape. The first alternative is that the MVW could arise in a hollow spherical shell, with LVW gas both inside and outside the shell. The second possibility is that the MVW is confined to two conical regions oriented along a symmetry axis perpendicular to our line of sight, as is shown in Figure 4(ii). The morphology of the optical reflection nebula shows that the bipolar outflow does have this orientation. The hollow shell geometry seems less likely, because the HCN(4–3) transition clearly shows the MVW, with the same relative intensity as it is seen in CO(3–2). Since HCN traces high density gas, some of the MVW gas is probably located very near the star.

The presence of two of the velocity components, the LVW and the MVW, could be explained by the binary model proposed by Morris (1987). In this model an accretion disk surrounds both stars. The LVW was expelled from the former red giant star, and the higher velocity material was expelled from the vicinity of the companion star. However the shape of the blue edge of the absorption feature at –55 km s^{-1} tells us that the LVW has a well ordered velocity field, with no turbulent motions in excess of $\sim$ 0.5 km s^{-1}. If CRL 2688 is an interacting binary system, it is likely that velocity variations comparable to the orbital velocity of the red giant star would be introduced to the LVW. For an interacting binary, such as envisioned by Morris (1981), velocity variations of at least a few km s^{-1} would be expected in the inner portion of expanding envelope. If the binary ejection model is correct, these variations must have been damped out as the LVW envelope expanded, presumably via collisions. It would be useful to observe the absorption feature in spectral lines arising from material at a higher temperature and/or density than is required to produce CO(3–2) emission. Such observations would probe more deeply into the envelope, and might reveal a more turbulent inner region.

Bieging and Nguyen–Quang-Rieu (1988) observed the HCN(1–0) transition with the Hat Creek interferometer. They produced a map of the velocity field of CRL 2688's inner region. The velocity field is dominated by a velocity gradient of 5 km s^{-1} aligned with the bipolar axis. In addition, they report a velocity gradient of 2.4 km s^{-1} along the orthogonal axis. The authors argue that this velocity gradient arises from the rotation of an expanding torus. The derived rotational speed is 1.2 km s^{-1}, at a radius of 5.6 $\times$ 10^{16} cm. If this material conserves angular momentum as it expands, then the velocity gradient across the entire torus should be 0.9 km s^{-1}

when the material passes through R_{MVW}. However if the model presented here for the formation of the absorption feature is correct, the LVW material absorbing radiation near the blue edge of the feature is located just outside of R_{MVW}. Therefore the rotation of the torus should produce a broader blue edge than is observed.

If the MVW region has expanded at a constant velocity of V_{MVW} = 43 km s^{-1}, the size estimate of 1.5×10^{17} cm gives an age for the MVW of $\sim 10^3$ years. This is similar to the times of 500 and 5000 years that Schönberner (1983) calculated as the times required for post-AGB stars with masses of $0.8M_\odot$ and $1.0M_\odot$, respectively, to reach spectral type F5 (T_{eff} = 6500 K). Perhaps the mass loss process changes as the star leaves the AGB, and this change results in the remainder of the red giant envelope being expelled at a higher velocity. On the other hand there is no spectral feature similar to that of the MVW in the spectrum of CRL 618, which also left the AGB recently.

6. Conclusions

The spectra of the post-AGB star CRL 2688 presented here have revealed several new features. A high velocity wind (HVW) of at least $\sim$ 100 km s^{-1} has been seen, along with the 45 km s^{-1} and 23 km s^{-1} winds which had been detected in earlier studies. In addition an absorption feature on the blue side of the spectrum has been observed at high spectral resolution and shown to have a distinctive shape. A simple model has been developed which accurately reproduces the shape of this feature, from which it is deduced that the radius of the MVW is about one half that of the LVW, and that the turbulent velocity is about 0.5 km s^{-1}. The velocity field is therefore well ordered, providing a constraint for binary models of this object. The shape of the blue edge of the absorption feature also argues against bulk motions exceeding 0.5 km s^{-1} in the expanding envelope, such as would be introduced by a rotation.

We would like to thank the staff of the CSO for their help and support, and particularly Antony Schinckel and Maren Purves, for collecting the $^1H^{12}C^{14}N$(4–3) data. We would also like to thank Tom Geballe for his helpful comments of this paper's original draft. This work was supported by NSF contract #AST 90–15755.

References

Bieging J. H., & Nguyen-Quang-Rieu 1988, ApJ, 324, 516

Burton, M. G., & Geballe, T. R. 1986, MNRAS, 223, 13p

Carsenty, U., & Solf, J. 1982, Astron. Astrophys, 106, 307, 1982

Cernicharo, J., Guélin, M., Martín-Pintado, J., Peñalver, J., and Mauersberger, R. 1990, A&A, 222, 1(L)

Crampton, D., Cowley, A. P., & Humphreys, R. M. 1975, ApJ, 198, L135

DeLucia, F., & Gordy, W. 1969, Phys. Rev., Vol 187, No 1, 58

Ellison, B. N., & Miller, R. E. 1987, Int'l J. IR & MM Waves, Vol. 8, No. 6, 609

Ellison, B. N., Schaffer, P. L., Schaal, W., Vail, D., & Miller, Ron E. 1989, Int'l J. IR & MM Waves, Vol. 10, No. 8

Gammie, C. F., Knapp, G. R., Young, K., Phillips, T. G., & Falgarone, E., 1989, Astrophys. Space Sci., 345, 87(L)

Heiligman, G. M., *et al.* 1986, ApJ, 308, 306

Iben, I., & Renzini, A. 1983, ARA&A, 21, 271

Kawabe, R., *et al.* 1987, ApJ, 314, 322

Keen N. J., Mischerikow, K. D., Ediss, G. A., Perchtold, E. 1986, Electronics Letters, Vol 22 No 7, 353

Knapp, G. R., Phillips, T. G., Leighton, R. B., Lo, K. Y., Wannier, P. G. and Wootten H. A. 1982, ApJ, 252, 616

Knapp, G.R. 1986, ApJ, 311, 731

Kwok, S., & Bignell, R. C. 1984, ApJ, 276, 544

Morris, M., Lucas, R., & Omont, A. 1985, A&A, 142, 107

Morris M., & Alcock, C. 1977, ApJ, 218, 687

Morris, M. 1980, ApJ, 236, 823

Morris, M. 1981, ApJ, 249, 572

Morris, M. 1987, PASP, 99, 1115

Ney, E. P., Merrill, K. M., Beklin, E. E., Neugebauer, G., & Wynn-Williams, C. G. 1975, ApJ, 198, L129

Olofsson, H. 1988, Space Science Reviews, 47, 145

Press, W. H., Flannery, B. P., Teukolsky, S. A., Vetterling, W. T., 1988, Numerical Recipes in C, (Cambridge University Press)

Rodriguez, L. F. 1987, Planetary and Proto-Planetary Nebulae: From IRAS to ISO, ed. A. P. Martinez, p. 55, (D Reidel)

Schönberner, D. 1983, ApJ, 272, 708

Smith, M. G., Geballe, T. R., Sandell, G. & Aspin, C. 1990, Submillimetre Astronomy, ed. G. D. Watt and A. S. Webster, p. 29, (Kluwer Academic Publishers)

Sopka, R. J., Olofsson, H., Johansson, L. E. B., Nguyen-Q-Rieu, and Zuckerman, B. 1989, A&A, 210, 78

Spergel, D. N., Giuliani, J. L., Knapp, G. R., 1983, ApJ, 275, 330

Truong-Bach, Morris, D., Nguyen-Q-Rieu, & Deguchi, S. 1990, A&A, 230, 431

Wannier, P. G., & Sahai, R. 1987, ApJ, 319, 522

Westbrook, W. E., Becklin, E. E., Merrill, K. M., Neugebauer, G., Schmidt, M., Willner, S. P., & Wynn-Williams, C. G. 1975, ApJ, 202, 407

Yusef-Zadeh, F., Morris, M., & White, R. L. 1984, ApJ, 278, 186

Addendum

The Existence of an H II Region in CRL 2688

Perhaps the most important conclusion of this chapter is that a protoplanetary nebula can produce a High Velocity Wind (HVW) before it has developed an H II region. This casts doubt on the idea that the fast wind often seen in the spectra of planetary and protoplanetary nebulae is accelerated by an ionization shock–front. Therefore, for the sake of completeness, is should be pointed out that Sahai, Claussen and Masson (1989) reported the "tentative" ($\sim 4\sigma$) detection of 1.5 cm continuum emission at the VLA. The authors suggest that this radiation arises in an optically thick H II region with a radius of 0.02". This would correspond to a few stellar radii at a distance of 1 kpc. It seems very unlikely that such a small H II region could be responsible for the acceleration of the HVW. If the HVW emission arose from the surface of a region this small, the CSO's 20" CO(3–2) beam would dilute the signal by a factor of $\gtrsim 10^5$. Detection of line emission from a region this small would probably only be possible if a CO maser were present, which seems *extremely* unlikely given the large width and smooth shape of the HVW profile. Other attempts to detect continuum emission using the VLA (e.g., Spergel, Giuliani and Knapp 1983) have been unsuccessful.

References

Sahai, R., Claussen, M. J. & Masson, C. R. 1989, A&A, 220, 92

Spergel, D. N., Giuliani J. L. Jr. & Knapp, G. R. 1983, ApJ, 275, 330

Neutral and Ionized Carbon in the Envelope of NGC 7027

K. Young[1], *Jocelyn Keene*[1], *T. G. Phillips*[1], *A. Betz*[2] *and R. Borieko*[3]

[1]California Institute of Technology, Pasadena, CA 91125

[2]Space Sciences Lab, University of California, Berkeley, CA 94720

[3]CASA, University of Colorado, Boulder, CO 80309

ABSTRACT

We have mapped the 609μm $^3P_1 \rightarrow {}^3P_0$ fine structure line of neutral atomic carbon (C I) in the young planetary nebula NGC 7027. The C I emission is extended over a region 30 – 40" in diameter. We deduce that in the inner half of the neutral envelope, its abundance is about 1/2 that of CO. We also obtained a spectrum of the 158μm $^2P_{3/2} \rightarrow {}^2P_{1/2}$ fine structure transition of singly ionized carbon (C II). We find that it is at least as abundant as CO in the inner "neutral" envelope. Based on these observations we suggest that the mass loss rate may be a factor of ~ 3 higher than the rate derived earlier from CO observations alone. This brings the mass loss rate into better agreement with that derived from observations of the H II region.

Subject headings: Planetary Nebulae: individual: NGC 7027 — ISM: atoms — Stars: circumstellar matter — Stars: post–asymptotic giant branch

1. Introduction

NGC 7027 is probably the most thoroughly studied of all the planetary nebulae. It is clearly quite young, because it still has a thick molecular envelope (Mufson and Lyon 1975) surrounding the ionized region, which is presumably a remnant of the material ejected while the star was

on the Asymptotic Giant Branch (AGB). The angular size of NGC 7027 is convenient for study with currently available instruments. Its H II region is about 8" across, allowing the ionized and molecular hydrogen to be mapped with an infrared array (Graham *et al.* 1993). Its CO envelope has a radius of $\sim 30''$, allowing the CO(1–0) line to be mapped with millimeter interferometers (Masson *et al.* 1985; Bieging *et al.* 1991) while higher J CO transitions can be mapped with single telescopes (Jaminet *et al.* 1991, hereafter JDS). Masson (1989) observed the nebula's free–free emission at 6 cm with the VLA. Using an innovative data processing algorithm, he was able to detect expansion of the ionized region, and to derive a distance of 880 pc, with a probable error of less than 20%.

Modeling of the thermal CO emission is believed to be one of the most reliable methods of deriving the mass loss rate ($\dot{M}$) for an evolved star. In addition, because CO is abundant in the outflows of both oxygen–rich and carbon–rich stars, this method can be applied to virtually any evolved star with a cool wind. Generally the assumption is made that all of the carbon (in the case of an oxygen–rich star) or oxygen (in the case of a carbon star) in the ejecta is locked up in CO molecules. At the outer edge of the molecular envelope (typically 0.1 to 0.3 pc from the star), the interstellar UV radiation field dissociates the CO. However a planetary nebula clearly has a source of UV radiation in the center, and it is likely that this radiation will destroy the molecular envelope from the inside out. In order to properly interpret the CO emission, it is essential to determine to what extent this has taken place.

Keene *et al.* (1993) have recently detected the 609μm C I line of neutral carbon in the prototypical carbon star IRC+10°216, an object which has not yet left the AGB. The CO emission is nearly as strong from NGC 7027 as from IRC+10°216; it seems reasonable to expect that NGC 7027's internal UV source would lead to even stronger 609μm emission in NGC 7027 than IRC+10°216. While an early attempt to detect the 609μm line in NGC 7027 was unsuccessful (Beichman *et al.* 1983), the advent of new more sensitive receivers combined with larger submillimeter telescopes on high mountain sites has allowed many heretofore undetectable objects to be detected and even mapped. The presence of ionized hydrogen in NGC 7027 also makes it natural to expect some ionized carbon to exist in a photodissociation region (PDR) surrounding the H II region. Although the 158μm transition of C II was previously detected (Ellis and Werner

1984), the Fabry–Perot spectrometer used did not have sufficient spectral resolution to provide a line profile. Resolving the line should provide important clues to the distribution of the C II gas.

2. Observations

The 609μm (492.1607 GHz) C I observations were carried out with the 10.4 m telescope of the Caltech Submillimeter Observatory* using the SIS receiver described by Walker *et al.* (1992). A typical single sideband (SSB) system temperature for this receiver is 1800 K, including the atmospheric noise contribution. A 1024 channel AOS with a total bandwidth of 500 MHz was used as the spectrometer backend.

Even on a high mountain site, the C I line can only be studied during periods of very good weather. Our C I observations were collected over 4 observing runs. The central position (α_{1950} = $21^h05^m09.46^s$, δ_{1950} = 42°02′02.6″) was observed during April 1992, and May 1992. Small maps were made during June 1992 and May 1993. In all cases, the spectra were calibrated by a chopper load at ambient temperature, giving antenna temperatures T_A^* which are corrected for atmospheric losses. This temperature was subsequently corrected for the main beam coupling efficiency measured on Jupiter, which ranged between 45% and 50% over the different obsering runs. Observations of Jupiter were also used to check the telescope pointing, which is believed to be accurate to $\lesssim$ 3".

The 158μm line of C II was observed in Oct 1992 with the far–infrared heterodyne spectrometer described by Boreiko *et al.* (1988), aboard the Kuiper Airborne Observatory. The beam is approximately 45" FWHM and the data were corrected for the efficiency measured on the moon. The receiver temperature was 13,000 K SSB.

---

* The CSO is operated by the California Institute of Technology under funding from the National Science Foundation, Contract #AST–9015755.

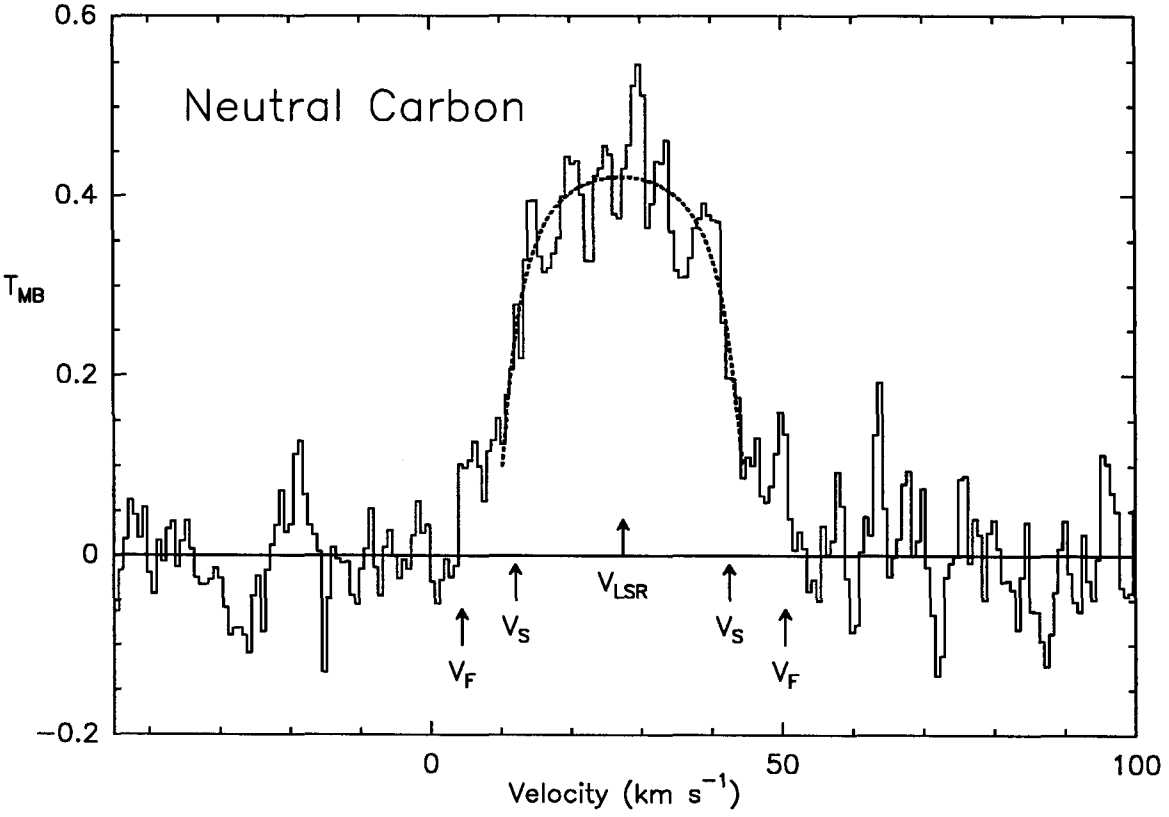

Fig. 1. A neutral carbon spectrum of the center position is shown. V_{LSR} is the systemic velocity, 27.4 km s^{-1}, deduced from this spectrum. The arrows marked V_S show the extent of the low velocity wind, which is seen to be extended in CO maps. V_F shows the extent of the high velocity wind, which is believed to be confined to a thin shell separating the low velocity wind from the HII region. Data from both April 1992 and May 1993 were combined to produce this spectrum. The dotted line shows the best fit of equation 1 to the low velocity wind portion of the profile.

3. Results

Figure 1 shows a combined C I spectrum from all the observations of the central position. Also shown is the least-squares best fit of a parameterized line profile (Morris 1984) for a circumstellar shell

$$T(v) = T_{max} W \left(\frac{1 - \exp(-\alpha/W)}{1 - \exp(-\alpha)} \right) \qquad \text{where} \quad W = 1 - \left(\frac{v - V_{LSR}}{V_o} \right)^2 . \qquad (1)$$

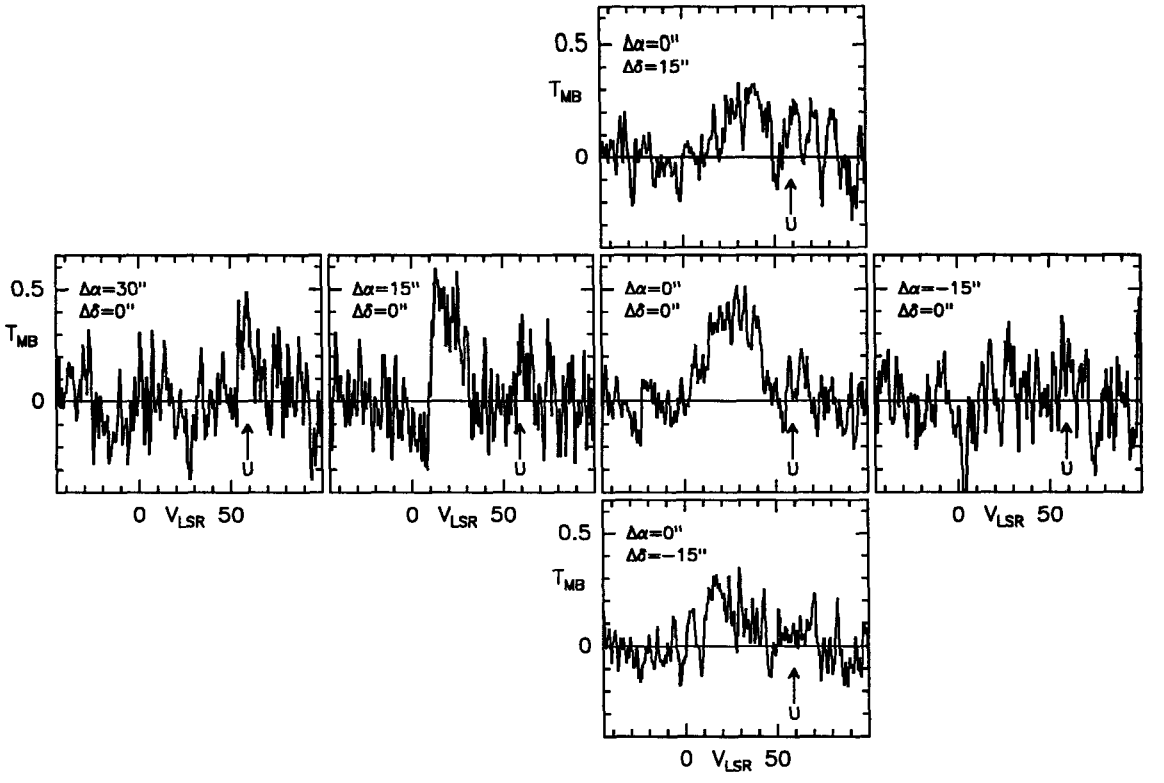

Fig. 2. A map of the neutral carbon emission from NGC 7027 is shown. The central position contains only about half the data that were averaged together to produce figure 1, because only the data taken during May of 1993 (when the rest of the map was made) were used. The adjacent cells are separated by one full beamwidth. The U marks the location of the additional unidentified line.

The best fit values were α = 0.6, T_{max} = 0.42 K, V_{LSR} = 27.3 km s^{-1} and V_o = 17.1 km s^{-1}. This value of α implies the optical depth of the line is modest. The best fit LSR velocity is about 2 km s^{-1} larger than is typically found by CO observations. JDS found that the CO envelope appears to have two regions with differing expansion velocities. Their data are best fit by an outer envelope expanding at 15.2 km s^{-1}, and an envelope unresolved by their 14" beam expanding at 23 km s^{-1}. The velocity extent of both of these wind components is shown in figure 1, and both components appear to have been detected.

Figure 2 shows the small C I map made in May 1993. The spectra in the map are separated from their nearest neighbors by 15", the FWHM of the CSO beam at 609μm. The source is clearly resolved by our beam, and there is a systematic velocity shift between the three spectra with $\Delta\alpha$ = 0. Perhaps the most striking feature of the map is the strength of the line at the

$\Delta\alpha = 15''$ position, especially when contrasted with the lack of emission at $\Delta\alpha = -15''$. Although this might indicate a significant East–West error in the telescope pointing, causing the map's $\Delta\alpha = 15''$ and central spectra to straddle the true center of the object, we believe that the effect is real for the following reasons. The map's central spectrum is quite symmetric and resembles the central spectrum obtained in April 1992. In contrast the $\Delta\alpha = 15''$ position is quite asymmetric with respect to the systemic velocity, with the integrated area of the blue–shifted half more than an order of magnitude larger than that of the red–shifted half. An RA strip map of C I was also made in June 1992. In spite of bad spectral baselines caused by very poor weather it too appears to show much stronger emission east of the center than west. It's unlikely that an identical pointing error would have occurred in three observing runs separated by a year. Finally, the CO emission is also stronger to the east of the source than to the west (JDS, Bieging *et al.* 1991 and Graham *et al.* 1993) through the asymmetry is not large in CO. If the optical depth of CO is greater than that of C I, that could explain why the asymmetry is stronger in a C I map. So we believe there is a real East–West asymmetry in the object, and while the map's central position could be offset to the west of the true center, the error must be considerably less than 1/2 of the beam width (7.5"), and was probably less than 3".

There appears to be an additional narrow line visible in most of the C I map positions, which peaks in intensity well away from the center. The frequency of this line, which we could not identify, is either 492.106 or 495.215 $\pm$0.003 GHz, depending on whether it was present in the signal or image sideband of the receiver. While the data were taken, the rest frequency of the center of the spectrometer backend was changed in steps over a range of about 30 MHz. It appears that the unidentified line moved relative to the C I line as a result of these frequency changes, which would indicate it was in the image sideband; but we cannot be certain of this. This unidentified line is not the same one as was seen by Keene *et al.* (1993) when they mapped C I in IRC+10°216.

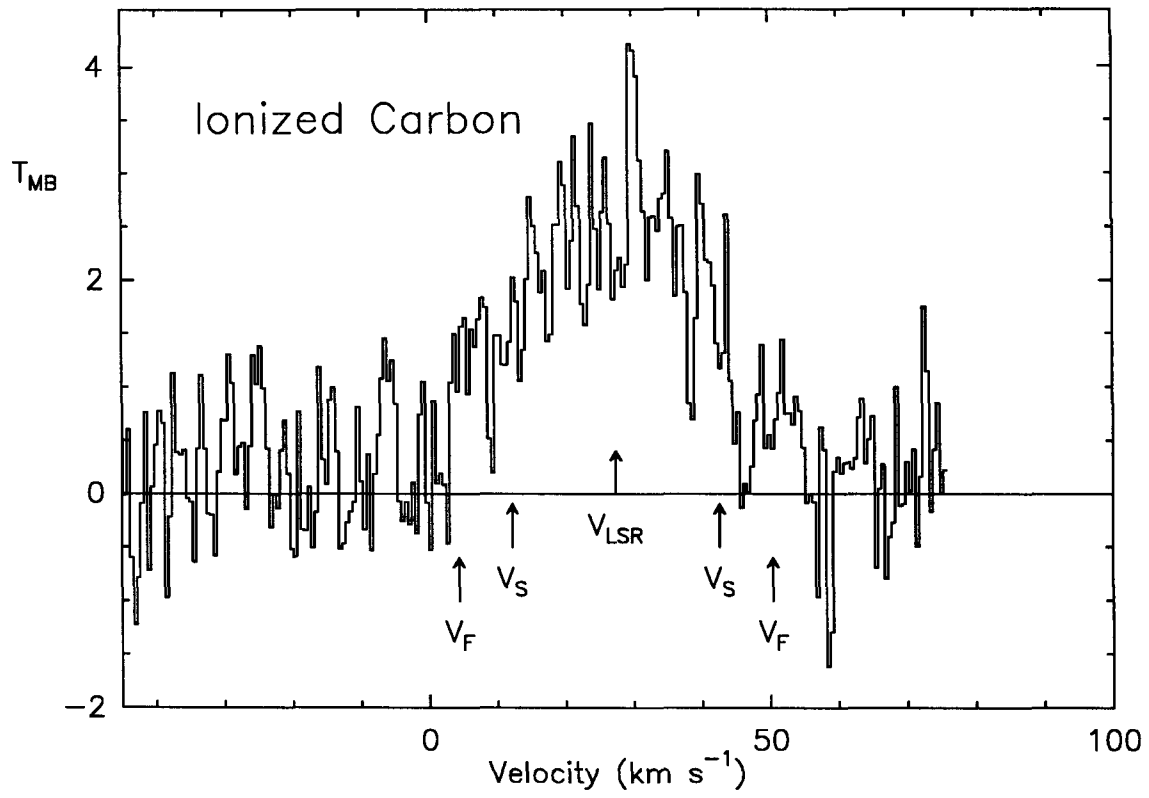

Fig. 3. A spectrum of the emission from singly ionized carbon is shown. The arrows are as explained in the caption of figure 1.

Figure 3 shows the 158μm spectrum taken from the KAO. While no map was made of this line, the KAO's beam has a FWHM of 44", which would cover most of the CO envelope. It appears that emission from the high velocity wind is visible in figure 3 also.

4. Analysis

4.1 Neutral Carbon

The velocity shifts of the spectral peaks in the C I map have the same signs as the shifts seen in the CO(1–0) interferometer maps and the JDS CO(3–2) map, which was made with a beam of the same size as ours. However in the JDS map, which covers a larger area and was sampled on a finer grid than our C I map, the CO lines are strongly asymmetric only at the 1/2 beam (7.5") offset positions. At the full beam offset points which overlap our map positions,

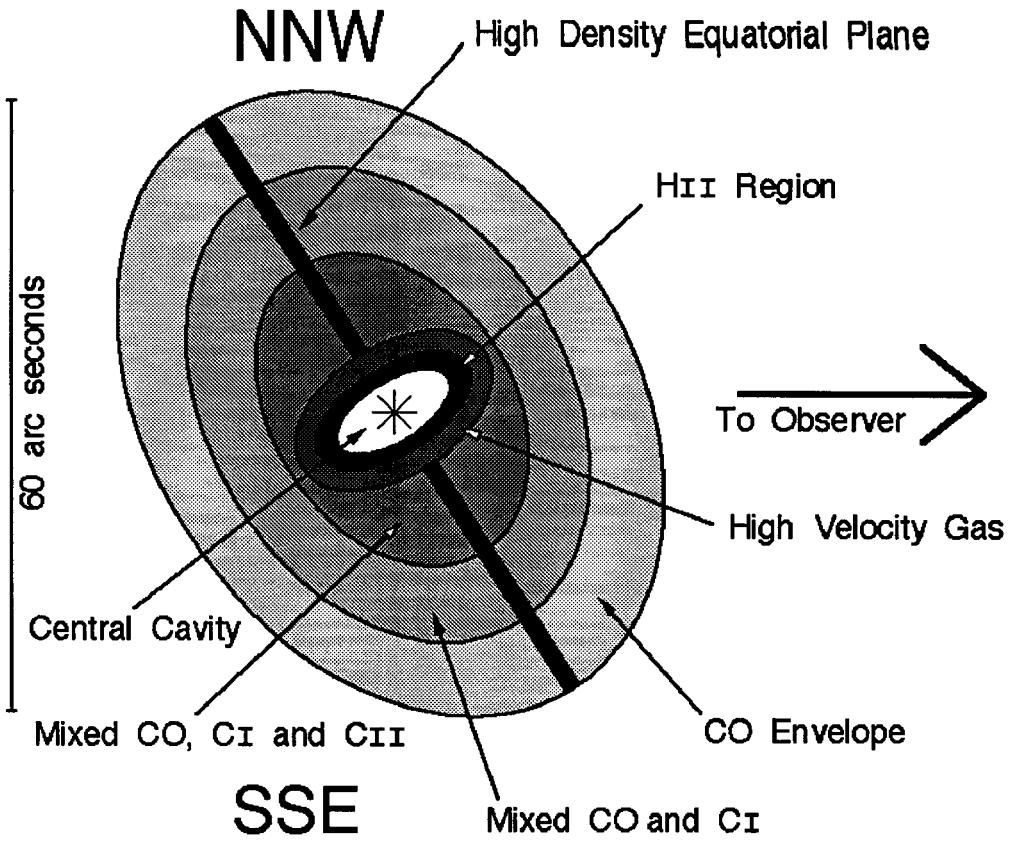

Fig. 4. A schematic representation of NGC 7027 is shown, with its various regions shown to approximately the same scale.

the velocity asymmetry in the JDS spectra is much weaker than in our CI map. Masson *et al.* (1985) deduced a model for the molecular and ionized regions of NGC 7027, which is reproduced schematically (along with additions indicating where we believe the CI and CII emission originates – see below) in figure 4. The CO envelope is an oblate spheroid, with enhanced density along the equatorial plane. The HII region, about 9" in diameter, is confined by the molecular envelope. The lower density of the symmetry axis of the molecular envelope has provided a preferred direction of growth, forming the H II region into a prolate spheroid with the same symmetry axis. Both optical emission line (Atherton *et al.* 1979) and radio interferometry studies (Masson 1989) have shown that this shared symmetry axis is inclined to our line of sight by about 30°.

While the wings on the C I spectrum in figure 1 indicate that some of the C I emission arises from the high velocity gas near the H II region (which was unresolved in the JDS map), our C I map shows that there is a significant amount of atomic carbon within the slower AGB

remnant wind. The best–fit of equation 1 produced a moderately rounded profile covering the low velocity wind region of the central position's spectrum. JDS present profiles of several ^{12}CO and ^{13}CO transitions obtained with beam sizes comparable to our 609μm beam. Optically thin emission from an expanding shell will produce spike or flat-topped spectra as are seen in the JDS ^{12}CO(1–0), ^{13}CO(2–1) and ^{13}CO(3–2) spectra. A moderately optically thick transition will produce a rounded profile. Finally at large optical depths, the line becomes asymmetric and the blue–shifted half is self-absorbed as is seen in the JDS ^{12}CO(3–2) spectrum. Thus if the C I is distributed in much the same way as the CO, as our map indicates it is, the rounded but symmetric shape of the central profile indicates the optical depth of the 609μm line is of order unity.

If we assume that the CI line is in LTE everywhere, then we can estimate the total amount of C I in the envelope. Ordinarily, it is difficult to make such an estimate from a single transition of low optical depth, because the excitation temperature, T_{ex}, is unknown. This problem is simplified in the case of C I. The atom has a triplet ground state giving rise to two hyperfine transitions; the 609μm $^3P_1 \rightarrow {}^3P_0$ line we observed, and the $^3P_2 \rightarrow {}^3P_1$ transition at 370μm. These two transitions have energies $h\nu/k$ of 23.6 K and 38.9 K respectively. The next highest electronic levels are 14,000 K above the ground state. Therefore there is a large range of T_{ex} over which only the ^{3}P ground states are populated, and throughout much of that range the fraction of carbon in the $^3P_1$ level,

$$N_1 = \left(1 + (1/3)e^{23.6/T_{ex}} + (5/3)e^{-38.9/T_{ex}}\right)^{-1}$$

(Phillips and Huggins 1981) is largely determined by the statistical weights of the ^{3}P states rather than T_{ex}. Using an LVG radiative transfer model, JDS derived physical parameters for the CO envelope. Their best–fit model has a kinetic temperature above 14 K out to a radius of 20". If we adopt the temperature profile of JDS, then N_1 varies by less than 30% over the area covered by the five innermost points in our map, excluding the H II region. Its mass weighted average is 0.42. The mass loss rate derived by JDS, $\sim 10^{-4}\ M_\odot \mathrm{yr}^{-1}$, is large enough to ensure that the density everywhere within our map is well above the critical density for the $^3P_1 \rightarrow {}^3P_0$ transition ($\sim 10^3$ cm^{-3}). However at radii larger than 20" the JDS model implies that a significantly smaller fraction of any atomic carbon would exist in the $^3P_1$ state, both because of a rapid change in

the partition function and because the gas density falls below the critical value. This drop in excitation, rather than an absence of C I, may be the reason that we saw no emission in our map's $\Delta\alpha = 30''$ spectrum.

Our 6 point map was undersampled, and certainly missed some of the C I emission. On the other hand the fact that no emission was seen in the $\Delta\alpha = 30''$ spectrum suggests that little or no 609μm emission is present much beyond 20" from the center. A fair estimate of the total 609μm flux from NGC 7027 can be obtained by adding the flux from the center position to twice the combined flux from the four adjacent offset positions. If we integrate the line over the entire extent of the high velocity wind, this procedure yields a total flux, F, of 2.74×10^{-21} W cm^{-2}. The mass of C I is

$$F \times 4\pi D^2 \times \frac{1}{h\nu} \times \frac{1}{A_{10}} \times \frac{1}{N_1} \times \frac{m_C}{M_\odot} \times \frac{\tau}{1 - e^{-\tau}} = 3.7 \times 10^{-4} M_\odot \qquad (2)$$

where D is the distance to the source, A_{10} is the Einstein A coefficient for the 609μm line (7.9×10^{-8} sec^{-1}), m_C is the mass of a carbon atom and τ is the optical depth, assumed here to be 1.

4.2 Ionized Carbon

The 158μm emission arises from downward transitions between the J = 3/2 and 1/2 levels of the ^{2}P ground state of C II. As with C I, the next highest level above the ground state requires so much energy, E/k = 62,000 K in this case, that it is not apt to be significantly populated. The ion is then a 2–level system, and the fraction of ionized carbon in the upper level is (Crawford *et al.* 1985)

$$N_{3/2} = \frac{2e^{-h\nu/kT}}{1 + 2e^{-h\nu/kT} + n_{crit}/n}$$

where n_{crit}/n is the ratio of the gas density to the critical value needed to thermalize the transition. This critical density for excitation by collisions is 3000 cm^{-3} for atomic hydrogen, 5000 cm^{-3} for H_2 and $0.79[T(K)]^{1/2}$ for electrons (Launay and Roueff 1977). If the C II emission arises

from a region with a density well above 5000 cm^{-3}, and a temperature well above 91 K, then the partition function reduces to $N_{3/2} \approx 2/3$. Unfortunately neither of these conditions is apt to hold throughout the envelope of NGC 7027, but because $N_{3/2}$ is never larger than 2/3, we can derive a lower limit for the amount of C II present by assuming that they do. The integrated line area in figure 3 is 86 K km s^{-1}, giving a flux of 2.4×10^{-18} W cm^{-2}. If we assume that the emission is optically thin ($\tau \ll 1$), and that the KAO's beam covers the entire emitting region, we can again use equation 2 to estimate the mass of the emitting material. In this case the relevant Einstein coefficient is 2.36×10^{-6}, and the implied minimum ionized carbon mass is $1.1 \times 10^{-3}\ M_{\odot}$.

Not having a map of C II, it will be difficult to determine where in the envelope 158μm emission originates. Some could arise from the H II region, but it is unlikely that more than a few percent does. Emission lines from higher transitions of C II were seen by the *IUE* (Middlemass 1990) , but the H II region contains other carbon ions (up to C V). Middlemass (1990) analysed dozens of emission lines from the ionized region, and concluded that less than 10% of the carbon in the H II region is in the C II state. Using the results of his model, the mass of carbon atoms in the H II region is $6 \times 10^{-5}\ M_{\odot}$, only 5% of our lower limit for the total amount of C II in the object. Further, the presence of UV emission lines from C II shows that not all of that C II is in the ^2P level, and capable of producing the 158μm emission line. Therefore the bulk of the C II we see must reside in the neutral envelope. In figure 3, the ratio of the intensity in the high velocity wings ($V_S < |V| < V_F$) to that of the line center is about 0.5; twice as high as in the central C I position (figure 1). Had the C I central spectrum been taken with as large a beam as that used for the C II spectrum, this disparity would have no doubt have been even greater, because nearly all of the emission seen in the off–center positions of the C I map arises within the velocity limits of the slow wind. It is therefore likely that a greater fraction of the C II emission originates in the high velocity gas than does the C I emission.

Could all of the C II reside in the high velocity wind region? We can calculate the minimum radial extent of the 158μm emission if we assume it arises from a layer in which all the carbon is atomic, singly ionized, and in the ^{2}P level. If we adopt the elemental abundances derived by Middlemass, the mass of C II we observe must have been shed along with 0.14 $M_\odot$of other elements. Assuming $\dot{M} = 1.6 \times 10^{-4}\ M_\odot \mathrm{yr}^{-1}$ (see section 5) and the outflow velocity of the fast wind, 23 km s^{-1}, the 0.14 $M_\odot$of material containing the C II would have to have a radial extent of 5". The interferometer maps of CO emission would then show a 5" gap between the outer edge of the H II region, and the inner edge of the CO. However Graham *et al.* (1993) present maps that show the separation between the CO and the H II region is not nearly this large. Therefore the C II must be coextensive with the CO, which requires the C II to be spread over a even larger region. Because the radius of the H II region is $\sim 4.5''$, the outer edge of the 158μm emission must be further than 10" from the center, which is the well beyond the outer edge of the region from which JDS claims the high velocity emission arises. Keeping in mind that our estimate of the mass of C II is merely a lower limit, it then seems extremely unlikely that the C II arises only from the high velocity region. A more likely picture is that the CO, C I and C II are coextensive in the high velocity wind region, and at least the inner portion of the slower AGB remnant wind from which most of the CO emission arises (see figure 4).

5. Discussion

The estimates of $\dot{M}$ for NGC 7027 derived from CO observations have shown considerable scatter. When scaled to Masson's distance estimate of 880 pc, the published estimates range from $6.0 \times 10^{-5}\ M_\odot \mathrm{yr}^{-1}$ (Jura 1983) to $3.3 \times 10^{-4}\ M_\odot \mathrm{yr}^{-1}$ (Knapp *et al.* 1982). None of the estimates is nearly as large as that derived by Masson *et al.* (1985) who calculated that a mass loss rate of $9.1 \times 10^{-4}\ M_\odot \mathrm{yr}^{-1}$ was required to produce a dense enough neutral envelope to confine the H II region. Some of the scatter in the CO based values is probably due to the fact that the CO line formation models have assumed spherical symmetry, even though the observations indicate that the envelope density is greater in the object's equatorial plane. JDS derived mass loss rates of 2.2×10^{-4} and $1.0 \times 10^{-4}\ M_\odot \mathrm{yr}^{-1}$ in the directions of the equatorial plane and polar axis, respectively. If we take the average of these two values to be the overall $\dot{M}$, we obtain

a rate which fits comfortably near the middle of the other CO based estimates. We may use this estimate to calculate the total number of carbon atoms locked up in CO molecules within the region covered by our C I and C II data. This region, which we shall refer to as the "inner neutral envelope", extends from the outer edge of the H II region, about 4.5" from the star, to 20". Using the slow wind velocity as the expansion rate, and the JDS estimate of the CO:H_2 abundance ratio (2×10^{-4}), the total mass of carbon in CO molecules within this region is $8 \times 10^{-4}\ M_{\odot}$. This is about twice the amount of carbon seen in our C I map, but only 3/4 as large as the lower limit to the mass of C II. Considering that the mass estimates for C II is a lower limit, it appears that in the inner neutral envelope no more than 1/3 of the gas phase carbon, and perhaps less, is to be found in CO.

NGC 7027's AGB progenitor was almost certainly a carbon star. Estimates of its [C]/[O] ratio, based on emission lines from the H II region, range from 2.3 (Middlemass 1990) to 3.5 (Zuckerman and Aller, 1986). The presence of HCN in the cool wind (Deguchi, Claussen and Goldsmith 1986) shows that the transition to a carbon star was not so recent as to have affected only the innermost envelope where the H II region resides. Thus not all of the carbon would have been incorporated into CO during the star's superwind phase, and several possible sources exist for the C I and C II now present.

There is both theoretical and empirical evidence that most of the atomic carbon we see in NGC 7027 was incorporated into either dust or molecular gas while the star was still on the AGB. Models of circumstellar chemistry predict that at the innermost portion of the AGB wind, chemical reactions reach thermodynamic equilibrium, and very little material is shed in the form of radicals such as atomic carbon (Omont 1987). It is likely that in the outer envelope photodissociation of CO and other carbides will give rise to thin shells of C I, and this is probably what is seen in IRC+10°216 (Keene *et al.* 1993). But a resolved shell of C I would lead to a spectrum with 2 peaks at $V_{LSR} \pm V_S$, markedly different than the line profile that we see at the central position of NGC 7027. Furthermore, the envelope of NGC 7027 appears to contain at least an order of magnitude more C I than Keene *et al.* saw in IRC+10°216. Finally, C II has been searched for but not detected in IRC+10°216. We established an upper limit on the 158μm flux for IRC+10°216, again using the KAO, of $\sim 1/4$ the flux we see in NGC 7027. So it appears that NGC 7027 has

much more atomic carbon in its envelope than a cool carbon star would have.

If the atomic carbon was not present in the original AGB wind, then it must have been liberated from some carbon reservoir. The shock front surrounding the H II region no doubt affects the envelope's chemistry. But the shock itself could not have released the atomic carbon, because our C I map shows that the atomic carbon exists throughout most of the neutral envelope. It is more likely that the UV radiation from the central star has freed the carbon. There are two potential reservoirs; the dust and the molecular gas. Assuming NGC 7027's AGB progenitor was a carbon star, much of the carbon which could not be incorporated into CO molecules must have been locked into carbon–rich dust grains. However there is abundant evidence that dust grains are less apt to be decomposed by UV radiation than is molecular material. Dust grain evolution models indicate that grains are more apt to be destroyed by sputtering collisions than by the action of radiation, and the large scale height of dust in our galaxy indicates that dust can survive for tens of megayears in the interstellar radiation field (Ferara *et al.* 1991). The molecular material, on the other hand, is unable to survive unshielded exposure to interstellar UV radiation even for a period of a few hundred years (Huggins and Glassgold 1982). The weakness of HCN emission from NGC 7027 (Sopka *et al.* 1989), relative to what is seen in carbon–rich protoplanetary nebulae such as CRL 618 and CRL 2688, indicates that some molecular species may have been nearly totally destroyed. One would expect that a self–shielding molecule such as CO would survive UV exposure for a longer period than would molecules which can be dissociated by broad–band UV radiation. But no other carbon–bearing molecular species is nearly as abundant as CO in an AGB star's wind (Omont 1987). Therefore, for atomic carbon to have an abundance greater than that of CO, as is the case in the inner neutral envelope, the carbon must have been liberated by the destruction of at more than half of the CO.

The fact that destruction of CO was the source for the atomic carbon can help resolve the discrepancy between estimates of $\dot{M}$ derived from CO observations, which cluster around $1.5 \times 10^{-4}\ M_{\odot}\ \mathrm{yr}^{-1}$, and that of Masson *et al.* (1985), who estimated that an $\dot{M}$ six times that large was required to confine the H II region. Because NGC 7027's envelope is carbon rich, it is usually assumed that the amount of CO is limited by the availability of oxygen, and that the CO:H_2 abundance ratio (hereafter f) is equal to the abundance ratio of oxygen alone (note that

this assumption was apparently not made in JDS). But if 2/3 of the CO molecules have been destroyed, a value for f obtained in this way will be a factor of 3 too high. Knapp and Morris (1985) showed that for their radiative transfer model the calculated value of $\dot{M}$ is approximately inversely proportional to f, as one would expect intuitively. Thus if f is only 1/3 of the abundance of oxygen, the CO based $\dot{M}$ should be increased by a factor of 3. This would bring most of the CO based estimates into agreement with that of Masson *et al.* , to within a factor of 2.

Finally, the presence of so much atomic carbon in the inner neutral envelope can help resolve a puzzle posed by JDS. These authors point out that the C:H ratio found in the H II region implies that if the ionized and neutral regions of the envelope have identical elemental abundances, then only about 5% of the total carbon is incorporated into CO molecules in the neutral region. They find this fraction implausibly low, and postulate that the heavy element abundance in the ionized region is considerably greater than in the neutral envelope. However if the atomic carbon we see arose at the expense of CO, then the CO in the neutral wind originally contained at least 15% as much carbon as is seen in the H II region and, perhaps more importantly, at least 50% of the oxygen found in the H II region. Therefore no dramatic difference in heavy element abundances between the neutral and ionized regions is required to explain the data.

We would like to thank the staff of the CSO and KAO for their help in acquiring the data presented here. Gene Serabyn provided numerous helpful suggestions to improve an early draft of this paper. This work was supported by NSF contract #AST 90–15755.

References

Atherton, P. D., Hicks, T. R., Reay, N. K., Robinson, G. J., Worswick, S. P. & Phillips, J. P. 1979, ApJ, 232, 786

Beichman, C., A., Keene, J., Phillips, T. G., Huggins, P. J., Wootten, H. A., Masson, C. & Frerking, M. A. 1983, ApJ, 273, 633

Beiging, J. H., Wilner, D. & Thronson, H. A. 1991, ApJ, 379, 271

Boreiko, R. T., Betz, A. L. & Zmuidzinas, J. 1988, ApJ, 325, L47

Crawford, M. K., Genzel, R., Townes, C. H. & Watson, D. M. 1985, ApJ, 291, 755

Deguchi, S., Claussen, M. J. & Goldsmith P. F. 1986, ApJ, 303, 810

Ellis, H. B. & Werner, M. W. 1984, B.A.A.S., 16, 463

Ferrara, A., Ferrini, F., Franco, J. & Barsella, B. 1991, ApJ, 381, 137

Graham, J. R., Serabyn, E., Herbst, T. M., Matthews, K., Neugebauer, G., Soifer, B. T., Wilson & T. D. & Beckwith, S. 1993, AJ 105, 250

Huggins, P. J. & Glassgold, A. E. 1982, ApJ, 252, 201

Jaminet, P. A., Danchi, W. C., Sutton, E. C., Russell, A. P. G., Sandell, G., Bieging, J. H. & Wilner, D. 1991, ApJ, 380, 461, (JDS)

Jura, M. 1983, ApJ, 275, 683

Keene, J., Young, K., Phillips, T. G., Büttgenbach, T. H. & Carlstrom, J. E. 1993, *submitted* ApJ letters.

Knapp, G. R., Phillips, T. G., Leighton, R. B., Lo, K. Y., Wannier, P. G., Wootten, H. A. & Huggins, P. J. 1982, ApJ, 252, 616

Knapp, G. R. & Morris, M. 1985, ApJ, 292, 640

Launay, J. M. & Roueff, E. 1977, J. Phys. B, 10, 879

Masson, C. R. 1989, ApJ, 336, 294

Masson, C. R., Cheung, K. W., Berge, G. L., Claussen, M. J., Heiligman, G., M., Leighton, R. B., Lo, K. Y., Moffet, A. T., Phillips, T. G., Sargent, A. I., Scott, S. L. & Woody, D. P. 1985, ApJ, 292, 464

Middlemass, D. 1990, NMRAS, 244, 294

Morris, M. 1984, Mass Loss from Red Giants, ed M. Morris and B. Zuckerman, page 129, D. Reidel

Mufson, S. L. & Lyon, J. 1975, ApJ, 201, L85

Omont, A. 1987, Astrochemistry, IAU Symp. 120, (Dordrecht: Reidel)

Phillips, T. G. & Huggins, P. J. 1981, ApJ, 251, 533

Sopka R. J., Olofsson, H., Johansson, L. E. B., Nguyen-Q-Rieu & Zuckerman, B. 1989, A&A, 210, 78

Walker, C. K., Kooi, J. W., Chan, M., LeDuc, H. G., Carlstrom, J. E., & Phillips, T. G. 1992, Int. J. IR and MM Waves, 13, 785

Zuckerman, B. & Aller, L. H. 1986, ApJ, 301, 772